ΕΘΝΙΚΟ ΜΕΤΣΟΒΙΟ ΠΟΛΥΤΕΧΝΕΙΟ
ΣΧΟΛΗ ΧΗΜΙΚΩΝ ΜΗΧΑΝΙΚΩΝ
NATIONAL TECHNICAL UNIVERSITY OF ATHENS
SCHOOL OF CHEMICAL ENGINEERING

ΠΡΟΣΟΜΟΙΩΣΕΙΣ ΠΟΛΛΑΠΛΗΣ ΚΛΙΜΑΚΑΣ ΔΙΣΚΟΜΟΡΦΩΝ ΥΛΙΚΩΝ

MULTISCALE SIMULATIONS OF DISCOTIC MATERIALS

Ορέστης Γεώργιος Ζιώγος
Orestis George Ziogos

Διδακτορική Διατριβή υποβληθείσα στη Σχολή Χημικών Μηχανικών του Εθνικού Μετσόβιου Πολυτεχνείου για την απόκτηση του τίτλου του Διδάκτορος του Εθνικού Μετσόβιου Πολυτεχνείου

Αθήνα
Athens, Greece

2018

Dedication

To my loved ones:
Ulysses, Agnes, Chrissa, and Dimitra

"What I cannot create, I do not understand"
R. Feynman

Contents

Acknowledgements

First and foremost, I would like to thank my supervisor Prof. Doros Theodorou for entrusting me with such a challenging and ambitious project that eventually materialized into this doctoral dissertation. My gratitude also accounts for the countless hours of scientific counseling and vivid discussions, and for procuring the necessary funding and resources which allowed the completion of the current work.

I owe many thanks to Assoc. Prof. Leonidas Tsetseris for introducing and coaching me into the realm of Computational Quantum Mechanics and for helping me tackle scientific conundrums emerging over the past years. I would also like to thank Prof. George Floudas for fruitful discussions regarding experimental aspects of discotic materials and Prof. Polykarpos Pissis for honoring me by participating in my three-member advisory committee. Special thanks are also due to Prof. Costas Charitidis, Assoc. Prof. Vagelis Harmandaris, and Prof. Christos Likos for accepting to participate in my seven-member examination committee.

I also thank Dr. Denis Andrienko for helping me sort out issues regarding atomistic simulations of discotic materials and Dr. Kenno Vanommeslaeghe for providing me with a stand-alone version of the CGenFF converter on behalf of the ParamChem project. I would also like to thank Dr. Georgios Vogiatzis for a series of interesting discussions about soft matter modeling and Dr. Stefanos Anogiannakis for providing me with critical insight regarding macromolecular simulations.

Last but not least, I would like to thank my parents, Ulysses and Agnes, for supporting me over the past years, my sister Chrissa for introducing me to the world of computer programming, and my wife Dimitra for the support and encouragement that helped me finish my doctoral studies.

As far as the funding bodies of this scientific endeavor are concerned, this research has been co-financed by the European Union (European Social Fund - ESF) and Greek national funds through the Operational Programme "Education and Lifelong Learning" of the National Strategic Reference Framework (NSRF) - Research Funding Programme: THALIS - Investing in knowledge society through the European social fund [grant number MIS 379436] and by the IKY Fellowships of Excellence for Postgraduate Studies in Greece - Siemens Programme [award number 11126/13a].

This work was also supported by computational resources granted by the Greek Re-

search & Technology Network (GRNET) on the National HPC facility "ARIS" under the projects "Multiscale Simulations of Crystalline and Liquid-Crystalline Systems - Multi-CLC", "Hierarchical Modeling of Soft Matter - HMSM", and "Molecular Simulations of Membrane- based Systems - MSMS".

Summary

Soluble disc-shaped organic molecules with the ability to self-organize into intricate supramolecular assemblies constitute a very promising materials family for a plethora of applications. In the case of polyaromatic hydrocarbon (PAH) mesogens, delocalized π interactions enable such materials to be used as active media for organic electronic applications.

This doctoral dissertation is primarily focused on multiscale simulations of discotic materials by means of *ab-initio* Density Functional Theory (DFT) calculations and empirical Molecular Mechanics and Molecular Dynamics (MD) simulations for the determination of structure-property relationships, ranging from electronic and charge transfer properties at the quantum level of description to structural, mechanical, and dynamical characterization of periodic bulk systems at the nanoscale regime.

As regards systems under study, molecules belonging to the so-called nanographene family are examined, with particular focus placed on the hexa-*peri*-hexabenzocoronene (HBC) molecule and its derivatives, utilizing a variety of peripheral functional groups. Quantum mechanical (QM) calculations are employed for the conduction of comparative studies involving molecules from the very smallest discotic unit, i.e. the benzene molecule, up to large polyaromatic assemblies, covalently-linked into forming articulate discotic "super-molecules". Electronic and charge transfer properties are examined at the single molecule and molecular dimer levels of description via ground-state DFT calculations.

Alkyl-substituted HBC derivatives, either in non-polar or polar variants by means of iodine atom peripheral functionalization, are examined through empirical MD simulations, aiming at the determination of structural, mechanical, and dynamical properties for given temperature and pressure conditions. PAH stacking patterns are thoroughly examined, a structural feature of paramount importance, since QM studies both in this work and in the literature confirm the direct link between charge transfer capabilities and core packing motifs.

Amphiphilic, "Janus-type" HBC derivatives are also examined by means of MD simulations. Mesogens under study carry both hydrophilic and hydrophobic side chains, thus enabling the formation of lamellar molecular crystals. The effect of temperature rise on structural and dynamical properties is examined, while gaining an atomistic insight of the melting process for such materials.

Atomistic MD simulations are also put to use for the examination of molecular crystals of functionalized extended discotics, namely the superphenalene C96 and the tetragonal C132 molecules, characterized by a 3-fold and 4-fold expanse, respectively, compared to HBC. Apart from single core discotics, covalently-linked assemblies in the form of the HBC dumbbell and star-shaped, tri-arm "super-molecules" with HBC, C96, and C132 terminal cores are modeled by means of MD simulations, elucidating their tendency to form structurally robust chiral molecular nanowires, densely packed into hexagonal molecular crystals. A multiscale methodology is adopted, using information from *ab-initio* DFT calculations, in order to provide insight for possible charge transfer mechanisms pertinent to such assemblies.

As regards initial configurations to be used as input for atomistic simulations, in cases where crystallographic constructions are not applicable or desirable, a hybrid MC bond-by-bond growth methodology is proposed and utilized, capable of growing soft nanophases out of rigid nanostructured areas in a given simulation domain.

Greek Summary - Περίληψη

Η κατηγορία των ευδιάλυτων δισκόμορφων οργανικών μορίων, με ικανότητες αυτο-οργάνωσης σε σύνθετες υπερμοριακές δομές, αποτελεί μία πολλά υποσχόμενη οικογένεια υλικών για τεχνολογικές εφαρμογές. Στην ειδική περίπτωση των πολυαρωματικών μεσογόνων, οι αλληλεπιδράσεις μεταξύ απεντοπισμένων π μοριακών τροχιακών καθιστούν τα υλικά αυτά κατάλληλα για χρήση ως ενεργά μέσα οργανικών ηλεκτρονικών διατάξεων.

Η παρούσα διδακτορική διατριβή πραγματεύεται μοριακές προσομοιώσεις δισκόμορφων υλικών σε πολλαπλές κλίμακες, με τη χρήση υπολογισμών πρώτων αρχών βάσει της θεωρίας Συναρτησιακού της Ηλεκτρονικής Πυκνότητας (Density Functional Theory, DFT) καθώς και ατομιστικών προσομοιώσεων Μοριακής Μηχανικής και Μοριακής Δυναμικής βάσει εμπειρικών εκφράσεων για την περιγραφή ατομικών αλληλεπιδράσεων. Σκοπός των μελετών αυτών είναι ο προσδιορισμός σχέσεων δομής-ιδιοτήτων, ξεκινώντας από το κβαντικό επίπεδο ως προς ηλεκτρονικές ιδιότητες και φαινόμενα μεταφοράς φορτίου, μέχρι τη νανομετρική κλίμακα, εξετάζοντας δομικές, μηχανικές και δυναμικές ιδιότητες περιοδικών μοριακών κρυστάλλων.

Όσον αφορά στα υπό μελέτη συστήματα, εξετάζονται μόρια της οικογένειας των λεγόμενων νανογραφενίων, με ιδιαίτερη βαρύτητα στο εξα-περι-εξαβενζοκορονένιο (hexa-peri-hexabenzocoronene, HBC), καθώς και σε παράγωγα αυτού που προκύπτουν μέσω περιφερειακής υποκατάστασης. Συγκριτικές μελέτες με τη χρήση κβαντομηχανικών υπολογισμών πάνω σε δισκόμορφα μόρια μεταβλητής έκτασης πυρήνα χρησιμοποιούνται για την εκτίμηση ηλεκτρονικών ιδιοτήτων και ποσοτήτων που θεωρούνται κρίσιμες στους μηχανισμούς μεταφοράς φορτίου. Ως προς τα μορφολογικά χαρακτηριστικά, τα υπό εξέταση δισκόμορφα μόρια κυμαίνονται από το μικρότερο δυνατό, δηλ. το βενζόλιο, μέχρι εκτεταμένα δισκόμορφα μοριακά συγκροτήματα που προκύπτουν μέσω συνένωσης πολυαρωματικών μονάδων με τη χρήση κατάλληλων αρθρωτών μορίων σύνδεσης.

Παράγωγα του μεσογόνου HBC που φέρουν αλκυλικές πλευρικές ομάδες, τόσο σε μη-πολική όσο και σε πολική μορφή μέσω της υποκατάστασης ενός ατόμου ιωδίου, εξετάζονται με τη χρήση προσομοιώσεων Μοριακής Δυναμικής, στοχεύοντας στη μελέτη δομικών, μηχανικών και δυναμικών ιδιοτήτων υπό δεδομένες καταστάσεις θερμοκρασίας και πίεσης. Τα ακριβή μοτίβα μοριακής στοίβαξης εξάγονται από εξισορροπημένες τροχιές Μοριακής Δυναμικής, καθώς αποτελούν το βασικότερο παράγοντα που ελέγχει την ικανότητα μεταφοράς φορτίου, όπως προκύπτει τόσο από τη βιβλιογραφία όσο και από τις μελέτες της

παρούσας εργασίας.

Επιπλέον, αμφιφιλικά μεσογόνα με βάση το μόριο HBC, που χαρακτηρίζονται από τη λεγόμενη γεωμετρία "Ιανού", εξετάζονται με τη χρήση προσομοιώσεων Μοριακής Δυναμικής. Μόρια αυτής της κατηγορίας φέρουν διαφορετικές πλευρικές ομάδες ως προς την υδροφιλικότητά τους, γεγονός που οδηγεί στην αυτο-οργάνωσή τους σε φυλλόμορφες υπερμοριακές δομές. Ατομιστικές προσομοιώσεις χρησιμοποιούνται για την μελέτη της επίδρασης της θερμοκρασίας σε δομικές και δυναμικές ιδιότητες τέτοιων φυλλόμορφων διατάξεων, λαμβάνοντας ταυτόχρονα μία πλήρη εικόνα ατομιστικής λεπτομέρειας αναφορικά με τη διαδικασία τήξης.

Μοριακοί κρύσταλλοι με βάση υποκατεστημένους πολυαρωματικούς δίσκους εκτεταμένης έκτασης, όπως το μόριο τριγωνικής συμμετρίας C96 και το μόριο τετραγωνικής συμμετρίας C132, εξετάζονται επίσης βάσει υπολογισμών Μοριακής Δυναμικής. Πέραν τέτοιων δισκόμορφων μορίων που χαρακτηρίζονται από έναν πολυαρωματικό δίσκο ανά μεσογόνο, στην παρούσα μελέτη λαμβάνονται υποψη και ομοιοπολικά συνδεδεμένα συγκροτήματα δισκόμορφων μοριών με συμμετρία αλτήρα αλλά και με τριγωνική αστεροειδή συμμετρία υπό τη μορφή μορίων με μία βασική συνδετική μονάδα και τρεις μοριακούς βραχίονες που καταλήγουν σε δισκόμορφα τμήματα των μορίων HBC, C96 και C132. Τέτοια αστεροειδή μόρια φαίνεται να αυτο-οργανώνονται σε κιονοειδής νανοφάσεις με συμμετρία τριπλής έλικας, με χαρακτηριστική δομική ευρωστία και ικανότητα σχηματισμού εξαγωνικών μοριακών κρυστάλλων. Μία μεθοδολογία πολλαπλής κλίμακας εφαρμόζεται για τον προσδιορισμό μηχανισμών μεταφοράς φορτίου σε τέτοια υλικά, κάνοντας χρήση πληροφοριών τόσο από το κβαντικό όσο και από το εμπειρικό-ατομιστικό επίπεδο.

Αναφορικά με τη δημιουργία αρχικών απεικονίσεων για τη χρήση σε ατομιστικές προσομοιώσεις στις περιπτώσεις που μία κρυσταλλογραφική προσέγγιση θεωρείται άτοπη ή μη επιθυμητή, αναπτύσσεται και εφαρμόζεται ένα υβριδικό σχήμα δεσμού-προς-δεσμό πιθανοκρατικής Monte Carlo κατασκευής αρθρωτών μακρομορίων, ικανό για την παραγωγή αλκυλικών νανοφάσεων πέριξ σκληρών νανοδομημένων περιοχών εντός δεδομένου χωρίου προσομοίωσης.

List of Figures

List of Tables

Abbreviations

ACF Autocorrelation Function

B3LYP B88 3-parameter LYP hybrid functional

B88 Becke GGA correlation functional

BHA*n* Benzene-hexa-*n*-alkanoates

c-HBC Contorted hexa-*peri*-hexabenzocoronene

C12 *n*-dodecane

C132 $C_{132}H_{34}$ nanographene

C16,4 Phytane

C60 Buckminsterfullerene

C8,2 2,6-dimethyloctane

C96 $C_{90}H_{30}$ nanographene

CASPT*n* Order-*n* Complete Active Space Perturbation Theory

CBMC Configurational Bias Monte Carlo

CC Coupled Cluster

CG Coarse-Grained

CGenFF CHARMM Generalized Force Field

CGTO Contracted Gaussian Type Orbital

CI Configuration Interaction

CMSE Computational Materials Science and Engineering

CoM Center of Mass

CTI Charge Transfer Integral

D-A Donor-Acceptor

DFT Density Functional Theory

DLC Discotic Liquid Crystal

EoM Equation of Motion

FET Field-Effect Transistor

FF Force Field

FMO Frontier Molecular Orbital

GAFF Generalized Amber Force Field

GB Gay-Berne

GGA Generalized Gradient Approximation

GTO Gaussian Type Orbital

HAT*n* Hexakis (*n*-alkoxy) triphenylene

HBC Hexa-*peri*-hexabenzocoronene

HBC-C12 Hexa-*n*-dodecyl-hexa-*peri*-hexabenzocoronene

HBC-DB Hexa-*peri*-hexabenzocoronene Dumbbell

HBP Hexabenzoperylene

HEG Homogeneous Electron Gas

HF Hartree-Fock

HK Hohenberg-Kohn

HOMO Highest Occupied Molecular Orbital

HPB Hexa-phenylbenzene

INDO Intermediate Neglect of Diatomic Overlap

KS Kohn-Sham

LDA Local Density Approximation

LJ Lennard-Jones

LSDA Local Spin Density Approximation

LUMO Lowest Unoccupied Molecular Orbital

LYP Lee-Yang-Parr GGA correlation functional

MC Monte Carlo

MCSCF Multi-Configurational Self-Consistent Field

MD Molecular Dynamics

MM Molecular Mechanics

MP*n* Order-n Møller-Plesset Perturbation Theory

MR Multi-Reference

MSD Mean Square Displacement

MTK Martyna-Tobias-Klein

NDDO Neglect of Differential Diatomic Overlap

NH Nosé-Hoover

ODR Orthogonal Distance Regression

OPLS Optimized Potential for Liquid Simulations

PAH Polyaromatic Hydrocarbon

PBC Periodic Boundary Condition

PBE Perdew-Burke-Ernzerhof GGA correlation functional

PBE0 Parameter-free PBE hybrid functional

PDF Probability Density Function

PDI Perylene diimide

PPPM Particle-Particle Particle-Mesh

PW-LDA Perdew-Wang LDA correlation functional

QM Quantum Mechanics

QMC Quantum Monte Carlo

SCF Self-Consistent Field

STO Slater Type Orbital

TEG Triethylene glycol

TPA Triphenylamine

TPB 1.3.5-triphenylbenzene

UB Urey-Bradley

vdW van der Waals

VWN Vosko-Wilk-Nusair LDA correlation functional

XC Exchange-Correlation

XRD X-ray Diffraction

Chapter 1

Introduction

In this chapter, a concise introduction to discotic materials is presented, covering a series of pivotal topics deemed essential for the understanding of the key subjects addressed by this thesis. An overview of contemporary computational material science techniques is outlined, with a detailed record of applications to discotic materials. Furthermore, thesis objectives are thoroughly presented, alongside major questions this work aims to resolve.

1.1 Discotic Materials

1.1.1 Discotic Molecules and Crystals

The term "discotic molecule" is used to characterize molecular structures that can be envisioned as planar disk-like assemblies of linked atoms. A fundamental member of the discotic molecules family is benzene (C_6H_6), first obtained by Michael Faraday in 1825 and structurally resolved by August Kekulé in 1865.[1] All six carbon atoms of benzene are sp^2-hybridized and arranged in a circular planar fashion that allows π electrons to delocalize in molecular orbitals that extend above and below the plane on which carbon atoms reside. Electron delocalization gives rise to resonant bonding behavior, an attribute inherent to so-called aromatic molecules.[2]

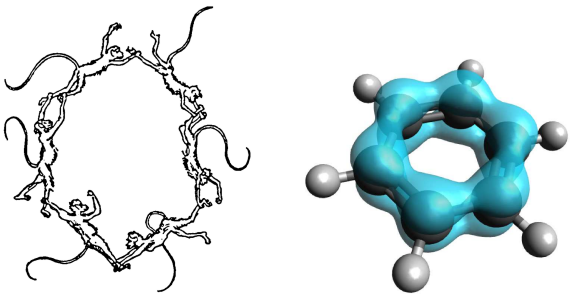

Figure 1.1: A satirical illustration of Kekulé's benzene formula from a special edition of *Berichte der Deutschen Chemischen Gesellschaft* (1886) and a representation of benzene with its delocalized π molecular orbital.

Benzene can also be considered as the building block of extended aromatic molecules, frequently referred to as condensed polycyclic arenes or polyaromatic hydrocarbons (PAHs). All PAHs are superimposable with the graphite lattice and can be classified into several groups given their connectivity characteristics. PAHs are usually characterized as *cata*- or *peri*- condensed according to the absence or presence of a common carbon atom to three rings.[3] Furthermore, the term nanographene is often used for PAH molecules that have an effective polyaromatic core radius exceeding ∼1 nm. Graphical representations of relatively low molecular weight PAH discotic molecules frequently encountered in technological applications[4;5] are depicted in Figure 1.2.

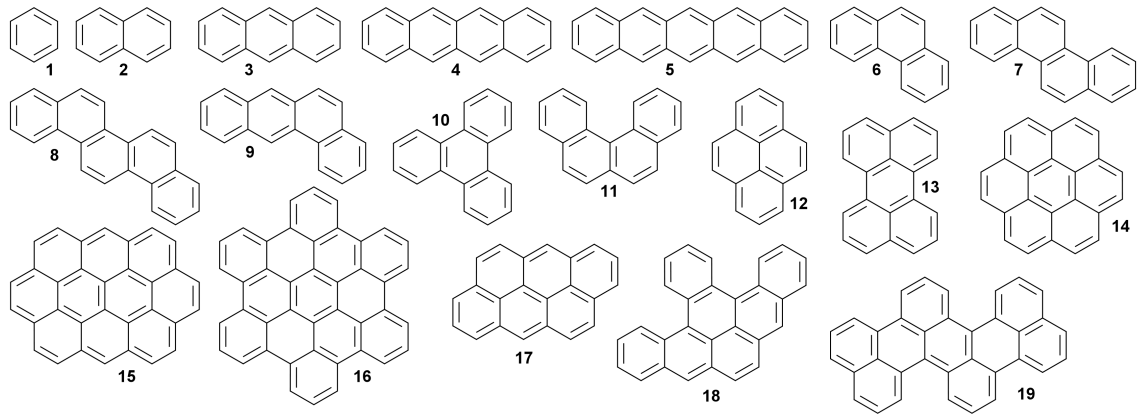

Figure 1.2: Graphical depictions of benzene (**1**) and various PAHs. From (**2**) to (**10**), the *cata*-condensed molecules naphthalene, anthracene, tetracene, pentacene, phenanthrene, chrysene, picene, benzanthracene, and triphenylene are shown. Molecule (**11**) corresponds to benzophenanthrene, a non-planar, chiral [*n*]helicene. From (**12**) to (**19**), the *peri*-condensed molecules pyrene, perylene, coronene, ovalene, hexa-*peri*-hexabenzocoronene, antanthrene, tribenzopyrene, and di(*peri*-naphthylene)anthracene are shown.

As far as the crystalline phase of PAH molecules is concerned, Desiraju and Gavezzotti[6] defined four basic structural types with respect to PAH bulk molecular arrangement. In their classification, a "herringbone" motif is identified when dominant non-bonded C$\cdots$C interactions are attributed to non-parallel nearest neighboring molecules. Characteristic examples bearing herringbone stacking symmetry are the crystals of benzene (**1**), naphthalene (**2**), chrysene (**7**), and triphenylene (**10**). The second motif is the so-called "sandwich herringbone" or "sandwich", in which the herringbone pattern is made up by sandwich-type dyads, e.g. pyrene (**12**) and perylene (**13**) molecular crystals. The third stacking type is the so-called "γ packing" and is frequent in extended discotic molecules like coronene (**14**), ovalene (**15**), and hexa-*peri*-hexabenzocoronene (HBC) (**16**). In this packing motif, the main C$\cdots$C interactions are between parallel translated molecules and can be considered as a flattened-out variant of the herringbone pattern. All of the three mentioned motifs also obtain crystal stabilization via

C···H intermolecular interactions. Finally, a fourth type labeled "β packing" is identified and corresponds to layered structures of graphitic planes characterized by strong C···C interactions with diminished C···H edge interactions, e.g. tribenzopyrene (**18**) and di(*peri*-naphthylene)anthracene (**19**) molecular crystals.

A remarkable feature of PAH molecules is their ability to accommodate a plethora of covalently linked substitutions about their periphery. When flexible functional groups are utilized, synthesized discotic molecules are rendered soluble in common organic solvents and are prone to self-organize into discotic mesophases comprised of columnar supramolecular assemblies.[7;8] The first reported case regarding a columnar mesophase based on a discotic molecule is dated back to 1977 to the work of Chandrasekhar *et al.*[9], establishing that (BHAn) (**20**) are capable of forming stacked columnar structures that, in turn, are arranged into liquid crystals of hexagonal symmetry.

Columnar supramolecular assemblies of functionalized discotic molecules are typically comprised of molecular nanowires made up by stacked rigid disk-like cores that are surrounded by a soft side chain mantle. The core-to-core separation is near ∼3.5 Å, thus enabling considerable π orbital overlap which leads to structural stability due to π-π interactions. The intercolumnar distance typically ranges in the interval of 2-4 nm, depending on the structural features of the utilized side chains. These very side chains play the role of an insulating nanophase that provides substantial spacing between discotic pillars, prohibiting intercolumnar core interactions. This characteristic reinforces intracolumnar orbital interactions, favoring this way one-dimensional charge migration inside each molecular nanowire.[10] Due to the aforementioned interactions between delocalized π orbitals inherent to polyaromatic molecular structures, the most straightforward utilization of discotic materials is for organic electronics applications.[11;12]

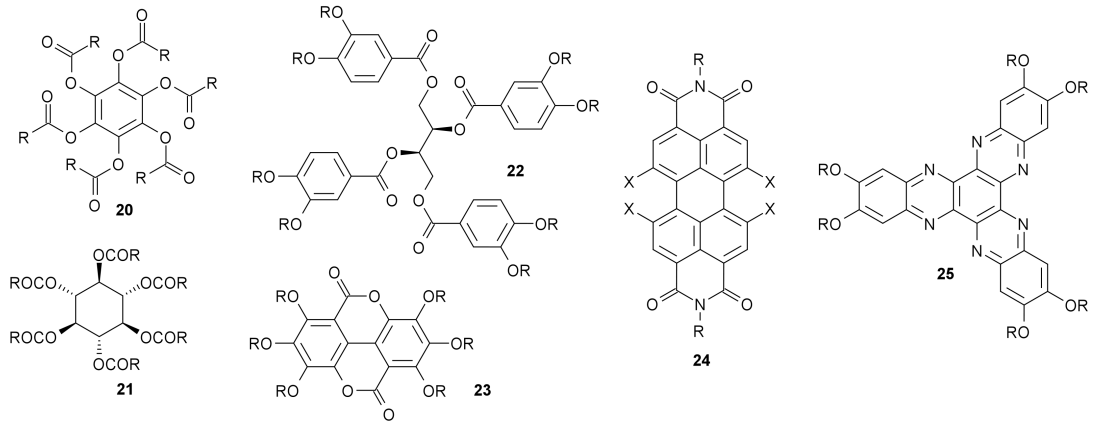

Figure 1.3: Examples of hexaester discotic units with benzoic (**20**) and cyclic (**21**) core, alongside to peracylated D-threitol molecule (**22**) and selected heterocyclic PAH molecules (**23**-**25**).

Functionalized discotic materials are not restricted only to homocyclic PAH cores. Similar to benzene hexaesters (**20**) that inaugurated the taxonomy of discotic liquid crys-

tals are cyclohexane hexaesters (**21**), mesogens displaying rich mesomorphism that can be suppressed via axial instead of radial functionalization. Furthermore, a series of disk-like molecular assemblies can be synthesized via alcohol benzoylation, forming liquid crystalline molecules like peracylated D-threitol sugar alcohol (**22**), whose discotic units are not situated on the molecular center but on the periphery. Moreover, heterocyclic PAH molecules also find numerous applications as discotic mesogens. Characteristic examples are products of flavellagic and ellagic acids, like molecule **23**, perylene diimide (**24**) and its derivatives, and triphenylene-based heterocyclics, like diquinoxalino[2,3-a:2,3-c]phenazine (**25**).[10]

Another interesting family of discotic materials is based on polyphenyls. Characteristic examples include the bowl-shaped metacyclophane **26** and the phenylacetylene macrocyclic mesogen **27**, both having void geometric centers, with their disk-like fragments situated on their periphery.[10] Similar in structure with respect to the position of the sub-discotic units are the so-called metallomesogens, such as porphyrin (**28**) and phthalocyanine (**29**) derivatives, accommodating metallic species, like Mn, Fe, Co, Cu, Zn, and Ag in the void of their core center.[13]

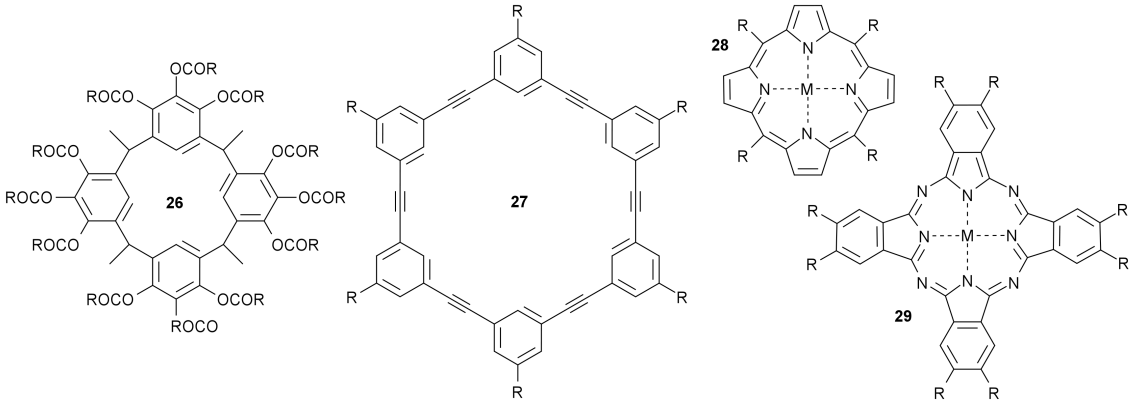

Figure 1.4: Examples of hollow center polyphenylic discotic molecules (**26**, **27**) and two characteristic metallomesogens (**28**, **29**).

Other examples of discotic mesogens include molecules that are products of the fusion of 6-member and 5-member rings, such as trisubstituted decacyclene derivatives (**30**) and also more "exotic" molecular species, like the star-shaped, thiophene substituted, hexaphenylbenzene (HPB) molecule (**31**) and discotic complexes held together via hydrogen bonding, e.g. 6,7-bis(alkoxy)2,3-dihydrophthalazine-1,4-dione derivatives (**32**).[10]

The physicochemical identity of functional groups attached on the periphery of discotic molecules vary according to the desired properties of bulk supramolecular assemblies. A characteristic selection of such side chains is depicted in Figure 1.6.

The simplest side chains involve linear alkanes (**a**) with variable length, typically bearing from eight to sixteen aliphatic carbon atoms and variants of them that carry

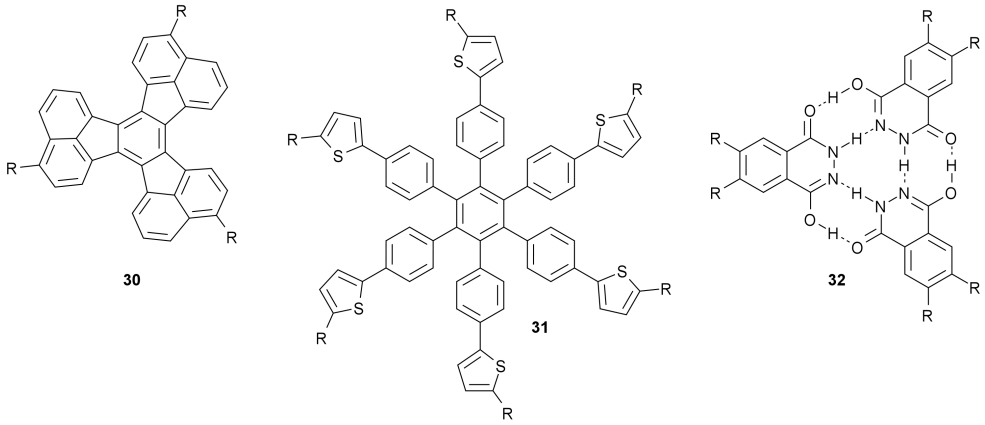

Figure 1.5: Graphical depictions of "non-conventional" discotic molecules: a decacyclene core (**30**), a star-shaped HPB-based mesogen (**31**), and an H-bonded discotic unit (**32**).

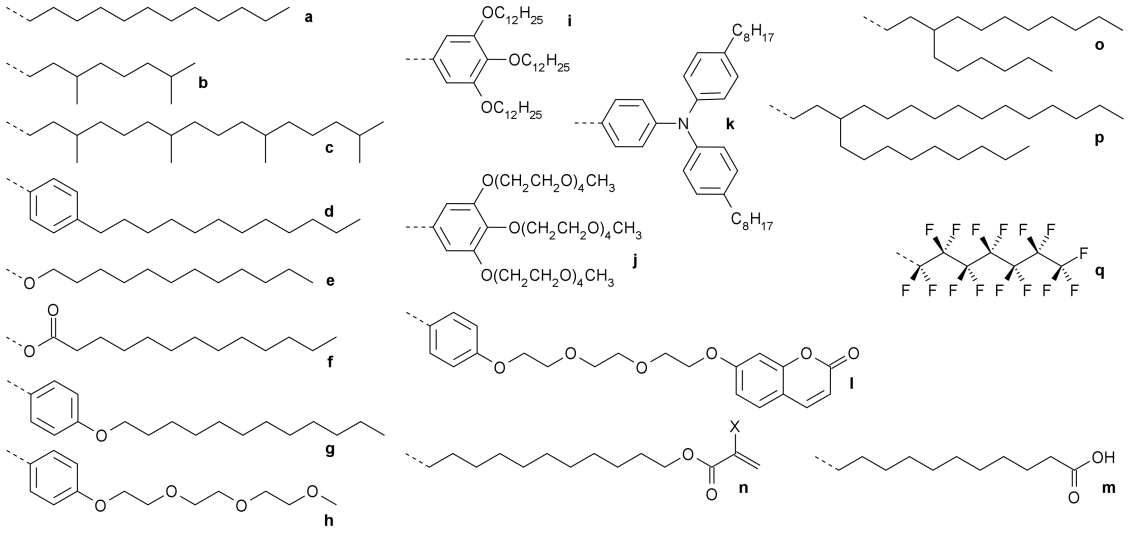

Figure 1.6: A selection of widely utilized side chain groups attached on the periphery of discotic molecules.

pendant methyl groups along the aliphatic backbone (**b**, **c**). The linkage onto the discotic core can be either direct or via intermediate linking units, such as phenyl rings (**d**), ether (**e**) or ester (**f**) units, and even combinations of them (**g**). In some applications, grafted phenyl rings are farther placed with respect to core edges through the utilization of ethyne spacers. Oxygen containing hydrophilic functional groups are also common, e.g. polyethylene glycol-based side chains (**h**). Except from their para substitution scheme, phenyl rings can appear in mixed *para*/*meta* states, thus accommodating three side chains per ring (**i**, **j**). In addition, more intricate phenyl-based linkers can be used, such as the di-*n*-octane substituted triphenylamine (TPA) unit (**k**). Specific side chains can be structurally augmented via polar terminations (**l**, **m**, **n**), rendering them capable of more complicated interactions, such as terminal π-π and/or hydrogen bonding. This short catalogue of indicative functional groups also contains branched alkyl side chains (**o**, **p**)

and linear fluorocarbons (**q**).[12]

Discotic molecules primarily exhibit only one mesophase type out of the so-called nematic, columnar, and lamellar phases. The nematic phase is further divided into three sub-types: the discotic nematic, chiral discotic nematic and nematic columnar mesophases. In the nematic discotic phase, mesogens are arranged in a parallel manner, retaining a high orientational order but without any long range translational order. In the chiral discotic nematic phase, molecules self-organize into parallel planes in a chiral fashion, similar to cholesteric liquid crystals. Finally, in the nematic columnar phase, discotic molecules stack on top of each other forming molecular pillars that, in turn, do not follow any intercolumnar positional ordering.[10]

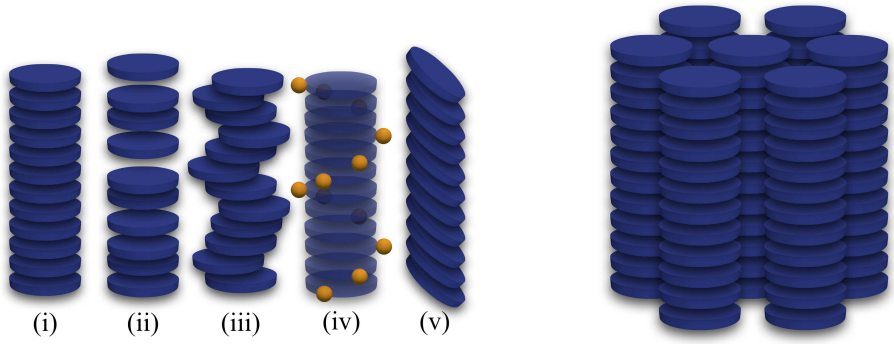

Figure 1.7: Major types of intracolumnar arrangement of discotic molecules: (i) ordered, (ii, iii) disordered, (iv) helical, and (v) tilted columns. An illustration of a hexagonal assembly of ordered columns is shown on the right.

In columnar mesophases, discotic mesogens form well-defined molecular nano-wires that are subsequently ordered into various two-dimensional lattices. As far as the internal structure of molecular pillar is concerned, discotic cores can be stacked in an ordered or disordered fashion and even form chiral or tilted assemblies, as is shown in Figure 1.7.[8] Perhaps the simplest intercolumnar arrangement is the one of a hexagonal lattice. Depending on the nature of the discotic mesogens, more complex lattices can occur. Moreover, further categorizations emanate from the molecular temporal behavior. For example, a sub-category of the columnar hexagonal phase is the crystalline columnar hexagonal phase, in which molecular cores exhibit minuscule translational or rotational movement. The exact opposite phase is the liquid crystalline columnar hexagonal phase where mesogens can freely rotate about the columnar axis and follow *en-masse* translations parallel to the stacking direction. Interestingly enough, an intermediate phase exists: the so-called columnar hexagonal plastic phase, in which molecules have no translational freedom but can rotate with respect to the columnar direction. Finally, in the case of the lamellar mesophase, molecular pillars are organized into stable lamellae that subsequently come in proximity to form lamellar molecular crystals.[10]

1.1.2 Hexabenzocoronene Derivatives

One of the most prominent members of the PAH discotic molecules family is the HBC molecule and its derivatives.[12;14;15] HBC is a nanographene molecule comprised of 42 sp^2 hybridized carbon atoms with hexagonal D_{6h} symmetry. The first synthesis of HBC was achieved by Clar *et al.*[16] in the late-1950s. The bromination of 2:3-7:8-dibenzo-*peri*-naphthene (**33**) in benzene resulted in a precipitate of hexabenzoperylene (HBP) (**34**) which, upon heating, led to the formation of HBC (**16**). In the same year, Halleux *et al.*[17] also reported synthesis of HBC via two alternative routes. The first involved the cyclodehydrogenation of HPB (**35**) by molten $AlCl_3$/NaCl and the second relied on the reaction of dibenz-1,9;2,3-anthrone (**36**) with Zn/$ZnCl_2$. Hendel *et al.*[18] reported a new method for HBC synthesis in 1986. The reaction of quinone **37** with phenyllithium resulted in the diols **38** in 29-46% yield. The intermediate diols were cyclized in an $AlCl_3$/NaCl melt and later on subjected to copper induced aromatization to give HBC in ∼0.4% yield. All aforementioned synthetic routes towards pristine HBC are graphically summarized in Figure 1.8.

A higher yield and less laborious synthetic root was introduced by Spiess, Müllen and co-workers[19] in 1996 based on oxidative cyclodehydrogenation of substituted HPB (**40**). The innovation of the synthetic method by Herwing *et al.* relied on functionalized tolanes (**39**) that were used as HPB precursors which were finally planarized into functionalized HBC molecules (**41**) in ∼80% yield. The synthetic root by Herwing *et al.* is illustrated in Figure 1.9.

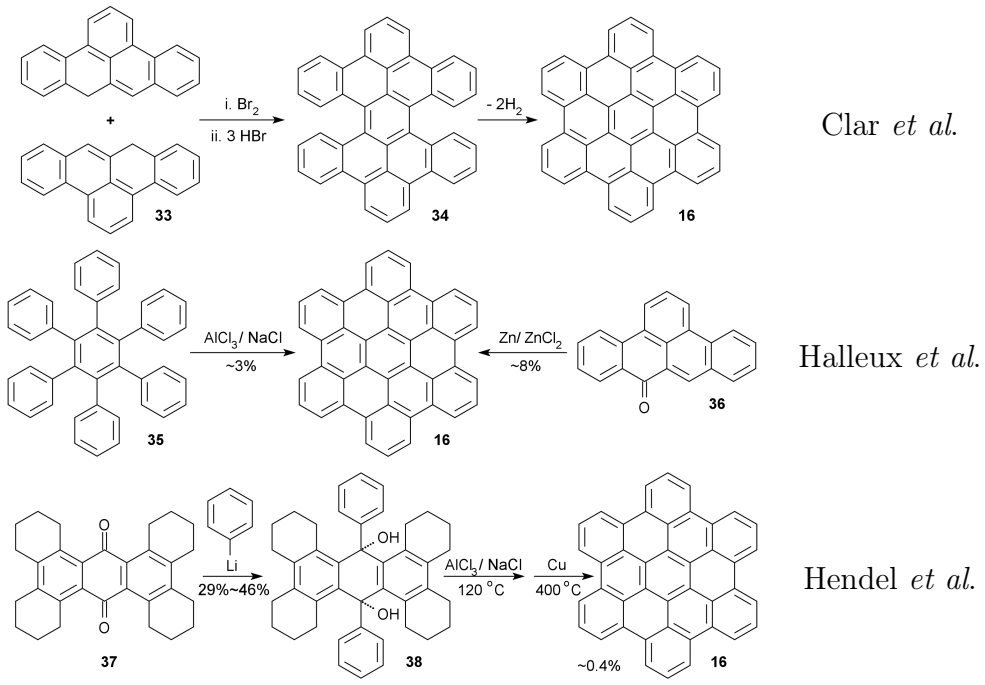

Figure 1.8: Early synthetic routes towards pristine HBC synthesis.

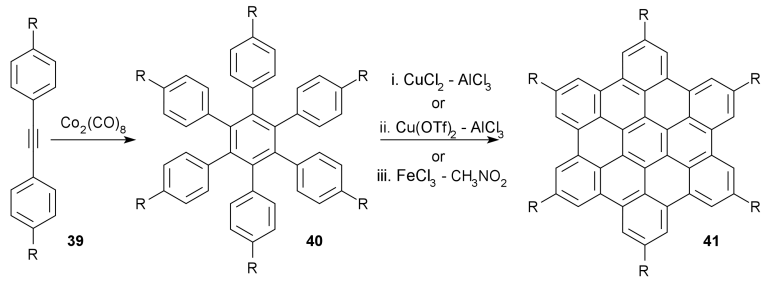

Figure 1.9: High yield synthetic route towards symmetrically functionalized HBC molecules.

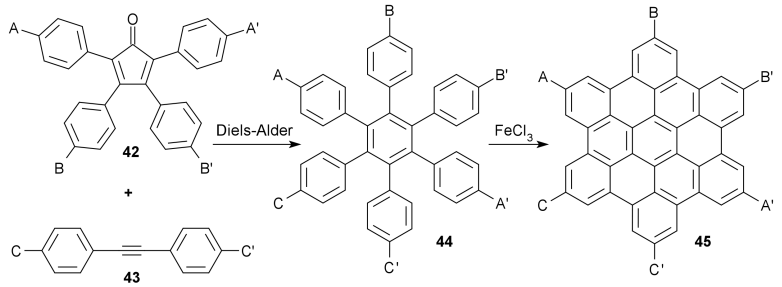

Figure 1.10: High yield synthetic route towards asymmetrically functionalized HBC molecules.

Substitutions with different regioisomeric patterns can be obtained through an alternative, also high yield, method pioneered by Müllen and co-workers.[20–23] According to the aforementioned synthetic route, Diels-Alder cycloadditions between selected tetraphenylcyclopentadienone derivatives (**42**) and substituted tolanes (**43**) result in HPB derivatives (**44**). These intermediate molecular products undergo oxidative dehydrogenation with $FeCl_3$, forming this way asymmetrically substituted HBC derivatives (**45**) as it is illustrated in Figure 1.10.

In its pristine, unsubstituted form, HBC crystallizes in monoclinic $P2_{1/a}$ molecular crystals, which are formed by neatly packed columnar arrays. Inside each column, HBC molecules are stacked in a tilted fashion with respect to the columnar direction, adopting a γ flattened herringbone packing motif, as can be clearly seen in the side view of Figure 1.11.

Although HBC molecules are tightly packed into a structurally robust molecular crystal, their utilization in this form for practical applications is rather difficult, mostly due to their high melting point (approximately 700°C) and the fact that they are nearly insoluble in all known organic solvents. A physicochemical workaround of this predicament is based on peripheral functionalization with flexible side chains. Such HBC derivatives with symmetrical substitutions can be synthesized via the route proposed by Herwing *et al.*.[19]

The flagship of the symmetrically substituted HBC family is the hexa-*n*-docedyl substituted HBC molecule (HBC-C12) which carries six *n*-dodecane (C12) side chains on

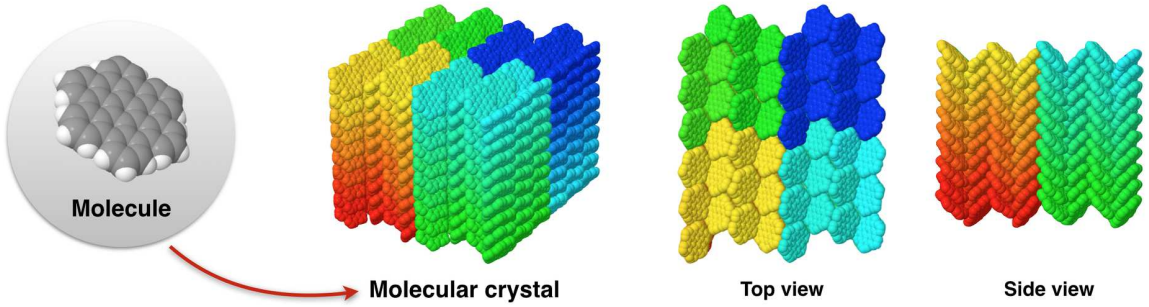

Figure 1.11: Molecular representation of a HBC crystal.

its periphery.[15;19;24;25] At room temperature, HBC-C12 crystallizes into orthorhombic molecular crystals, with the polyaromatic cores regularly stacked on top of each other in a tilted, herringbone-like manner and the dodecane side chains forming a highly interdigitated alkyl nanophase.

HBC cores adopt an AA' graphitic-like stacking pattern[26] that leads to an intracolumnar charge mobility ranging up to 1.13 $cm^2V^{-1}s^{-1}$, a value close to 3.0 $cm^2V^{-1}s^{-1}$, which is the electron mobility of graphite in the perpendicular direction with respect to the graphitic sheets.[27] Upon heating, orthorhombic molecular crystals of HBC-C12 gradually melt to hexagonal molecular crystals with liquid crystalline characteristics that manifest as *en-masse* columnar displacements along the stacking direction.[15;25] This phase transition is followed by a radical shift to core stacking patterns that leads to charge carrier mobility drop.[28;29]

HBC-C12 has been successfully used as active medium in organic field-effect transistors (FET) via the zone casting technique[30] that prompts the self-organization of alkyl substituted HBC molecules into highly oriented thin films. The transfer and output characteristics of HBC-based organic FETs resulted a good on-off ratio of 10^4 and a field-effect mobility in the saturation regime at 5×10^{-3} $cm^2V^{-1}s^{-1}$.[12] Moreover, operational organic FETs have also been realized using as active medium spin-cast thin films of tetra-alkyl substituted contorted *cata*-condensed HBC (c-HBC) cores.[31] Furthermore, HBC cores with alkylphenyl peripheral substitution (HBC-PhC12) were combined with perylene diimide (PDI) derivatives for the formation of nanophase separated blends for organic photovoltaic devices. In such a device, the HBC derivative acts as an electron-donating p-type material whereas the PDI derivative plays the role of an electron-accepting n-type material, thus forming a p-n bilayer junction connected by an interpenetrating network. The measured external quantum efficiencies of these devices reached high values of up to 34% near 490 nm.[11]

As far as other HBC derivatives except HBC-C12 are concerned, the grafting of different peripheral functional groups results in a broad spectrum of diverse material properties

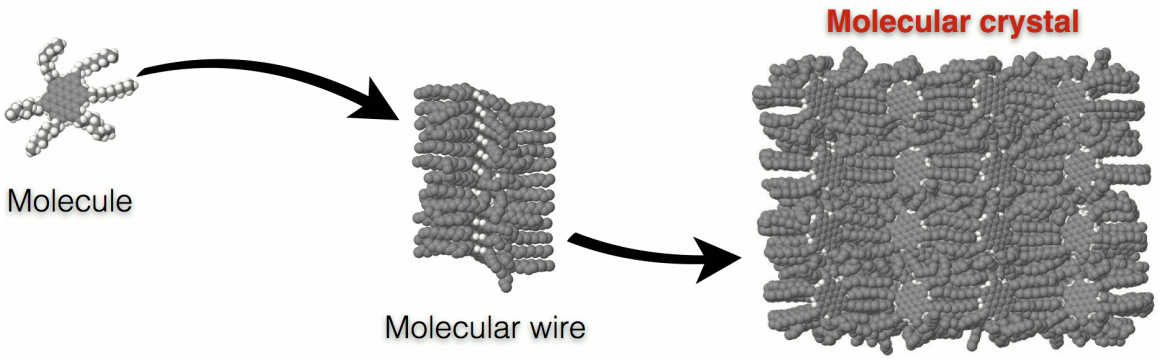

Figure 1.12: Graphical representation of the two levels of self-organization of HBC-C12, first in molecular wires and then in tightly packed molecular crystals.

and potential applications. The grafting branched alkyl side chains is found to suppress the crystallization to a herringbone-like structure and promote the self-organization into a hexagonal plastic columnar phase that melts away to a regular hexagonal columnar phase upon temperature rise.[32] Furthermore, molecular crystal properties can be tuned via the utilization of side chains capable of hydrogen bonding, the introduction of polar units and through different substitution schemes on the very same HBC core using alternating combinations of hydrophobic and hydrophilic side chains.[33;34] Specifically the effect of dipole substitution on the self-organization, thermodynamics, and dynamical properties of soluble HBC derivatives has been thoroughly investigated by Floudas, Müllen, and co-workers.[35–41]

The introduction of oxygen-bearing side chains to HBC cores opened up new pathways to discotic material processing and applications. A striking example is found in the work of Wu *et al.*[42] that involved the synthesis of water-soluble oligo(ethylene glycol) substituted HBC mesogens that successfully self-organize into columnar assemblies in water solutions and in their bulk, and also serving as templates for the fabrications of other functional organic-inorganic composites under controllable sol-gel procedures. Moreover, the selectivity of functionalization sites offered by Diels-Alder cycloadditions is a fundamental tool for the synthesis of highly asymmetrical HBC derivatives. A special case are the so-called Janus-type (or Gemini-shaped) mesogens that carry hydrophilic, oxygen-containing side chains on one side of the discotic core and hydrophobic aliphatic side chains on the opposite side. Such amphiphilic, Janus-type HBC derivatives like C12-HBC-PhOTEG (**46**) were successfully synthesized and used for the formation of self-assembled graphitic nanotubes in certain solvent conditions.[43;44]

Another interesting case study from the broad family of HBC derivatives involves nitrogen containing HBC cores in the form of TPA-based peripheral functionalization groups. The usage of TPA units carrying aliphatic side chains, either via direct linkage or through ethyne molecular spacers, results in the formation of coaxial hole-transport molecular nanowires.[45] Furthermore, when it comes to charge transport properties, struc-

tural defects and pronounced molecular movement hinder the charge hopping mechanisms. A proposed and applied permanent workaround to this issue relies on side chain polymerization (e.g. using acryloyl-terminated side chains similar to **n** in Figure 1.6, where X=H, CH_3) that, in turn, can effectively suppress phase transitions between different columnar mesophases and minimize core movement at elevated temperatures.[46;47]

The interplay between HBC derivatives that serve as donor molecules with various acceptor molecules is of high importance in organic electronic applications. A characteristic example is the interaction of HBC cores with Buckminsterfullerene molecules (C60). A major geometrical obstacle concerning the contact of the aforementioned molecules is the fact the most HBC derivatives are relatively flat, thus easily enabling slippage with a neighboring C60 molecule. A solution was proposed and applied by Wang *et al.*[48] and involved the replacement of all peripheral hydrogen atoms of HBC with methoxy groups. Due to severe steric hindrance, HBC cores adopt a "double-concave" shape that can accommodate a neighboring C60 molecule, leading to HBC-C60 cocrystals. Analogous "double-concave", non-planar HBC variants have been realized via edge chlorination, forming well-defined molecular monolayers on specific substrates, capable of receiving C60 molecules in a nanopatterned fashion.[49] Apart from physisorbed C60 molecules, recent advances have led to chemisorbed C60 molecules on HBC cores, creating this way permanently linked HBC-C60 dyads - a compound molecule appealing to donor-acceptor (D-A) molecular electronic applications.[50] The notion of donor-acceptor molecular dyads has also been explored by Aida and co-workers by synthesizing soluble graphitic nanotubes based on amphiphilic HBC derivatives, first with trinitrofluorenone units[51] (**47**) and then with C60 molecules[52] (**48**) attached to hydrophilic side chains, resulting in discrete coaxial cylindrical shells capable of independent electron and hole transport.

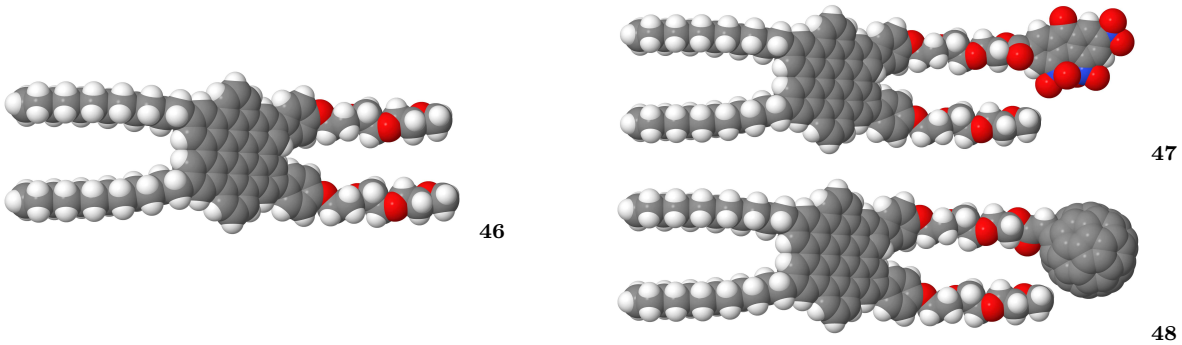

Figure 1.13: Janus-type amphiphilic HBC derivatives.

Finally, recent advances in synthesis and processing methods have led to a remarkable augmentation of the spectrum of HBC derivatives potential applications, including materials capable of supporting both electronic and ionic conductivity.[53] When coupled with polymer technology, HBC molecules find applications in polymer electrolyte membranes[54], nanographene containing polymers for organic electronics with discotic

molecules utilized either as pendant[55] or polymer backbone units[56], and in nanoporous polymers suitable for separation processes.[57;58] Besides the utilization of discotics in their bulk, effects of nano-confinement in one-dimensional supramolecular discotic nanowires have been probed.[59;60]

1.1.3 Extended Core and Covalently Linked Discotics

Soluble PAH molecules with more extended cores compared to HBC can be synthesized via Diels-Alder planarization of polyphenylene precursors with well-defined structure.[21] Discotic molecules obtained through this route possess a variable number of benzoic rings and diverse symmetry. Some medium size compounds are shown in Figure 1.14. Molecule **49** can be envisioned as a HBC core peripherally augmented by extra benzoic rings and mesogens **50**-**52** can be described as uniaxially extended HBC cores with a ribbon-like structure.[21;61;62] Even more extended discotics with trigonal and tetragonal symmetry are accessible via the same synthetic method, like the so-called superphenalene $C_{96}H_{30}$ (C96)[21;63] (**53**), the supertriphenylene $C_{132}H_{42}$ molecule[21] (**54**), and the tetragonal $C_{132}H_{34}$ (C132) molecule[64–66] (**55**), all depicted in Figure 1.15.

The rationalization behind potential practical utilizations of extended discotic mesogens can be traced back to the work of van de Craats and Warman who attempted to link charge transfer to discotic core size.[27] Based on available experimental data from molecular crystals comprised of alkyl substituted discotic molecules with core sizes ranging from triphenylene to HBC, the conjecture that charge mobility should follow and increasing trend with respect to core size was proposed. A straightforward extrapolation postulating that larger cores would yield higher charge mobility seemed at that time plausible. Alas, experimental studies by Debije *et al.*[29] employing polyaromatic cores larger than HBC proved the aforementioned hypothesis incorrect. Theoretical studies have identified the root cause of charge mobility drop as being attributable to equilibrium discotic stacking patterns that diminish charge transfer rates[67], albeit solubility and purification issues during material synthesis and processing are common experimental culprits.[29]

Although extended core discotics yield lower charge mobilities compared to crystalline HBC derivatives with herringbone-like intracolumnar arrangements, the lack of thermotropic mobility variations for some of them is considered a highly sought characteristic. Ribbon-like alkyl substituted mesogens **50** and **51** exhibit temperature driven phase transitions from the crystalline to the hexagonal columnar liquid-crystalline phase, a phenomenon which is expected to hinder charge hopping mechanisms in a similar manner to HBC derivatives.[28;29] On the other hand, functionalized variants of extended cores like the planar star-shaped molecule **49**, the superphenalene C96 molecule (**53**), and the tetragonal core C132 (**55**) are organized into hexagonal phases over a wide temperature range, without any structural transformations due to temperature rise.[34] This structural

robustness results in stable supramolecular assemblies, capable of well-defined conduction at room and elevated temperatures.[29]

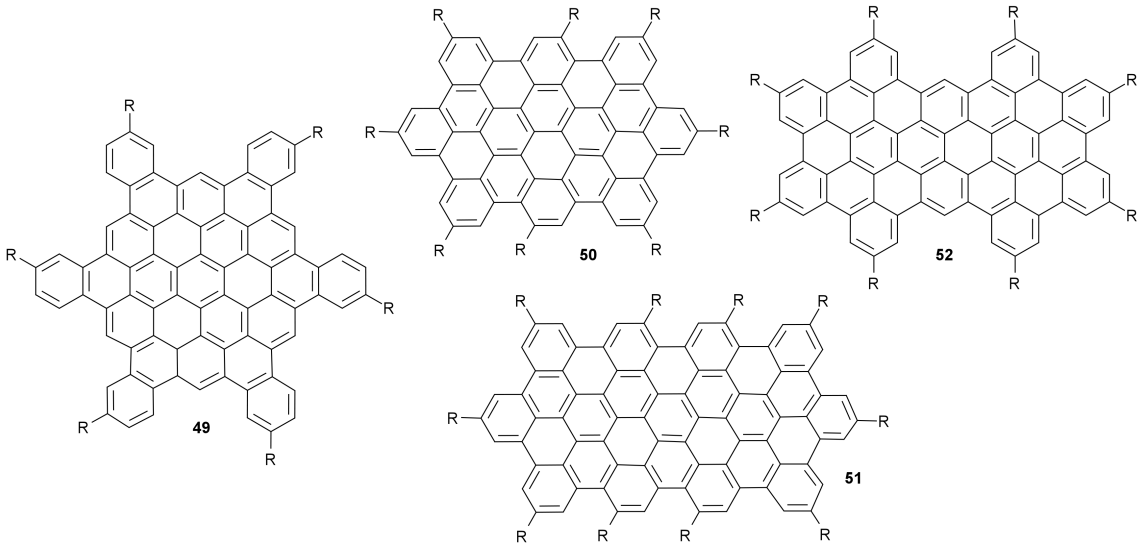

Figure 1.14: Medium size extended PAH molecules.

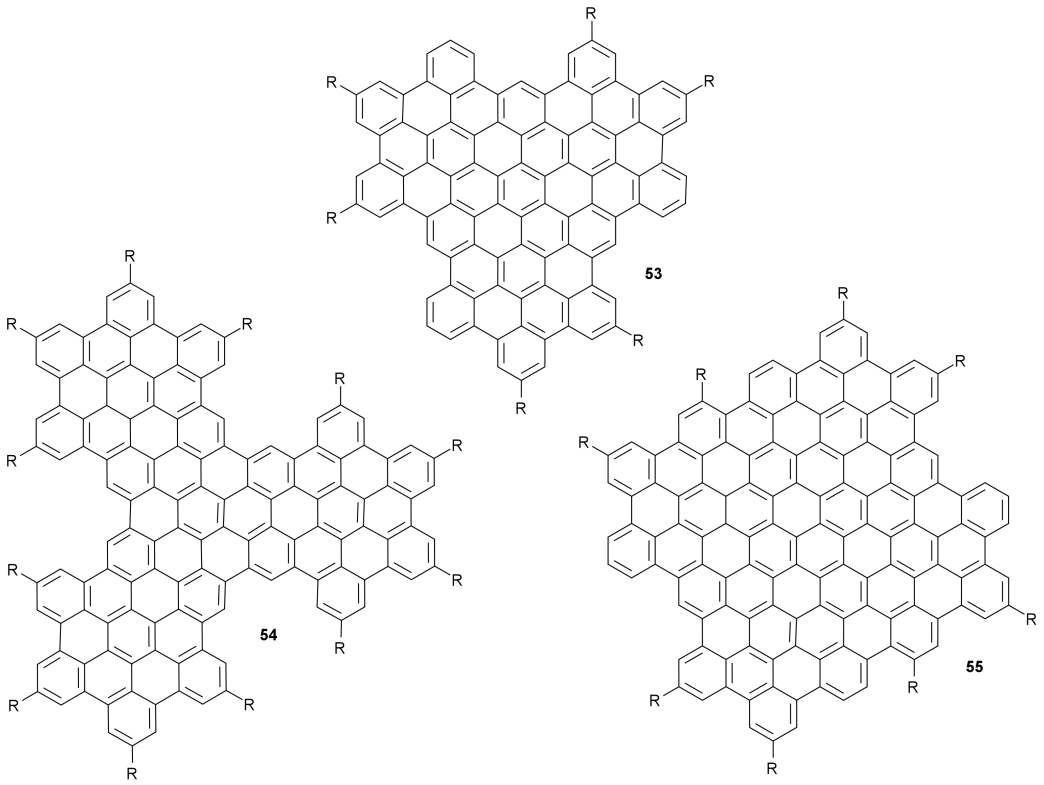

Figure 1.15: Large size extended PAH molecules.

Besides the apparent utilization as active media for organic electronic applications, neatly stacked arrangements of large PAH cores can find applications in the field of hydrogen or ion storage[68], since the extended cores can – in principle – augment the

storage capacity of such materials. Discotics like C96 have already found experimental applications in the field of molecular quantum dot technology.[69–72] Furthermore, from a nanographene quantum dot perspective, extended PAH molecules have been used in high efficiency, low cost solar cells, due to their unique optoelectronic properties.[73]

Another wide class of discotic materials results from the permanent attachment of functionalized PAH cores, either via direct covalent linking or through articulate linkers, forming this way a series of soluble discotic "super-molecules".[12;74] The simplest case of linked PAH molecules is the one having a dumbbell-like geometry, comprised of two connected discotic units. One of the first successful synthetic attempts towards such a molecule was achieved by Boden *et al.*[75] based on triphenylene discotic cores (**56**). Soluble HBC-based dumbbell molecules can also be synthesized (**57**) with a variety of intermediate linkers X, ranging from direct covalent bonding to aliphatic linkers with controllable length and even bulkier and complex molecular segments.[74;76;77] Upon careful selection of the linking unit, molecular assemblies with various functionalities can be achieved, like sandwich-like dimers that can be further expanded into polymeric systems.[78] In the family of tethered HBC derivatives, a prominent role plays the so-called HBC cyclophane (**58**) which is made up by two functionalized HBC cores, both para-connected via a *n*-octane alkylic segment.[79] Asymmetric discotic dumbbells with respect to the type of the linked disc-like units are also accessible via available synthetic roots. Mesogens of this kind find numerous optoelectronic applications as D-A molecules.[80] Moreover, D-A dumbbell molecules, such as the anthraquinone-grafted HBC molecule **59**, have been utilized as the active medium of single molecule chemical FETs.[81;82]

As far as the bulk organization of alkyl substituted HBC dumbbells **57** with no intermediate linker except a single C-C bond is concerned (referred to as HBC-DB hereafter), experimental studies have shown that such mesogens self-organize into a columnar phase with tilted intracolumnar structure due to steric hindrance. Apart from HBC-DB, *para*- and *ortho*- connected functionalized HBC trimers have been synthesized, with the *para*-connecetd trimers also stacked into columnar assemblies. In the case of *ortho*-connected trimers, no columnar phase was identified, mostly because of the twisted conformation exhibited due to core proximity. Surprisingly enough, the number of *para*-connected HBC cores has a strong effect on bulk self-organization: soluble HBC-DB molecular pillars crystallize into a two-dimensional orthorhombic lattice while HBC trimer pillars into a monoclinic lattice.[83]

Furthermore, the family of discotic "super-molecules" contains star-shaped molecular assemblies with variable symmetry, characterized by a plethora of central linking units and peripheral discotic fragments attached to the central unit via articulate or rigid bonding.[8;74;77] The number and directionality of protruding peripheral arms is dictated by the stereochemical identity of the central linking unit. A typical molecular central linker found amongst tri-arm discotic "super-molecules" is benzene, in various functionalization

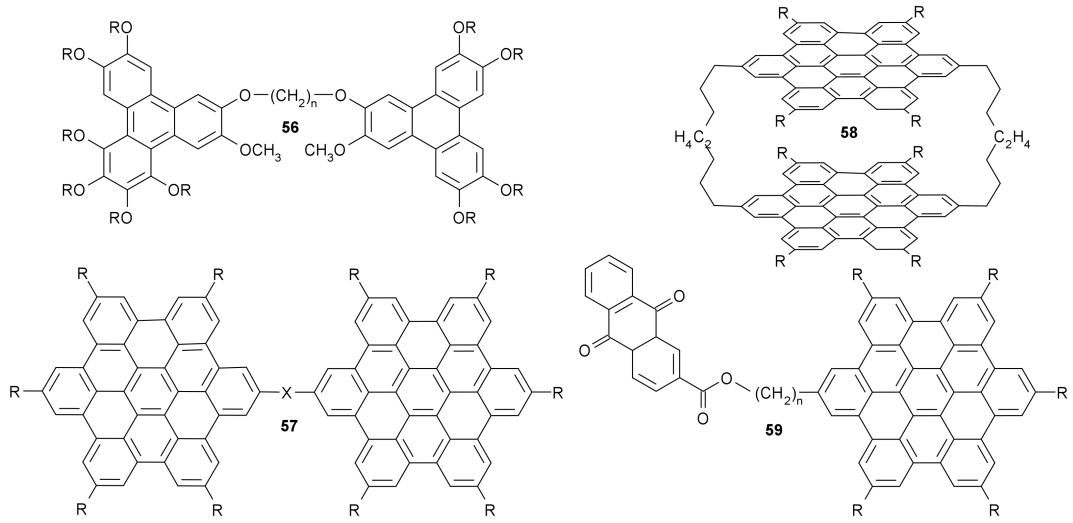

Figure 1.16: Prototype dumbbell-like discotic mesogens (**56**, **57**) and the HBC cyclophane (**58**). A characteristic example of a core-type asymmetric dumbbell (**59**) is also shown.

states. Benzene-based discotic liquid crystals (DLCs) constitute a wide category of soft matter materials with a plethora of applications. Members of this class of molecules contain covalently linked benzene and heteroatom 6-member and 5-members rings, all connected in such a way leading to star-shaped extended molecules. The utilization of flexible functional groups on specific sites via various linkers grants solubility and thermotropic and/or lyotropic behavior. The category of tri-arm DLCs with central benzene units is further augmented via the peripheral grafting of discotic segments with different core size, geometry, and side chains. Three characteristic examples are illustrated in Figure 1.17.

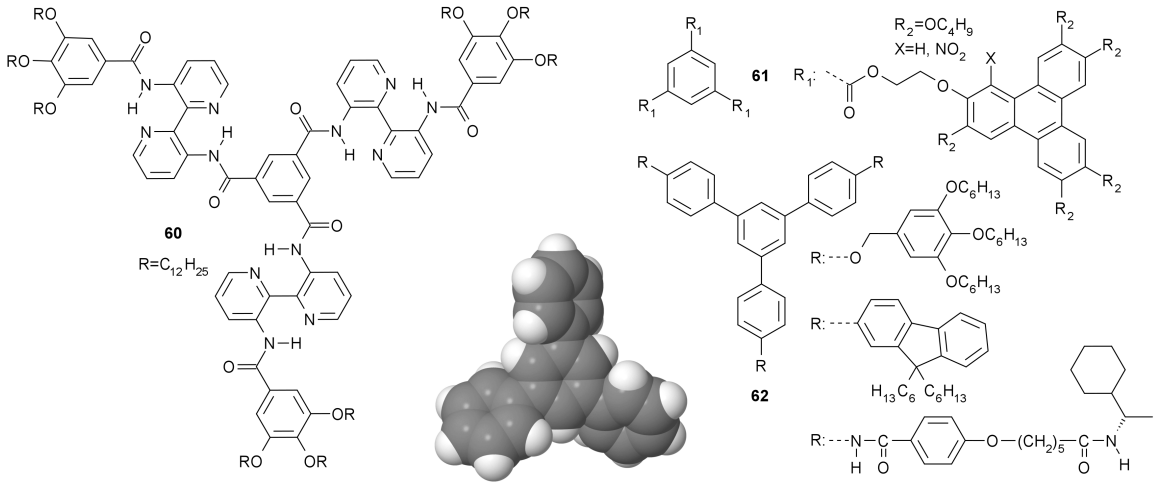

Figure 1.17: Star-shaped molecules with tri-arm geometry, utilizing benzene central linking units and various low molecular weight peripheral discotic segments. The inset depiction illustrates the propeller-like shape of TPB.

Molecule **60** contains pyridine and benzene rings on the peripheral segments and

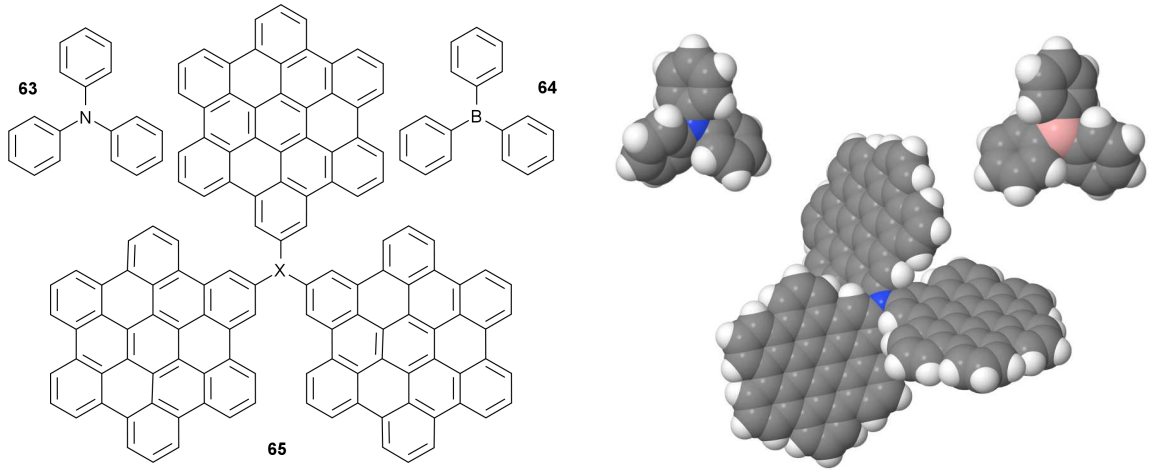

Figure 1.18: Chemical structure of TPA (**63**) and BPh3 (**64**), and a generic representation of a tri-arm HBC "super-molecule" (**65**). The left panel depicts their propeller-like structure.

is further stabilized via intramolecular hydrogen bonding whereas molecule **61** carries triphenylene terminal discotic units.[8] Should benzene receive 3-fold aryl substitution, the propeller-like 1.3.5-triphenylbenzene (TPB) molecule is formed, capable of playing the role of a bulkier central linking unit. Derivatives of TPB (**62**) also have a prominent role in the family of star-shaped discotics.[84–88] Besides its homocyclic form, heterocyclic variants of benzene are also utilized as central linking units, such as triazine and boroxine.[8;74;84]

Tri-arm molecular geometries can also be achieved via the utilization of atomic species capable of 3-fold covalent bonding, such as nitrogen and boron. A characteristic example involves TPA (**63**) propeller-like molecules as central linking units. Applications of TPA derivatives are frequently encountered in the literature in D-A systems of optoelectronic usage, typically combined with other polyphenyls and heterocyclic compounds, e.g. thiophene, pyrrole, and perylene derivatives.[89–92] An electron-deficient propeller-like discogen similar to TPA is obtained by switching the central nitrogen linking atom with boron. The resulting star-shaped molecule is triphenylborane **64** (BPh3), possesses an analogous geometry to TPA, but acts as an acceptor unit in organic electronic applications.[93;94]

The family of tri-arm star-shaped molecules undoubtedly contains far more members than the aforementioned case studies. Some characteristic examples include purely organic and metal-containing cyclophanes, and macrocyclic molecules as central linkers,[74] tri-arm units substituted with polar groups[8;74] and planar tri-substituted discotic molecules, such as triphenylene, triazatruxene, and decacyclene.[8;95] Moreover, non-articulate, rigid bonding can be utilized for the grafting of the peripheral arms, e.g. triphenylene-tris(naphthaleneimidazole)s,[96] while lean 3-fold PAH cores can be synthesized through the fusion of tetracene and pentacene derivatives.[97]

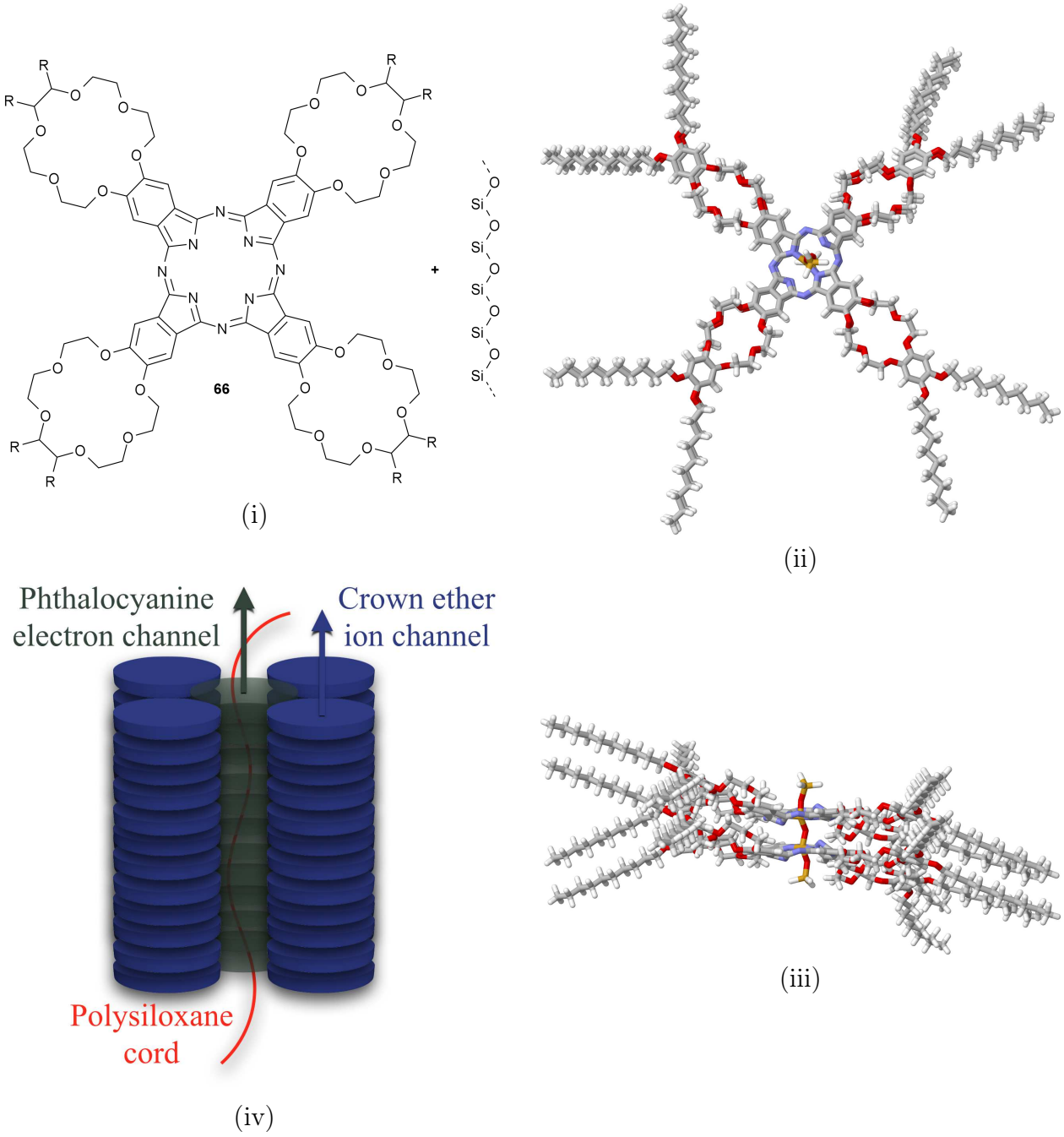

Figure 1.19: Different levels of self-organization of a spinal columnar phthalocyanine polymer: from (i) a discotic monomer to (ii, iii) a threaded dimer, and to (iv) a polymerized molecular nanowire.

As far as propeller-like nanographene molecules are concerned, advances in methods of synthesis[62] have paved the way towards the building of tri-arm discotic molecules with extended terminal PAH cores via the cyclodehydrogenation of appropriate polyphenylene dendrimers, resulting in materials with tunable properties.[77;98] Star-shaped discotic "super-molecules" with HBC and more extended cores are already accessible via available synthesis methods, utilizing a variety of molecular central linkers, such as benzene and TPA,[77] and even single atom linkers like nitrogen. Moreover, nitrogen-linked tri-arm

HBC derivatives, carrying a series of peripheral substitutions have been successfully used as three-dimensional nanographene assemblies for lithium storage as anode materials.[99]

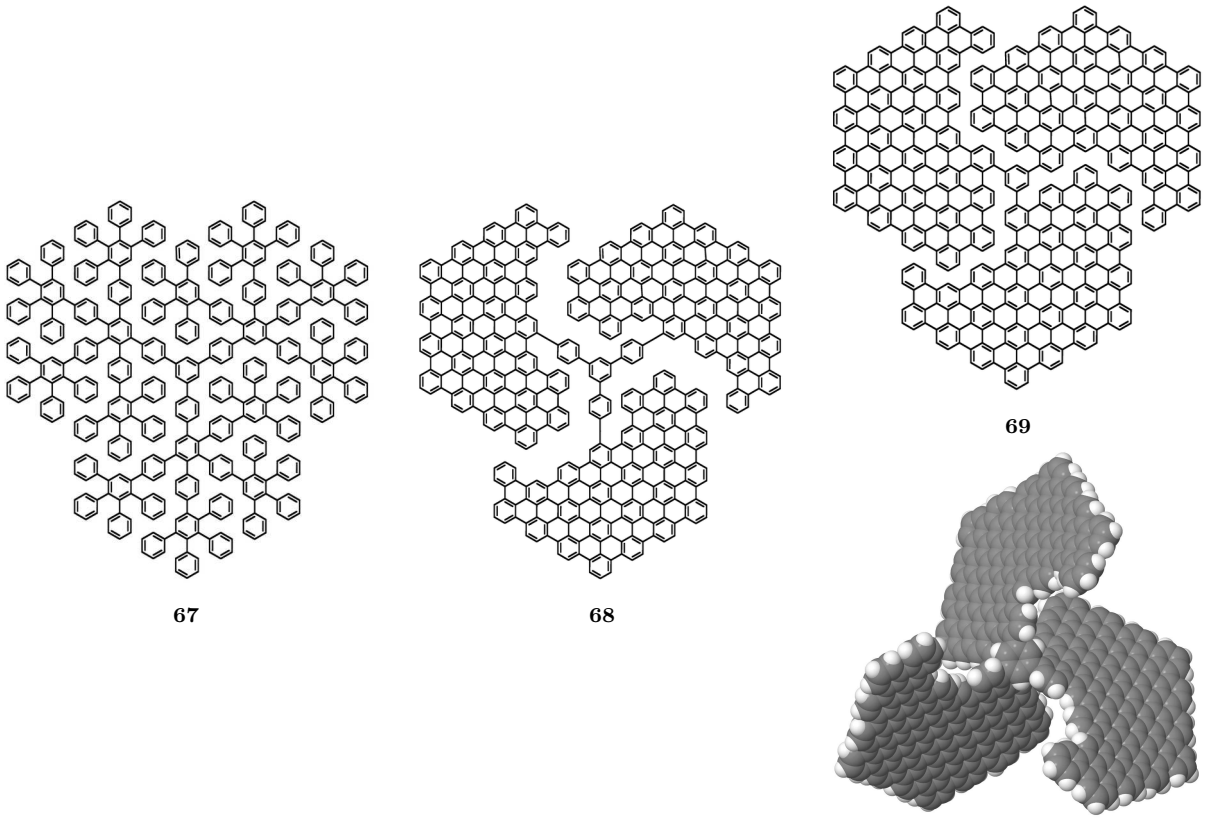

Figure 1.20: The synthetic route from a polyphenylene dendrimer precursor **67** to nanopropellers with a TPB (**68**) or benzene (**69**) core.

Perhaps the most suitable way to conclude this concise introduction to discotic materials is through two final examples from the literature that elucidate the interdisciplinary nature of discotic materials and the extraordinary capabilities of contemporary methods of synthesis towards multifunctional molecular assemblies. The first example involves a discotic polymer with a characteristic spinal columnar (or "shish kebab") structure that results from core polymerization of phthalocyanine derivatives with diverse intramolecular structure.[8] The fusion products of a phthalocyanine discotic core and crown ether moieties bearing various side chains constitute prototype "exotic" cores, capable of electronic conduction from the phthalocyanine part and ionic transfer from cyclic ether segments. Such mesogens can undergo a peculiar type of core polymerization, thus forming more robust assemblies from a structural point of view. To be more precise, the hollow nature of phthalocyanine cores prompts their threading by linear polymers that can bind with inner nitrogen atoms via permanent covalent bonds. Nolte and co-workers[100;101] successfully produced siloxane-threaded phthalocyanine cores decorated with alkyl-functionalized crown ethers on their periphery (**66**), resulting in novel discotic elastomers with hybrid ionoelectronic capabilities. Characteristic illustrations are shown

in Figure 1.19.

The second example is linked to the culmination of cyclodehydrogenation synthetic processes towards nanomaterials with diverse structural features. The pivotal work of Müllen and co-workers has enabled the fabrication of intricate nanometric molecular architectures using appropriate polyphenylene dendrimer precursors.[77;97;98] A truly remarkable product of this method is the nanopropeller **69** shown in Figure 1.20: a novel tri-arm molecular assembly comprised of three PAH "fan blades", connected via a benzene linker or a TPB linker (**68**).[102] Future applications of such molecules in the fields of organic electronics, hydrogen and ion storage, nanometric graphite intercalation compounds, and nanomechanics are within technological reach and will most definitely position nanographene-based materials in the epicenter of the ever-evolving universe of nanoscience and nanotechnology.

1.2 Computational Materials Science and Engineering

1.2.1 Overview

One of the most influential milestones of the 20th century is undoubtedly the advent of computers, with crucial impact on the advancement of research and technology. The first electronic, general purpose, large scale, digital computer was the "Electronic Numerical Integrator and Computer" (ENIAC), commissioned and financed by the United States Army and constructed between 1943 and 1945 at the University of Pennsylvania's Moore School of Electrical Engineering. From the mid-1940s till now, computers and their high-performance progeny called "supercomputers" have undergone a fascinating evolutionary track. Some noteworthy keynote achievements along this track are the construction of the "Illinois Automatic Computer" (ILLIAC) in 1951, the deployment of MANIAC* at the Los Alamos Scientific Laboratory in 1952, the first "Cray-1" vector supercomputer installed at Los Alamos National Laboratory in 1976, and a series of breakthroughs from 1982 to 1996 by Japanese and American manufacturers, including Fujitsu's "Numerical Wind Tunnel", Intel's "Paragon", and the famous "Deep Blue" chess-playing supercomputer developed by IBM. Supercomputer evolution has reached a current pinnacle with the deployment of powerful (and power-hungry) massively-parallel supercomputers, such as the Chinese "Sunway TaihuLight" and "Tianhe-2", the Swiss "Piz Daint", the Japanese "Gyoukou", and the USA-based "Titan" and "Sequoia", all capable of performing at the peta-floating point operations per second (petaFLOP) regime.[103–106]

The unprecedented computational power available nowadays is a direct consequence

*The name MANIAC (Mathematical Analyzer, Numerical Integrator, and Computer or Mathematical Analyzer, Numerator, Integrator, and Computer) was sarcastically proposed by N. Metropolis in an attempt to stop such "baptismal practices". History showed that it might have had the opposite effect!

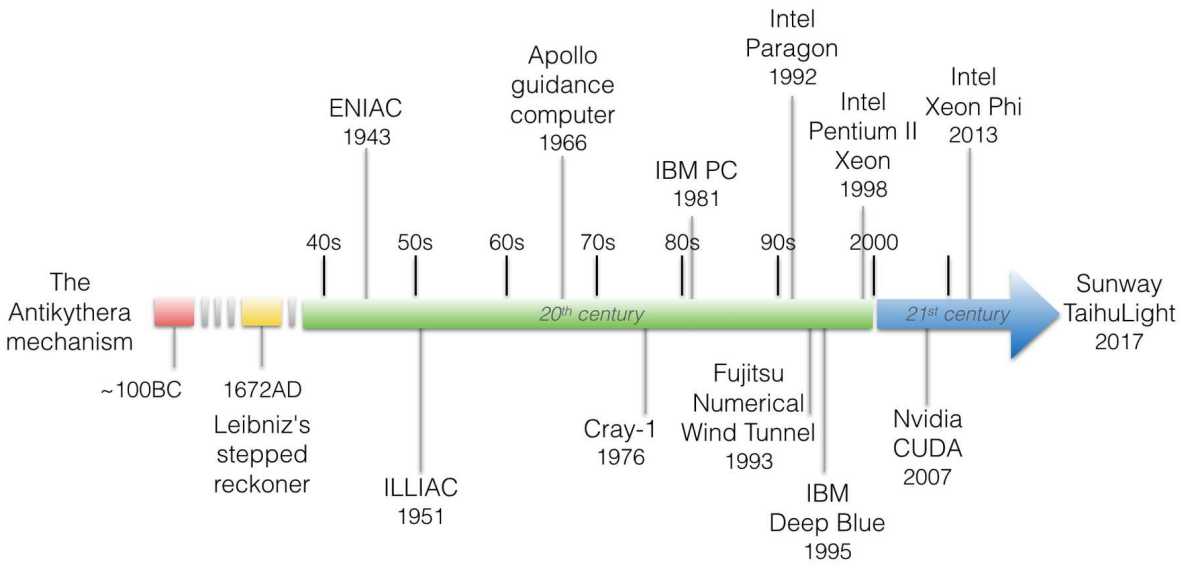

Figure 1.21: The evolution of computing: from the first mechanical computer to the currently fastest supercomputer.

of microchip miniaturization that has evolved following the so-called "Moore's law", i.e. an observation stated by Gordon Moore, co-founder of Intel, stating that the number of transistors in a dense integrated circuit (IC) doubles approximately every two years. Besides the apparent effect on supercomputer technology, Moore's law has propelled the capabilities of commodity personal computers (PC) at such a level, rendering scientific calculations possible using both regular PCs and high-end workstations. Computational efficiency has been augmented by a plethora of IC advancements, with the most prominent being the dawn of simultaneous multithreading by Intel, thus improving the parallelization of computations performed on a microprocessor. Furthermore, computational power has been steadily fortified at all levels of computer interconnection, i.e. from single units to relatively small clusters of connected computing elements and to contemporary supercomputers, via the utilization of alternative supporting technologies, e.g. graphics processing units pioneered by Nvidia and Intel's Xeon Phi many-core co-processors.[106–108]

This abundance of computational resources finds multitudinous applications in various scientific disciplines such as climate and earthquake modeling, plasma and high-energy physics, bioinformatics and computational biology, geophysical exploration and geoscience, astrophysics, materials science and engineering, and computational nanotechnology. Other fields of high performance computing utilization are defense applications, e.g. the US Stockpile Stewardship program, a framework for reliability testing and maintenance of nuclear weapons without the use of nuclear testing, signals intelligence, transportation, societal health and safety, and macroeconomical and sociotechnical systems studies.[109]

The field of computational materials science and engineering (CMSE) is in its essence the utilization of computer calculations towards the understanding and prediction of

material properties and behavior through modeling and simulations. CMSE is a many-purpose discipline. In its basic form, simple models that incorporate the fundamental physical behavior of a system can be established and then put to use via computer-aided calculations in order to examine properties and processes in a qualitative manner, seeking overall understanding of manifested phenomena. On the other hand, more detailed and elaborate methodologies and models can be utilized, thus aiming at qualitative results regarding properties and behavior of specific materials. When coupled to experimental findings, either for validation purposes or for guided model and method selection, CMSE performs at its best, providing deep understanding of phenomena that experiments alone cannot see and even contribute to the discovery of new materials.[110]

Modern CMSE can be understood in a triptych framework that includes the notions of theory, modeling, and simulation.[111] A theory is a set of axioms and procedures resulting in a predictive mathematical description of the natural world. CMSE can be addressed within the fold of theories such as (i) non-relativistic *ab-initio* Quantum Mechanics (QM), (ii) classical and continuum mechanics, (iii) statistical mechanics and thermodynamics, and (iv) classical thermodynamics. Systems described by means of QM methods follow the Schrödinger equation in its time-dependent or independent forms. A widely used wavefunction-based theoretical approach relies on the so-called Hartree-Fock (HF) theory. Furthermore, the pioneering work of Hohenberg, Kohn and Sham led to the advent of the Density Functional Theory (DFT) which reformulates quantum mechanical problems in the context of electron density instead of wavefunctions. Classical mechanics deals with classical particles trajectories, having in its epicenter the time evolution of position and momentum via either a Newtonian formulation or by means of analytical mechanics methods based on Lagrangian or Hamiltonian formulations. The extension of classical mechanics from the level of a collection of particles to mass distributions and vector and tensor fields leads to the realm of continuum mechanics. A macroscopic view of material properties based on microscopically-accessed information constitutes the core of statistical mechanics and statistical thermodynamics, thus dealing with average values and fluctuations of observables. Finally, the theory of classical thermodynamics revolves around the principle of entropy maximization of an isolated system by relating macroscopic state variables via fundamental equations.

The need of different levels of theory was vividly outlined in 1948 by D. R. Hartree in his work "The calculation of atomic structures":[112]

"*The problem of calculating the atomic structure of an atom or ion, other than one with just a single electron, is the problem of solving the wave equation for a many-particle system. This equation has no exact formal solution in finite terms, and it is necessary to use approximations both for this reason and for a more practical one, which is this: for an atom of p electrons, the solution is a function of 3p variables, and even if it were possible to evaluate such a solution to any degree of numerical accuracy required, no satisfactory*

way of presenting the results, either in tabular or graphical form, is known. It has been said that the tabulation of a function of one variable requires a page, of two variables a volume, and of three variables a library; but the full specification of a single wave function of neutral Fe is a function of seventy-eight variables. It would be rather crude to restrict to ten the number of values of each variable at which to tabulate this function, but even so, full tabulation of it would require 10^{78} *entries, and even if this number could be reduced somewhat from considerations of symmetry, there would still not be enough atoms in the whole solar system to provide the material for printing such a table.*"
Hartree's profound conclusion justifies the imperative demand for the development of appropriate theories and for the examination of different aspects of the material world.

Within the fold of a selected level of theory, various models can be established that act as prescribed quantification media. The so-called Kohn-Sham formulation is a characteristic DFT model that projects the many-body quantum system to non-interacting single-particle representations under the influence of an effective potential. In the case of classical mechanics, particle interactions are reduced to interatomic potentials used in a classical Hamiltonian that dictates the temporal evolution of a given system. Interactions at the level of continuum mechanics can be approached via field models, such as phase, compositional and stress/strain fields, based on the existence of a free energy functional expressed by such fields that can represent the thermodynamics of the system under study.

The third and final constituent of the described fundamental triptych is the notion of simulation. A simulation is a computer-aided realization of a given model by means of algorithmic approaches. Both deterministic and stochastic simulation methods driven by probabilistic evolution schemes (e.g. Markov processes) can be utilized towards the system propagation through the phase space. Deterministic paradigms include matrix-based algorithms for energy minimization of quantum systems obeying the so-called Rayleigh-Ritz variational principle, the Molecular Dynamics (MD) approach based on the integration of equations of motion using either classical models for interaction representations or quantum-derived forces in the context of the Born-Oppenheimer approximation, and – undoubtedly – a series of robust algorithms for ordinary and partial differential equations pertinent to continuum mechanics models. Stochastic methods include atomistic Monte Carlo (MC) simulations that evaluate system configurations without providing dynamical information via the utilization of normal and "unnatural" real space moves for a more efficient phase space sampling. Non-atomistic MC simulations include the Quantum Monte Carlo (QMC) method that puts to use stochastic approaches for the solution of quantum many-body problems at the wavefunction level and various spin models, like the Ising and Potts models.

Phenomena, processes and properties governing materials response span an extreme range of length and time scales. Length scales can vary from a few Å up to meters,

whereas time scales span from femtosecond-resolved atomic vibrations to decades of years of materials use. As a result, no single simulation technique is available that can function on all length and time scales, resulting in method development that is focused on specific physicochemical and engineering phenomena, and mechanisms which dictate the spatial and temporal resolution.[110;113]

The most popular wavefunction-oriented *ab-initio* simulation methods encountered at the nanometric level are Self-Consistent Field (SCF) HF calculations and the so-called post-HF methods, like Møller-Plesset perturbation theory calculations of order n (MPn), and Configuration Interaction (CI) and Coupled Cluster (CC) techniques, along with the commonly named Multi-Reference (MR) methods, e.g. Multi-Configurational SCF (MCSCF) and order n Complete Active Space Perturbation Theory (CASPTn). Although post-HF and MR methods yield highly accurate quantitative results, describing in the most satisfying way electron correlation and even dispersion interactions, their scaling with respect to system size is forbidding, should one try to cross the spatial boundaries towards larger systems, restricting usage to systems of a few atoms.[114;115]

An ingenious theoretical workaround in SCF *ab-initio* QM methods with respect to scaling, performance, and quantitative robustness was introduced via DFT simulations. In its essence, DFT translates the quantum mechanical problem from the wavefunction level to the electronic density, postulating that properties of a quantum many-body system can be derived through the use of density functionals. Within the context of DFT, the ground-state electronic density distribution contains the same information as the ground-state wave function, thus simplifying spin-independent calculations from a $3N$-dimensional space (where N is the number of electrons) to three-dimensional space. Furthermore, a total energy density functional exists which attains a global minimum at the equilibrium electronic density. This revolutionary approach shifts the focus scientific endeavors from cumbersome wavefunction-based techniques to the search for a best suited functional, with the "Holy Grail" of DFT being the realization of a universal functional. Current DFT breakthroughs have enabled *ab-initio* simulations of thousands of atoms, crossing the few Å barrier and reaching the realm of the nanoscale. When coupled to MD techniques, time-dependent DFT simulations are currently performing at the picoseconds level.[114;116;117]

Further up ahead on the ladder of spatial and temporal resolution lie the so-called semi-empirical simulation methods. From a physicist's point of view, the starting point of semi-empirical methods is the Tight Binding method based on Kohn-Sham type effective Hamiltonians, inaugurated by the seminal work of Slater and Koster for band structure calculations of simple crystals. As far as quantum chemistry is concerned, such methods rely on the HF formalism, approximating or omitting certain electronic degrees of freedom (e.g. two-electron integrals) by introducing effective Hamiltonians. The most important issue for the construction of a plausible effective Hamiltonian is the selection

of appropriate terms for omission and the tuning of empirical parameters bearing in mind either experimental data or *ab-initio* findings. Examples of widely used semi-empirical quantum chemical simulation techniques are the Pariser-Parr-Pople and Hückel-based methods for extended π systems, the methods introduced by Pople and co-workers, such as Intermediate Neglect of Differential Overlap (INDO) and Neglect of Diatomic Differential Overlap (NDDO)[†] methods, and a series of semi-empirical Hamiltonians (MNDO, AM1, PM3, ZINDO, etc.) emanating from the work of Zerner, Dewar, Thiel, Steward, and co-workers.[118–120]

When explicit quantum phenomena drop out of focus during the computational exploration of specific properties or mechanisms, the torch is passed to the field of empirical atomistic simulations. At this level of theory, atoms are treated as classical particles following empirical interaction rules derived either from methods further down the scale ladder (*ab-initio* or semi-empirical information) or from experimental knowledge. Once these interaction rules are quantified by means of – typically – a position-dependent mathematical model for the description of the potential energy (also called a force field; FF), a plethora of simulation methods exists to put to use for the derivation of properties at and away from equilibrium. Deterministic empirical MD simulations are commonly utilized for computer-aided examination of materials at the nanoscale level, for both spatial and temporal scales, involving up to hundreds of thousands of particles. Furthermore, when algorithm scalability to massively-parallel infrastructure permits it – and occasionally via further force field simplifications for specific systems – the upper scale boundaries can be pushed up by order(s) of magnitude.[121] On the other hand, a series of force fields with embedded "chemical intuition" have been developed, the so-called reactive FFs, capable of bond formation and breaking according to the physicochemical environment in the vicinity of each atom. This type of reactive MD simulations manage to yield satisfactory results right on the apex between qualitative and quantitative predictions for specific material systems, but with a computational cost which currently prohibits their scalability compared to non-reactive MD simulations.[122]

The "alter ego" of MD simulations are stochastic particle-based MC simulations, performing in similar length and time scales, and containing a wide family of algorithms and techniques that find use in multiple areas of CMSE. In their simplest form, atomistic MC simulations rely on the so-called Metropolis-Hastings algorithm for efficient sampling over the configuration space. More sophisticated variants have emerged over the decades, finding an abundance of applications primarily to molecular and – in general – soft matter systems. A characteristic example is the Gibbs ensemble MC method for phase separation processes. Examples in the field of macromolecular simulations include the work of Frenkel, Siepmann, and co-workers on the so-called Configurational Bias MC (CBMC)

[†]Modified Neglect of Diatomic Overlap (MNDO); Austin Model 1 (AM1); Parameterized Model number 3 (PM3); Zerner's Intermediate Neglect of Diatomic Overlap (ZINDO)

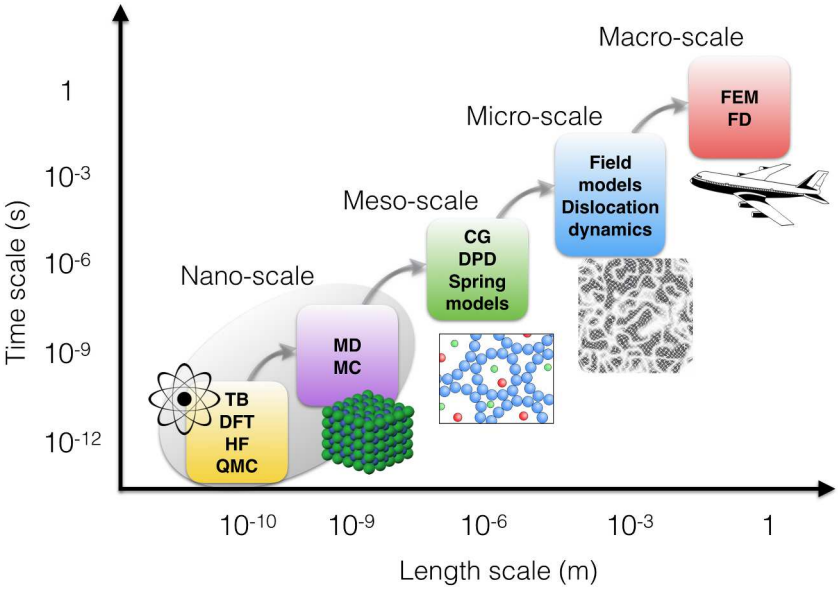

Figure 1.22: Simulation methods hierarchy in CMSE across length and time scales.

methods and the advances introduced by Theodorou and co-workers via Connectivity-altering MC algorithms for the equilibration and study of high molecular weight polymer systems.[123;124]

Accessible length and time scales can be further advanced via reducing the number of interaction sites in a particle-based system. Such approaches are utilized in so-called Coarse-Grained (CG) MD or MC simulations. Their realization is based on the clustering of groups of atoms to new CG sites that interact through a more computationally efficient effective FF, bridging this way the atomistic and the mesoscopic levels. Other mesoscale simulation methods include – but are not limited to – deterministic and stochastic cellular automata with global and local transformation rules, field methods, dislocation dynamics, and topological and vertex models. Finally, macroscale materials-related simulations typically rely on finite element and finite differences methods where the microstructure is incorporated via averaging constitutive laws.[113;125]

Multiscale approaches in the context of CMSE constitute a crucial and persistent contemporary research area. The concept of multiscaling across various temporal and spatial domains can be formulated in either a sequential or concurrent manner. Sequential multiscale methods rely on the cascade of information in the direction from lower to upper time and length scales. Customarily, this procedure is based on calculations on fundamental levels that are subsequently used to evaluate parameters as input to coarser phenomenological models that are capable of performing at an elevated scale. A simple example would be the methods of FF parametrization for atomistic simulations based on quantitative structural, thermodynamic, and dynamical information derived via *ab-initio* simulations. In a complete analogy, such procedures can be used for higher scales, like in the case of CG models based on appropriate analyses of atomistic trajectories at

equilibrium.[111]

On the contrary, concurrent multiscale methods are based on the principle of describing physical mechanisms inside a material in a compartmental fashion via the definition of well-defined areas in which different levels of modeling are applied that are seamlessly interfaced through appropriate "handshake" regions. An example of such a procedure would be to divide the space into atomistic regions and to continuum regions modeled via finite element methods. A proposed way towards a smooth interfacial "handshake" is based on the introduction of intermediate CG-modeled areas to couple the atomistic MD domain to a finite element mesh. Moreover, an important issue of concurrent multiscale modeling is the challenge of the so-called "scale-parity", insuring that all simulation domains are treated even-handedly.[111]

1.2.2 Modeling and Simulations of Discotic Materials

Computational studies of discotic materials span a wide range of modeling and simulations methods: from highly-accurate quantum chemical calculations to continuum mechanics, practically engulfing all intermediate spatial and temporal levels of description, with a plethora of multiscale approaches. Over the following pages, a short review of the computational literature regarding discotic materials is presented from the *ab-initio* level to the micro-scale, with emphasis on *peri*-condensed PAH molecules, macrocyclic cores, and disk-like polyphenyls, in either pristine or substituted forms.

As far as single molecule QM studies are concerned, multi-theory investigations of PAH cores have been carried out by Torres *et al.*[126], utilizing CASPT, CC, and MP2 quantum chemical techniques alongside to with DFT calculations, towards the examination of electronic properties with respect to core extent. Other interesting properties, such as the polyradical character of PAHs[127], non-linear optical properties versus core edge shape[128] and the evaluation of ring-current maps on macrocycles as means of aromaticity visualization on the magnetic criterion[129] have been realized via HF and DFT calculations. At the level of DFT modeling, structural and electronic properties of relatively small discogens like pyrene, coronene, and corannulene (a variant of coronene with a 5-membered ring in its center) have been also investigated in the literature.[130–133]

Triphenylene derivatives are a relatively popular molecular species of the discotics family, with hexakis (n-alkoxy) triphenylene (HATn) being the flagship of this division. HATn molecules have been examined at a single molecule DFT level of theory for the determination vibrational properties[134] and by means of semi-empirical Hamiltonians[135] for the evaluation of structural and electronic properties. Furthermore, in the category of discotic macrocycles, ground-state and excited-state electronic properties have been probed by Belviso *et al.*[136] for metal-free and nickel-containing porphyrin molecules via DFT calculations and the structural, electronic, vibrational, and optical properties of

prototype trigonal macrocycles have been investigated by Gallant *et al.*[137] through DFT and semi-empirical simulations complementary to experimental studies. In the case of HBC single molecules, of particular interest is the work of Maghsoumi *et al.*[138] on DFT-derived structural, vibrational, and electronic properties of chlorinated HBC, coupled to vibrational spectroscopy measurements. Moreover, DFT calculations of structural, electronic, and vibrational properties of extended PAH molecules with variable geometry have recently emerged in the computational literature of discotic materials.[139–142]

The next foremost level of molecular arrangement treated via *ab-initio* calculations involves dimer structures of discotic molecules. Of particular interest are the post-HF quantum chemical investigations of Monari *et al.*[143] on metal-free phthalocyanine cation dimers by means of CASPT and MR methods and the work of Yurtsever[144] utilizing MP2 calculations for the structural investigation of triphenylene dimers. Less computationally demanding calculations are based on DFT approaches for the determination of structural, electronic, vibrational, and optical properties, using either empirical dispersion corrections or appropriate exchange-correlation functionals capable of treating long-range interactions in a correct manner.[145–151] Additional noteworthy studies of discotic dimers via dispersion-corrected DFT calculations include the work of Antony *et al.*[152] on PAH molecules with variable symmetry, Guan *et al.*[153] on heterocyclic coronene and c-HBC dimers and "exotic" [*n*]circulenes, and Paraschiv *et al.*[154] on the examination of hydrogen bonding in tri-arm molecules bearing HAT*n* peripheral discotic units. Moreover, *ab-initio* dimer calculation results on various levels of theory, such as MP2, HF, and DFT, have been used for the parametrization and benchmarking of empirical force field simulations for large scale investigations of PAH clusters.[155;156] Discotic dimers can also be considered as prototypes for the examination of small scale organometallic systems. To this end, metal-intercalated discotic dimers of either pristine[157] or polyradical forms[158] of coronene have been examined at *ab-initio* levels of theory for the determination of structural, electronic, vibrational, and magnetic properties inherent to such metal-PAH complexations.

Molecular dimer geometries constitute the first level of approach for the examination of hopping charge transfer mechanisms. One of the first such applications on discotic molecules was the work of Cornil *et al.*[159] on homocyclic and heterocyclic triphenylene dimers via a semi-empirical INDO Hamiltonian, utilizing the so-called frontier molecular orbital splitting method for the evaluation of transfer integrals. This very method has been adapted to DFT calculations on a variety of systems, such as thiophene dendrimers[160] and fluorinated PAH molecules[161]. More robust methods for the derivation of transfer integrals relying on Kohn-Sham Hamiltonian matrix element manipulations have been utilized for the quantification of charge hopping mechanisms of dimers comprised of discotic molecules such as triphenylene[162;163], corannulene and sumanene derivatives[164;165], TPA-based mesogens[166], bisphenazine[167] and tetraphenyldipyranyli-

dene derivatives[168], and hexathienocoronene[169]. Other discotic mesogens examined via the aforementioned matrix element method include contorted, functionalized PAHs[170] and tri-arm covalently linked assemblies, such as triphenylene-tris(naphthaleneimidazole)s[96]. In addition, the interacting dimer approach for hopping conductivity can be further expanded to cluster approaches that deal with first-neighboring molecules and distribute charge migration pathways in a statistical manner. Such calculations have been carried out for small PAH molecules[171;172], pristine[173] and functionalized coronene molecules[174;175], and metal-free phthalocyanines[176].

Conductive capabilities of bulk, condensed phases of discotic materials can be quantified through density of states and periodic band structure calculations by means of DFT simulations employing periodic supercells. This type of approach has been successfully applied in the literature for molecular crystals made up of medium size *peri*-condensed discotic units and macrocycles, such as homocyclic[177] and heterocyclic[178] coronenes, PDI derivatives with variable peripheral functionalization and geometries[179–181], and mesogens of the phthalocyanine macrocyclic category[182;183]. Apart from bulk simulations using supercells with three-dimensional periodicity, DFT calculations can be put to use in systems with periodicity in only one dimension resembling molecular wires, as in the case of HATn clusters examined by Cinacchi *et al.*[184] and in metal-intercalated HBC molecular stacks[185].

The need for the examination of structural, thermodynamic, and dynamical properties of bulk discotic molecular assemblies at larger temporal and spatial scales results in the replacement of *ab-initio* and semi-empirical approaches by empirical atomistic methods. As far as functionalized discotic mesogens are concerned, two early simulation works of high importance are those of Maliniak[186] on BHAn molecules and of Bast and Hentschke[187] on HATn micellar aggregates in explicit aquatic solution. HATn derivatives have also been examined via atomistic simulations by Kearley *et al.*[188] in combination with experimental studies, and by Cinacchi *et al.* in both pure[189] and compound[190] discotic phases. Literature on MD studies of triphenylene derivatives also includes the works of Merekalova *et al.*[191] and Kruglova *et al.*[192], as well as the stacking pattern analyses via MC simulations conducted by Muccioli *et al.*[193]. Soluble HBC derivatives have been extensively studied by means of MD simulations by Andrienko *et al.*[194] and Marcon *et al.*[195], providing hybrid all-atom/united-atom interaction descriptions for discotic mesogens. Other noteworthy computational approaches at the atomistic level include the work of Cristinziano and Lelj[196] and Yoneya *et al.*[197] on phthalocyanines, and the simulations conducted by Costa *et al.*[198] regarding asphaltene molecules. Pristine PAH molecules have been also examined using empirical atomistic simulations.[199–204] Some intriguing cases include the work of Wilson *et al.*[205] on the formation of a cubatic phase by square platelets, the simulations of Chen *et al.*[206;207] on solid-liquid transitions of PAH clusters, and the work of Mao *et al.*[208] investigating the formation of soot particles from PAH

molecules via reactive FF MD simulations.

A major portion of the simulation literature on discotic materials currently contains multiscale combinations of atomistic modeling and dimer- and/or cluster- based QM analyses towards the incorporation of entropic phenomena and local disorder for the evaluation of charge transfer mechanisms in the bulk or for the utilization of structural information obtained from empirical Molecular Mechanics (MM) or MD simulations as input to QM calculations. An early computational work following such procedures was performed by Markovitsi *et al.*[209] examining the photophysical properties of HATn columnar phases via the utilization of a semi-empirical INDO Hamiltonian for excited-state calculations, coupled to MC algorithmic approaches for the rationalization of experimental fluorescence decay curves.

One of the first incorporations of empirical MM calculation results to QM charge transfer simulations is found in the work of Lemaur *et al.*[210] for triphenylene derivatives and HBC. The coupling between MD simulations and charge transport was investigated for HATn derivatives by Kruglova *et al.*[211] by calculating electronic properties using MD trajectories at equilibrium. An analogous approach was followed by Haverkate *et al.*[212], also for HATn discotic cores, exploiting structural information from MD simulations in order to comprehend the charge transfer mechanisms. A more laborious and robust multiscale methodology involving electronic structure calculations, atomistic MD and kinetic MC simulations for establishing direct correlations between molecular structure and charge mobility was introduced by Kirkpatrick *et al.*[213] for HBC derivatives. This very methodology has been extensively applied for more detailed calculations involving HBC derivatives[214–219], phthalocyanine cores[220], PDI derivatives[221–223], triphenylene-like mesogens[224], carbazole macrocycles[225], small discotic fragments[226], and star-shaped triazine derivatives[227]. Of particular importance is also the work of Idé *et al.*[228], elucidating aspects pertinent to charge transfer phenomena in prototype discotic heterojunctions comprised of perylene donor and benzoperylene diimido diester acceptor molecules. In addition, another interesting approach is found in the work of Navarro *et al.*[229] regarding charge transport analyses based on DFT calculations on D-A tri-arm molecules utilizing the so-called ONIOM model that partitions the systems under study into sub-units treated by QM methods of variable accuracy.

In order to access meso-scale phenomena, appropriate reductions to empirical interaction laws are essential. The most frequently encountered simplification route in the literature is to abandon detailed atomistic representations and adopt coarser, approximate expressions that capture the geometrical and interaction features inherent to discotic mesogens. The most straightforward method relies on the so-called bead-spring models in which appropriate groups of atoms are fused into spherical "super-atoms" with well-defined but coarser intra- and inter-molecular interactions. Such methods have been applied to computational studies of self-assembly mechanisms of tethered, disk-like nanopar-

ticles[230], structural properties and phase transitions of disk-coil macromolecules[231;232], shape-persistent macrocycles[233] and discotic liquid crystalline polymers[234], and to CG investigations of pristine PAH stacking behavior[235].

Abandoning altogether intramolecular discrete structural information, geometrically-derived approaches have been introduced, including the utilization of hard cut-spheres[236] and oblate hard spherocylinders[237] or ellipsoids[238] based on excluded volume interactions, sometimes augmented by long-range interaction terms, e.g. the effective Yukawa potential for the simulation of charged colloidal platelets[239]. In addition, soft interaction potentials have been used for the evaluation of structural properties and phase transitions by means of Dissipative Particle Dynamics simulations incorporating orientational interparticle dependences.[240–242]

Perhaps the most popular CG approach relies on the so-called Gay-Berne (GB) potential: an anisotropic generalization of the celebrated Lennard-Jones interaction potential that takes into account the orientational state of neighboring interacting molecules with appropriate variations to the attractive and repulsive terms. In the concept of GB approach, discotic mesogens are effectively replaced by ellipsoidal shaped molecules without any internal atomistic structure. Applications to discotic systems via MD and MC simulations have managed to capture mesophase structural, thermodynamic and dynamical properties, and phase transitions.[243–248] Some specialized applications of GB discotics include the work of Berardi and Zannoni[249] on biaxial mesogens, the studies of Chakrabarti and Wales[250] on tilted and helical arrangements of GB discogens, and the work of Cienega-Cacerez *et al.*[251] on binary mixtures. Moreover, GB simulations have elucidated mechanisms pertinent to nano-confinement[252] and MC simulations have been successfully applied for the study of the morphology of DLC vapor nanodrops[253]. In addition, GB ellipsoids have found applications in the field of multiscale charge transport simulations on discotic materials through a cascade of sequential computational techniques.[254;255]

Variants of the GB potentials have also been put to use, like the so-called hybrid Gay-Berne-Luckhurst-Romano[256;257] potential and the Corner-type S-function modified GB potential[258;259] that treats interacting disks as ellipsoids with embedded central sphere components, the so-called U particles[‡]. Other modified versions of the GB potential include corrections due to electrostatic interactions[260] and the so-called Oblate Gay-Berne-Kihara potential introduced by Martínez-Haya and Cuetos[261], while alternatives to GB potentials are also encountered in the literature, e.g. the utilization of the Paramonov-Yaliraki potential used by Hernandez-Rojas *et al.*[262] for the examination of coronene octamers.

Finally, micro-scale properties of discotic materials have been also probed by a series of computational works in the literature. Ray and co-workers have examined rheological

[‡]Also known as "ufo" particles due to their geometric resemblance to flying saucers.

properties exhibited by discotic mesophases via a nonlinear second-order tensor Landau-de Gennes (LdG) model, taking into account short-range order elasticity, long-range elasticity, and viscous effects.[263–267] Other characteristic continuum theory modeling include the work of Hong and Chan[268], utilizing the Ericksen and LdG models to investigate the structure development and texture formation across mesophase pitch-based carbon fibers, and the work of Noroozi and Grecov[269] on LdG theory studies of time transient isothermal flow of lyotropic nematic DLCs.

1.3 Thesis Objectives

The major questions to be addressed by this doctoral dissertation regarding multiscale simulations of discotic materials are the following:

- *What is the interplay between discotic molecular identity and electronic and charge transfer properties?* The chemical composition and morphology of discotic mesogens should - in principle - affect various aspects regarding material properties on the quantum level. *Ab-initio* Density Functional Theory calculations are put to use in order to examine effects of molecular-level alterations on electronic and charge transfer properties. Findings are gathered and presented in Chapter 3.

- *Which is the level of information accessible by means of empirical Molecular Dynamics simulations regarding bulk supramolecular assemblies of soluble discogens?* Thorough analyses on HBC derivatives are carried out for the determination of structural, mechanical, and dynamical properties via relatively simple empirical force fields, using state-of-the-art atomistic simulation techniques and analytical procedures. Results of the aforementioned endeavor are located in Chapter 4.

- *Can morphologically diverse discotic molecules be used for the creation of plausible structures for organic electronic applications?* A rather differentiated version of the typical alkyl-functionalized HBC core is examined: the amphiphilic, "Janus-type" HBC mesogen, carrying both hydrophilic and hydrophobic side chains, capable of intricate, solvent-controlled self-organization. Lamellar molecular crystals comprised of this mesogen are examined by means of Molecular Dynamics simulations, elucidating structural and dynamical phenomena at equilibrium in Chapter 5.

- *Does size actually matter?* Extended core mesogens and novel discotic "supermolecules", comprised of medium to large discotic cores covalently-linked via appropriate linkers, are examined via Molecular Dynamics simulations. Charge transfer capabilities of such exotic supramolecular nanowires are deduced using a multiscale methodology, thus bridging the realm of equilibrated atomistic trajectories with

finding from the quantum world. Methodological details and results are presented in Chapter 6.

Chapter 2

Theoretical Background

This chapter covers all essential theoretical notions related to the modeling and simulation methods utilized in this thesis. In the context of ab-initio modeling, elements of Density Functional Theory are briefly presented, along with a concise picture of contemporary computational charge transport methodologies applied to molecular hopping conductivity mechanisms. Moreover, concepts of empirical atomistic methods are presented, with particular focus on fixed-topology Molecular Dynamics simulation techniques.

2.1 Density Functional Theory

2.1.1 Fundamentals: from the Wavefunction to the Electronic Density

In its essence, DFT is a modeling paradigm treating many-electron, many-nuclei quantum problems. Before delving into the details behind this multi-purpose theory, a conceptual coverage of fundamental wavefunction-based QM methods is presented, along with some nomenclature that will be used later on.

If we consider a system of N electrons with coordinates $\vec{r}_1, \vec{r}_2, ..., \vec{r}_N$ and M nuclei with coordinates $\vec{R}_1, \vec{R}_2, ..., \vec{R}_M$, quantum theory dictates that the evolution of the system and all properties are described by a many-body wavefunction $\Psi = \Psi\left(\vec{r}_1, ..., \vec{r}_N; \vec{R}_1, ..., \vec{R}_M\right)$, with $|\Psi|^2$ representing the probability density for simultaneously finding electron 1 at position $\vec{r}_1$, electron 2 at position $\vec{r}_2$, and so on.[114;116;117;270] For the sake of simplicity, spin variables are currently omitted. The total electronic charge density is defined as the probability of finding any electron at $\vec{r}$ and is expressed as

$$n\left(\vec{r}\right) = N \int \left|\Psi\left(\vec{r}, \vec{r}_2, ..., \vec{r}_N; \vec{R}_1, \vec{R}_2, ..., \vec{R}_M\right)\right|^2 d\vec{r}_2 ... d\vec{r}_N d\vec{R}_1 ... d\vec{R}_M \tag{2.1}$$

following the normalization condition

$$\int n\left(\vec{r}\right) d\vec{r} = N \tag{2.2}$$

while the density operator is defined as:

$$\hat{n}\left(\vec{r}\right) \equiv \sum_{i} \delta\left(\vec{r} - \vec{r}_i\right) \tag{2.3}$$

The non-relativistic, time-independent Schrödinger equation for such a system is written as

$$\hat{H}_{\text{tot}}\Psi = E_{\text{tot}}\Psi \tag{2.4}$$

where

$$\begin{aligned}\hat{H}_{\text{tot}}\left(\vec{r}_1, ..., \vec{r}_N; \vec{R}_1, ..., \vec{R}_M\right) = \\ = -\sum_i \frac{\nabla_i^2}{2} - \sum_I \frac{\nabla_I^2}{2M_I} + \frac{1}{2}\sum_{I\neq J} \frac{Z_I Z_J}{\left|\vec{R}_I - \vec{R}_J\right|} - \sum_{i,I} \frac{Z_I}{\left|\vec{r}_i - \vec{R}_I\right|} + \frac{1}{2}\sum_{i\neq j} \frac{1}{|\vec{r}_i - \vec{r}_j|}\end{aligned} \tag{2.5}$$

the many-body quantum Hamiltonian and E_{tot} the total energy, both expressed in Hartree atomic units*. Lowercase and uppercase indices correspond to electronic and nuclear variables respectively; M symbolizes the nuclear mass and Z atomic number.

The direct solution of Equation 2.4 is an immensely complicated problem and practically impossible for even simple polyelectronic systems. This predicament is referred to as the "exponential wall"[271] in the solution of the many-body Schrödinger equation, due to the fact that the complexity of the solution grows exponentially with system size. In order to circumvent this "pathogenic" condition, a series of approximations have been proposed and utilized.

The first simplification relies on the so-called Born-Oppenheimer approximation dictating that due to the massiveness of atomic nuclei compared to electrons ($M \to \infty$), the motions of nuclei and electrons can be separated. Under this assumption, nuclear coordinates are treated as external parameters and the nuclear Coulomb interaction is practically a constant, thus leading to the "clamped nuclei", many-electrons Schrödinger equation

$$\begin{aligned}\left[-\sum_i \frac{\nabla_i^2}{2} - \sum_{i,I} \frac{Z_I}{\left|\vec{r}_i - \vec{R}_I\right|} + \frac{1}{2}\sum_{i\neq j} \frac{1}{|\vec{r}_i - \vec{r}_j|}\right]\Psi = \left[E_{\text{tot}} - \frac{1}{2}\sum_{I\neq J} \frac{Z_I Z_J}{\left|\vec{R}_I - \vec{R}_J\right|}\right]\Psi \Leftrightarrow \\ \Leftrightarrow \hat{H}\Psi = E\Psi\end{aligned} \tag{2.6}$$

where $\Psi = \Psi\left(\vec{r}_1, \vec{r}_2, ..., \vec{r}_N\right)$ is the many-electrons wavefunction.

*$m = e = \hbar = 4\pi\varepsilon_0 = 1$. In this unit system, energy is expressed in Ha and distance in Bohr radii.

The many-electrons Hamiltonian

$$\hat{H}\left(\vec{r}_1,...,\vec{r}_N\right) = -\sum_i \frac{\nabla_i^2}{2} - \sum_{i,I} \frac{Z_I}{\left|\vec{r}_i - \vec{R}_I\right|} + \frac{1}{2}\sum_{i\neq j} \frac{1}{|\vec{r}_i - \vec{r}_j|} \tag{2.7}$$

can be written in a more compact form should a single electron Hamiltonian

$$\hat{H}_0\left(\vec{r}\right) = -\frac{\nabla^2}{2} - \sum_I \frac{Z_I}{\left|\vec{r} - \vec{R}_I\right|} = -\frac{\nabla^2}{2} + V_{\mathrm{n}}\left(\vec{r}\right) \tag{2.8}$$

be defined, where

$$V_{\mathrm{n}}\left(\vec{r}\right) = -\sum_I \frac{Z_I}{\left|\vec{r} - \vec{R}_I\right|} \tag{2.9}$$

the Coulomb potential of the nuclei experienced by the electrons. All of the above result to the following elegant version of the many-electrons Hamiltonian

$$\hat{H}\left(\vec{r}_1,...,\vec{r}_N\right) = \sum_i \hat{H}_0\left(\vec{r}_i\right) + \frac{1}{2}\sum_{i\neq j} \frac{1}{|\vec{r}_i - \vec{r}_j|} \tag{2.10}$$

The next simplification step after the Born-Oppenheimer approximation is the so-called independent-electrons (or independent-particles) approximation. One simplified approach is attributed to Hartree for the examination of polyelectronic atoms, expressing the Ψ_{H} wavefunction as a product of orthonormal single-particle wavefunctions $\phi_i\left(\vec{r}_i\right)$

$$\Psi_{\mathrm{H}}\left(\vec{r}_1,...,\vec{r}_N\right) = \prod_i \phi_i\left(\vec{r}_i\right) \tag{2.11}$$

with the electronic density written as

$$n\left(\vec{r}\right) = \int \Psi^* \hat{n}\left(\vec{r}\right) \Psi d\vec{r}_1 ... d\vec{r}_N = \sum_i \left|\phi_i\left(\vec{r}\right)\right|^2 = \sum_i n_i\left(\vec{r}\right) \tag{2.12}$$

The expected value of the energy under Hartree's approximation is expressed as

$$E_{\mathrm{H}} = \sum_i \int \phi_i^*\left(\vec{r}_i\right) \hat{H}_0\left(\vec{r}_i\right) \phi_i\left(\vec{r}_i\right) d\vec{r}_i + \frac{1}{2}\sum_{i\neq j} \int \phi_i^*\left(\vec{r}_i\right) \phi_j^*\left(\vec{r}_j\right) \frac{1}{|\vec{r}_i - \vec{r}_j|} \phi_i\left(\vec{r}_i\right) \phi_j\left(\vec{r}_j\right) d\vec{r}_i d\vec{r}_j \tag{2.13}$$

The utilization of first order variational calculus for the minimization of E_{H} with respect to orthonormal single-particle wavefunctions $\phi_i\left(\vec{r}_i\right)$ results in Hartree's mean-field equations:

$$\left[-\frac{1}{2}\nabla_i^2 + V_{\mathrm{n}}\left(\vec{r}_i\right) + V_i^{\mathrm{H}}\left(\vec{r}_i\right)\right] \phi_i\left(\vec{r}_i\right) = \varepsilon_i \phi_i\left(\vec{r}_i\right) \tag{2.14}$$

where

$$V_i^{\mathrm{H}}\left(\vec{r}_i\right) = \sum_{j \neq i} \int \frac{\phi_j^*\left(\vec{r}_j\right) \phi_j\left(\vec{r}_j\right)}{\left|\vec{r}_i - \vec{r}_j\right|} d\vec{r}_j \tag{2.15}$$

the so-called Hartree potential and ε_i the Lagrange multipliers resulting from the orthonormality of single-particle states. The simultaneous solution of Equations 2.12, 2.14, and 2.15 consists the SCF Hartree method.

A further improvement on Hartree's method is based on the utilization of appropriate wavefunctions to account for Pauli's exclusion principle, stating that the many-body wavefunction of a fermionic system must be antisymmetric upon particle variable exchange. Wavefunctions that obey this restriction are the so-called Slater determinants of single-particle states

$$\Psi = \frac{1}{\sqrt{N!}} \begin{vmatrix} \phi_1\left(\vec{r}_1\right) & \ldots & \phi_1\left(\vec{r}_N\right) \\ \vdots & \ddots & \vdots \\ \phi_N\left(\vec{r}_1\right) & \ldots & \phi_N\left(\vec{r}_N\right) \end{vmatrix} \tag{2.16}$$

The mere utilization of Slater determinants on the many-electrons Hamiltonian of Equation 2.10 results in the following expected energy value:

$$\begin{aligned} E_{\mathrm{HF}} = \sum_i \int \phi_i^*\left(\vec{r}_i\right) \hat{H}_0\left(\vec{r}_i\right) \phi_i\left(\vec{r}_i\right) d\vec{r}_i + \frac{1}{2} \sum_{i \neq j} \int \frac{\phi_i^*\left(\vec{r}_i\right) \phi_j^*\left(\vec{r}_j\right) \phi_i\left(\vec{r}_i\right) \phi_j\left(\vec{r}_j\right)}{\left|\vec{r}_i - \vec{r}_j\right|} d\vec{r}_i d\vec{r}_j - \\ - \frac{1}{2} \delta\left(\sigma_i, \sigma_j\right) \sum_{i \neq j} \int \frac{\phi_i^*\left(\vec{r}_i\right) \phi_j^*\left(\vec{r}_j\right) \phi_i\left(\vec{r}_j\right) \phi_j\left(\vec{r}_i\right)}{\left|\vec{r}_i - \vec{r}_j\right|} d\vec{r}_i d\vec{r}_j \end{aligned} \tag{2.17}$$

where σ_i the spin variable of orbital i and δ Kronecker's delta function. The Hartree-Fock equations are derived via a first order variational minimization of the HF energy (Eq. 2.17) with respect to wavefunctions in the form for Slater determinants (Eq. 2.16):

$$\left[-\frac{1}{2}\nabla_i^2 + V_{\mathrm{n}}\left(\vec{r}_i\right) + V_i^{\mathrm{H}}\left(\vec{r}_i\right)\right] \phi_i\left(\vec{r}_i\right) + \sum_{j \neq i} \delta\left(\sigma_i, \sigma_j\right) \int \frac{\phi_j^*\left(\vec{r}_j\right) \phi_i\left(\vec{r}_j\right) \phi_j\left(\vec{r}_i\right)}{\left|\vec{r}_i - \vec{r}_j\right|} = \varepsilon_i \phi_i\left(\vec{r}\right) \tag{2.18}$$

By introducing the single-particle exchange density

$$n_i^{\mathrm{X}}\left(\vec{r}_i, \vec{r}_j\right) = \sum_{j \neq i} \frac{\phi_i\left(\vec{r}_j\right) \phi_i^*\left(\vec{r}_i\right) \phi_j\left(\vec{r}_i\right) \phi_j^*\left(\vec{r}_j\right)}{\phi_i\left(\vec{r}_i\right) \phi_i^*\left(\vec{r}_i\right)} \tag{2.19}$$

HF equations can be recast as:

$$\left[-\frac{1}{2}\nabla_i^2 + V_{\mathrm{n}}\left(\vec{r}_i\right) + V_i^{\mathrm{H}}\left(\vec{r}_i\right) + V_i^{\mathrm{X}}\left(\vec{r}_i\right)\right] \phi_i\left(\vec{r}_i\right) = \varepsilon_i \phi_i\left(\vec{r}_i\right) \tag{2.20}$$

where the Hartree and the so-called exchange V_i^{X} potentials are expressed as

$$V_i^{\mathrm{H}}(\vec{r}_i) = \int \frac{n(\vec{r}_j) - n_i(\vec{r}_j)}{|\vec{r}_i - \vec{r}_j|} d\vec{r}_j,\ V_i^{\mathrm{X}}(\vec{r}_i) = -\int \frac{n_i^{\mathrm{X}}(\vec{r}_i, \vec{r}_j)}{|\vec{r}_i - \vec{r}_j|} d\vec{r}_j \tag{2.21}$$

The exchange potential is a direct consequence of the utilization of Slater determinants, describing the effects of non-local exchange interaction.

Having established some essential notions on wavefunction-based SCF theory, the focus in now redirected to the electronic density. The foundation of DFT is the Hohenberg-Kohn (HK) theorem[272] stating that the ground-state energy of a many-electron system is a functional of the electronic density. The implications of the HK theorem are profound from a computational point of view, since it reformulates the quantum problem from the wavefunction level of $3N$ variables to the electronic density level with only three dimensions. According to the HK theorem, and following the compact Dirac *bra-ket* notation, the energy is expressed as the following functional:

$$E[n] = \langle\Psi| - \sum_i \frac{\nabla_i^2}{2} + \sum_i V_{\mathrm{n}}(\vec{r}_i) + \frac{1}{2}\sum_{i\neq j} |\vec{r}_i - \vec{r}_j|^{-1} |\Psi\rangle \tag{2.22}$$

A more compact notation for the kinetic and Coulomb term is commonly used according to the definitions

$$\hat{T} \equiv -\sum_i \frac{\nabla_i^2}{2},\ \hat{W} \equiv \frac{1}{2}\sum_{i\neq j} |\vec{r}_i - \vec{r}_j|^{-1} \tag{2.23}$$

Furthermore, the utilization of the density operator (Eq. 2.3) results in the following elegant expression for the expected value of the electron-nuclei interaction term:

$$\begin{aligned}
&V_{\mathrm{n}}(\vec{r}_i) = \textstyle\int V_{\mathrm{n}}(\vec{r})\,\delta(\vec{r} - \vec{r}_i)\,d\vec{r} \Leftrightarrow \\
&\Leftrightarrow \textstyle\sum_i V_{\mathrm{n}}(\vec{r}_i) = \sum_i \int V_{\mathrm{n}}(\vec{r})\,\delta(\vec{r} - \vec{r}_i)\,d\vec{r} = \int V_{\mathrm{n}}(\vec{r}) \sum_i \delta(\vec{r} - \vec{r}_i) d\vec{r} \Leftrightarrow \\
&\Leftrightarrow \langle\Psi| \textstyle\sum_i V_{\mathrm{n}}(\vec{r}_i) |\Psi\rangle = \langle\Psi| \int V_{\mathrm{n}}(\vec{r}) \sum_i \delta(\vec{r} - \vec{r}_i) d\vec{r} |\Psi\rangle = \\
&= \textstyle\int V_{\mathrm{n}}(\vec{r}) \langle\Psi| \sum_i \delta(\vec{r} - \vec{r}_i) |\Psi\rangle\, d\vec{r} \overset{(2.22)}{\Leftrightarrow} \\
&\Leftrightarrow \langle\Psi| \textstyle\sum_i V_{\mathrm{n}}(\vec{r}_i) |\Psi\rangle = \int V_{\mathrm{n}}(\vec{r}) \langle\Psi| \hat{n}(\vec{r}) |\Psi\rangle\, d\vec{r} = \int V_{\mathrm{n}}(\vec{r})\, n(\vec{r})\, d\vec{r}
\end{aligned} \tag{2.24}$$

As a result, definitions 2.23 and Equations 2.24 bring the energy functional to the form below

$$E[n] = \int V_{\mathrm{n}}(\vec{r})\, n(\vec{r})\, d\vec{r} + \langle\Psi| \hat{T} + \hat{W} |\Psi\rangle \tag{2.25}$$

The first term of the functional has an explicit dependence on the density whereas the kinetic and Coulomb terms depend on the electronic density in an implicit manner

via the wavefunction. Through exact functional minimization of $E[n]$ with respect to the electronic density n by means of orthonormal independent-particle wavefunctions ϕ_i, the so-called Kohn-Sham (KS) equations[273] are derived[†]:

$$\left[-\frac{1}{2}\nabla^2 + V_{\mathrm{n}}(\vec{r}) + \int \frac{n(\vec{r}\,')}{|\vec{r}-\vec{r}\,'|}d\vec{r}\,' + V_{\mathrm{XC}}(\vec{r})\right]\phi_i(\vec{r}) = \varepsilon_i\phi_i(\vec{r}) \tag{2.26}$$

and the energy functional is rewritten as

$$E[n] = \int V_{\mathrm{n}}(\vec{r})\, n(\vec{r})\, d\vec{r} - \frac{1}{2}\sum_i \int \phi_i^*(\vec{r})\,\nabla^2\phi_i(\vec{r})\, d\vec{r} + \frac{1}{2}\iint \frac{n(\vec{r})\, n(\vec{r}\,')}{|\vec{r}-\vec{r}\,'|}d\vec{r}d\vec{r}\,' + E_{\mathrm{XC}}[n] \tag{2.27}$$

The first three terms correspond to the external potential, kinetic, and Coulomb terms associated with the independent-electrons approximation and whatever left out is incorporated in the fourth term: the so-called exchange and correlation (XC) functional. Furthermore, the XC potential V_{XC} in KS equations is defined as the functional derivative of the XC functional with respect to the electronic density.

$$V_{\mathrm{XC}}(\vec{r}) = \left.\frac{\delta E_{\mathrm{XC}}[n]}{\delta n}\right|_{n(\vec{r})} \tag{2.28}$$

To sum up, the seminal work of Hohenberg, Kohn and Sham for the foundation of DFT postulates that a functional $E_{\mathrm{XC}}[n]$ exists that gives the exact ground-state energy and density through Equations 2.26 and 2.28. The only obstacle is that the form of this functional is currently unknown. As a result, the theoretical problem is now oriented towards a new level: constructing useful and realistic approximations for this very functional.

KS equations are numerically solved via a self-consistent scheme in terms of the electronic density. Once nuclear coordinates are specified, an initial guess for the density is formulated, typically using isolated-atom electronic density distributions. Using the density, Coulomb, and XC potentials are evaluated and the eigensystem described by Equation 2.26 is numerically solved, thus yielding the appropriate eigenvalues and eigenvectors that reflect the independent-particle energy values and wavefunctions. The obtained single-particle wavefunctions are used to create a new estimate for the electronic density via Equation 2.12. The process continues until the acquired density matches the one of the previous step within a defined tolerance[‡], at which point the algorithm is successfully terminated since self-consistency has been achieved. A flowchart of the aforementioned procedure is illustrated in Figure 2.1.

[†]For the sake of simplicity, i indices are dropped from electronic coordinates and j indices are replaced by the prime symbol ($'$).

[‡]Practically, energy-based criteria are commonly utilized to check for convergence, since it is more convenient from a computational perspective.

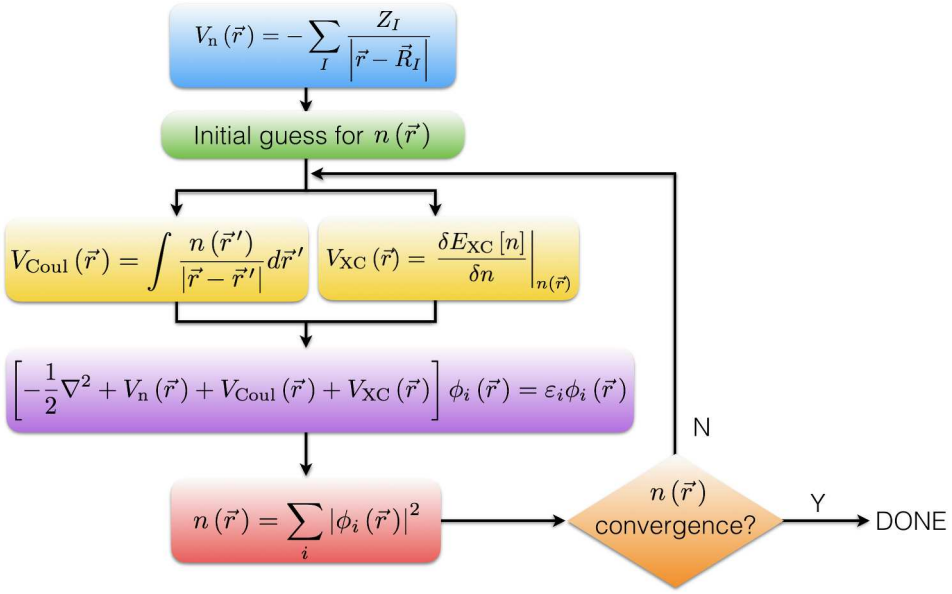

Figure 2.1: Flowchart of a typical self-consistent algorithm for the numerical solution of KS equations.

Once self-consistency is achieved, the resulting electronic density and nuclear positions determine the total energy of the system. The gradient of the total energy is used for the evaluation of the forces exerted on nuclei through the utilization of the Feynman-Hellmann force theorem:

$$\vec{F}_I = -\frac{\partial E_{\mathrm{tot}}}{\partial \vec{R}_I} = -\int n(\vec{r}) \frac{\partial V_{\mathrm{n}}(\vec{r})}{\partial \vec{R}_I} d\vec{r} - \frac{1}{2}\frac{\partial}{\partial \vec{R}_I} \sum_{I \neq J} \frac{Z_I Z_J}{\left|\vec{R}_I - \vec{R}_J\right|} \tag{2.29}$$

Forces obtained this way are used by appropriate numerical schemes for geometry optimization. A word of caution should be added here regarding the validity of Equation 2.29: its direct implementation is valid when KS single-particle wavefunctions have no explicit dependency on atomic positions. In the opposite case, correction terms have to be included.[117]

2.1.2 Exchange-Correlation Functionals

As far as XC functionals are concerned, a plethora of approaches are available from numerous contributors and at variable levels of quantitative accuracy.[274;275] One of the first approaches is the Local Density Approximation (LDA), according to which the exchange part is taken from the homogeneous electron gas (HEG)[276]:

$$E_{\mathrm{X}}^{\mathrm{LDA}}[n] = -\frac{3}{4}\left(\frac{3}{\pi}\right)^{1/3} \int n^{4/3} d\vec{r} \tag{2.30}$$

In the case of spin-polarized calculations, the above equation is expressed as the Local Spin Density Approximation (LSDA):

$$E_{\mathrm{X}}^{\mathrm{LSDA}}\left[n_\alpha, n_\beta\right] = -\frac{3}{2}\left(\frac{3}{4\pi}\right)^{1/3} \int \left(n_\alpha^{4/3} + n_\beta^{4/3}\right) d\vec{r} \tag{2.31}$$

following the general spin-scaling relation

$$E_{\mathrm{X}}\left[n_\alpha, n_\beta\right] = \frac{1}{2}\left(E_{\mathrm{X}}\left[2n_\alpha\right] + E_{\mathrm{X}}\left[2n_\beta\right]\right) \tag{2.32}$$

respected by all exchange functionals.

Correlation functionals have been based on the QMC simulations of the HEG by Ceperley and Alder.[277] Selected LDA correlation functionals include the work of Vosko *et al.*[278] (Vosko-Wilk-Nusair; VWN) and Perdew and Wang (PW-LDA)[279]. The VWN functional is expressed as:

$$\begin{aligned} E_{\mathrm{C}}^{\mathrm{VWN}} = \int \Big\{ & \epsilon_0^{\mathrm{VWN}}\left(x_{01}, a_1, b_1, c_1\right) + 4.5\epsilon_0^{\mathrm{VWN}}\left(x_{02}, a_2, b_2, c_2\right)\left(f_1 - 2\right)\left(1 - \zeta^4\right) + \\ & + \left[\epsilon_0^{\mathrm{VWN}}\left(x_{03}, a_3, b_3, c_3\right) - \epsilon_0^{\mathrm{VWN}}\left(x_{01}, a_1, b_1, c_1\right)\right]\left(f_1 - 2\right)\left(2^{1/3} - 1\right)^{-1}\zeta^4 \Big\} d\vec{r} \end{aligned} \tag{2.33}$$

where

$$\begin{aligned} \epsilon_0^{\mathrm{VWN}}\left(x_0, a, b, c\right) = \frac{a}{2}\Bigg\{ & \ln\left(\frac{r_{\mathrm{s}}}{r_{\mathrm{s}} + b\sqrt{r_{\mathrm{s}}} + c}\right) + \frac{2b}{\sqrt{4c - b^2}}\tan^{-1}\left(\frac{\sqrt{4c - b^2}}{2\sqrt{r_{\mathrm{s}}} + b}\right) - \\ & - \frac{bx_0}{x_0^2 + bx_0 + c}\left[\ln\left(\frac{\left(\sqrt{r_{\mathrm{s}}} - x_0\right)^2}{r_{\mathrm{s}} + b\sqrt{r_{\mathrm{s}}} + c}\right) + \frac{2\left(b + 2x_0\right)}{\sqrt{4c - b^2}}\tan^{-1}\left(\frac{\sqrt{4c - b^2}}{2\sqrt{r_{\mathrm{s}}} + b}\right)\right]\Bigg\} \end{aligned} \tag{2.34}$$

and

$$f_1 = \frac{\left(1 + \zeta\right)^{4/3} + \left(1 - \zeta\right)^{4/3}}{2},\ \zeta = \frac{n_\alpha - n_\beta}{n_\alpha + n_\beta} = \frac{n_\alpha - n_\beta}{n} \tag{2.35}$$

In the equation above, r_{s} stands for the Seitz radius defined by $(4/3)\,\pi r_{\mathrm{s}}^3 = n^{-1}$ and ζ is commonly referred to as the relative spin polarization. The VWN LDA correlation functional has 12 parameters, given in five variants from Vosko *et al.*, with the third (VWN3) and fifth (VWN5) versions being the most usually employed.

The PW-LDA correlation functional is given by the following equation:

$$E_{\mathrm{C}}^{\text{PW-LDA}} = \int n\bar{E}_{\mathrm{C}}^{\text{PW-LDA}}\left[n\right] d\vec{r},\ \bar{E}_{\mathrm{C}}^{\text{PW-LDA}}\left[n\right] = -2a\left(1 - \alpha r_{\mathrm{s}}\right)\ln\left\{1 + \left[2a\sum_{i=1}^{4}\beta_i(\sqrt{r_{\mathrm{s}}})^i\right]^{-1}\right\} \tag{2.36}$$

where a, α, β_i are appropriate parameters and $\bar{E}_{\mathrm{C}}$ represents the integral kernel of the correlation functional.

A major improvement upon LDA was introduced via the utilization of the electronic density gradient for the exchange part according to the following equation of the so-called Generalized Gradient Approximation (GGA)

$$E_{\mathrm{X}}^{\mathrm{GGA}}[n,x]=\int n^{4/3}F(x)\,d\vec{r} \tag{2.37}$$

where $x=|\nabla n|/n^{4/3}$ is the dimensionless reduced gradient and $F(x)$ an appropriate gradient expansion. Three widely used approaches are based on Becke's B88 functional[280] and the original[281] and revised[282] versions of the PBE functional by Perdew, Burke, and Ernzerhof:

$$E_{\mathrm{X}}^{\mathrm{B88}}=-\sum_{\sigma=\alpha,\beta}\int n_{\sigma}^{4/3}\left[\frac{3}{4}\left(\frac{6}{\pi}\right)^{1/3}+\frac{\beta x_{\sigma}^{2}}{1+6\beta x_{\sigma}\sinh^{-1}x_{\sigma}}\right]d\vec{r} \tag{2.38}$$

$$E_{\mathrm{X}}^{\mathrm{PBE}}=-\int n^{4/3}\left[\frac{3}{4}\left(\frac{3}{\pi}\right)^{1/3}+\frac{\mu s^{2}}{1+\mu s^{2}/\kappa}\right],\ s=\frac{x}{2(3\pi^{2})^{1/3}} \tag{2.39}$$

where β, μ, and κ are fundamental constants.

GGA correlation functionals are typically classified into two types: the density gradient approximation and the Cole-Salvetti[283] functionals. In the former type, a commonly encountered correlation functional is the PBE functional whereas in the latter type a characteristic member is the well-established GGA correlation functional LYP, developed by Lee, Yang, and Parr[284]. The PBE and LYP correlation functionals are given by the following expressions:

$$\begin{aligned}
&E_{\mathrm{C}}^{\mathrm{PBE}}=E_{\mathrm{C}}^{\text{PW-LDA}}+\int nH[n,\zeta,t]\,d\vec{r}\\
&H[n,\zeta,t]=\gamma\varphi^{3}\ln\left[1+\frac{\beta}{\gamma}t^{2}\frac{1+At^{2}}{1+At^{2}+A^{2}t^{4}}\right]\\
&A=\frac{\beta}{\gamma}\left\{\exp\left(-\frac{\bar{E}_{\mathrm{C}}^{\text{PW-LDA}}[n]}{\gamma\varphi^{3}}\right)-1\right\}^{-1}\quad\varphi=\frac{(1+\zeta)^{2/3}+(1-\zeta)^{2/3}}{2},\ t=\frac{|\nabla n|}{2\varphi k_{\mathrm{s}}n}
\end{aligned} \tag{2.40}$$

$$\begin{aligned}
&E_{\mathrm{C}}^{\mathrm{LYP}}=-\int\frac{a}{1+dn^{-1/3}}\times\\
&\times\left\{n+bn^{-2/3}\left[\frac{3}{10}\left(3\pi^{2}\right)^{2/3}n^{5/3}-2t_{\mathrm{W}}+\frac{1}{9}\left(t_{\mathrm{W}}+\frac{1}{2}\nabla^{2}n\right)\right]\exp\left(-cn^{-1/3}\right)\right\}d\vec{r}\\
&t_{\mathrm{W}}=\frac{1}{8}\left(\frac{|\nabla n|^{2}}{n}-\nabla^{2}n\right)
\end{aligned} \tag{2.41}$$

In the PBE functional expression, the Thomas-Fermi screening wavevector $k_{\mathrm{s}}=\sqrt{4k_{\mathrm{F}}/\pi}$

is used, where $k_F = \sqrt[3]{3\pi^2 n}$ is the Fermi wavevector.

Another interesting and widely used class of XC functionals are the hybrid functionals that mix GGA XC parts with the non-local, exact HF exchange integral at constant ratios. The HF exchange part is practically the third term of Equation 2.17:

$$E_X^{HF} = -\frac{1}{2}\sum_{i,j,\sigma}\int \frac{\phi_{i\sigma}^*(\vec{r})\,\phi_{j\sigma}(\vec{r})\,\phi_{j\sigma}^*(\vec{r}')\,\phi_{i\sigma}(\vec{r}')}{|\vec{r}-\vec{r}'|}d\vec{r}d\vec{r}' \tag{2.42}$$

Hybrid functionals based on the B88 correlation functional follow the general form[285]:

$$E_{XC}^{B3} = aE_X^{HF} + (1-a)\,E_X^{LDA} + b\Delta E_X^{B88} + cE_C^{GGA} + (1-c)E_C^{LDA} \tag{2.43}$$

with the parameters a, b, c fitted to experimental data sets and ΔE_X^{B88} symbolizing the GGA exchange part of B88. A widely used hybrid functional of the B3 family is the so-called B3LYP functional, utilizing LYP GGA and VWN LDA correlation via the following parametrization:

$$E_{XC}^{B3LYP} = 0.2E_X^{HF} + 0.8E_X^{LDA} + 0.72\Delta E_X^{B88} + 0.81E_C^{LYP} + 0.19E_C^{VNW} \tag{2.44}$$

The PBE XC functional has also been augmented in a hybrid HF fashion by Adamo and Barone[286], giving birth to the parameter-free PBE0 hybrid XC functional:

$$E_{XC}^{PBE0} = E_{XC}^{PBE} + \frac{1}{4}\left(E_X^{HF} - E_X^{PBE}\right) \tag{2.45}$$

A partially eluding concept of all XC functionals covered so far is van der Waals (vdW) interaction. The vdW interaction is a compound term describing dipole-dipole, dipole-induced dipole, and London dispersion interactions.[287] Both dipole-dipole and dipole-induced dipole interactions are covered in the context of the KS equations via the Coulomb correlation term. On the other hand, London dispersion, which manifests itself in the absence of charge and multipole moments, is the only vdW component left untreated in KS calculations. Attempts to include dispersion interaction in the KS *ansatz* fall into five categories: classical corrections, perturbative approaches, linear-response theory, vdW functionals, and semiempirical dispersion-corrected functionals.[275]

The most frequently used approach for the treatment of vdW dispersion is via semiempirical dispersion-corrected functionals, like the the so-called DFT-D functionals[288] that are categorized into three levels of approach, namely the D1, D2, and D3 corrections.

The highest level DFT-D3 functionals[289] take the form:

$$E^{DFT\text{-}D3} = E^{KS} + E_{disp}^{(2)} + E_{disp}^{(3)} \tag{2.46}$$

The interatomic term between atoms A and B at distance R_{AB} is

$$E_{\text{disp}}^{(2)} = -\sum_{A>B} \sum_{n=6,8,\cdots} \frac{s_n C_n^{AB}}{(R_{AB})^n} \left[1 + 6 \left(\frac{R_{AB}}{s_{r,n} R_0^{AB}} \right)^{-a_n} \right]^{-1} \tag{2.47}$$

where R_0^{AB} interaction cutoff radii, s_n parameters fitted to benchmark calculations data depending on the utilized XC functional, $s_{r,n}$ order-dependent cutoff radii scaling factors, and a_n exponents controlling the steepness for the interaction following the recursive relation $a_{n+2} = a_n + 2$, where $a_6 = 12$. Coefficients C_n^{AB} are derived from time-dependent KS calculations on explicit atomic pairs.[289]

The three-atom $E_{\text{disp}}^{(3)}$ term includes angular dependencies and is expressed as:

$$E_{\text{disp}}^{(3)} = -\sum_{A<B<C} \frac{(3\cos\theta_a \cos\theta_b \cos\theta_c + 1)\, C_9^{ABC}}{(R_{AB} R_{BC} R_{CA})^3} \left[1 + 6 \left(\frac{3\bar{R}_{ABC}}{4 R_0^{ABC}} \right)^{-16} \right]^{-1} \tag{2.48}$$

where θ the internal angles of the triangle formed by atoms A, B, and C, $\bar{R}_{ABC}$ the geometrically-averaged radii, R_0^{ABC} an appropriate cutoff radius, and C_9^{ABC} the triple-dipole constant, typically approximated as $C_9^{ABC} \cong -\sqrt{C_6^{AB} C_6^{AC} C_6^{BC}}$. The first fraction from the left inside the summation of Equation 2.48 is the so-called non-additive Axilrod-Teller-Muto dispersion term for non-collinear atomic arrangements.

The field of XC functional development and utilization is by all means not confined to the approaches outlined thus far. The evolution of DFT XC functionals is most suitably described by Perdew's "Jacob's Ladder": a metaphorical concept portraying the evolution of XC functionals from the "Hartree World" (the basis of the ladder, lacking any XC notions) towards chemical accuracy (the ultimate destination) via discrete intermediate "rungs" of approximations, starting from LSDA, to GGA, meta-GGA, and hybrid functionals, including over 200 XC functionals.[290;291]

Furthermore, numerous corrections and novel approaches have been proposed and applied over the past decades to DFT methods for the enhancement of overall quantitative predictive capabilities. Characteristic examples include self-interaction corrections and the GW approximation, DFT+U methods, range-separated functionals, relativistic corrections, and TD-DFT methods for excited states calculations, with the enhancement "catalog" constantly evolving and containing an abundance of entries.[117;274;275]

2.1.3 Basis Sets

Once the XC functional is selected for a particular system, the next prerequisite for the solution of KS equations is the form of single-particle wavefunctions $\phi_i(\vec{r})$, commonly referred to as the basis set. The nature of the basis set employed for the solution of the eigenproblem described by Equation 2.26 is inherent to the physicochemical characteris-

tics and phenomena of the system under study and must comply with two major factors: normalization and boundary conditions.

In the context of condensed matter under periodic boundary conditions, a typical approach is formulated through Bloch's theorem, thus allowing single-particle wavefunctions to be expanded in a complete set of an orthonormal plane-waves Fourier series

$$\phi_i\left(\vec{r}\right) = \sum_{\vec{q}} c_{i,\vec{q}} \frac{1}{V} \exp\left(\mathrm{i}\vec{q}\cdot\vec{r}\right) \tag{2.49}$$

where V is the volume of the periodic supercell which encloses all electrons and nuclei, $c_{i,\vec{q}}$ the expansion coefficients, and $\vec{q} = \vec{k} + \vec{G}$ a compound wavevector defined as the sum of wavevectors $\vec{G}$ of the reciprocal lattice and a contiguous wavevector $\vec{k}$ confined in the first Brillouin zone.[292] Formulations based on orthonormal plane-waves have paved the way towards highly accurate and efficient electronic structure calculations. Some pronounced advantages of plane-wave utilization is basis completeness upon convergence, generic usage regardless of chemical species, and realistic treatment of electronic delocalization. On the other hand, plane-waves are not suited for localized electronic behavior and the efficient description of core states, although the latter case is usually circumvented by means of workarounds, such as the pseudopotential method. Moreover, from a computational point of view, a drawback is rooted in the fact that plane-wave integrals cannot be treated in an analytical manner.[117]

Although plane-waves are a favorable choice for solid-state calculations, their utilization in non-periodic molecular systems regularly encountered in quantum chemical *ab-initio* modeling is commonly avoided, since localized basis sets provide a satisfying and computationally more efficient description of molecular electronic structure. One standard approach involves analytic atom-centered orbitals, expressed as a product of a radial function and a spherical harmonic

$$\chi_p\left(\vec{r}\right) \equiv \chi_{nml}\left(\vec{r}\right) = \rho_{nl}\left(r\right) Y_{lm}\left(\hat{r}\right) \tag{2.50}$$

with striking similarities to the exact solutions of the Schrödinger equation for the hydrogen atom. Using such orbital functions, the basis set is formulated as a typical series expansion

$$\phi_i\left(\vec{r}\right) = \sum_{p} c_{i,p} \chi_p\left(\vec{r}\right) \tag{2.51}$$

The analytic nature of such orbitals results in computationally inexpensive analytic integrals and derivatives for most QM methods, although certain limitations exist, such as the hard description of pronounced electronic delocalization and selected issues occurring due to periodicity.[117;120;293]

Two major atom-centered orbital types are Slater type orbitals (STO) and Gaussian

type orbitals (GTO). STOs have the following functional form:

$$\chi^{\mathrm{STO}}_{\zeta,nlm}\left(\vec{r}\right) = Nr^{n-1}\exp\left(-\zeta r\right)Y_{lm}\left(\hat{r}\right) \tag{2.52}$$

where N is a normalization constant and ζ is the orbital range parameter. Characteristic traits of STOs is that their radial exponential dependency resembles hydrogen-like $1s$ orbitals while simultaneously exhibiting correct short- and long-range behavior, describing quite accurate the so-called electron-nuclei cusp condition. However, their functional form prohibits analytic evaluation of three- and four-center two-electron integrals, rendering them inappropriate for DFT applications that include exact exchange.

GTOs are expressed as:

$$\chi^{\mathrm{GTO}}_{\zeta,nlm}\left(\vec{r}\right) = Nr^{2(n-1)-l}\exp\left(-\zeta r^2\right)Y_{lm}\left(\hat{r}\right) \tag{2.53}$$

with the r^2 exponential dependence leading to a smooth curve at short distances, thus failing to comply with the cusp condition, and to a quantitatively unrealistic long-range behavior, since they exhibit a faster tail decay. On the other hand, GTOs compensate any shortcomings through their friendliness towards analytic integral expressions. Moreover, linear combinations of GTOs lead to a satisfactory approximation of the cusp condition and to an exact long-range asymptotic behavior[§], rendering them almost universally used ingredients for molecular electronic structure calculations basis sets.

Having selected GTOs as basis functions for the description of single-particle states, the next crucial factor to be determined is the number of utilized functions given the chemical species present in the system under study. It should be noted that GTOs are not used in the simple format of Equation 2.53 but with a predefined additive multiplicity with respect to the radial component, resulting in the commonly referred to as multiple-zeta basis sets, since the radial function is replaced by a sum of exponential terms with different ζ range parameters while keeping the lm channel constant. The importance of ζ-multiplicity is that it grants radial flexibility for the description of heteroatomic bonding and different hybridization states. In practical terms, radial augmentation is applied for valence states, since chemical bonding mainly occurs through valence electrons. In the quantum chemical nomenclature, this type of basis sets are referred to as "split valence" sets.

Another crucial technique is the addition of higher, formally unoccupied angular momentum functions denoted as "polarization" functions that enhance electronic distributions via angular flexibilization. In addition, when special circumstances require a detailed representation of the wavefunction's outer part (e.g. polarizability and hyperpolarizability studies) or if loosely bound electrons are present (e.g. anionic or excited state

[§]A rule of thumb dictates that three times as many GTOs as STOs are enough for an adequate level of accuracy.

calculations), the basis set is further augmented by small exponent terms, the so-called "diffuse" functions.

Once the number of basis functions is selected, the subsequent step involves the determination of exponential ζ coefficients. This is typically carried out via variational HF or DFT calculations on isolated atoms or small molecules. The latter are indispensable for the parametrization of polarization functions, since in a single atom these states are unoccupied and do not contribute to the energy in any way.

Current computationally efficient quantum chemical calculations by means of localized gaussian functions rely on the notion of contracted basis sets. GTO contraction is achieved by partitioning basis functions into well-defined groups with appropriate weighting factors, thus shrinking the number of expansion coefficients. Under the contraction approximation, GTOs in the form of Equation 2.53 are referred to as "primitive" GTOs; a contracted GTO (CGTO) is then expressed as a linear combination of primitive GTOs:

$$\chi_{p'}^{\mathrm{CGTO}}\left(\vec{r}\right) = \sum_{p} a_p \chi_p^{\mathrm{GTO}}\left(\vec{r}\right) \tag{2.54}$$

Then single-particle wavefunctions are written down as CGTO series in the form:

$$\phi_i\left(\vec{r}\right) = \sum_{p'} c_{i,p'} \chi_{p'}^{\mathrm{CGTO}}\left(\vec{r}\right) \tag{2.55}$$

Upon CGTO employment for a quantum chemical calculation, both exponents and contraction coefficients inside CGTOs remain unaltered; the only variable factors are the expansion coefficients in the basis of CGTO functions. Furthermore, two types of GTO contraction are utilized: the segmental contraction scheme where each primitive GTO contributes only to a specific CGTO and the general contraction scheme where all primitives can contribute to all CGTOs with compatible symmetry.

A wide variety of basis sets is currently available from the computational quantum chemistry literature. A popular family contains the so-called Pople style basis sets, based on the seminal work of Pople and co-workers. Most significant members of the aforementioned family include the 3-21G, 6-31G, and 6-311G split-valence contracted basis sets. To each of these basis sets, a number of diffuse and/or polarization functions can be added, denoted by "+" and "*" symbols respectively. The following Table 2.1 lists 20 Pople style basis sets, along with applicable chemical species.[294]

As far as the nomenclature is concerned, the first number before the dash corresponds to the number of functions used to describe core orbitals. The presence of two of three numbers after the dash characterize the basis set as double and triple split valence respectively. The internal numbering of the dyad or triad corresponds to the level of contraction inside each successive valence shell. In the case of polarization and diffuse orbitals, singular identifier occurrence means that the modification is applied only for heavy elements

whereas a double occurrence includes light atoms, i.e. hydrogen and helium.

Table 2.1: Pople style split-valence CGTO basis sets in original, diffuse, polarized, and diffuse-polarized forms, along with supported chemical species.

Basis set	Species†	Basis set	Species†
3-21G	H-Cs	6-31++G**	H; Li-Ca
3-21++G	H; Li-Ca	6-311G	H-Kr§; I
6-31G	H-Zn	6-311G*	
6-31G*	H-Kr	6-311G**	
6-31G**	H-Zn	6-311+G	H-Ca
6-31+G	H-Ca	6-311++G	H; Li-Ca
6-31++G	H; Li-Ca	6-311+G*	H-Ca
6-31+G*	H-Ca	6-311+G**	
6-31+G**		6-311++G*	H; Li-Ca
6-31++G*		6-311++G**	

†: Notation X-Y corresponds to a contiguous listing from element X to Y

§: Excluding transition metals.

Other all-electron basis sets with analytic expression commonly encountered are the Dunning-Huzinaga sets in their original and correlation- or polarization- consistent versions, the Ahlrichs type basis sets, and the MINI, MIDI, and MAXI basis sets by Takewaki and Huzinaga.[120] Just as in the case of XC functionals, the selection of a proper basis set is solely dependent on the system and properties under study.

2.1.4 Charge Transport Modeling in Soft Matter

Charge transport in solid materials is manifested via various complex mechanisms. Two extreme transport types are band-like and hopping conductivity. As regards the former case, charge carriers propagate as highly delocalized plane waves with broad bandwidth and relatively large mean free path. In the latter case, carriers are strongly localized and move through site-to-site hopping, being practically scattered at almost every step.[295]

A classification of transport type can be achieved through the magnitude and temperature dependence of the charge carrier mobility μ. In band-like conductivity, $\mu \gg 1\,\mathrm{cm^2V^{-1}s^{-1}}$ and the temperature dependence follows a power-law $\mu \sim T^{-n}$, where $n > 1$. On the other hand, hopping conductivity is characterized by a mobility $\mu \ll 1\,\mathrm{cm^2V^{-1}s^{-1}}$ and an Arrhenius exponential temperature dependence $\mu \sim \exp\left(-E_\mathrm{a}/k_\mathrm{B}T\right)$, where E_a is the activation energy and k_B Boltzmann's constant.

Carrier movement can be disrupted by several factors. A common case is structural scattering in a material, where any deviations from structural regularity (e.g. vacancies, dislocations, impurities, and grain boundaries) can scatter a charge carrier into a different momentum state. Another case is dynamical scattering induced by temporal,

temperature driven, structural asymmetries, such as carrier-phonon interactions. The theoretical treatment of all aforementioned processes is a formidable task; thus practical computational studies adopt simple models that capture a single process and ignore the rest.

Hopping charge migration can be modeled via a simple tight-binding Hamiltonian

$$\hat{H}^{\mathrm{tb}} = \sum_{m} \epsilon_m a_m^{+} a_m + \sum_{m \neq n} t_{mn} a_m^{+} a_n \tag{2.56}$$

where a_m^{+} and a_m the charge creation and annihilation operators on the molecular site m, ϵ_m the charge site energy, and t_{mn} the charge transfer integral.[162;295;296] The intersite charge transfer (CT) rate k_{mn}^{CT} from site m to n in the high-temperature regime, where all vibrational modes can be treated classically, obeys the following expression taken from the so-called semi-classical Marcus theory[296;297]:

$$k_{mn}^{\mathrm{CT}} = \frac{t_{mn}^2}{\hbar} \sqrt{\frac{\pi}{\lambda k_{\mathrm{B}} T}} \exp\left[-\frac{(\Delta E_{mn} + \lambda)^2}{4 \lambda k_{\mathrm{B}} T} \right] \tag{2.57}$$

where λ is the reorganization energy due to geometric relaxations induced by the charge transfer, $\Delta E_{mn} = \epsilon_n - \epsilon_m$ the energy variation during the transfer process, and T the temperature.

As regards the reorganization energy, in condensed-state systems, where no solvent reorganization occurs during the charge transfer, a common approach relies on the utilization of the internal reorganization energy, ignoring surrounding relaxation phenomena and variations in electronic polarization between an isolated system and the solid-state counterpart.[298] In the context of this approach, electron $\lambda^{(-)}$ and hole $\lambda^{(+)}$ internal reorganization energies can be expressed as:

$$\lambda^{(-/+)} = E_{(-/+)}^{0} - E_0^0 + E_0^{(-/+)} - E_{(-/+)}^{(-/+)} \tag{2.58}$$

with E_0^0 and $E_{(-/+)}^{(-/+)}$ referring to the ground-state energies of the neutral and ionic states respectively, $E_0^{(-/+)}$ to the energy of the ionic state using the equilibrium geometry of the neutral molecule, and $E_{(-/+)}^{0}$ to the energy of the neutral state considering the equilibrium geometry of the ionic molecular state.[171;297;298]

Under the tight-binding model for intersite charge transfer, the hopping mechanism can be treated at the level of nearest-neighboring frontier molecular orbital (FMO) interactions. This approach provides a simple and yet reliable way to estimate charge transfer integrals (CTIs) based on dimer studies instead of infinite periodic systems. In the case of hole transport, calculations are conducted at the basis of monomer Highest Occupied Molecular Orbitals (HOMOs) whereas for electrons the calculations make use of monomer Lowest Unoccupied Molecular Orbitals (LUMOs). Given a dimer configuration comprised

of two monomers, one-electron dimer states can be defined in terms of localized monomer orbitals. In the case of hole transport, provided that the dimer HOMO and HOMO-1 result from monomer HOMO (denoted as Ψ_m^{mon}) interactions, dimer orbital energies are given by the following secular equation:

$$\mathbf{HC} - E\mathbf{SC} = \mathbf{0} \tag{2.59}$$

where $\mathbf{H}$ and $\mathbf{S}$ the Hamiltonian and overlap matrices and $\mathbf{C}$ the eigenvectors.[296;299] The aforementioned matrices can be formally written as:

$$\mathbf{H} = \begin{pmatrix} e_1 & J_{12} \\ J_{12} & e_2 \end{pmatrix} \tag{2.60}$$

$$\mathbf{S} = \begin{pmatrix} 1 & S_{12} \\ S_{12} & 1 \end{pmatrix} \tag{2.61}$$

with the associated matrix element expressed as:

$$e_m = \langle \Psi_m^{\text{mon}} | \, \hat{H}^{\text{tb}} \, | \Psi_m^{\text{mon}} \rangle \tag{2.62}$$

$$J_{mn} = \langle \Psi_m^{\text{mon}} | \, \hat{H}^{\text{tb}} \, | \Psi_n^{\text{mon}} \rangle \tag{2.63}$$

$$S_{mn} = \langle \Psi_m^{\text{mon}} | \, \Psi_n^{\text{mon}} \rangle \tag{2.64}$$

Matrix elements e_m and J_{mn} have analogous physical meaning as the parameters ϵ_m and t_{mn} in Equation 2.56 but are not identical, since orbitals Ψ_m^{mon} are non-orthogonal and the tight-binding approximation is based on orthonormal states. An orthonormal set can be obtained by means of a Löwdin's symmetrical transformation[300], resulting to the effective Hamiltonian matrix:

$$\mathbf{H}^{\text{eff}} = \begin{pmatrix} e_1^{\text{eff}} & J_{12}^{\text{eff}} \\ J_{12}^{\text{eff}} & e_2^{\text{eff}} \end{pmatrix} \tag{2.65}$$

where

$$e_{1(2)}^{\text{eff}} = \frac{1}{2} \frac{(e_1 + e_2) - 2J_{12}S_{12} \pm (e_1 - e_2)\sqrt{1 - S_{12}^2}}{1 - S_{12}^2} \tag{2.66}$$

$$J_{12}^{\text{eff}} = \frac{J_{12} - 0.5\,(e_1 + e_2)\,S_{12}}{1 - S_{12}^2} \tag{2.67}$$

Quantities e_m^{eff} and J_{mn}^{eff} are now identical to ϵ_m and t_{mn}.[296]

Once the charge transfer rate between neighboring molecules is evaluated using Equa-

tion 2.57, the charge diffusion constant D is calculated as

$$D = \frac{1}{2d}\sum_i r_i^2 k_i^{\mathrm{CT}} P_i \tag{2.68}$$

where index i corresponds to first-neighboring hopping pathways between molecular sites separated by distance r_i, d symbolizes the dimensionality of the transfer process and P_i the hopping probability along a given pathway.[171] The latter is calculated in a statistical manner as

$$P_i = \frac{k_i^{\mathrm{CT}}}{\sum_j k_j^{\mathrm{CT}}} \tag{2.69}$$

Finally, the hopping mobility μ is given by the Einstein relation

$$\mu = \frac{e}{k_{\mathrm{B}}T} D \tag{2.70}$$

where e is the electron charge.

2.2 Empirical Molecular Dynamics Simulations

2.2.1 MD Preliminaries

A theoretical and modeling crossover from quantum to classical descriptions of matter is essential in order to address properties and phenomena near the upper temporal and spatial bounds of the nanoscale. Classical approaches factor out any quantum detail, thus treating atoms as classical particles that typically interact via a position-dependent potential energy function U. The time evolution of such systems can be modeled by means of Newtonian mechanics though the so-called "Newton's second law":

$$\vec{F}_i = \frac{d\vec{p}_i}{dt} = m_i \ddot{\vec{r}}_i \tag{2.71}$$

where $\vec{F}_i$ is the total force acted on particle i with mass m_i at position $\vec{r}_i$, carrying a momentum $\vec{p}_i$. Conservative forces can be expressed as the gradient of the potential energy:

$$\vec{F}_i = -\nabla_i U \tag{2.72}$$

Given an "interaction law" quantified via the potential energy U, forces exerted on every classical particle can be evaluated via 2.72, hence enabling the solution of the second-order ordinary differential equations described by Equation 2.71 that constitutes the very core of Molecular Dynamics simulations.[123;124;293]

A series of approaches can be found in the literature for the numerical integration of Equations 2.71. The most commonly utilized integration scheme is the Velocity-Verlet algorithm, based on appropriate Taylor expansions that result to the following set of difference equations for the position $\vec{r}_i$ and velocity $\vec{u}_i$ of a particle:

$$\vec{r}_i\left(t+dt\right)=\vec{r}_i\left(t\right)+dt\vec{u}_i\left(t\right)+\frac{\left(dt\right)^2}{2m_i}\vec{F}_i\left(t\right) \tag{2.73}$$

$$\vec{u}_i\left(t+dt\right)=\vec{u}_i\left(t\right)+\frac{dt}{2m_i}\left[\vec{F}_i\left(t\right)+\vec{F}_i\left(t+dt\right)\right] \tag{2.74}$$

with dt symbolizing the integration step, also commonly referred to as the simulation timestep. Equations of motion (EoM) 2.73 and 2.74 can be readily utilized for simulations at the microcanonical statistical ensemble, keeping constant the number of atoms N, the volume V, and the total energy E, with the remaining thermodynamic quantities, i.e. the temperature T and pressure P, responding accordingly.

Initial position and velocity for each atom in a given simulation domain are explicitly required in order to commence the integration of Velocity-Verlet EoMs. Velocity assignment is linked to an initial temperature value, since for classical particles, the equipartition theorem states the following relationship between kinetic energy K and instantaneous temperature $\mathcal{T}$:

$$K=\frac{1}{2}\sum_i m_i u_i^2=\frac{3}{2}Nk_{\mathrm{B}}\mathcal{T} \tag{2.75}$$

with the thermodynamic temperature T resulting from the average value of the instantaneous temperature:

$$T\equiv\left\langle\mathcal{T}\right\rangle_{\mathrm{t}} \tag{2.76}$$

where $\left\langle A\right\rangle_{\mathrm{t}}\equiv\lim_{\tau\to\infty}\frac{1}{\tau}\int_0^\tau A\left(t\right)dt$ corresponds to the time average of a quantity $A\left(t\right)$.[301]

Velocity assignments are usually carried out by means of pseudo-random numbers. An easy to implement method is based on the Box-Muller transformation which maps uniform to normal random numbers[¶], obeying Gaussian statistics.[302]

As regards the pressure in a MD simulation and given the assumption of pairwise additivity of the forces between particles, the virial equation relates the pressure with atomistic properties of a particles system[301;303]:

$$PV=Nk_{\mathrm{B}}T+\frac{1}{3}\left\langle\sum_{i=1}^{N}\sum_{j>i}^{N}\vec{r}_{ij}\cdot\vec{F}_{ij}\right\rangle_{\mathrm{t}} \tag{2.77}$$

A crucial issue pertinent to atomistic simulations is linked to system size effects.

[¶]From here on, pseudo-random numbers will be plainly referred to as random numbers.

Although the implementation of empirical laws for the quantification of particle interactions allows the treatment of relatively large multi-atom systems, a direct comparison with real-life systems is currently out of context. Nevertheless, the utilization of appropriate periodic boundary conditions (PBCs) allows realistic evaluation of bulk material properties, should the so-called system correlation length be smaller that the system size. Such boundary conditions practically factor out interfacial effects, thus examining materials inside their bulk "core".[293]

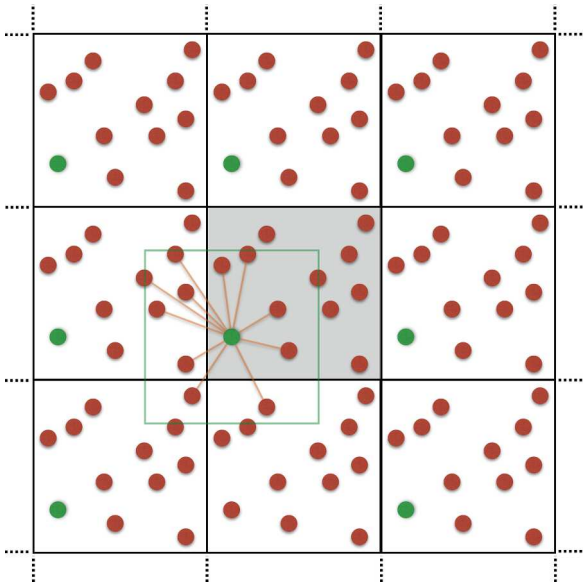

Figure 2.2: Two-dimensional illustration of PBC. The shaded box corresponds to the primary supercell. Line segments indicate interacting pairs for a highlighted particle.

PBCs are manifested in two different aspects. The first refers to kinematic PBCs, dictating that moving particles crossing a specific domain boundary must "emerge" in the diametrically opposite area of the periodic supercell that encloses all particles. The second aspect is linked to the application of periodicity for specific interactions, defining a selection rule for interacting particle pairs: every particle situated in the so-called primary supercell must interact with its foremost neighbors, belonging either in the primary supercell or in another periodic supercell. This condition is commonly referred to in the literature as the "minimum image convention" and is illustrated in Figure 2.2.[123;293]

2.2.2 Empirical Force Fields

When it comes to empirical atomistic simulations, a plethora of particle interaction laws for the quantification of the total potential energy is found in the literature. These mathematical descriptions are commonly referred to as Force Fields (FF) and their sole purpose is to capture interatomic interactions in the most accurate way, without resolving to QM calculations during an atomistic simulation. FF derivation is a laborious procedure, usually based on high quality *ab-initio* data or experimental information or even

on combinations of them.

Should the level of particle detail be taken into consideration, FFs can be categorized into all-atom and united-atom variants. In the former case, every atom is explicitly considered as an interaction site while in the latter case light atoms (typically hydrogen and fluorine) are fused with first-neighboring heavier atoms towards the creation of interacting super-atoms. Another differentiation is with respect to the evolution of bonding characteristics. The so-called reactive FFs can deduce the bonding state of an atom by considering the physicochemical atomic environment, thus leading to "on-the-fly" bond formation and breaking.[119] On the contrary, non-reactive FFs retain the initial bonding information and are used for constant topology simulations.

As far as non-reactive FFs are concerned, interactions between atoms are classified into two distinct classes: bonded and non-bonded interactions.[123;293;302] In the former case, first-neighboring covalent bonding is normally expressed by means of harmonic interactions, characterized by an equilibrium distance r_0 and an appropriate vibration constant k_b. The quantification relies on Hooke's law, stating that the stretching energy of a bond is expressed as

$$E_\mathrm{b} = \sum_{\text{bonds}} k_\mathrm{b} \left(r - r_0\right)^2 \tag{2.78}$$

where r the distance between two atoms forming a permanent covalent bond.

Bending interactions between three atoms forming a chain-like configuration are modeled through angle depended expressions, involving an equilibrium angle value θ_0 and an appropriate force constant k_a , with the associated energy written as

$$E_\mathrm{a} = \sum_{\text{angles}} k_\mathrm{a} \left(\theta - \theta_0\right)^2 \tag{2.79}$$

Variants of the aforementioned formula are based on harmonic expressions of cosines of current and equilibrium angle values. Moreover, a common addition to bending interactions found in some FFs, accounting for more accurate vibrational characteristics, is based on the utilization of "Urey-Bradley" terms (UB) that consider extra harmonic interactions between the atoms situated on the ends of a "1-2-3" triad and separated by a distance S:

$$E_\mathrm{UB} = \sum_{\text{1-3 pairs}} k_\mathrm{UB} \left(S - S_0\right)^2 \tag{2.80}$$

where k_UB the force constant and S_0 the equilibrium "1-3" distance.

Another significant interaction type, essential for modeling articulated molecules, involves chain-like configurations of four atoms. Should a "1-2-3-4" bonding sequence be taken into consideration, the so-called proper dihedral or torsion angle φ is defined as the

angle formed by the two planes that are defined by the non-collinear triads "1-2-3" and "2-3-4" respectively.

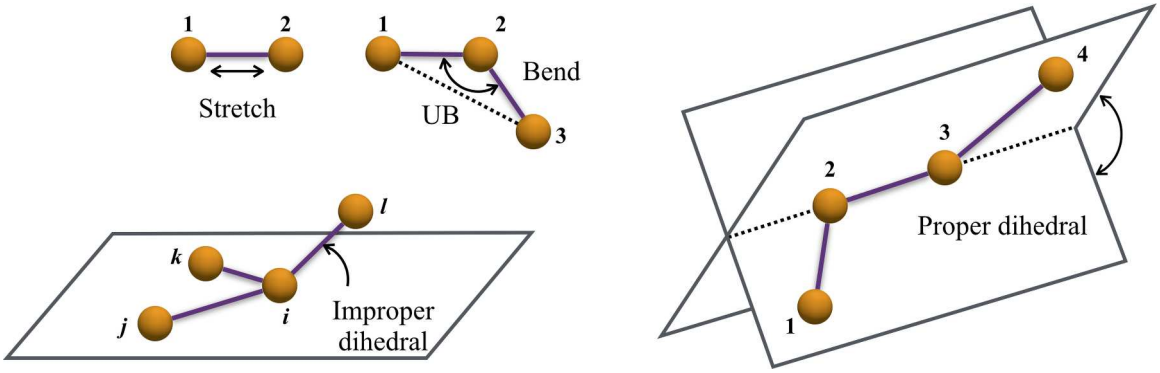

Figure 2.3: Geometrical interpretations of stretching, bending, proper torsion, and improper torsion bonded interactions.

Energy expressions for torsional interactions vary between FFs, from simple, single cosine expressions

$$E_{\mathrm{d}} = \sum_{\text{dihedrals}} k_{\mathrm{d}} \left[1 + \cos\left(n\varphi - d\right)\right] \tag{2.81}$$

to appropriate expansions with multiple coefficients, e.g.:

$$E_{\mathrm{d}} = \sum_{\text{dihedrals}} \sum_{n} A_n \cos^n \varphi \tag{2.82}$$

and

$$E_{\mathrm{d}} = \sum_{\text{dihedrals}} \sum_{n} A_n \left[1 + (-1)^n \cos\left(n\varphi\right)\right] \tag{2.83}$$

where k_{d} and A_n appropriate force constants, n integer indices or coefficients, and d relevant angle values.

Furthermore, a special kind of improper dihedral angles χ can be defined, capable of describing out-of-plane bending motions of atomic complexes made up by "Y-shaped" atomic quadruplets, essential in some cases in order to maintain planarity or specific stereochemical chirality in chain structures. Given a central atom i, an improper dihedral angle can be formed by three more atoms labeled j, k, and l, all forming covalent bonds with the central atom. For such a geometric arrangement, the improper angle is defined as the angle between the plane formed by atoms i, j, k and the line segment joining sites i and l, following cyclic index permutations. Typical expressions for improper dihedral angle energy contributions are similar to the harmonic expression of Equation 2.79 and its cosine variant. In the special case of planar configurations, the cosine expression

$$E_{\mathrm{i}} = \sum_{\text{impropers}} k_{\mathrm{i}} \left(1 - \cos \chi\right) \tag{2.84}$$

is encountered, where k_{i} appropriate force constant.

All of the above bonded interaction types belong to the so-called "Class I" FF family and are illustrated in Figure 2.3. More intricate and computationally demanding FFs belong to the "Class II" category and include higher order, non-harmonic terms and/or special cross-term expressions that correlate stretching, bending, and torsional motions in order to improve FF accuracy.[302;304]

Non-bonded pairwise expressions in empirical FFs are commonly used to describe two major contributions to the potential energy: the London dispersion part of vdW interactions and electrostatic forces. In the case of vdW interactions, two widely utilized central potentials are the celebrated Lennard-Jones (LJ) "6-12" potential:

$$E_{\mathrm{vdW}}^{\mathrm{LJ}} = \sum_{i<j} 4\varepsilon_{ij} \left[\left(\frac{\sigma_{ij}}{r_{ij}} \right)^{12} - \left(\frac{\sigma_{ij}}{r_{ij}} \right)^{6} \right] \tag{2.85}$$

with ε_{ij} controlling the interaction well depth and σ_{ij} the equilibrium distance, and the Buckingham "exponential-6" (X6) potential:

$$E_{\mathrm{vdW}}^{\mathrm{X6}} = \sum_{i<j} \left[A_{ij} \exp\left(-\frac{r_{ij}}{\rho_{ij}} \right) - \frac{C_{ij}}{r_{ij}^{6}} \right] \tag{2.86}$$

where A_{ij}, ρ_{ij}, and C_{ij} appropriate adjustable parameters modulating the form of the potential.

Electrostatic interactions are quantified by means of the Coulomb potential:

$$E_{\mathrm{Coul}} = \sum_{i<j} \frac{1}{4\pi\varepsilon_{\mathrm{r}}\varepsilon_0} \frac{q_i q_j}{r_{ij}} \tag{2.87}$$

where ε_0 the permittivity of vacuum and ε_{r} the material's dielectric constant or relative electric permittivity, and q_i the point charge of an atom i expressed in electron charge units.

A practical consideration regarding non-bonded interactions emanates from the distance dependent attenuation of specific potentials. From a computational point of view, a classification into short-range and long-range interactions is commonly applied via the introduction of a cut-off radius r_{cut}. Interacting atomic pairs separated by distances smaller than r_{cut} - thus belonging to the short-range domain - are explicitly calculated, whereas interactions falling into the long-range domain, for which the interatomic distances are larger than r_{cut}, are treated through special considerations.[123;293]

In the case of vdW interactions, atoms separated by distances larger than a system-dependent r_{cut} can be treated through various approaches. The crudest one is based

on simple potential truncation, omitting all interactions outside the short-range domain. This approach is rarely applied as-is, since it can lead to wrong estimates of thermodynamic quantities. Truncated interaction descriptions are coupled to the so-called analytical tail corrections to the potential energy and pressure, described by the following equations:

$$\Delta E_{\mathrm{vdW}}^{\mathrm{tail}} = 2\pi \frac{N\left(N-1\right)}{V} \int_{r_{\mathrm{cut}}}^{\infty} r^2 E_{\mathrm{vdW}}\left(r\right) g\left(r\right) dr \tag{2.88}$$

$$\Delta P_{\mathrm{vdW}}^{\mathrm{tail}} = 2\pi \frac{N}{3k_{\mathrm{B}}TV} \int_{r_{\mathrm{cut}}}^{\infty} r^3 \frac{\partial E_{\mathrm{vdW}}\left(r\right)}{\partial r} g\left(r\right) dr \tag{2.89}$$

where $g\left(r\right)$ the pair correlation function:

$$g\left(r\right) = \frac{2V}{N\left(N-1\right)} \frac{\left\langle n\left(r\right)\right\rangle}{4\pi r^2 \Delta r} \tag{2.90}$$

calculated by keeping a histogram $n\left(r\right)$ containing all pairs whose radial distance belong to interval $[i\Delta r, \left(i+1\right)\Delta r]$.[293]

Alternative approaches also exist, including the truncated and shifted scheme that merely subtracts the vdW energy value at r_{cut}:

$$E_{\mathrm{vdW}}^{\text{tr-sh}} = \begin{cases} E_{\mathrm{vdW}}\left(r\right) - E_{\mathrm{vdW}}\left(r_{\mathrm{cut}}\right) & r \leq r_{\mathrm{cut}} \\ 0 & r > r_{\mathrm{cut}} \end{cases} \tag{2.91}$$

along with an appropriate shifting to the force expression and various smoothing procedures via the application of switching functions, e.g. the CHARMM-based scheme:

$$E_{\mathrm{vdW}}^{\mathrm{smooth}} = \begin{cases} E_{\mathrm{vdW}}^{\mathrm{LJ}}\left(r\right) & r \leq r_{\mathrm{in}} \\ s\left(r\right) E_{\mathrm{vdW}}^{\mathrm{LJ}}\left(r\right) & r_{\mathrm{in}} < r \leq r_{\mathrm{out}} \\ 0 & r > r_{\mathrm{out}} \end{cases} \tag{2.92}$$

$$s\left(r\right) = \frac{\left(r_{\mathrm{out}}^2 - r^2\right)^2 \left(r_{\mathrm{out}}^2 + 2r^2 - 3r_{\mathrm{in}}^2\right)}{\left(r_{\mathrm{out}}^2 - r_{\mathrm{in}}^2\right)^3} \tag{2.93}$$

utilizing inner and outer cut-off radii.[302]

The validity of energy tail corrections described by Equation 2.88 is controlled by how rapidly the energy expression decays with respect to the distance. In the case of electrostatic interactions modeled via the Coulomb potential, the decay is proportional to r^{-1}, thus rendering tail correction integrals divergent. This is the major reason prohibiting a tail-corrected truncation scheme for such interactions. A common workaround, circumventing this predicament, is based on carrying out long-range interaction calculations in the reciprocal space by means of the so-called Ewald summation.[119;123;293;305]

The electrostatic energy of a charge-neutral periodic system is expressed as

$$E_{\text{Coul}}^{\text{PBC}} = \frac{1}{4\pi\varepsilon}\frac{1}{2}\sum_{\vec{R}}\sum_{i}\sum_{j}{}' \frac{q_i q_j}{\left|\vec{r}_{ij}+\vec{R}\right|} \tag{2.94}$$

where $\vec{R} = n_1\vec{a} + n_2\vec{b} + n_3\vec{c}$ the vector carrying out the periodic repetition in space in the basis of the vectors spanning the primary periodic supercell, $\varepsilon \equiv \varepsilon_{\text{r}}\varepsilon_0$ the electric permittivity, and the prime indicating that the $i = j$ interaction is omitted when $\vec{R} = \vec{0}$.

Ewald's approach is based on a short-range (SR) and long-range (LR) decomposition of atomic charge distributions with the utilization of an intermediate Gaussian charge distribution:

$$\rho_i(\vec{r}) \equiv \rho_i^{\text{SR}}(\vec{r}) + \rho_i^{\text{LR}}(\vec{r}) = [q_i\delta(\vec{r}-\vec{r}_i) - q_i G_\sigma(\vec{r}-\vec{r}_i)] + [q_i G_\sigma(\vec{r}-\vec{r}_i)] \tag{2.95}$$

where $G_\sigma(\vec{r}) = (2\pi\sigma^2)^{-3/2}\exp\left(-0.5\left|\vec{r}\right|^2/\sigma^2\right)$ a typical Gaussian distribution function. The charge splitting suggested by the above equation, in conjunction with appropriate mathematical manipulations of Poisson's equation governing electrostatic interactions emanating from arbitrary charge distributions, brings the expression of the electrostatic energy to the following form:

$$E_{\text{Coul}}^{\text{PBC}} = E_{\text{Coul}}^{\text{SR}} + E_{\text{Coul}}^{\text{LR}} + E_{\text{Coul}}^{\text{self}} \tag{2.96}$$

where $E_{\text{Coul}}^{\text{SR}}$ the short-range part calculated in real space via the minimum image convention scheme, $E_{\text{Coul}}^{\text{LR}}$ the long-range part evaluated in the reciprocal space where it converges rapidly due to the presence of the exponential term inherent to the Gaussian approximation, and $E_{\text{Coul}}^{\text{self}}$ the so-called self-interaction term:

$$E_{\text{Coul}}^{\text{SR}} = \frac{1}{4\pi\varepsilon}\frac{1}{2}\sum_{\vec{R}}\sum_{i}\sum_{j}{}' \frac{q_i q_j}{\left|\vec{r}_{ij}+\vec{R}\right|}\text{erfc}\left(\frac{\left|\vec{r}_{ij}+\vec{R}\right|}{\sqrt{2}\sigma}\right) \tag{2.97}$$

$$E_{\text{Coul}}^{\text{LR}} = \frac{1}{2V\varepsilon}\sum_{\vec{k}\neq\vec{0}}\frac{\exp\left(-0.5\sigma^2\left|\vec{k}\right|^2\right)}{\left|\vec{k}\right|^2}\left|S\left(\vec{k}\right)\right|^2 \tag{2.98}$$

$$E_{\text{Coul}}^{\text{self}} = \frac{1}{4\pi\varepsilon}\frac{1}{\sqrt{2\pi}\sigma}\sum_{i} q_i^2 \tag{2.99}$$

with

$$S\left(\vec{k}\right) = \sum_{j} q_j \exp\left(\text{i}\vec{k}\cdot\vec{r}_j\right) \tag{2.100}$$

corresponding to the structure factor of the charge distribution.

Contemporary efficient calculation schemes of reciprocal-space Ewald sums are based

on grid methods by means of Fast Fourier Transformation (FFT). Three commonly encountered FFT-accelerated Ewald summation algorithms are the Particle-Particle Particle-Mesh (PPPM) method by Hockney and Eastwood[306], the Particle Mesh Ewald (PME) method by Darden *et al.*[307] and its upgrade, the so-called smooth PME method[308]. In their essence, such grid-based algorithms carry out four basis steps for the evaluation of Coulomb energy and forces. Since FFT is a finite and discrete transformation, point charges need to be mapped from continuous coordinates to an appropriate grid embedded into the periodic supercell. Once the charge assignment onto the grid is carried out, Poisson's equation is solved on the grid, forces are evaluated on its nodes and are - finally - back-interpolated to particles inside the simulation box.[305]

Besides distance-dependent categorizations of non-bonded interactions, another criterion is also encountered in atomistic simulations of macromolecular systems, taking into consideration molecular topological information. Based on this approach, non-bonded interactions between atoms belonging to the same molecule are characterized as intramolecular, whereas when the interaction sites correspond to atoms belonging to different molecules interactions are referred to as intermolecular. In the latter case, interaction conditions are solely related to distance cut-off criteria, while in the former case, certain limitations apply. To be more precise, well-defined, topologically-controlled exclusion rules apply for intramolecular non-bonded interactions, depending on the level of neighboring. Most FFs ignore such interactions when atoms are separated by one ("1-2" pairs) and two ("1-3" pairs) bonds, while atoms on the ends of a proper dihedral ("1-4" pairs), linked via three consecutive bonds, are subjected to FF-dependent scaling rules.[293;302] All of the above notions are illustrated in Figure 2.4.

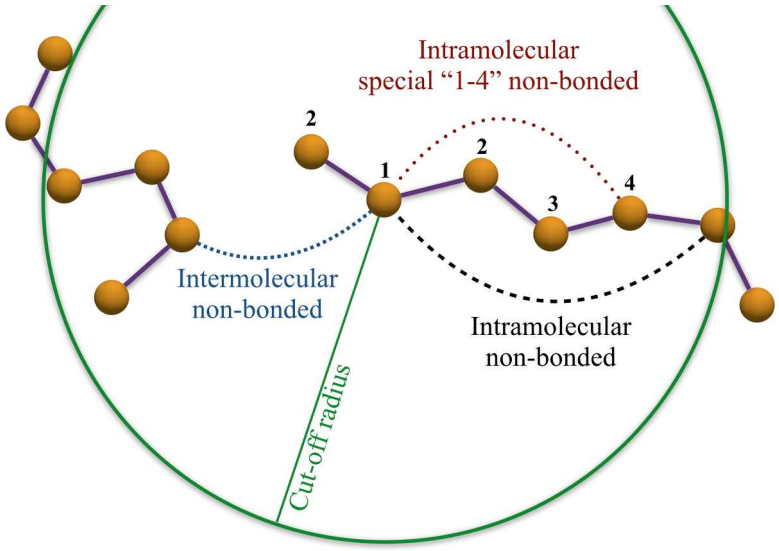

Figure 2.4: Non-bonded interaction schemes encountered in macromolecular atomistic simulations.

2.2.3 Temperature and Pressure Control

Material properties and mechanisms are customarily examined via MD simulations under desired temperature and pressure conditions. In a straightforward utilization of Velocity-Verlet EoMs, both temperature and pressure are non-controllable quantities, dictated by the microcanonical state of the under study system. In order to apply specific thermodynamic conditions, certain algorithmic approaches or even a different theoretical basis are necessary. Numerical algorithms and alternative differential equation forms linked to temperature and pressure control are commonly referred to as thermostats and barostats respectively.

The simplest thermostatting technique relies on the Andersen method, a stochastic approach replacing particle velocities during the EoM integration by a suitable normal distribution with characteristics defined by the desired temperature.[309] This velocity replacement scheme is applied in a controllable frequent fashion and is more or less analogous to the actual physical process of thermal equilibration stating that a system's temperature is imposed via interactions with a surrounding heat bath of infinite thermal capacity. Although Andersen's method is a natural choice for temperature control, it suffers by its very essence: the stochastic description renders it inappropriate for MD studies of dynamical and transport properties, since it perturbs the deterministic dynamical behavior of the simulated system.

A deterministic method for temperature control resides in the so-called Berendsen thermostat: a relatively simple algorithmic approach, widely used for constant temperature MD simulations, based on a synchronized with the integration step velocity rescaling by a factor $\lambda_T = \left[1 - \tau^{-1} dt \left(1 - T_0/\mathcal{T}\right)\right]^{1/2}$, where $\tau \gg dt$ symbolizes the time constant controlling the coupling to a heat bath of temperature T_0.[310] Berendsen's thermostat is a good, computationally inexpensive technique for temperature control, but with a serious drawback: its application fails to capture the exact canonical distribution, while suffering from artefacts inherent to velocity rescaling methods.

The breakthrough towards thermodynamically correct temperature control was introduced by Nosé[311] through the utilization of an extended Hamiltonian, resulting in the addition of an appropriate friction factor to the differential equation of motion:

$$m_i \ddot{\vec{r}}_i = \vec{F}_i - \zeta m_i \dot{\vec{r}}_i \tag{2.101}$$

where ζ a friction parameter, same for all particles, which is negative or positive should heat need to be added or drained from the system, respectively. The most widely used variant of the friction parameter, both time-reversible and complying with the canonical ensemble, is based on Nosé's method in the formulation of Hoover[312], defined via the differential equation:

$$Q\dot{\zeta} = \sum_i m_i u_i^2 - 3Nk_{\mathrm{B}}T_0 \tag{2.102}$$

where Q the coupling constant, a fictitious "heat bath mass". Equations 2.101 and 2.102 constitute the so-called Nosé-Hoover (NH) thermostat, typically recast into the following set of Hamilton's equations:

$$\begin{aligned}
\dot{\vec{r}}_i &= \frac{\vec{p}_i}{m_i} \\
\dot{\vec{p}}_i &= \vec{F}_i - \frac{p_\eta}{Q}\vec{p}_i \\
\dot{\eta} &= \frac{p_\eta}{Q} \\
\dot{p}_\eta &= \sum_i \frac{p_i^2}{m_i} - 3Nk_{\mathrm{B}}T_0
\end{aligned} \tag{2.103}$$

where η the fictitious generalized coordinate for temperature control and p_η its conjugate momentum.

Unfortunately, Equations 2.103 fail to properly reproduce the characteristics of the canonical statistical ensemble, since the derived momentum distributions are far from the Gaussian $f(p) = (2\pi m k_{\mathrm{B}}T)^{-1/2} \exp(-p^2/2mk_{\mathrm{B}}T)$.[313] In order to alleviate this behavior, additional variables can be inserted in the above EoMs: correct momentum statistical distributions can be achieved should the momenta themselves be coupled to a to a NH-like thermostat, giving birth to a new set of η_j and p_{η_j} variables. Correct statistical distributions are acquired asymptotically via the utilization of a chain of thermostats of order M.[314] Under this approach, the so-called NH chain EoMs are expressed as:

$$\begin{aligned}
\dot{\vec{r}}_i &= \frac{\vec{p}_i}{m_i} \\
\dot{\vec{p}}_i &= \vec{F}_i - \frac{p_{\eta_1}}{Q_1}\vec{p}_i \\
\dot{\eta}_j &= \frac{p_{\eta_j}}{Q_j},\ j = 1, 2, ..., M \\
\dot{p}_{\eta_1} &= \sum_i \frac{p_i^2}{m_i} - 3Nk_{\mathrm{B}}T_0 - \frac{p_{\eta_2}}{Q_2}p_{\eta_1} \\
\dot{p}_{\eta_j} &= \frac{p_{\eta_{j-1}}^2}{Q_{j-1}} - k_{\mathrm{B}}T_0 - \frac{p_{\eta_{j+1}}}{Q_{j+1}}p_{\eta_j},\ j = 2, ..., M-1 \\
\dot{p}_{\eta_M} &= \frac{p_{\eta_{M-1}}^2}{Q_{M-1}} - k_{\mathrm{B}}T_0
\end{aligned} \tag{2.104}$$

Constant pressure MD simulations are realized via appropriate response of supercell size and shape in order to adhere to prescribed pressure conditions. In the case of isotropic systems enclosed into a periodic orthogonal simulation domain, a simple method is based

on the Berendsen barostat that scales both cartesian coordinates and supercell edges by a factor $\lambda_P = \left[1 - \beta\tau_P^{-1} dt\,(P_0 - P)\right]^{1/3}$ in order to achieve a hydrostatic pressure P_0, where β the isothermal compressibility of the system and τ_P the barostat time constant.[310] Anisotropic system response to decoupled external pressure components along the three cartesian directions can be achieved via the introduction of separate scaling factors per direction and by treating the pressure in its tensorial form.

The idea of an extended Hamiltonian, including the volume and its conjugate momentum, towards a thermodynamically-consistent pressure control scheme dates back to the work of Andersen, providing EoMs for the isoenthalpic-isobaric statistical ensemble.[309] Parrinello and Rahman extended Andersen's approach to systems with anisotropic response to external pressure via the utilization of triclinic simulation boxes, capable of size and shape variations.[315;316]

The current state-of-the-art integration scheme at the isothermal-isostress statistical ensemble is based on the work by Martyna, Tobias, and Klein, commonly referred to as the MTK EoMs.[317] In their generalized form, using a triclinic supercell, the aforementioned equations are written as:

$$\begin{aligned}
\dot{\vec{r}}_i &= \frac{\vec{p}_i}{m_i} + \frac{\mathbf{p}_\mathrm{g}}{W_\mathrm{g}}\vec{r}_i \\
\dot{\vec{p}}_i &= \vec{F}_i - \frac{\mathbf{p}_\mathrm{g}}{W_\mathrm{g}}\vec{p}_i - \frac{1}{N_f}\frac{\mathrm{Tr}\,(\mathbf{p}_\mathrm{g})}{W_\mathrm{g}}\vec{p}_i - \frac{p_{\eta_1}}{Q_1}\vec{p}_i \\
\dot{\mathbf{h}} &= \frac{\mathbf{p}_\mathrm{g}}{W_\mathrm{g}}\mathbf{h} \\
\dot{\mathbf{p}}_\mathrm{g} &= \det(\mathbf{h})\left(\mathbf{P}^\mathrm{int} - \mathbf{P}_0\right) - \frac{1}{N_f}\sum_i \frac{p_i^2}{m_i}\mathbf{I} - \frac{p_{\xi_1}}{Q'_1}\mathbf{p}_\mathrm{g} \\
\dot{\xi}_j &= \frac{p_{\xi_j}}{Q'_j} \\
\dot{p}_{\xi_1} &= \frac{\mathrm{Tr}\,(\tilde{\mathbf{p}}_\mathrm{g}\mathbf{p}_\mathrm{g})}{W_\mathrm{g}} - 9k_\mathrm{B}T_0 - \frac{p_{\xi_2}}{Q'_2}p_{\xi_1} \\
\dot{p}_{\xi_j} &= \frac{p_{\xi_{j-1}}}{Q'_{j-1}}p_{\xi_1} - k_\mathrm{B}T_0 - \frac{p_{\xi_{j+1}}}{Q'_{j+1}}p_{\xi_1} \\
\dot{p}_{\xi_M} &= \frac{p_{\xi_{M-1}}^2}{Q'_{M-1}} - k_\mathrm{B}T_0
\end{aligned} \tag{2.105}$$

where $\mathbf{h} = \left\{\vec{a}, \vec{b}, \vec{c}\right\}$ is the supercell matrix, $\mathbf{p}_\mathrm{g}$ its conjugate momentum matrix and W_g, Q, and Q' suitable timescale parameters dictating the frequency of volume change and general chain-like temperature and pressure control respectively. The tilde symbolizes the transpose matrix. In a complete analogy to the NH method, ξ_j and p_{ξ_j} are used to achieve proper statistical behavior via a scheme of connected barostats. Temperature control chain equations are identical to the NH chain method of Equations 2.104. Furthermore, $\mathbf{P}^\mathrm{int}$ and $\mathbf{P}_0$ correspond to the instantaneous pressure tensor and the desired pressure in

matrix format, $\mathbf{I}$ is the 3×3 identity matrix, and $N_f = 3N - N_c$ the number of degrees of freedom, where N_c the number of any constraints.[313]

The numerical integration of both NH chain Equations 2.104 and MTK Equations 2.105 is a non-trivial task. Current implementations rely on the so-called Liouville operator formalism applied for such non-Hamiltonian systems via appropriate factorizations of the time propagator and are supported by the majority of available MD simulation codes.[318–320]

Chapter 3

Density Functional Theory Studies of Discotic Molecules

This chapter contains a series of results gained from ab-initio DFT simulations of discotic molecules. After a brief introduction to the systems under study and the methods employed at the quantum level of description, single molecule structural, electronic, and charge transfer properties are presented, followed by dimer studies aiming at the evaluation of charge transfer integrals with respect to intermolecular relative position and orientation.

3.1 Systems of Interest and Computational Details

The main focus of this chapter is concentrated on *ab-initio* studies of pristine and mono-substituted nanographene molecules, along with molecular assemblies resulting from un-substituted cores that have been covalently connected through appropriate articulated linkers.

As regards single PAHs, three key molecules are on the epicenter: HBC (Figure 1.2: **16**), superphenalene C96 (Figure 1.15: **53**) and the extended PAH of tetragonal symmetry C132 (Figure 1.15: **55**). C96 is a molecule with 92 carbon atoms with trigonal shape, exhibiting an analogous D_{3h} point symmetry. C132 is made up by 132 carbon atoms, characterized by tetragonal C_{2v} symmetry. These two molecules can be envisioned as the fusion product of three and four HBC molecules, respectively. The coronene molecule (Figure 1.2: **14**) is also considered as a prototype small PAH molecule for comparison purposes.

In the case of functionalized discotics, studies are limited to HBC cores. Mono-substituted HBC-X cores (**70**) under study fall into two categories: dipole-substituted and ring-substituted molecules. In the former case, atoms or molecular fragments with sizable electronegativity difference compared to carbon atoms are grafted onto a single peripheral site, hence resulting in HBC cores with non-zero electric dipole moment. As

regards the latter case, phenyl substitution is treated in different variants, along with the special case of thiophene ring grafting.

The family of discotic molecules examined via QM methods also contains the contorted c-HBC molecule (**71**), along with two HBC precursor disk-like molecules: HPB and HBP[321;322] (Figure 1.8: **35** and **34**, respectively). Graphical depictions of newly introduced discotics are illustrated in Figure 3.1.

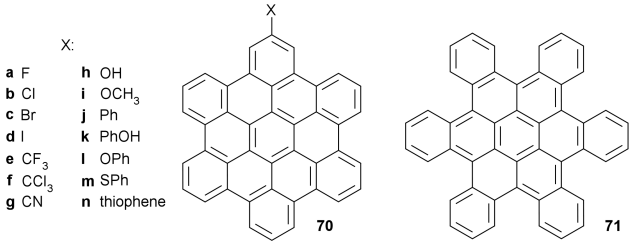

Figure 3.1: Mono-substituted HBC-X molecules (**70**), along with the contorted c-HBC mesogen (**71**).

Along with single PAH core molecules, a series of covalently linked "super-molecules" are also considered. The first kind of "super-molecule" is the dumbbell-like molecule HBC-DB (1.16: **57**) resulting from direct covalent linkage. The rest are mesogens belonging to a multitudinous family possessing a "tri-arm" geometry, containing a series of covalent linkers that hold together three nanographene molecules. Four linking units are considered: a single nitrogen atom, a TPA unit (Figure 1.18: **63**), a benzene molecule, and a TPB molecule (Figure 1.17: **62**). HBC-based covalently linked "super-molecules" under study are depicted in Figure 3.2. Furthermore, the TPB linker is utilized for the realization of tri-arm "super-molecules" bearing extended C96 and C132 discotic segments.

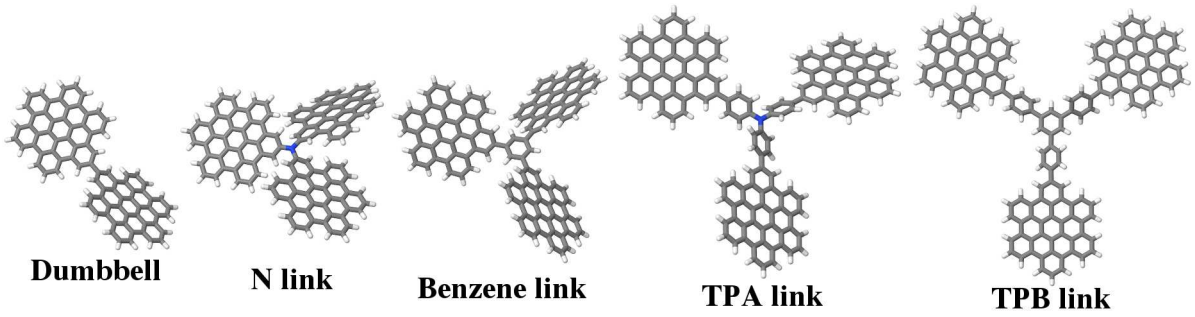

Figure 3.2: HBC-based "super-molecules" with different linkages.

Particular interest is also placed on nitrogen-containing star-shaped mesogens, since TPA holds a prominent role as a donor molecule in polyphenyl-based organic electronics applications. A comparative analysis is carried out on tri-arm geometries comprised of disk segments linked via a nitrogen atom, either directly or through phenyl linkage, considering terminal discotic units with variable core size, such as benzene, pyrene, and peropyrene.

Due to the presence of various heteroatoms, mono-substituted HBC cores are treated at the B3LYP/6-311G** level of theory. HPB, HBP, and c-HBC molecules are also treated at the aforementioned level. Properties of the remaining single PAHs and their covalently linked complexations of dumbbell and tri-arm symmetries are evaluated at the B3LYP/6-31G**, with DFT-D3 dispersion corrections where deemed necessary.

Electron and hole reorganization energies are calculated using the four point method via Equation 2.58. CTIs are evaluated via molecular dimer calculations under the assumption that dimer molecular orbitals involved in the charge transfer process result from the interaction of monomer FMOs.[296] In the case of degenerate frontier orbitals, a root mean square average approach is adopted, taking into consideration all possible orbital combinations.[215] It should be noted that for CTI calculations, the relatively small Gaussian basis set 6-31G is used, since larger basis sets render calculations for large molecular dimers (e.g. the ones created by C132) more demanding from a computational resources point of view.

All quantum mechanical calculations are carried out using the open-source software NWCHEM.[323] Charge transfer integrals are evaluated by means of the FMO-ET module embedded into NWCHEM.

3.2 Results and Discussion

3.2.1 Structural Properties

In the case of pristine PAHs, geometry optimizations result in planar molecular structures with 3-fold carbon atom coordination and the $C-C$ and $C-H$ bond lengths at 1.42 Å and 1.08 Å, respectively. Structural features in the form of characteristic bond, angle and proper dihedral equilibrium values for dipole- and ring-substituted HBC derivatives are listed in Table 3.1. Dyads, triplets, and quadruplets of atomic labels correspond to specific bond, angle, and dihedral types, respectively. As regards the notation, subscripts "ar", "3", and "1" accordingly indicate aromatic, aliphatic, and sp^1 hybridized carbon atoms. Labels denoted with an asterisk correspond to atoms belonging to the functional group and not to the discotic core.

All dipole substituents are protruding in a coplanar fashion with respect to the HBC core. Direct phenyl-based functionalization (**70j**, **70k**) is manifested via a non-planar arrangement, with the proper dihedral angle between the phenyl ring and the PAH core at ∼40°, in fair agreement with literature data.[195] Analogous behavior is found for the thiophene side group (**70n**), but with the torsion angle at the smaller value of 32.8°. Of particular interest is the case of phenyl grafting via an intermediate sulfur bridge (**70m**), since the arrangement of the phenyl ring is near-perpendicular with respect to the core plane. Molecular representations of compounds **70l** and **70m** are shown in Figure 3.3.

Table 3.1: Structural features of mono-substituted HBC-X molecules (**70**).

X	Feature	Value	X	Feature	Value
a	$C_{ar} - F$	1.35 Å	**i**	$C_{ar} - O$	1.36 Å
b	$C_{ar} - Cl$	1.76 Å		$O - C_3$	1.42 Å
c	$C_{ar} - Br$	1.92 Å		$C_3 - H$	1.10 Å
d	$C_{ar} - I$	2.13 Å		$C_{ar} - O - C_3$	118.7°
e	$C_{ar} - C_3$	1.50 Å		$O - C_3 - H$	109.6°
	$C_3 - F$	1.35 Å		$H - C_3 - H$	109.3°
	$C_{ar} - C_3 - F$	116.0°	**j**	$C_{ar} - C^*_{ar}$	1.49 Å
	$F - C_3 - F$	106.8°		$C_{ar} - C_{ar} - C^*_{ar} - C^*_{ar}$	41.4°
f	$C_{ar} - C_3$	1.52 Å	**k**	$C_{ar} - C_{ar} - C^*_{ar} - C^*_{ar}$	40.2°
	$C_3 - Cl$	1.81 Å	**l**	$C_{ar} - C_{ar} - O - C^*_{ar}$	32.4°
	$C_{ar} - C_3 - Cl$	111.3°		$C_{ar} - O - C^*_{ar} - C^*_{ar}$	48.6°
	$Cl - C_3 - Cl$	107.6°	**m**	$C_{ar} - S$	1.79 Å
g	$C_{ar} - C_1$	1.43 Å		$C_{ar} - S - C^*_{ar}$	103.2°
	$C_1 - N$	1.15 Å		$C_{ar} - C_{ar} - S - C^*_{ar}$	43.5°
h	$C_{ar} - O$	1.37 Å		$C_{ar} - S - C^*_{ar} - C^*_{ar}$	54.5°
	$O - H$	0.96 Å	**n**	$C - C^*_{ar}$	1.47 Å
	$C_{ar} - O - H$	109.4°		$C_{ar} - C_{ar} - C^*_{ar} - S$	32.8°

Moving on to the structural features of selected HBC precursor molecules, i.e. HPB and HBP, the different stages of planarization have profound effects on the molecular morphology. The torsion angle in HPB between the central benzene unit and the peripheral phenyl rings is 68.0°, with the outer rings positioned following a "face-on" arrangement, thus leading to a 6-fold point symmetry and to a non-planar geometry. On the other hand, HBP can be envisioned as a rugged discotic molecule made up by two planar segments linked via two intermediate aromatic bonds. Steric interactions due to the presence of hydrogen atoms near the rigid linkage lead to a "bow tie" morphology, with the two planar segments forming an angle of ∼56°. Equilibrium geometries of HPB and HBP are shown in Figure 3.4.

In the case of c-HBC, two structural variants are examined: the 6-fold and 3-fold symmetric cases, referred to as the first (v1) and second (v2) variant, respectively. c-HBC-v1 is characterized by a "shallow" morphology, with the outer, *cata*-condensed benzoic rings forming an angle of ∼20° with respect to the main coronene core, rotated along the zigzag direction of the honeycomb arrangement. On the other hand, c-HBC-v2 possesses a more buckled, bowl-shaped geometry, with the outer rings bending alternatively by an angle of ∼23° rotated about the armchair direction, leading to an overall benzoic angular spread of 46° on the so-called PAH "fjord" peripheral region. From an energetic point of view, the second variant is more stable by an energy difference of 1.4 eV. Both variants are depicted in Figure 3.4.

The family of discotic "super-molecules" is comprised of relatively flat PAH cores,

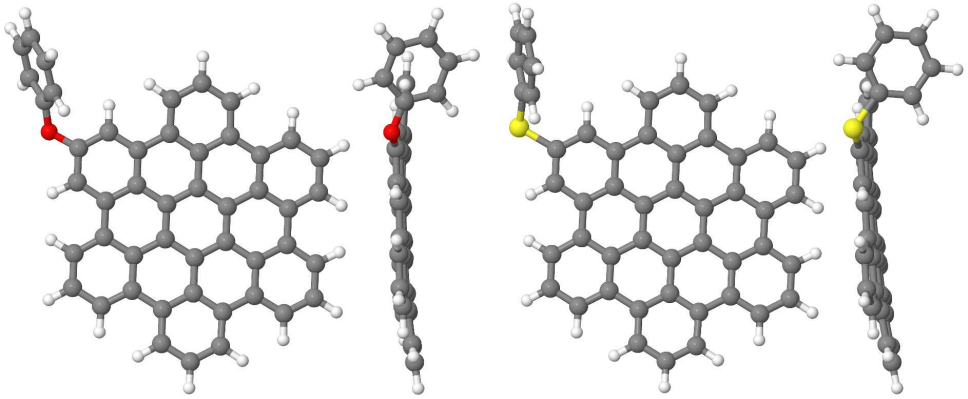

Figure 3.3: Ball and stick representations of local ring arrangement in the case of phenyl-substituted HBC molecules via oxygen (**70l**; left) and sulfur (**70m**; right) bridging.

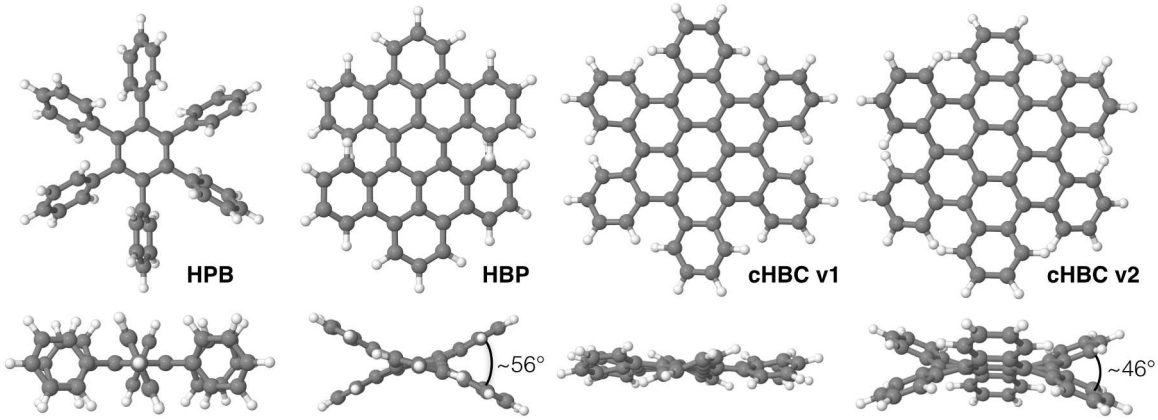

Figure 3.4: Top (upper panel) and side (lower panel) views of equilibrium structures of HBC precursors and of two variants of the c-HBC molecule.

linked together via appropriate articulate linkers. The overall morphology of such molecules is directly controlled by the torsional characteristics of the linkers. In the case of HBC-DB, the proper dihedral angle centered on the linking covalent bond is at 39.7°, slightly larger than its biphenyl counterpart at 38.3°. Tri-arm "super-molecule" morphology is deduced from the articulate proper dihedral angles present in each molecule type. The utilization of benzene, TPB, N, and TPA linkers gives rise to two different torsion types: the phenyl and amine proper dihedral angles, rotatable about a single bond. These angles are further categorized with respect to their topology into inner and outer torsion angles, should they be situated near or far from the linker's center of mass, respectively. A graphical representation of the aforementioned structural features is depicted in Figure 3.5, where the left panel shows a TPB linker with its phenyl inner and outer torsion angles and the right panel a TPA linker with an inner amine and an outer phenyl torsion angle.

Optimized torsion angle values for all examined tri-arm discotics are gathered in

Table 3.2, listing the type of linker and terminal PAH. "Pyr" and "Pero" correspond to the pyrene and peropyrene molecules and the core/linker designations "Benz"/"N" and "Benz"/"Benz" refer to the TPA and TPB molecules respectively. The nature of each dihedral angle type is denoted via appropriate superscripts.

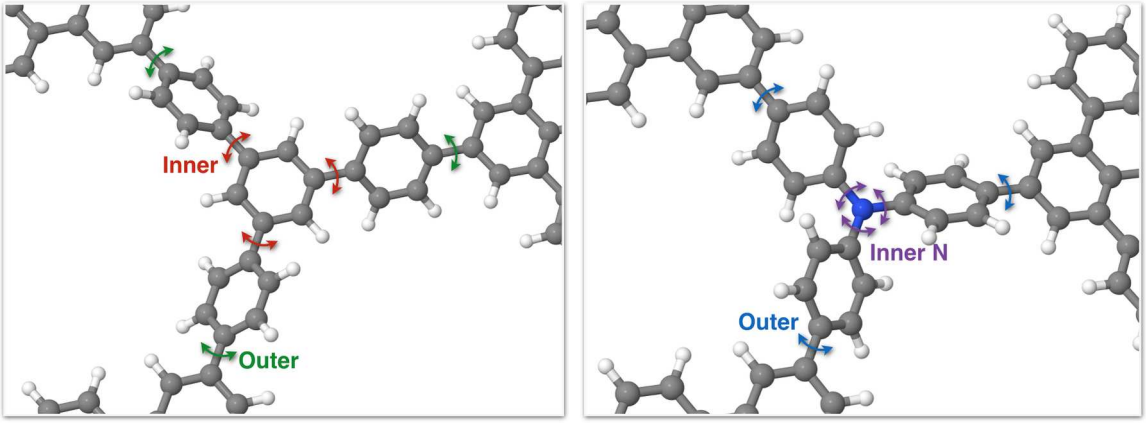

Figure 3.5: Proper dihedral types found in tri-arm geometries with variable linkers.

Table 3.2: Linker torsion angles of tri-arm discotic "super-molecules".

Disk	Link	Torsion angle (°)	Disk	Link	Torsion angle (°)	Disk	Link	Torsion angle (°)
Benz	N	$40.8^{\dagger}$	Benz	TPA	$40.2^{\dagger}/37.5^{\S}$	Benz	Benz	$40.0^{¤}$
Pyr	N	$40.5^{\dagger}$	Pyr	TPA	$40.3^{\dagger}/37.8^{\S}$	HBC	Benz	$39.0^{¤}$
Pero	N	$40.2^{\dagger}$	Pero	TPA	$40.3^{\dagger}/37.2^{\S}$	HBC	TPB	$39.0^{¤}/38.0^{\S}$
HBC	N	$34.9^{\dagger}$	HBC	TPA	$40.4^{\dagger}/37.3^{\S}$	C96	TPB	$41.1^{¤}/35.9^{\S}$
						C132	TPB	$40.7^{¤}/37.8^{\S}$

†: Inner amine
§: Outer phenyl
$^{¤}$: Inner phenyl

A first differentiation with respect to previous structural results can be found for TPB compared to HPB, with phenyl torsion angles decreasing from 68.0° for HPB to 40.0° for TPB - an effect attributed to the relative grafting site separation, since TPB peripheral phenyls do not interact strongly with one another via steric and π-π interactions as in the case of HPB. The level of conjugacy of peripheral cores in the case of N-linked tri-arm molecules seems to have a minuscule effect on amine dihedral angles, nevertheless exhibiting a decreasing trend with respect to core size, with striking example the ∼6° difference when going from benzene to HBC terminal units.

In the case of TPB- and TPA-linked star-shaped "super-molecules", inner torsion angles retain values close to pristine TPB and TPA molecules, respectively. An interesting feature pertinent to all tri-arm discotics with intermediate phenyl rings is that outer phenyl dihedral angles appear at smaller values compared to inner torsion angles, re-

gardless of the utilization of benzene or nitrogen as the central 3-fold block on which intermediate phenyls are attached.

Of particular importance are the structural variations induced by molecular ionization to the anionic or cationic state during the process of charge hopping. Spin-polarized DFT calculations are utilized for the structural optimization of ionic molecular species obtained from all molecules under study. In order to quantify intramolecular alterations due to ionization, an internal coordinates approach is adopted using bond, angle, and proper dihedral values. The aforementioned quantification is achieved by calculating absolute differences between all structural features from the optimized neutral and ionic states. Histograms of bond, angle, and dihedral absolute differences for cationic molecules are illustrated in Figure 3.6. Star-shaped, tri-arm geometries are abbreviated using a slash, with the outer discotic type and linker situated on the left and right side of the slash, respectively. The designation "HBC-thio" stands for the thiophene mono-substituted HBC core. Values of the coronene and ovalene, and biphenyl molecules are also included for comparison purposes.

Should pristine, planar discotic molecules be taken into consideration, the cationic state induces dominant angular deviations, without compromising core planarity, except for the marginal case of the C132 core that exhibits elevated torsional variations compared to the smaller discotics. HBC precursor molecules examined, i.e. HPB and HBP, undergo structural relaxation upon reaching the cationic state via torsional variations.

In the case of dipole mono-substituted HBC derivatives, structural deviations are limited to small angular distortions, except for the case of HBC-CN, for which a relative core bending near the functionalization site is reported. Ring-substituted HBC derivatives respond to the charge excess of the cationic state by following torsional variations primarily localized about the linking covalent bond. Articulated "super-molecules" with either dumbbell or tri-arm geometry exhibit pronounced torsional variations in the cationic state, except for the case of the peropyrene/TPA molecule. These alterations to the molecular structure are mostly manifested about the linking bonds.

Analogous structural patterns are exhibited by discotic anions, with the absolute difference bar charts depicted in Figure 3.7. Notable geometric alterations upon ionization are shown by the most articulated mono-substituted HBC derivatives: the HB-OPh and HBC-SPh molecules. Both molecules rearrange the pendant phenyl groups so that the outer phenyl ring plane is perpendicular to the core plane. In the case of the anion, the linking proper dihedral angle is near zero whereas for the cation, the value lies near 90°. The drastic rearrangements of functional groups are illustrated in Figure 3.8 for the HBC-OPh discotic core.

Another notable difference between the anionic and cationic versions of discotic molecules is found in the case of the HBC-CCl_3 core. The relatively extreme values compared to other mono-substituted HBC derivatives are due to the carbon-chlorine separation for one

chlorine atom at 2.7 Å, effectively removing the atom from the discotic complex upon ionization, as is shown in Figure 3.9.

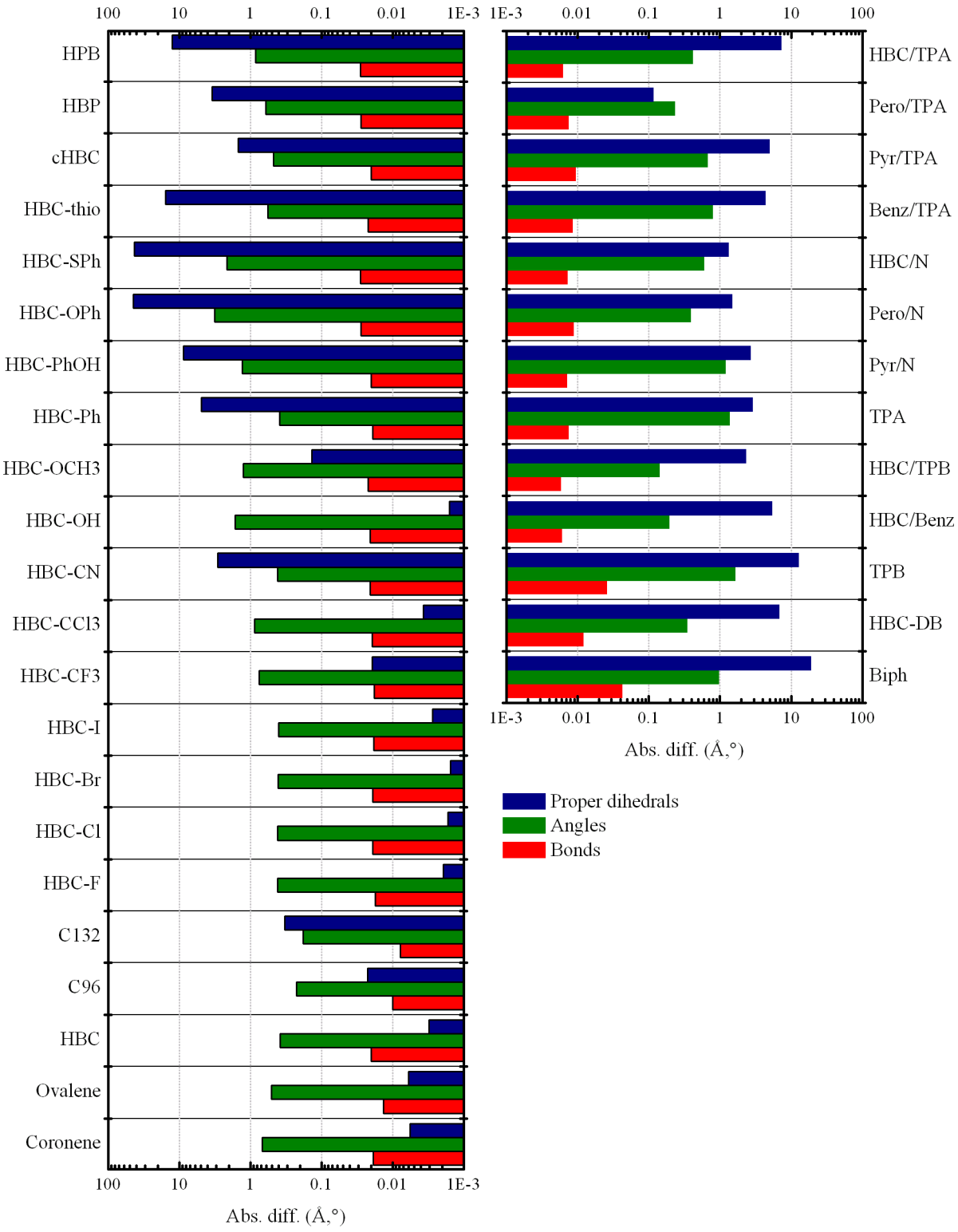

Figure 3.6: Maximum absolute differences between neutral and cationic discotics in terms of internal coordinates.

A mapping of structural differences in terms of internal coordinates with respect to the

ionization state is possible using color-coded CPK representations of discotic molecules, coloring each atom with a specific hue when it belongs to a bond, angle, or dihedral with a specific absolute difference value, taking into consideration the maximum of values should an atom belong to multiple internal coordinates.

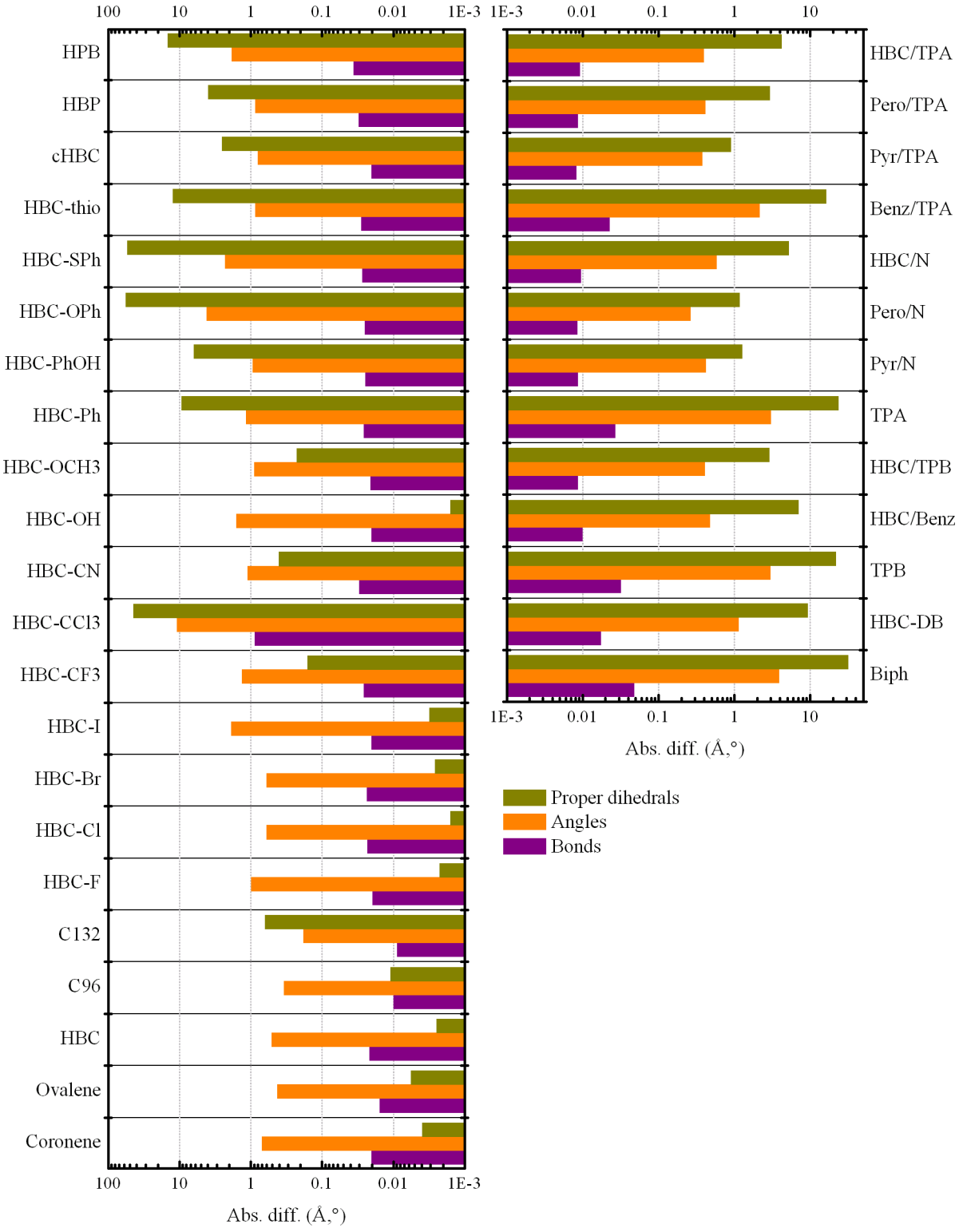

Figure 3.7: Maximum absolute differences between neutral and anionic discotics in terms of internal coordinates.

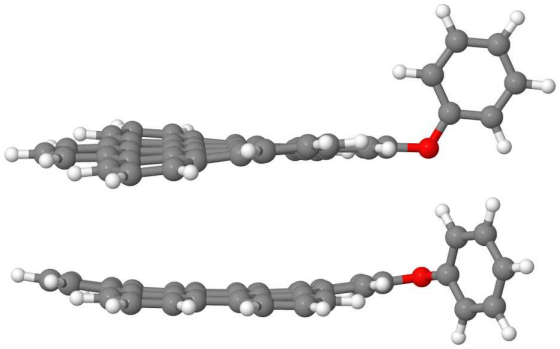

Figure 3.8: Molecular representations of the effect of ionization on the relative position of the pendant phenyl group. The top and bottom illustrations correspond to the anionic and cationic species, respectively.

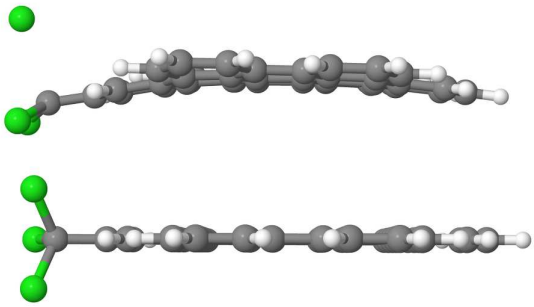

Figure 3.9: Molecular representations of the anionic (top) and cationic (bottom) species of the HBC-CCl_3 discotic molecule.

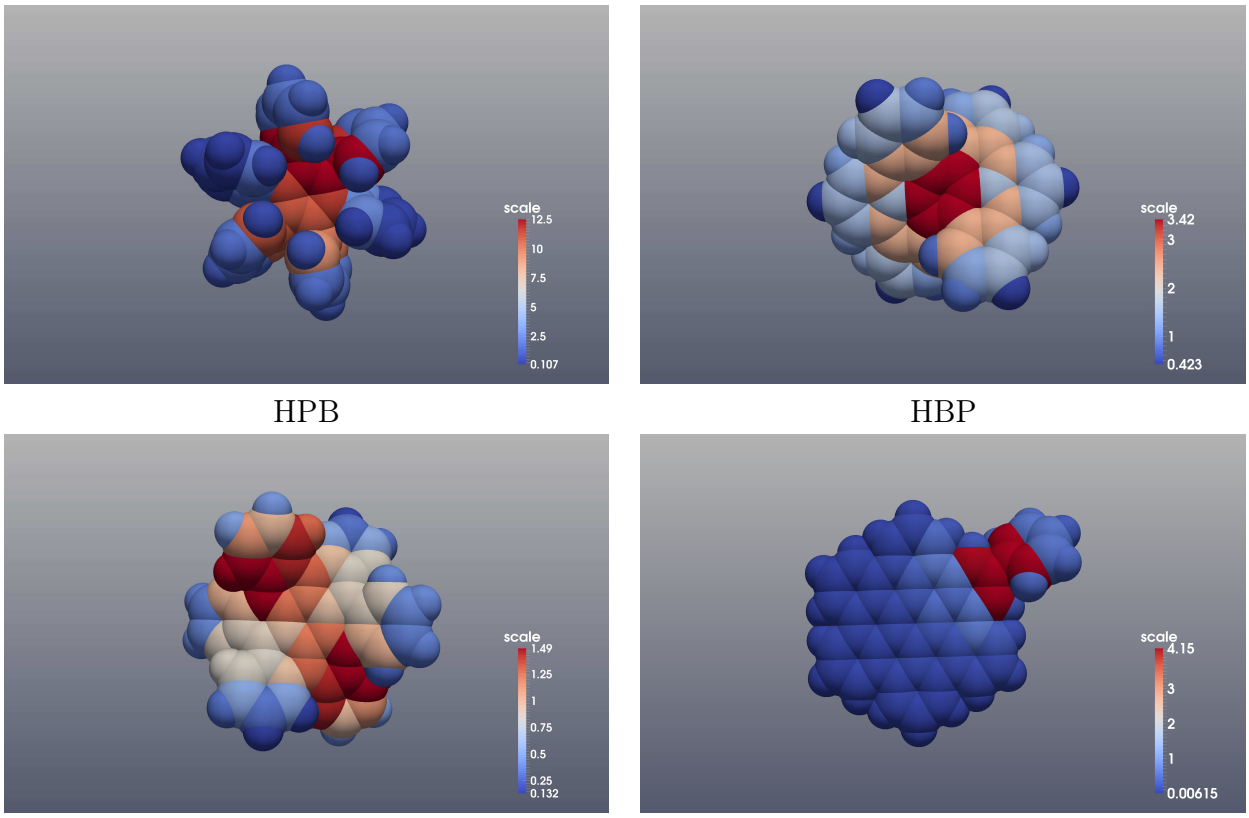

Figure 3.10: Color-coded molecular representations of torsional variations at the cationic state of various discotic molecules.

Color-coded molecular representation that illustrate molecular parts that participate

strongly to local torsional variations are shown in Figure 3.10 for selected single-core discotics in their cationic state. Absolute dihedral angle differences are read from the inset color legends. Analogous plots are provided for the ionic and cationic states of the TPB-linked HBC tri-arm molecule in Figure 3.11.

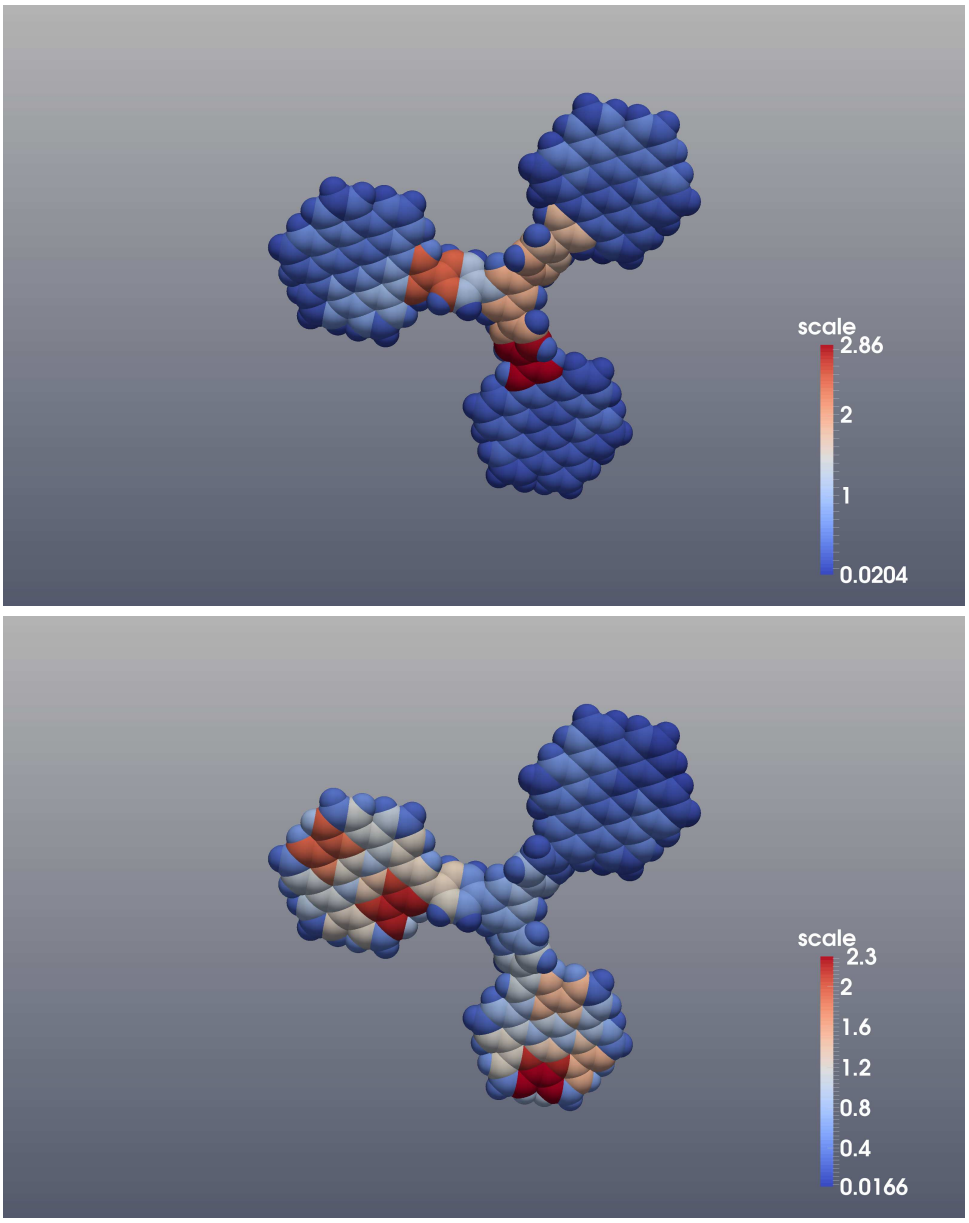

Figure 3.11: Color-coded molecular representations of torsional variations for the ionized versions of the TPB-linked HBC tri-arm molecule.

Structural rearrangements upon ionization for articulated discotic molecules are manifested mostly via variations to the torsional state about linking bonds, although in the case of the utilization of HBC terminal cores, deviations from core planarity seem to take place as part of the structural relaxation.

3.2.2 Electronic and Charge Transfer Properties

As far as single molecule electronic properties of unsubstituted HBC, C96 and C132 are concerned, the expanse of the polyaromatic core affects the relative positions of the HOMO and LUMO levels, along with the associated gap. The aforementioned energy levels accompanied by graphical depictions of FMOs are illustrated in Figure 3.12 including results regarding the coronene molecule.

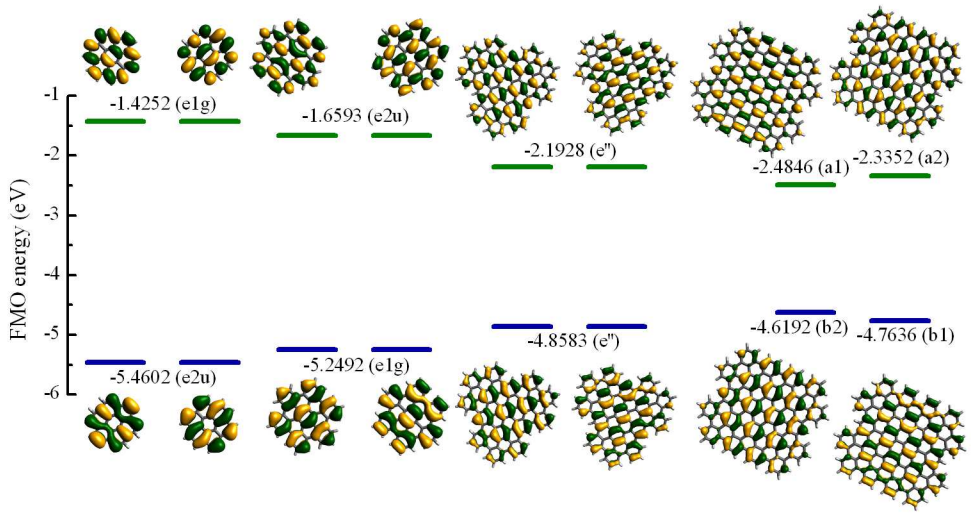

Figure 3.12: FMOs of coronene, HBC, C96 and C132 molecules, with associated symmetry elements inside parentheses. Occupied and unoccupied orbitals are depicted as blue and green lines respectively.

From coronene to C96, both HOMO and LUMO appear doubly degenerate. This degenerate character is lifted for C132 due to the C_{2v} point group characterizing this specific molecule. It should be noted that the molecular orbital morphology follows a distinctive benzoic character. The addition of extra benzoic rings leads to a decrease of both the HOMO-LUMO gap and the absolute position of LUMO levels, while HOMO levels show an increasing trend.

In the case of covalently linked HBC molecules, all of the examined linkage types result in a steady decrease of the HOMO-LUMO gap. FMOs retain a level of degeneracy in the case of benzene and TPB tri-arm linked molecules. Both HBC dumbbell and nitrogen linked tri-arm HBC molecules exhibit definitely non-degenerate HOMO and LUMO levels, while the TPA linked tri-arm HBC molecule shows a non-degenerate HOMO level and a degenerate LUMO state. A graphical representation of molecular levels in the energy interval between -7.0 eV and -0.5 eV is depicted in Figure 3.13, including states of the HBC molecule for comparison, accompanied by illustrations of spatial distributions of FMOs. The ladder-like orbital layout in the aforementioned figure for states near the gap is used in order to show degenerate and near-degenerate states. Graphical depictions of

extra FMOs for all "super-molecules" are included in Figures I.1 to I.5 in the Appendices.

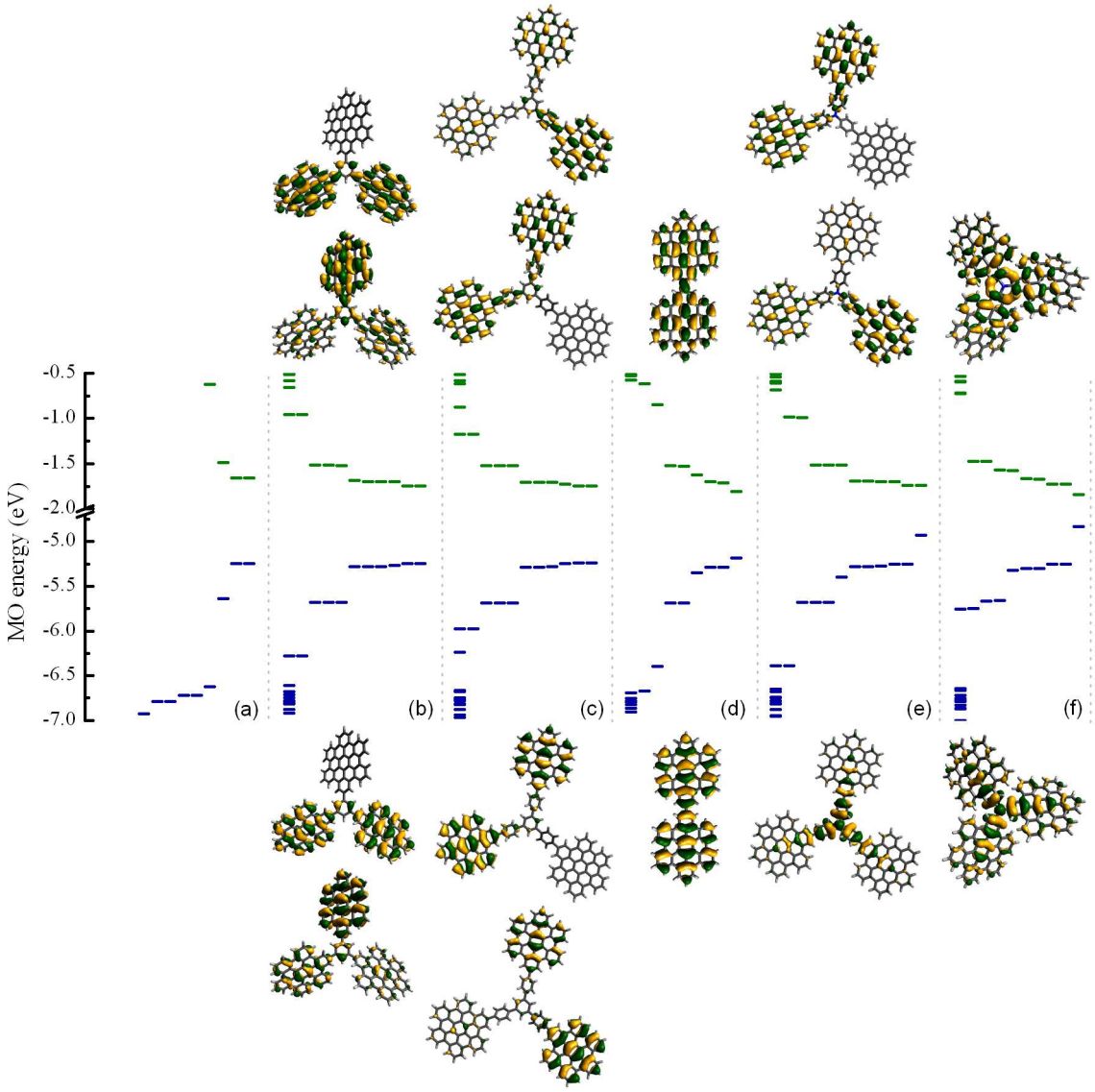

Figure 3.13: Molecular orbital energy levels and HOMO (bottom) and LUMO (top) illustrations of (a) HBC, (b) benzene tri-arm HBC, (c) TPB tri-arm HBC, (d) dumbbell HBC, (e) TPA tri-arm HBC and (f) N tri-arm HBC. The left to right arrangement follows the decrease in the HOMO-LUMO gap. Occupied and unoccupied orbitals are depicted as blue and green lines, respectively.

In the case of "super-molecules" that do not contain nitrogen in their linking unit, an orbital delocalization over HBC cores is evident. On the other hand, nitrogen containing molecules show a HOMO density buildup near the nitrogen atom, a characteristic inherent to the strong electron withdrawing nature of nitrogen, while LUMO levels extend around the central nitrogen atom to the HBC periphery, with a small depletion and a degeneracy lift evident for N-linked tri-arm HBC.

Upon careful investigation, the nine frontier levels near and including the HOMO state of benzene and TPB linked HBC molecules appear to emanate from the HOMO(e1g),

HOMO-1(e1g) and HOMO-2(a1u) states of pristine HBC, as is shown in Figures I.2 and I.3 in the Appendices. The same feature is observed for the nine levels near and including the LUMO state as well, for which the orbital manifold is comprised by the LUMO(e2u), LUMO+1(e2u) and LUMO+2(b1g) states of HBC. The benzene and TPB covalent linkers exhibit strong contributions to the electronic levels situated near -6 eV and -1 eV for the occupied and unoccupied orbitals, respectively.

Another interesting characteristic is associated with the contribution of the TPA LUMO state to the unoccupied orbitals of nitrogen and TPA linked HBC molecules. In the case of nitrogen linked HBC, the LUMO state mimics the spatial features of the "parent" LUMO state of TPA, whereas for TPA-linked HBC, the LUMO states that appear near-degenerate are dominated by contributions from the discotic cores, with the "parent" TPA LUMO state appearing near -0.6 eV. In order to rule out possible exchange-correlation functional artefacts, molecular orbital spatial distributions for the nitrogen and TPA linked HBC "super-molecules" were validated against restricted Hartree-Fock calculations that yielded the same results. All relevant orbital depictions for nitrogen containing tri-arm molecules are included in Figures I.4 and I.5 in the Appendices.

Finally, the HBC dumbbell (Figure I.1) shows a typical orbital geometric layout inherent to the D_2 symmetry point group, with its FMOs constituted by HBC molecular orbitals similarly to benzene and TPB linked HBC molecules but with a 2-fold degeneracy.

DFT calculations regarding neutral "super-molecules" utilizing the PBE0 hybrid functional[286] were also carried out, yielding the same level of FMO degeneracy and identical orbital spatial distributions.

Absolute HOMO and LUMO levels, HOMO-LUMO gaps and electron and hole reorganization energies for all aforementioned molecules are summarized in Table 3.3. Records are listed with a decreasing order with respect to the energy gap.

Table 3.3: FMO energies, HOMO-LUMO gap and reorganization energies of all molecules under study.

Molecule	HOMO (eV)	LUMO (eV)	Gap (eV)	Hole λ (meV)	Electron λ (meV)
Coronene	-5.4602	-1.4252	4.0350	130.06	171.53
HBC	-5.2492	-1.6593	3.5898	98.40	130.57
Benzene-linked tri-arm HBC	-5.2433	-1.7457	3.4976	39.88	56.77
TPB-linked tri-arm HBC	-5.2398	-1.7493	3.4905	32.93	51.31
Dumbbell HBC	-5.1810	-1.8106	3.3704	78.81	112.64
TPA-linked tri-arm HBC	-4.9281	-1.7420	3.1862	66.14	50.61
N-linked tri-arm HBC	-4.8352	-1.8441	2.9911	54.44	92.48
C96	-4.8583	-2.1929	2.6654	60.32	74.24
C132	-4.6192	-2.4846	2.1347	45.63	52.64

Given the fact that the absolute HOMO and LUMO levels of benzene and TPB are

situated at -6.72 eV and 0.07 eV and -6.01 eV and -0.85 eV respectively, FMO energy levels of benzene- and TPB-linked HBC tri-arm "super-molecules" are dominated by the corresponding levels of HBC. This behavior is reversed for TPA-linked HBC for the HOMO state, since TPA's HOMO is at -4.94 eV.

Charge carrier reorganization energies for non-nitrogen containing "super-molecules" and for all planar PAHs under study, alongside values for benzene, naphthalene and a series of *peri*-condensed PAHs of low molecular weight (pyrene, perylene and ovalene) are plotted against the number of atoms of each molecule in Figure 3.14.

For planar PAHs, a decreasing trend with respect to molecular weight is evident. This general trend seems to hold even for non-planar, HBC "super-molecules". An analogous variation of hole reorganization energy with respect to the size of the molecules has been reported in the literature for small, *cata*-condensed PAHs.[171] As far as the covalently linked discotics are concerned, their reorganization energies are expected to be lying at lower levels with respect to pristine HBC, since the covalent linking in the case of the dumbbell molecule and the linking units (benzene and TPB) of tri-arm "super-molecules" facilitate a less cumbersome structural relaxation for the ionic states.

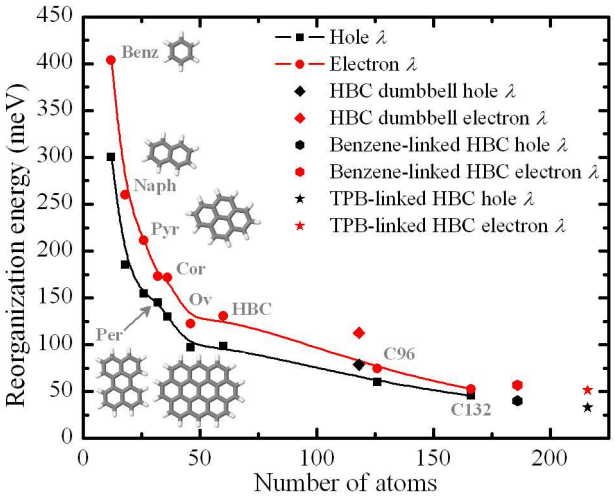

Figure 3.14: Electron and hole reorganization energies of planar PAHs and HBC "super-molecules" with respect to the number of atoms in every molecule. Solid lines correspond to spline interpolations on planar PAH data as a visual aid.

Besides the trend with respect to the core size, another interesting feature resides in the fact that all examined molecules except the TPA-linked discotic are characterized by smaller hole reorganization energies compared to electron reorganization energies, prompting such materials for *p*-type organic electronic applications. For TPA-linked tri-arm HBC, a marginal reversal of the aforementioned behavior is found. Analogous reorganization energy modulations via covalent linking have also been reported in the literature for TPA-substituted anthracene derivatives. The utilization of articulated, aryl-based mono-substitution on TPA is found by Yang *et al.*[324] to lower the $\lambda^{(+)}/\lambda^{(-)}$

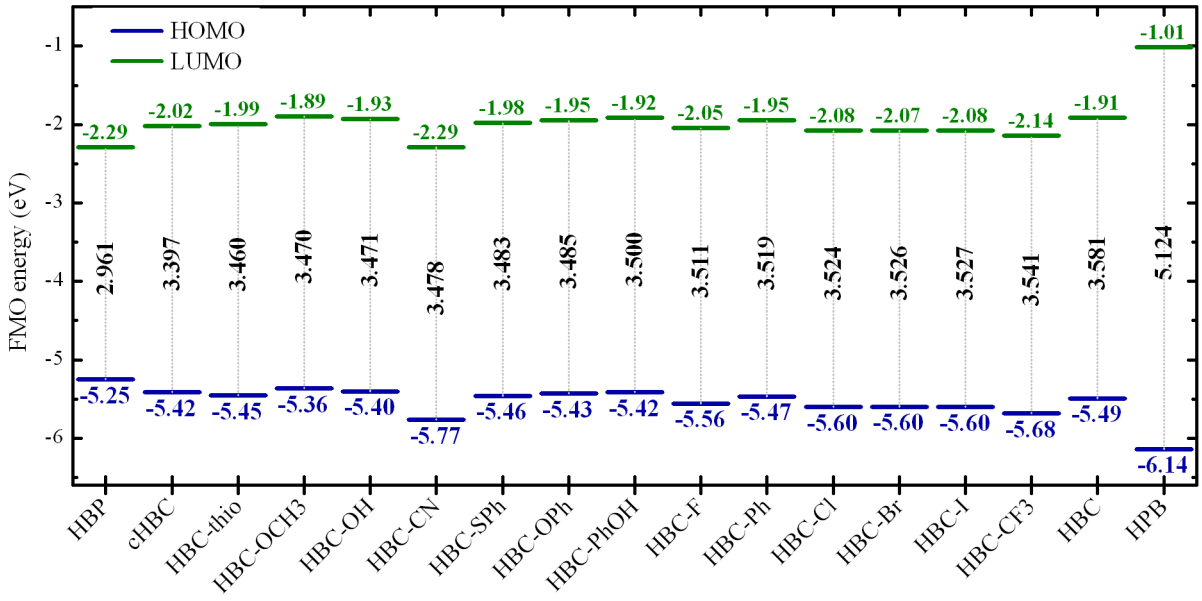

Figure 3.15: FMO energies and HOMO-LUMO gap for mono-substituted HBC cores and selected disk-like molecules. The entries are listed from left to right in an ascending order with respect to the HOMO-LUMO gap.

ratio, without achieving an inversion similar to the one reported in this current study that makes use of rigid HBC discotic cores in a tri-arm fashion.

Another interesting aspect involves the effect of peripheral mono-substitution and core planarization to electronic and single molecule charge transfer properties. Ground state DFT calculations are put to use for the evaluation of FMO energies and HOMO-LUMO gaps, and hole and electron reorganization energies for all single core discotic molecules that result from mono-substitution, also including the two precursor molecules (HPB, HBP) and the contorted variant c-HBC. FMO energy levels and their associated gap are illustrated in Figure 3.15 in an ascending order with respect to the HOMO-LUMO gap.

It turns out that peripheral substitution by means of dipole- and ring-functionalization induces a mild variation to the HOMO-LUMO gap, yielding relatively lower values compared to pristine HBC. Some more pronounced effect is attributed to cyano mono-substitution, since the presence of the NC- group lowers both HOMO and LUMO absolute levels. Of particular importance are the FMO levels of the two precursor molecules, with the HBP and HPB molecules exhibiting the lowest and highest gaps, respectively. Finally, the contorted variant c-HBC shows small deviation in electronic properties compared to the HBC molecule.

Hole and electron reorganization energies are situated at values relatively close to the ones of the reference HBC molecule, except for HPB, due to difficulties related to structural relaxation in the ionic states that are rooted in complex steric hindrance effects. Calculated values are depicted in Figure 3.16. Higher reorganization energies are also registered for the HBP precursor molecule, since the associated relaxation mechanism

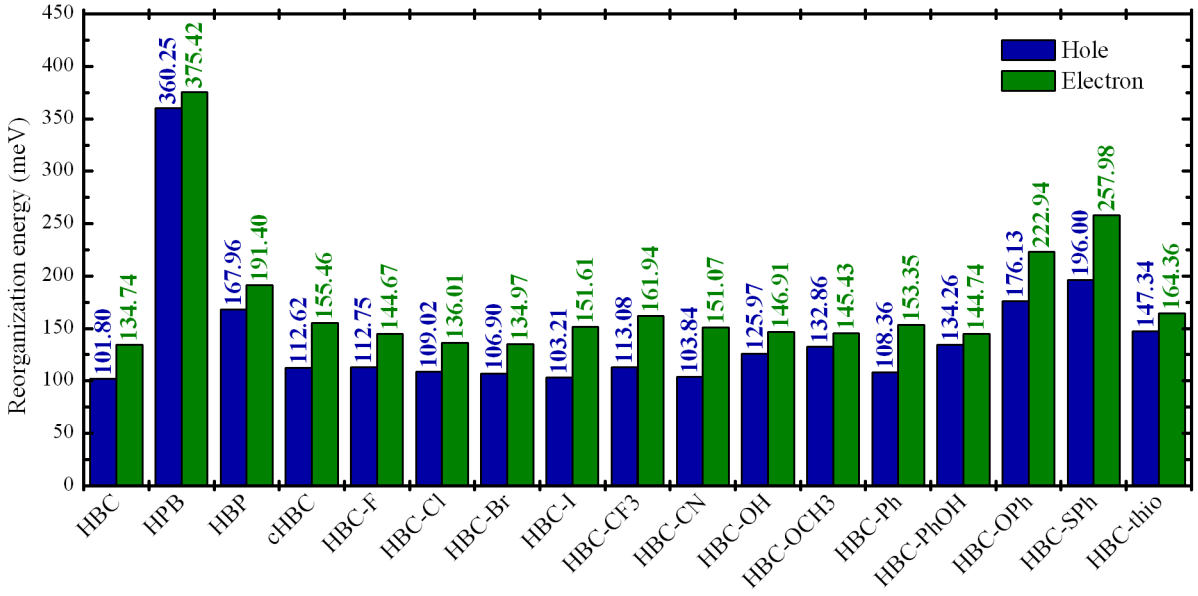

Figure 3.16: Hole and electron reorganization energies for mono-substituted HBC cores and selected disk-like molecules.

involves inner core torsional variations, as it is shown in Figure 3.10. From the mono-substituted HBC variants, the highest λ values belong to the most articulated HBC-OPh and HBC-SPh molecules, and the thiophene-substituted HBC core, in accordance with the ionization structural relaxation analyses previously reported.

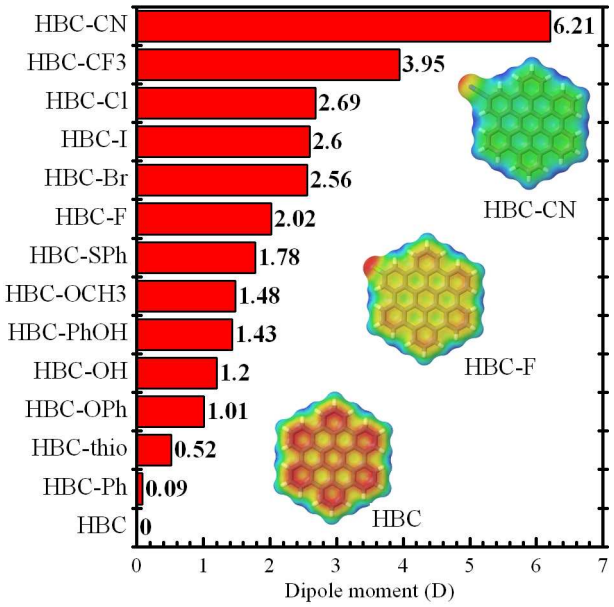

Figure 3.17: Electric dipole moment variations with respect to peripheral functionalization. Inset pictures illustrate charge distribution for selected mesogens.

One of the most important goals of peripheral functionalization with small units capable of creating electronegativity changes is the induction of finite, permanent electric dipole moment to discotic cores. Ground state DFT calculations are utilized for the determination of electric dipole moments. For benchmarking purposes, partially fluorinated versions of the benzene molecule were initially treated. At the B3LYP/6-311G** level

of theory, the calculated values of the molecular dipole moment of fluorobenzene and of the *ortho*, *meta*, and *para* variants of difluorobenzene are 1.52, 2.52, 1.50, and 0.0 D, respectively. Experimental values[325] for the aforementioned dipole moments are reported at 1.66, 2.59, 1.51, and 0.0 D, thus fortifying the validity of the utilized level of theory.

The variation of core electric dipole moment with respect to peripheral substitution is illustrated in Figure 3.17. As expected, the pristine HBC molecule has no dipole moment, as it is expected by the molecular point symmetry. The utilization of dipole- and ring-substitution by means of various atomic and molecular species results in a wide range of induced electric dipole moment, ranging from minuscule charges due to phenyl substitution to drastic alterations for HBC-CN.

Moving on to the last group of molecules under study, the nitrogen-linked star-shaped molecules with discotic terminal units of variable core extent, analogous analyses on the basis of FMO energy levels and charge reorganization energies are carried out, with the results obtained by means of DFT calculations summarized in Figure 3.18.

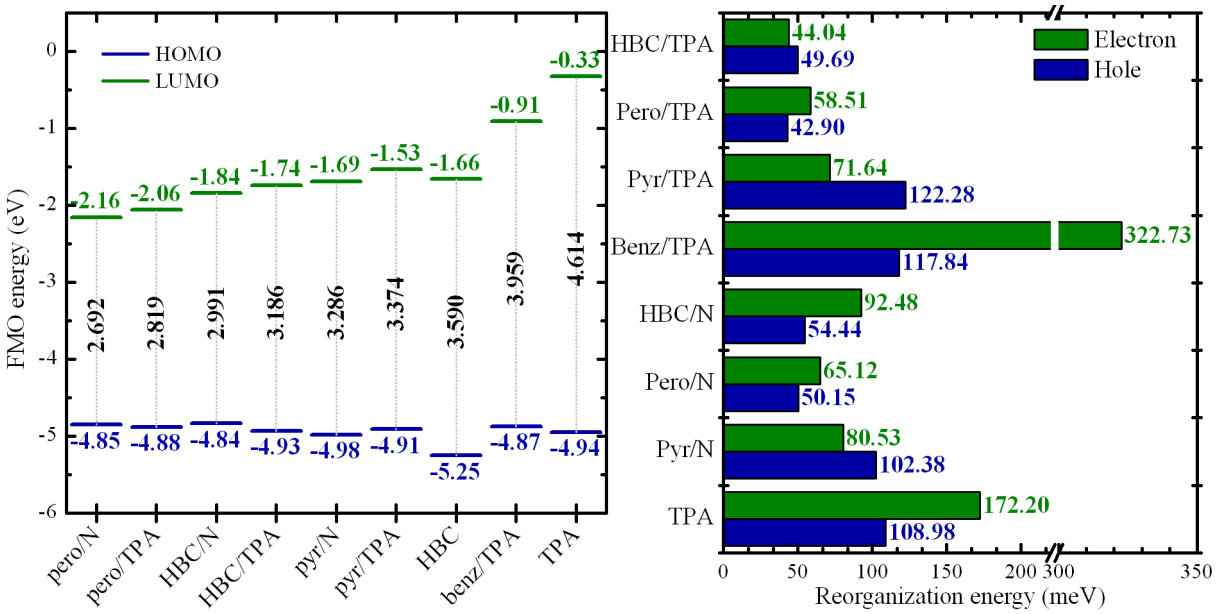

Figure 3.18: FMO energy levels and HOMO-LUMO gap values (left) and charge reorganization energies (right) for nitrogen-containing star-shaped molecules with terminal discotic units.

The utilization of atomic nitrogen or TPA as a central linker for tri-arm geometries with pyrene, peropyrene, and HBC cores enables the synthesis of star-shaped mesogens with variable electronic properties. HOMO-LUMO gap values can be tuned from 2.69 eV in the case of N-linked tri-arm peropyrene molecule to 3.37 eV reported for the TPA-linked tri-arm pyrene molecule. It should be noted that all assemblies carrying terminal discotic groups except benzene are characterized by HOMO absolute levels consistently over the HBC HOMO level, while the associated HOMO-LUMO gap values are all smaller that the one of the reference HBC molecule. The only nitrogen containing star-shaped

molecule showing different electronic properties compared to HBC is the TPA-linked tri-arm benzene mesogen, whose properties are more alike to the TPA "parent" molecule.

As regards charge reorganization energies, no distinctive trend is evident with respect to molecular architecture. Some of the examined molecules exhibit lower reorganization energies compared both to TPA and HBC, also registering selective $\lambda^{(+)}/\lambda^{(-)}$ ratio inversions. Of particular importance is the case of TPA-linked tri-arm benzene, with an electron reorganization energy almost twice that of the linking TPA unit.

3.2.3 Charge Transfer Integrals from Dimer Studies

Hole CTIs are evaluated for molecular dimers of pristine coronene, HBC, C96, and C132 molecules under different geometrical conditions. The most straightforward analysis is linked to the dimer twist angle. Perfectly aligned molecules at a constant vertical distance of 3.6 Å are subjected to twist angle variations by rotating the upper molecule by a prescribed angle about the direction normal to the cores. The dependence of the hole transfer integral on the twist angle is shown in Figure 3.19.

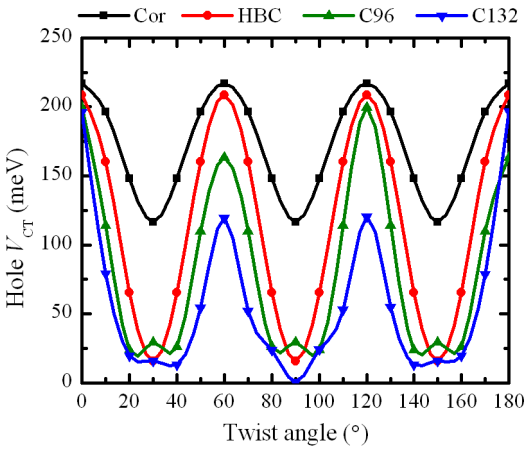

Figure 3.19: Evolution of the hole CTI with respect to dimer twist angle for coronene, HBC, C96 and C132.

The rotational variations for coronene and HBC are in accordance with previously published work[67;216], although absolute values differ slightly due to the utilization of a different basis set and level of theory. All of the examined molecules exhibit large CTI values for graphitic-like AA stacking patterns that are manifested when the twist angle is an integer multiple of 60°. Both HBC and C96 molecules show a CTI minimum threshold near ∼20 meV; this behavior is not observed for C132, since for a twist angle of 90° the transfer integral is effectively diminished to zero.

The next geometric alteration to molecular dimers relies on parallel displacements along molecular high symmetry directions. For coronene, HBC and C96, parallel sliding of the top molecule by a constant step is applied along the so called armchair and zigzag

graphitic directions. Due to the different edge geometry of C132, a total of four high symmetry directions are taken into consideration: two armchair and two zigzag. In the following figures, hole CTIs are plotted with respect to parallel displacements. Dimer geometries that correspond to CTI maxima are also shown, with the armchair and zigzag displaced molecules depicted in black and blue colors for all molecules except C132.

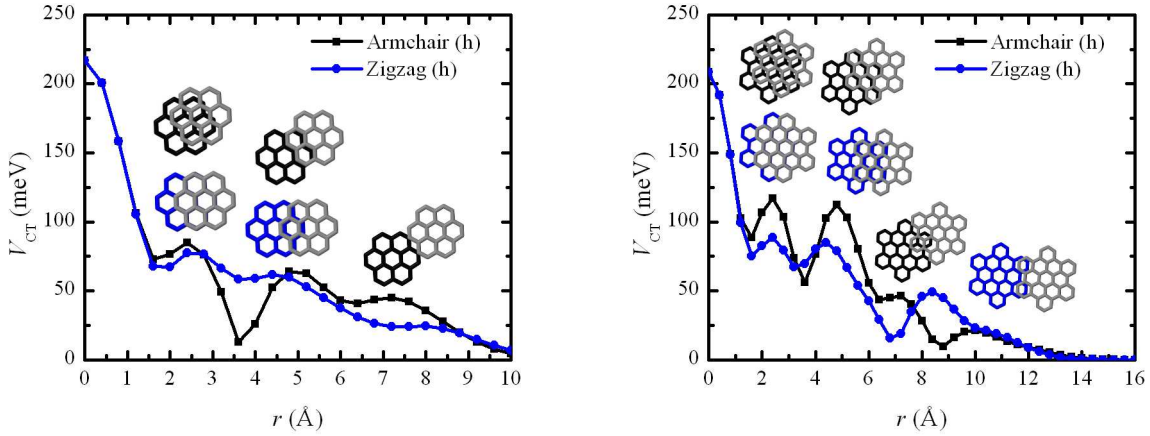

Figure 3.20: Evolution of the hole CTI with respect to parallel displacements for coronene and HBC.

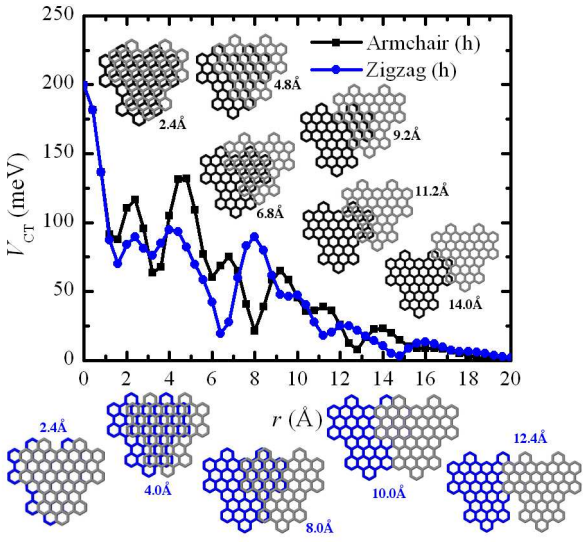

Figure 3.21: Evolution of the hole CTI with respect to parallel displacements for C96.

All discotic molecules exhibit CTI maxima when the applied displacement manages to reproduce a graphitic AA stacking pattern or variants of the so-called AA' stacking pattern [Lee2016]. For C132 molecular dimers, AA' stacking motifs are depicted in detail in Figure 3.22 as insets. It should be noted that manifestations of AB-like graphitic stacking patterns do not generally yield high transfer integral values. This observation

is vividly shown in Figure 3.22 where AB stacking patterns arising when shifting a C132 molecule along an armchair direction are highlighted using discrete red stars.

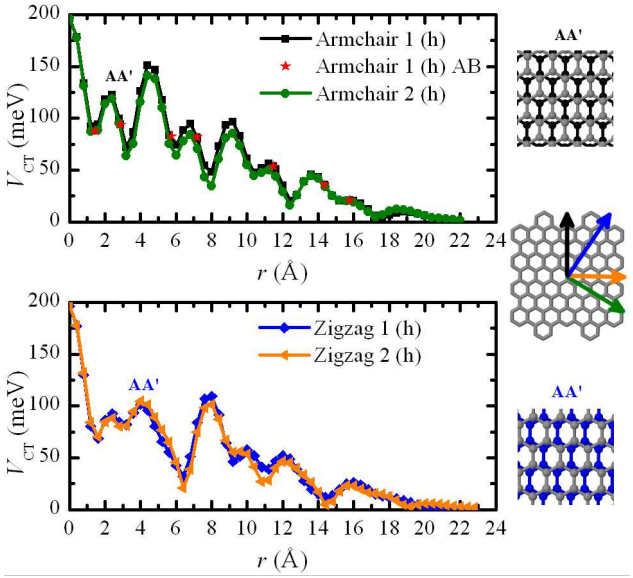

Figure 3.22: Evolution of the hole CTI with respect to parallel displacements for C132. The arrows indicate the different sliding directions. Red stars in the upper diagram correspond to AB stacking patterns. Selected AA' stacking patterns are also highlighted.

Interestingly enough, the sliding direction seems to affect the CTI maxima heights for small displacement values. Although this behavior is quite subtle for coronene, this is not the case for HBC, C96 and C132. These molecular dimers show more pronounced maxima along the armchair displacement direction, registering two major peaks for displacements up to 6 Å, with associated heights over 100 meV.

3.3 Conclusions

Single molecule DFT studies elucidate the effect of discotic core size of planar PAHs on electronic and charge transport properties, with the HOMO-LUMO gap and reorganization energies decreasing as the core size is extended. In the case of HBC "super-molecules", covalent linking of HBC cores has been proven to be an effective way to tune the gap between the values of HBC and C96, also altering the level of degeneracy in the case of the HBC dumbbell and nitrogen containing linkers.

As far as hole and electron reorganization energies are concerned, a monotonic decrease with respect to the number of atoms is found. Moreover, the utilization of articulated covalent linkers is proven to be a promising molecular alteration in order to reduce reorganization energies. A detailed investigation of the geometric relaxation mechanisms for tri-arm mesogens with terminal discotic cores suggests that such molecules respond to

the ionization process by torsional variations, either localized about articulated linking bonds or on the very discotic cores as edge out-of-plane distortions.

In the case of HBC derivatives, peripheral functionalization using specific atomic species and small molecular fragments with notable electronegativity difference compared to sp^2 carbon atoms can serve as a route towards the induction of permanent electric dipole moment to the otherwise non-polar HBC core. A series of substituents are screened, establishing a direct linking between functionalization type and core dipole moment, registering cyano substitution as the most drastic one with an electric dipole moment of 6.21 D. The effect of peripheral mono-substitution on electronic and single molecule charge transfer properties is evaluated, resulting in minimal property alteration, except for the case of articulated side groups that tend to raise charge reorganization energies due to less subtle geometric relaxation mechanisms upon ionization.

Disk-like molecules with morphological differences compared to the celebrated HBC core are also taken into consideration. Two HBC precursor molecules, namely the HPB and HBP mesogens, exhibit differentiated electronic properties, mostly as a result of the different planarization state with respect to HBC. HPB registers the highest charge reorganization energy amongst all molecules under study. On the other hand, the contorted HBC mesogen c-HBC is characterized by slightly elevated charge reorganization energy values compared to HBC while showing a lower HOMO-LUMO gap and completely different charge relaxation mechanisms.

As regards star-shaped, nitrogen-containing mesogens bearing different discotic cores as terminal units, a modulation of FMO energy levels and HOMO-LUMO gap values can be achieved via different molecular architectures. All TPA-based tri-arm molecules exhibit lower hole reorganization energy compared to pristine TPA. This characteristic, combined with the fact that the utilization of larger terminal core segments (pyrene, peropyrene, HBC) provides more potential "active area" for intersite charge hopping, renders such molecules promising candidates for hole-transport organic electronics applications.

At the molecular dimer level, *ab-inito* calculations of CTIs for the coronene, HBC, C96, and C132 molecules with respect to core twist angle exhibit maxima at graphitic-like stacking. For the C132 mesogen, a global minimum at a twist angle of 90° at which CTI drops to zero is identified, exposing a highly "unwanted" dimer configuration for charge transport calculations. Studies based on parallel displacements along high symmetry directions return non-zero CTI values even for dimer configurations with minimum overlap and pronounced maxima at AA and AA' stacking patterns in the case of significant geometric overlap.

Chapter 4

Molecular Simulations of Alkyl Substituted HBC Molecular Crystals

This chapter contains empirical MD simulation results regarding molecular crystals comprised of alkyl-substituted HBC mesogens. Soluble, with all side chains present, and mono-substituted systems derived by replacing a single side chain with a hydrogen or iodine atom are modeled, with variable side chain length. Structural, mechanical, and dynamical properties at thermodynamic equilibrium are presented and discussed in detail.

4.1 Systems of Interest and Computational Details

4.1.1 Preliminaries

This chapter is focused on empirical MD simulations of pristine HBC molecular crystals with dodecane (HBC-C12), decane (HBC-C10) and octane (HBC-C8) peripheral aliphatic chains, and mono-substituted mesogens produced by replacing a side chain with a hydrogen or iodine atom (HBC-X-Cn where X = H,I and n = 12,10,8).

MD simulations are employed in order to equilibrate the model systems and study their structural, mechanical, and dynamical properties. Calculations in the isothermal-isostress statistical ensemble are carried out by means of the extended ensemble method utilizing the MTK EoMs[317] using a time constant of 100 fs for temperature control and 2500 fs for pressure control. A time step of 1 fs is used for all simulations and typical periodic boundary conditions are applied in every direction, simulating the systems in their bulk phase.

In order to correctly take into consideration the full effect of long-range forces, non-bonded interactions are calculated using mesh-based techniques. For the mesh-based calculations, the PPPM method is used for the evaluation of electrostatic and LJ interactions in reciprocal space with a force tolerance of 10^{-4} kcal mol^{-1} Å^{-1} and a cutoff of 10 Å.[306;326] All atomistic MD calculations were performed using the LAMMPS simulation

package.[318]

4.1.2 Force Field

As far as the FF is concerned, bonded interactions are modeled by a compilation of the Generalized Amber Force Field (GAFF)[327] and Optimized Potential for Liquid Simulations (OPLS)[328;329] FFs, together with a proper dihedral energy term proposed by Marcon *et al.*[195] in order to account for the tendency of the side chains to arrange themselves in a perpendicular manner with respect to the polyaromatic cores. Atoms belonging to the polyaromatic cores are treated fully atomistically, while the atoms of the side chains are treated using a united atom representation, where the -CH_2- and terminal -CH_3 groups are treated as superatoms, with the hydrogen atoms absorbed into the carbons. A depiction of the different atom types used in the simulations is shown in Figure 4.1.

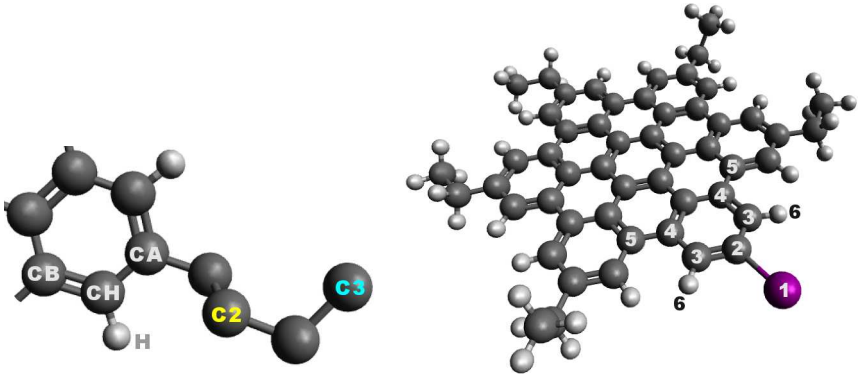

Figure 4.1: Major atom types in all simulations (left) along with the additional charge sites of the alkyl-substituted HBC-I molecule (right).

As far as the labelling is concerned, CB stands for body aromatic carbon atoms that belong to the inner part of the core, CH are the peripheral aromatic carbons that are bonded to hydrogen atoms, CA are the linking aromatic carbon atoms where the aliphatic chains are grafted, C2 correspond to the -CH_2- atomic groups and C3 to the terminal -CH_3 groups.

The non-bonded interactions, namely the electrostatic and vdW forces, are modeled through the Coulomb and LJ potentials, respectively, excluding from the calculations particles separated by up to three bonds. The partial charges are extracted from semi-empirical quantum chemical NDDO calculations through a Mulliken population analysis method using the PM7 Hamiltonian as it is incorporated in the MOPAC package.[330] The LJ parameters are taken from the OPLS FF.[328;329] As far as the combining rules are concerned, in the case of ε_{ij} and σ_{ij}, the geometric and arithmetic mean values are taken, respectively.

Simulations of the crystalline phases are carried out at a temperature of 300 K and pressure of 1 atm, while the liquid-crystalline phases are examined at 400 K and 1 atm.

The FF is generally described by Equation 4.1, where the primed dihedral angles refer to the term introduced by Marcon *et al.*[195] with the parameterization $V_1 = -0.01$, $V_2 = 2.26$, $V_3 = 0.11$, $V_4 = -1.23$, $V_5 = 0.11$, and $V_6 = 0.0$, all expressed in kcal mol^{-1}. The remaining FF parameters are listed in Table 4.1.

$$E = \sum_{\text{bonds}} k_\text{b} \left(r - r_0\right)^2 + \sum_{\text{angles}} k_\text{a} \left(\theta - \theta_0\right)^2 + \sum_{\text{dihedrals}} \sum_{n=1}^{3} \frac{V_n}{2} \left[1 + (-1)^n \cos\left(n\varphi\right)\right] + \\ + \sum_{\text{dihedrals}'} \sum_{n=1}^{6} V_n \cos^n \varphi + \sum_{i<j} \left\{ \frac{1}{4\pi\varepsilon_0} \frac{q_i q_j}{r_{ij}} + 4\varepsilon_{ij} \left[\left(\frac{\sigma_{ij}}{r_{ij}}\right)^{12} - \left(\frac{\sigma_{ij}}{r_{ij}}\right)^{6} \right] \right\} \tag{4.1}$$

Table 4.1: Force field parameters for bonded and non-bonded interactions pertinent to alkyl-functionalized nanographene molecules.

Bond	k_b[†]	r_0 (Å)
$C_{ar} - C_{ar}$	478.4	1.387
$C_{ar} - H$	344.3	1.087
$C_{ar} - C_3$	323.5	1.513
$C_3 - C_3$	303.1	1.535
$C_{ar} - I$	252.4	2.095

Angle	k_a[§]	θ_0 (°)
$C_{ar} - C_{ar} - C_{ar}$	67.2	119.97
$C_{ar} - C_{ar} - H$	48.5	120.01
$C_{ar} - C_{ar} - C_3$	63.8	120.63
$C_{ar} - C_3 - C_3$	62.5	114.61
$C_3 - C_3 - C_3$	63.2	110.63
$C_{ar} - C_{ar} - I$	58.6	118.47

[†]: kcal mol^{-1} Å^{-2}
[§]: kcal mol^{-1} rad^{-2}

Torsion	V_1[¤]	V_2	V_3
$X - C_{ar} - C_{ar} - X$	0.00	7.25	0.00
$C_{ar} - C_3 - C_3 - C_3$	1.41	-0.27	3.14
$C_3 - C_3 - C_3 - C_3$	1.41	-0.27	3.14

Atom type	ε[¤]	σ(Å)	m (amu)
CB	0.070	3.550	12.011
CH	0.070	3.550	12.011
CA	0.070	3.550	12.011
H	0.030	2.420	1.008
C2	0.118	3.905	14.027
C3	0.175	3.905	15.035
I	0.400	4.187	126.904

[¤]: kcal mol^{-1}

Table 4.2: Partial charges for the simulation of iodine substituted HBC mesogens. For the numbering, see Figure 4.1.

Atom type	Charge (e)	Atom type	Charge (e)
I(1)	-0.043850	CB(5)	+0.015348
C(2)	-0.018750	H(6)	+0.168647
CH(3)	-0.172300	CH	-0.148150
CB(4)	-0.007550	H	+0.153578

As regards the nomenclature in Table 4.1, aromatic carbon atoms are labelled as C_{ar} and correspond to the CB, CH, and CA atom types, whereas aliphatic carbon atoms are labelled as C_3 and correspond to the C2 and C3 atom types.

In the case of the HBC, HBC-C12 and HBC-H-C12 systems, partial charges are situated only on the periphery of the mesogens, with the atom types CH and H having charge values $q_{\mathrm{CH}} = -0.151$ and $q_{\mathrm{H}} = +0.151$, respectively. In order to reproduce the electric dipole moment of the HBC-I-C12 mesogen, additional charged sites are needed. The position of the charged sites is depicted in Figure 4.1 and their values are listed in Table 4.2.

4.1.3 Initial Configurations

Regarding the initial configurations, a simple stacking of HBC-C12 mesogens followed by an arrangement on a two-dimensional lattice does not lead to the desired herringbone crystal, since a special interdigitation of the side chains is needed in order to create a stable, tilted pattern in accordance to experimental structural data.[15] If the side chains retain an all-*trans* conformation while forming a dihedral angle of $\pm 90^{\circ}$ with respect to the molecular cores, an orthogonal arrangement is not likely; their mutual repulsion, together with their thermal motion leads to a tetragonal two-dimensional lattice. Therefore, certain side chains need to adopt a mixed *trans-gauche* conformation, forming folded cilia, lodged between the remaining all-trans side chains and the pillars of tilted cores. In this way, the lattice spacings of the simulated molecular crystal can be in fair agreement with the experimental ones.

It is clear that a simple crystallographic construction of the initial lattice is out of the question, since it would lead to serious overlaps between the side chains and the polyaromatic cores of the mesogens. In order to overcome this obstacle, the following strategy has been devised and implemented: following the work of Carminatti *et al.*[25], we create in a crystallographic manner an orthorhombic lattice of tilted molecules that resembles a herringbone molecular crystal, initially disregarding the unavoidable overlaps. The basis molecule is an HBC-C12 mesogen brought to a "chair" geometry: all side chains are transplanar with respect to the molecular core, with three adjacent chains pointing upwards and the remaining three pointing downwards. Then, we equilibrate the system statically, using the conjugate-gradient method. If the minimization were carried out in the traditional manner, the overlaps would dislodge the molecules from their columns, leading to a severe deviation from the herringbone phase, with the mesogens losing their tilt and forming random aggregates.

By following an adiabatic approximation wherein the atoms belonging to the molecular cores are assigned a zero total force, the columns remain intact and the side chains adapt to such an environment. This process, followed by an also adiabatic finite temperature MD simulation in the isothermal-isostress ensemble, leads to the formation of herringbone molecular crystals that remain stable at room temperature when all atoms are finally treated in a Newtonian manner (i.e., the adiabatic constraint is lifted). The key concept

of the whole procedure is to keep the molecular cores totally frozen during the energy minimization but allow them to follow the supercell's expansion and contraction during the isothermal-isostress MD run. This is accomplished in a MD simulation by simply zeroing the total force acting on each of the core particles.

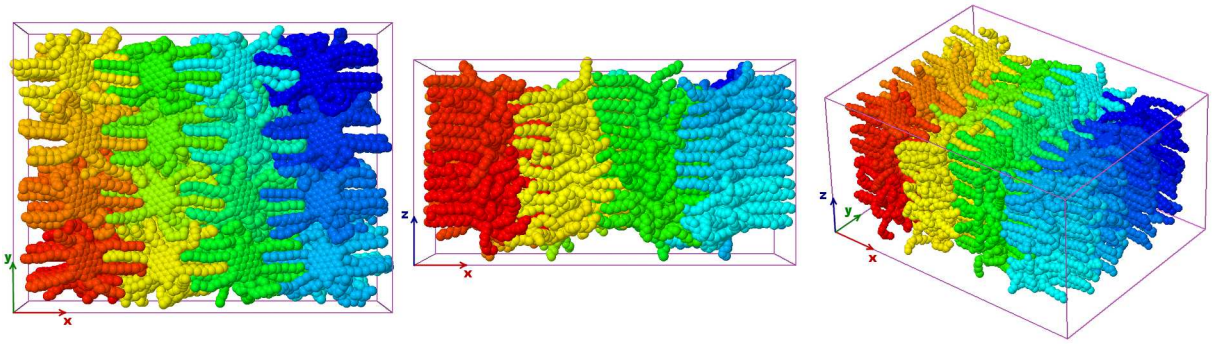

Figure 4.2: Top, side, and perspective view of a HBC-C12 herringbone molecular crystal at 300 K and 1 atm.

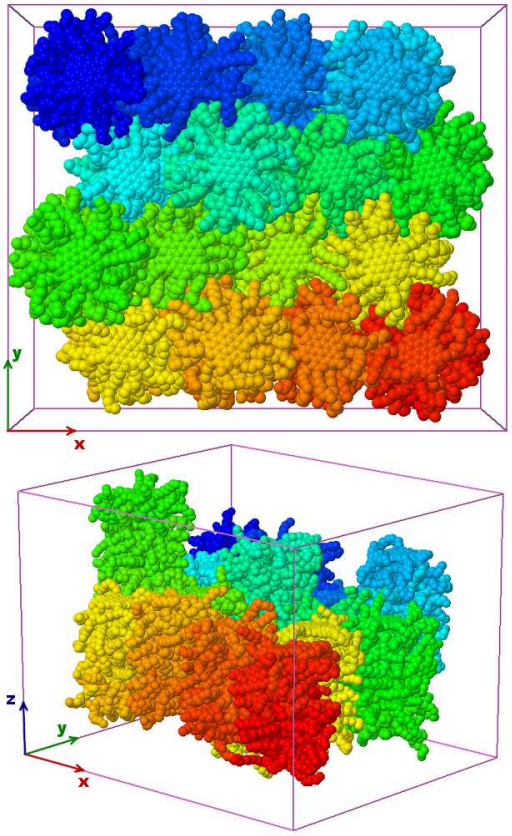

Figure 4.3: Top and perspective view of a HBC–C12 hexagonal liquid crystal at 400 K and 1 atm. The snapshot shown was obtained after 30 ns of MD simulation starting from a configuration contained in a rectangular box. The columnar *en-masse* diffusion along the stacking direction is evident.

Utilizing the methodology outlined above, herringbone molecular crystals of the HBC-C12 mesogen comprised of 192 molecules are created and equilibrated at a temperature of 300 K and pressure of 1 atm in the isothermal-isostress ensemble for approximately 50 ns. The resulting stable structures (Figure 4.2) are used as reference states for the creation

of the dipole substituted HBC-H-Cn and HBC-I-Cn (n = 8,10,12) molecular crystals by replacing a whole side chain with a hydrogen or iodine atom, respectively, in a random manner. The hexagonal liquid-crystalline phases of the pristine and mono-substituted systems are obtained by introducing a step change in the temperature of the crystalline structures at a value near the transition temperature of 400 K. In Figure 4.3, a hexagonal liquid crystal of the HBC-C12 mesogen is shown, where the bottom view depicts clearly the single file diffusion of each column.

4.1.4 Properties Under Study

Structural Properties

The structural characterization of the systems under study is accomplished by two complementary methods: via typical molecular radial distribution functions and through theoretical X-ray diffraction (XRD) spectra.

The XRD spectra are calculated using periodically wrapped atomic coordinates, scaled with respect to the three orthogonal vectors $\vec{a}$, $\vec{b}$, $\vec{c}$ that define the supercell of the simulation. If x'_j, y'_j, z'_j are the fractional coordinates and $\vec{a}^*$, $\vec{b}^*$, $\vec{c}^*$ the associated lattice vectors that span the reciprocal space, the following equations hold for the position vector $\vec{r}_j$ of an atom j and the position vector $\vec{s}_{hkl}$ of a (hkl) node of a mesh point in the reciprocal space:

$$\begin{aligned} \vec{r}_j &= x'_j\vec{a} + y'_j\vec{b} + z'_j\vec{c} \\ \vec{s}_{hkl} &= h\vec{a}^* + k\vec{b}^* + l\vec{c}^* \end{aligned} \tag{4.2}$$

The structure factor associated with a certain (hkl) node is expressed as

$$F_{hkl} = \sum_j f_j\left(\vec{s}_{hkl}\right) \exp\left(-2\pi \mathrm{i} \vec{r}_j \cdot \vec{s}_{hkl}\right) \tag{4.3}$$

where $f_j\left(\vec{s}_{hkl}\right)$ are the atomic form factors.[331;332] The intensity of the XRD scattering spectrum for a given inverse distance s is analogous to the square of the norm of the structure factor

$$I_{hkl}\left(s\right) \propto \left|F_{hkl}\left(s\right)\right|^2 \tag{4.4}$$

All XRD spectra are calculated as time averages from successive simulation snapshots, integrating in this way the effect of thermal motion without having to resort to Debye thermal corrections.

Additional structural information is gained through monitoring two specific vectors associated with every mesogen. These are (i) a vector perpendicular to the core, which provides information about the tilt angle of the molecules with respect to a given direction;

and (ii) a vector coplanar with the core, connecting two diametrically opposed aromatic carbon atoms to which aliphatic side chains are grafted, which gives information about possible rotations about the respective columnar axis. Coplanar vectors are also used in order to calculate the core twist angle between neighboring mesogens in pairs.

Moreover, given an assembly of molecular wires comprised of functionalized discotic mesogens, the intracolumnar molecular alignment is examined through a so-called orthogonal distance regression (ODR) line method: once PAH centers of mass (CoMs) are calculated for each column, the ODR method returns a line that contains the CoM centroid and describes in the most optimal fashion the spatial distribution of all columnar CoMs, defining this way a CoM director $\hat{n}_{\mathrm{CoM}}$ for every molecular pillar. Thee-dimensional ODR geometric analyses are presented in detail in the Appendices.

As far as the structural properties of the aliphatic nanophase are concerned, the conformation of the peripheral side chains is studied through the calculation of the proper dihedral angles formed by their superatoms. Moreover, the orientational characteristics of side chain end-to-end vectors $\vec{R}_{\mathrm{e}}$ are examined through their definition for every side chain by calculating the vector that connects the linking PAH atom and the terminal -CH_3 unit.

For the determination of side chain orientation, the following geometrical analysis is carried out. For every column, the CoM director $\hat{n}_{\mathrm{CoM}}$ is used to define an axial direction vector $\hat{z}_{\mathrm{e}}$. We then define a radial direction vector $\hat{y}_{\mathrm{e}}$ that emanates in a perpendicular manner from the ODR line and points to the linking core atom from from which the side chain under study protrudes. Lastly, the cross product of the latter two vectors defines the tangential to the columnar pillar vector $\hat{x}_{\mathrm{e}}$. All three vectors define a local tangential Cartesian system that is centered on each linking carbon atom and can be used to evaluate the two spherical angles capable of describing the orientation of each $\vec{R}_{\mathrm{e}}$ vector: the azimuthal angle θ belonging in the $x_{\mathrm{e}} - y_{\mathrm{e}}$ plane and formed by the projection of $\vec{R}_{\mathrm{e}}$ on this plane and the vector $\hat{x}_{\mathrm{e}}$, and the polar angle φ that is formed by Re and $\hat{z}_{\mathrm{e}}$. A graphical depiction of the aforementioned coordinates system can be found in Figure 4.4.

Mechanical Properties

The mechanical response of the systems is probed via constant stress MD simulations in the isothermal-isostress statistical ensemble. The normal stress components P_{xx}, P_{yy}, and P_{zz} are controlled by means of a MTK barostat in an anisotropic manner, allowing the simulation box to respond with a different rate along each direction while maintaining the supercell's orthogonality. The thermostat and barostat time constants are the same as in the equilibration procedure.

The methodology for the application of compressive and tensile stress to each system is

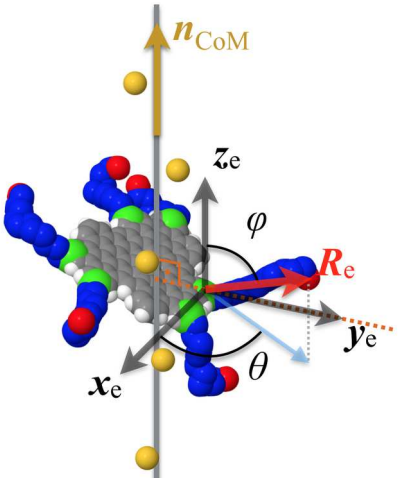

Figure 4.4: Graphical depiction of the local tangential Cartesian system used to quantify the orientational profile of side chain end-to-end vectors.

as follows: well-equilibrated configurations are subjected to an ascending (descending for the case of tensile stress) ladder-like pressure profile over time, with a ramping interval of duration t_r and a plateau of constant pressure of duration t_p. The plateau regions provide the necessary intervals for averaging structural and thermodynamic properties of the stressed systems. By accumulating and averaging both pressure and volume along the aforementioned plateaus, characteristic stress-strain $P(V)$ curves are drawn, through which a numerical estimation of bulk moduli is obtained.

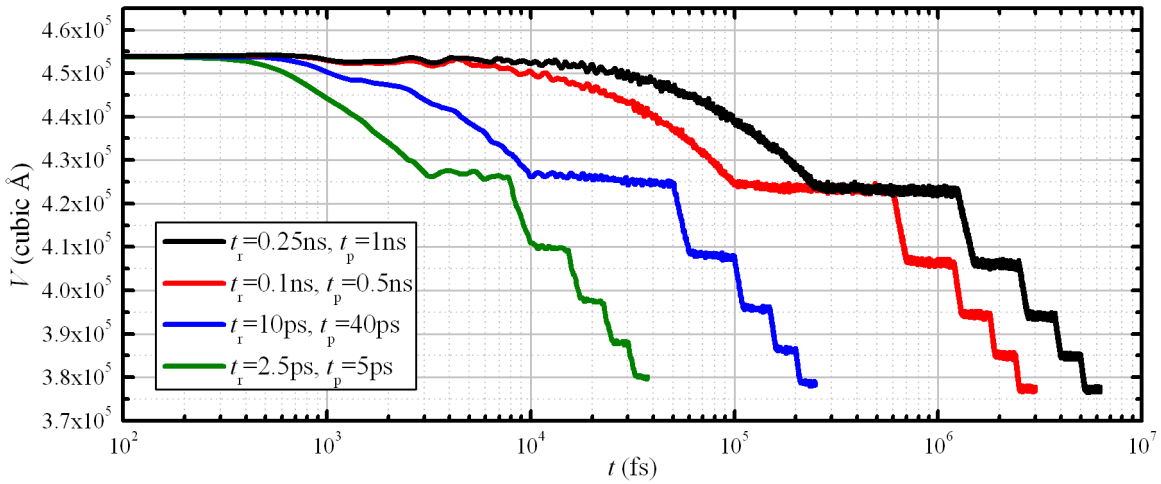

Figure 4.5: Convergence analysis of the impact of time constants t_r and t_p on the resulting volume of the HBC-C12 system at 300 K when applying five successive compressive pressure plateaus of 4, 8, 12, 16, and 20 katm.

The utilization of mesh-based techniques for the calculation of non-bonded interactions eliminates the need for tail corrections to the pressure, a procedure that is not accessible in an analytic manner for the anisotropic systems under study. Due to the dynamic nature of the virtual stress-strain experiments, a convergence analysis for the determination of suitable time intervals is required. In Figure 4.5, the results of such an analysis are depicted for the HBC-C12 crystalline system. Based on this analysis, the

time intervals are set to 0.1 ns and 0.5 ns for t_{r} and t_{p} for all calculations.

Complementary to the stress-strain calculations described above, the strain fluctuation theory is implemented for the determination of the full compliance tensor.[333;334] Zero stress simulations in the isothermal-isostress statistical ensemble are carried out, using a fully flexible triclinic simulation cell. The isothermal compliance tensor elements are calculated according to the following equation:

$$S_{ijkl}^{T} = \frac{V_0}{k_{\mathrm{B}}T}\left(\langle \eta_{ij}\eta_{kl}\rangle_t - \langle \eta_{ij}\rangle_t \langle \eta_{kl}\rangle_t\right) \tag{4.5}$$

where V_0 is the average system volume at zero stress conditions and η_{ij} the strain matrix element with respect to a zero stress average cell shape. The strain matrix is expressed as

$$\boldsymbol{\eta} = \frac{1}{2}\left(\tilde{\mathbf{h}}_0^{-1}\tilde{\mathbf{h}}\mathbf{h}\mathbf{h}_0^{-1} - \mathbf{I}\right) \tag{4.6}$$

with the tilde corresponding to the transpose matrix and $\mathbf{h}_0$ and $\mathbf{h}$ the reference and instantaneous cell shape matrices, respectively. The singular 9×9 compliance matrix obtained is transformed to a non-singular 6×6 matrix by applying the Voigt convention.[335] From the new matrix, the isothermal elastic constants are calculated by a simple matrix inversion.

It should be noted that the complete elastic behavior can be quantified directly also through the 6×6 compliance matrix, without having to calculate the inverse matrix; the bulk modulus B is expressed as the sum of the upper 3×3 submatrix elements[335]

$$B = S_{11} + S_{22} + S_{33} + 2\left(S_{12} + S_{23} + S_{31}\right) \tag{4.7}$$

and a measure of the shear modulus G_{R} is accessible via the so-called Reuss averaging[336] according to the expression

$$G_{\mathrm{R}} = 15 \times \left[4\left(S_{11} + S_{22} + S_{33}\right) - 4\left(S_{12} + S_{23} + S_{31}\right) + 3\left(S_{44} + S_{55} + S_{66}\right)\right]^{-1} \tag{4.8}$$

Dynamical Properties

A good measure of the manifestation of liquid-crystalline behavior is the mean square displacement (MSD) of the center of mass of the mesogens. In order to examine the appearance of liquid-crystalline phases and, generally, to estimate the mobility of the systems, the MSD is calculated as a function of time according to the equation

$$g_{\mathrm{CoM}}(t) = \frac{1}{N}\sum_{i=1}^{N}\left[\vec{r}_{\mathrm{CoM}}^{\,(i)}(t) - \vec{r}_{\mathrm{CoM}}^{\,(i)}(0)\right]^2 \tag{4.9}$$

where $\vec{r}_{\mathrm{CoM}}^{(i)}(t)$ corresponds to the position vector of the CoM of molecule i at a given time t.

Further information concerning the dynamical behavior of the systems is extracted through the study of the time correlation of the perpendicular and coplanar core vectors via the second-order Legendre polynomial autocorrelation function (ACF)

$$P_2(t) = \frac{3}{2}\left\langle \cos^2\theta(t) \right\rangle - \frac{1}{2} \tag{4.10}$$

where $\theta(t)$ is the angle formed between a vector at time 0 and the same vector at time t and the angular brackets $\langle \cdots \rangle$ correspond to an average over all vectors of the same type.

The autocorrelation functions of the perpendicular and coplanar vectors are a measure of disc mobility. Similar analyses are carried out for the end-to-end vector of each aliphatic side chain that joins the anchoring aromatic carbon atom and the terminal -CH_3 group. Decorrelation of this vector is considered as a measure of side chain mobility. All autocorrelation functions are calculated using a multiple time origin scheme[303], in order to obtain as complete as possible a picture of the dynamical phenomena.

4.2 Results and Discussion

4.2.1 Structural Properties

The utilized force field yields a stable herringbone crystalline phase at 300 K and 1 atm, with a distinctive tilt of ∼30° with respect to the columnar direction (parallel to the z-axis). Upon heating, the molecular crystals lose the initial herringbone pattern and gradually transform to a hexagonal liquid-crystalline phase, with the mesogens being parallel to the x-y plane.

MD simulations are able to predict the melting to the liquid-crystalline state, in agreement with similar computational work in the literature.[195] Unfortunately, the method fails to describe the reverse phenomenon of crystallization below the transition temperature; the time scale of the atomistic MD simulation is apparently too short to sample the rare cooperative events whereby nucleation of the solid phase from the liquid crystal takes place.

In Figure 4.6, two characteristic theoretical XRD spectra are shown at equilibrium for the HBC-H-C10 system. The vertical dotted lines point to the (100), (110), (200) and (001) reflections of a hexagonal lattice and the five peaks before 0.15 $Å^{-1}$ belonging to the Cr spectrum correspond to the (100), (010), (110), (200) and (210) reflections of an orthogonal lattice. The arrow highlights the so-called alkyl chain halo of the spectra, which is attributed to the contribution of the amorphous-like aliphatic nanophase. It should be noted that the room temperature spectrum shows additional features near

the end of the alkyl chain halo due to the highly ordered and well-interdigitated side chains. This behavior is absent in systems at high temperature, since this particular spatial correlation vanishes because of the general disorder of the side chains.

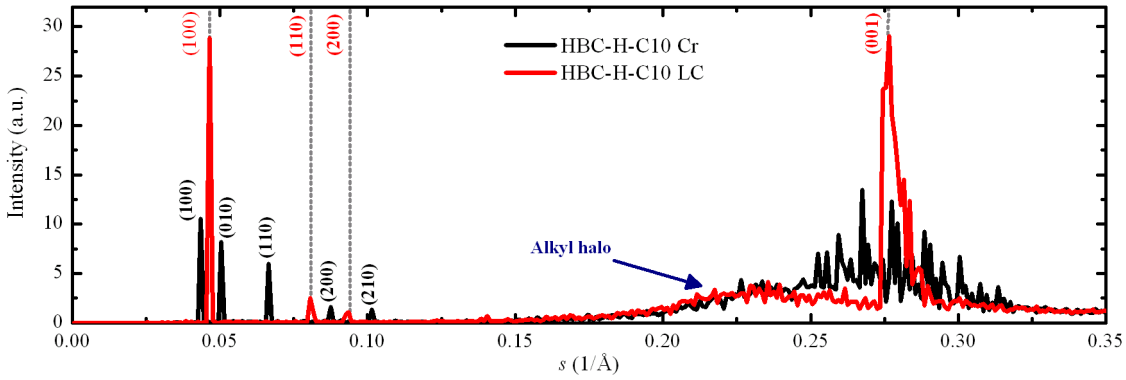

Figure 4.6: Theoretical XRD spectra of the orthogonal crystalline (Cr) and hexagonal liquid-crystalline (LC) phase of the HBC-H-C10 molecular crystal at 300 K and 400 K under 1 atm.

The lattice parameters and other structural data for the dodecane grafted systems are reported in Table 4.3 and for the decane and octane grafted, pristine and mono-substituted systems, in Table 4.4. The distance d corresponds to the vertical core-to-core separation of the mesogens and is calculated geometrically, taking into account the mean tilt angle ω and separation of the molecules' centers of mass along the columnar direction. A distribution of the latter is depicted in Figure 4.7 for the crystalline phase of the HBC-C12 system, where a broadening of the line shapes due to the substitution is evident.

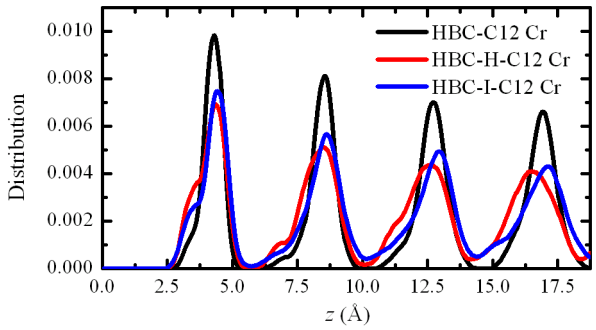

Figure 4.7: Distribution of the separation of molecular centers of mass along the columnar direction for pristine and mono-substituted HBC-C12 crystals at 300 K and 1 atm.

Apart from the broadening of the curves about the maximum values, a relative shift is present, which is also attributable to the substitution: hydrogen substituted mesogens are packed more closely than iodine substituted mesogens due to the massive presence of the iodine atom that pushes the cores farther away. The theoretical structural data are in fair agreement with the available experimental data, especially in the case of the hexagonal liquid-crystalline phases, a behavior that was to be expected, since the FF terms associated with the side chains were fitted in the literature to melt-like systems[328;329], similar to the liquid-crystalline phase of the systems under study.

Table 4.3: Structural parameters of pristine, mono-hydrogen and mono-iodine HBC-C12 crystals of orthogonal and hexagonal symmetry. The bold entries correspond to experimental values.

	300 K/ 1 atm					400 K/ 1 atm	
System	a (Å)	b (Å)	γ (°)	ω (°)	d (Å)	a (Å)	c (Å)
HBC-C12	27.25	20.50	90.00	31.19	3.63	28.30	3.60
Exp. value[15]	**30.50**	**23.80**	**90.00**	**30.00**		**28.60**	**3.50**
HBC-H-C12	25.25	20.20	90.00	28.83	3.71	26.80	3.60
Exp. value[40]				**30.00**		**27.00**	**3.65**
HBC-I-C12	25.20	20.10	90.00	30.86	3.72	27.00	3.58
Exp. value[39;40]	**25.20**	**17.80**	**85.00**	**30.00**		**28.00**	**3.56**

Table 4.4: Structural parameters of pristine, mono-hydrogen and mono-iodine HBC-C10 and HBC-C8 crystals of orthogonal and hexagonal symmetry.

	300 K/ 1 atm					400 K/ 1 atm	
System	a (Å)	b (Å)	γ (°)	ω (°)	d (Å)	a (Å)	c (Å)
HBC-C8	20.70	19.70	90.00	35.89	3.66	25.00	3.60
HBC-C10	24.20	20.20	90.00	33.16	3.62	27.20	3.60
HBC-H-C8	20.50	20.50	90.00	23.21	3.56	23.00	3.62
HBC-H-C10	22.90	19.80	90.00	27.98	3.72	24.80	3.62
HBC-I-C8	20.50	19.80	90.00	27.98	3.74	23.50	3.59
HBC-I-C10	22.55	20.10	90.00	30.40	3.70	25.20	3.60

As far as core twist angles are concerned, for HBC-C12 molecular crystals at room temperature, the distribution of the twist angle of neighboring mesogens exhibits two peaks; a major peak near 4°, which corresponds to molecules primarily with graphitic-like stacking patterns, and a minor diffuse peak near 25°, in which molecules form a "daisy-like" stacking motif. Upon reaching the temperature of 400 K, the crystals melt to a liquid-crystalline state, with the molecular wires forming a hexagonal lattice. The mesogens lose their tilt and the twist angle between neighboring molecules exhibits one single peak around 30°, eliminating the graphitic-like stacking pattern motifs. Twist angle distributions for both temperatures are depicted in Figure 4.8, along with an inset illustrating the "daisy-like" stacking pattern inherent to the liquid-crystalline phase.

In order to obtain a quantitative picture regarding stacking patterns from equilibrium MD simulations, the following two-step analysis is carried out. Given a first-neighboring discotic pair made up by a "lower" and "upper" disc, a projection of the upper CoM to the core plane of the lower core takes place, hence quantifying their relative position, provided that all PAHs belonging to the same column are more or less situated in a parallel fashion. For the consistency of the geometric calculations, the lower CoM is placed on the origin of a two-dimensional Cartesian coordinates system. Then, for each pair, the twist angle is recorded as the angle formed by the associated coplanar vectors.The outlined procedure is depicted in Figure 4.8, with the aliphatic side chains and hydrogen atoms omitted for

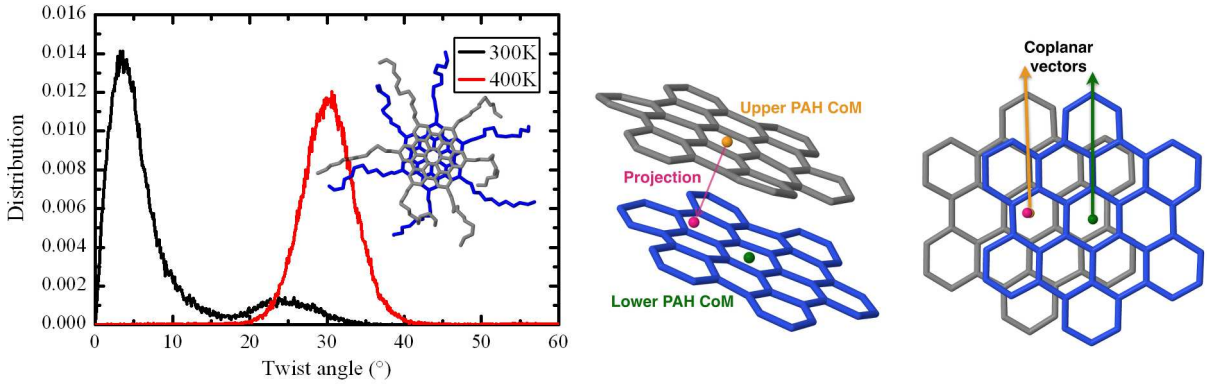

Figure 4.8: Left panel: Twist angle distributions for HBC-C12 molecular crystals at room and elevated temperature, alongside to "daisy-like" pattern of the liquid-crystalline phase at 400 K. Right panel: Graphical depiction of the method employed for the quantification of core stacking patterns.

clarity. Data accumulation is achieved over all core pairs using consecutive trajectory snapshots at equilibrium.

A contour plot of projected core CoM for HBC-C12 molecular crystals at ambient conditions is shown on the upper left panel in Figure 4.9, with a wireframe structure of the HBC molecule embedded, in order to show the geometric correlation of the contour plot maxima with respect to the disc plane on which CoMs are projected. The aforementioned diagram confirms the offset nature of tilted core stacking but without providing any structural information regarding the precise packing motif. A detailed picture of the latter is acquired should selection criteria with respect to the twist angle be applied. To this end, a twist angle binning is carried out with an interval of 10°, starting from 0° to 30°, resulting in the remaining panels of Figure 4.9.

Through careful inspection of stacking patterns in the first angle bin (0°-10°), accounting for the majority of recorded stacking motifs, two primal graphitic-like patterns occur, with major geometrical similarities to the AB and AA' patterns, denoted by a dot (●) and a square (■), respectively. These two characteristic maxima are joined by a "neck" region, where AA' (✚) and AA (▲) are accessed. The next twist angle bin from 10° to 20° contains twisted variants of the AA and AA' patterns, whereas the last twist angle bin from 20° to 30° accounts for stacking patterns similar to the "daisy-like" motif.

In order to figure out the orientational characteristics of side chains of variable end-to-end vector length, a series of contour plots for given end-to-end distances are produced and depicted in Figure 4.10. At 300 K, the longest side chains ($1.2\,\mathrm{nm} < R_\mathrm{e} < 1.6\,\mathrm{nm}$) seem to protrude perpendicularly ($\varphi \simeq 90°$) with respect to the columnar direction, exhibiting sharp maxima in their angular distribution functions. This picture is drastically altered in the hexagonal phase at 400 K, since a broadening of the distributions is evident, alongside a symmetry reversal; the longest side chains diverge from the normal direction of extrusion they had in the orthorhombic crystalline phase and form a fan line spatial

profile, attributed to the pronounced peaks near the value of 90° for the θ angle. The temperature dependence of such side chain orientation contour plots is illustrated in Figure III.1 in the Appendices.

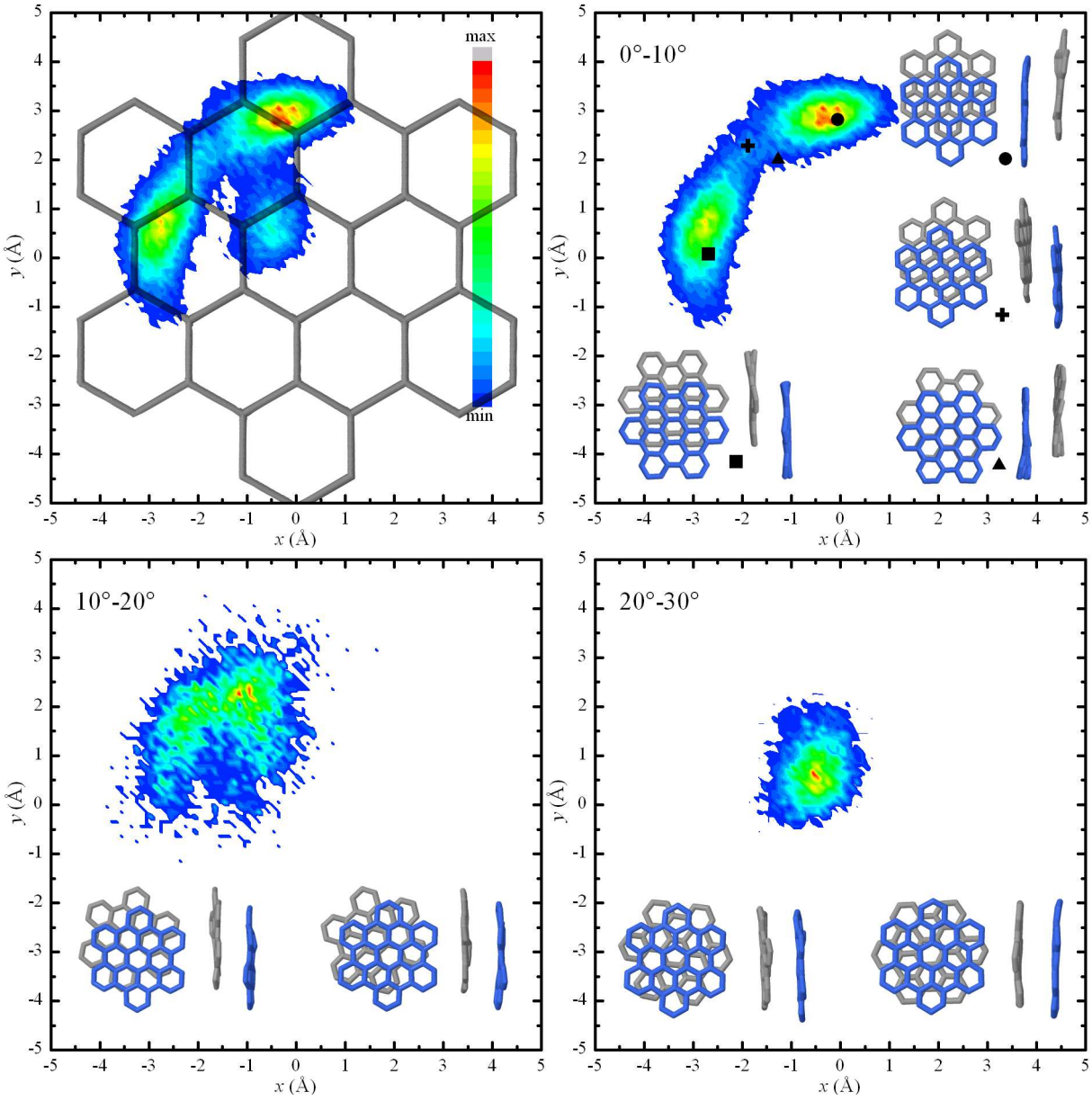

Figure 4.9: Projected core CoM contour plots: the upper left panel depicts the total distribution and the rest the partial contours with respect to appropriate twist angle binning.

The effect of the peripheral substitution and of the reduction of the side chain molecular weight on the conformation of the aliphatic part of the mesogens is accessible via the distribution of dihedral angles. In the case of the crystalline phases, the general trend observed throughout all simulations is that both substitution and side chain length reduction lead to increased disorder in the alkyl chain nanophase. In the case of the substitution, this is attributed to the fact that more free space is available for the side chains

to accommodate themselves; a phenomenon which encourages them to adopt higher entropy conformational distributions.

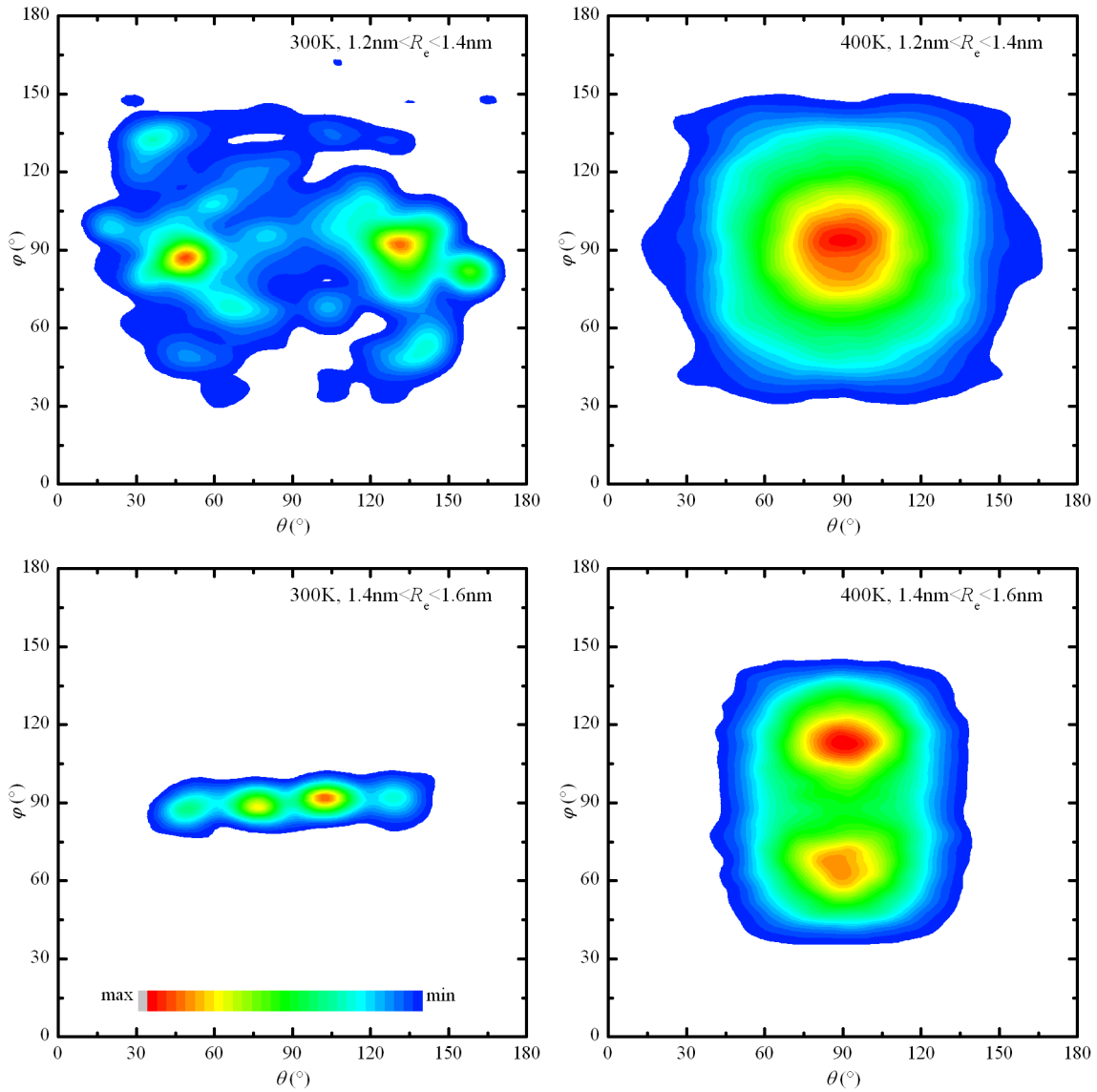

Figure 4.10: Contour plots of the orientational distribution of end-to-end side chain vectors of different length in the orthorhombic (300 K) and hexagonal (400 K) phase of HBC-C12.

In the case of the side chain length reduction, shorter length is linked to larger thermal fluctuations - a behavior consistent with our findings that are outlined in the "Dynamical properties" section. Upon melting, the hexagonal phases have higher *gauche* populations than the crystalline phases, in good qualitative agreement with experimental findings[41]; side chain conformational distributions become insensitive to both the substitution and the chain length reduction. Some selected diagrammatic representations of the above findings are depicted in Figure 4.11, where half of the symmetric distribution, from 0° to 180°, of the $-CH_2-CH_2-CH_2-CH_2-$ dihedral angle is sketched. The inset shows

details of the area near the gauche conformation, where there is significant differentiation in the crystalline phase.

It should be noted that other aliphatic dihedral angles (namely the ones involving terminal methyls and anchoring CA aromatic carbon atoms) also have symmetric *gauche* and *gauche´* populations and show the same behavior upon substitution and side chain length reduction.

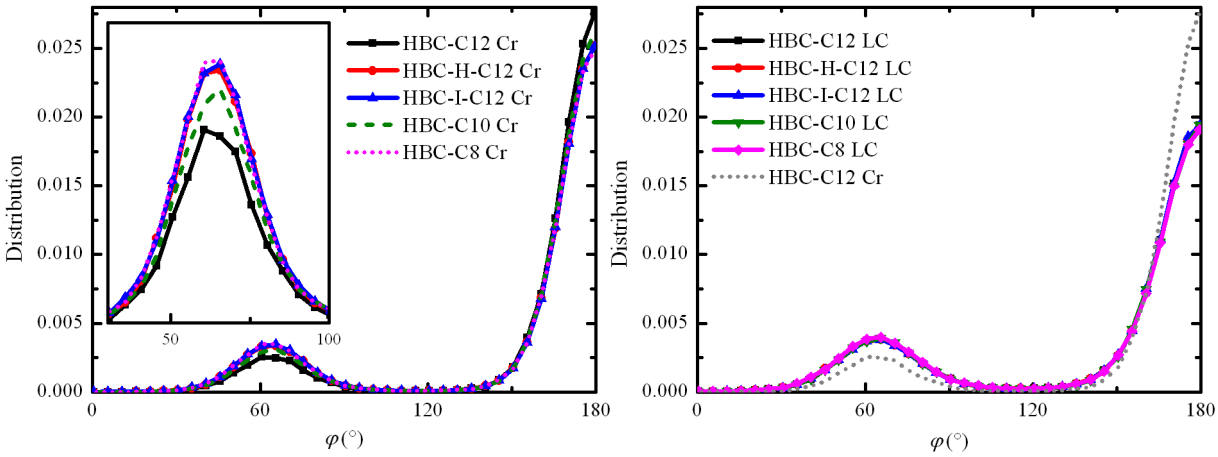

Figure 4.11: Effect of substitution and side chain length reduction on the conformation of the backbone aliphatic dihedral angle for crystalline (left) and liquid-crystalline (right) systems.

4.2.2 Mechanical Properties

The mechanical response of all examined systems through virtual stress-strain experiments under compressive load is illustrated in the following stress-strain curves in Figure 4.12, where the hydrostatic pressure P is plotted versus the fractional volume change $V/V_0 - 1$, with V_0 being the volume at 1 atm.

In all total compression stress-strain diagrams, two families of non-linear isotherm curves are evident. The first family describes the room temperature crystalline systems, whereas the second describes the elevated temperature liquid-crystalline systems, elucidating the effect of temperature on these nanographene molecular crystals: the rise in temperature causes the transition to the hexagonal liquid-crystalline phase, which is found to be softer than its crystalline counterpart. All systems exhibit an elastic response to the applied compression; the reverse process returns them to their initial configuration following the same stress-strain curve, without retaining any plastic deformation. Furthermore, a characteristic feature of the alkyl substituted HBC molecular crystals under study is that they exhibit a general robustness in their mechanical behavior with respect to substitution and side chain length reduction, since the two families of isotherms of Figure 4.12 can roughly describe all systems.

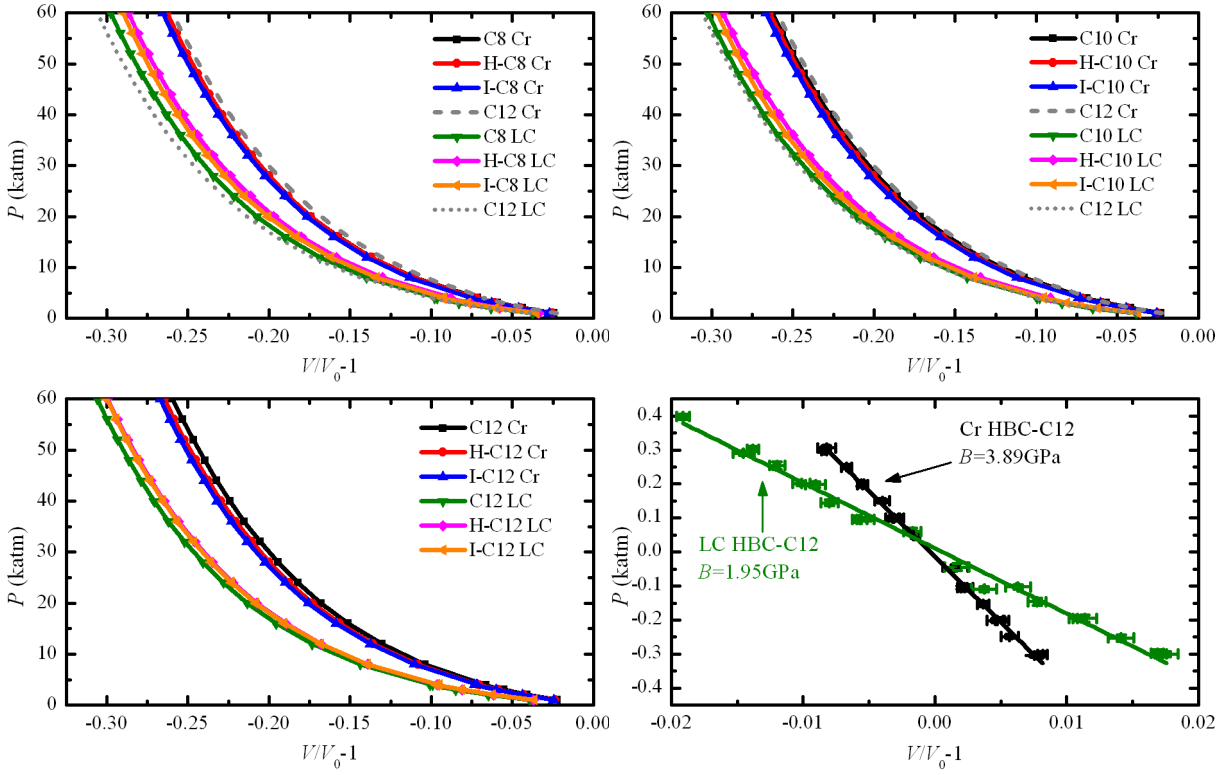

Figure 4.12: Compressive stress-strain curves of crystalline (300 K) and liquid-crystalline phases (400 K) of all examined systems, along with a detailed picture of the linear response of Cr and LC HBC-C12 for small compressive and tensile loading.

Table 4.5: Bulk moduli obtained from virtual stress-strain experiments.

System	B_{Cr} (GPa)	B_{LC} (GPa)	System	B_{Cr} (GPa)	B_{LC} (GPa)
HBC-C12	3.89	1.95	HBC-I-C10	3.16	2.06
HBC-H-C12	3.27	1.98	HBC-C8	3.38	1.93
HBC-I-C12	3.22	2.07	HBC-H-C8	3.15	2.12
HBC-C10	3.50	1.97	HBC-I-C8	3.13	2.10
HBC-H-C10	3.24	2.18			

As it is clearly shown in the lower right panel of Figure 4.12 for HBC-C12, up to a small volume variation of approximately ±1% for the crystalline and ±2% for the liquid-crystalline phase, the systems show a linear response to the applied compressive and tensile stress. A quantification of the hardness of the materials under study is obtained by calculating the bulk moduli via linear least-square fitting in this linear region. The numerical results of these analyses are reported in Table 4.5, with the relative error in the bulk modulus calculations situated around 0.03 GPa.

In order to understand how the applied compressive stress is mitigated in the two distinct nanophases, namely the aliphatic phase composed of the side chains and the columnar phase formed by the polyaromatic cores, a volume ratio analysis is carried out. In particular, the fractional volume change for the aliphatic phase $V_{\mathrm{aliph}}/V_{\mathrm{aliph},0}$ and that of the columnar phase $V_{\mathrm{col}}/V_{\mathrm{col},0}$ are calculated, where the volume in the fractions'

denominators corresponds to the equilibrium volume of each nanophase at atmospheric pressure.

A geometric calculation of the volume of the columnar nanophase in the liquid-crystalline system is quite straightforward given the mean radius of the mesogens, since the projections of the peripheral atoms of the polyaromatic cores onto the x-y plane are almost perfect circles. Hence, the volume of the defined cylinder can be easily calculated. The situation differs in the case of the crystalline system due to the pronounced tilt of the mesogens. In the herringbone pattern, the projection of the peripheral atoms onto the x-y plane form ellipses that, in many cases, are not perfectly aligned. In order to alleviate the pitfalls of any miscalculation through a geometric method, the total area which encloses the projected peripheral atoms is calculated numerically through the determination of the convex envelope of these points. The calculated area from all 16 columns is multiplied by the l_z length of the simulation box, obtaining this way the volume of the columnar nanophase V_{col}. The volume of the aliphatic nanophase is calculated by subtracting V_{col} from the total volume. The stress-strain curves of the individual nanophases for the HBC-C12 system are depicted in Figure 4.13. The strain variation of the mean molecular tilt with respect to the columnar direction and core radius is illustrated in Figure 4.14.

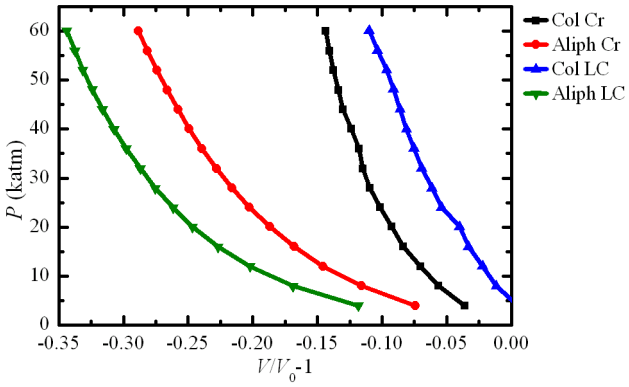

Figure 4.13: Stress-strain curves of the distinct columnar and aliphatic nanophases of the HBC-C12 crystalline (Cr) and liquid-crystalline (LC) phases to compression.

After a closer examination of this volumetric response, one realizes that the columnar nanophase, at both room and elevated temperatures, suffers a reduction in volume of approximately 10% upon compression to 60 katm, while the aliphatic nanophase contracts by ∼27% in the crystalline sample and by ∼35% in the liquid-crystalline sample. This indicates that the two nanophases absorb compression in a different manner. Focusing on the columnar nanophase of the crystalline material, up to a certain pressure, the tilt angle of the mesogens with respect to the columnar axis decreases, i.e., the herringbone pattern becomes flatter. For larger compression, the tilt reaches a plateau, so that the herringbone pattern does not disappear. For the liquid-crystalline material, the tilt has already been reduced to ∼3 degrees in the course of the melting process, with this value changing very little with compression. As far as the mean radius of the core is concerned, a monotonic decrease with respect to the applied compression is found, with the relative

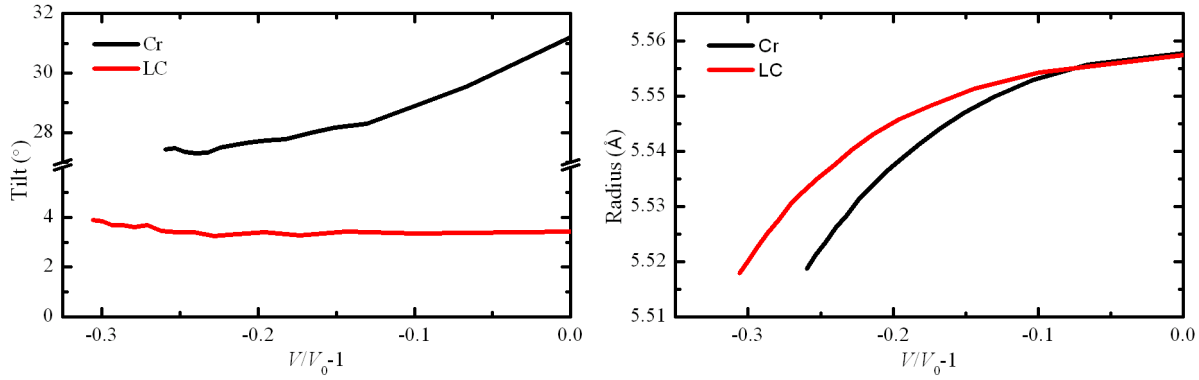

Figure 4.14: Tilt angle and core radius variation with respect to compressive stress.

change at full load (60 katm) being less than 1%.

An interesting property of these materials is that the conformation of the side chains, along with the presence or absence of a herringbone pattern, induces spatial anisotropy in the mechanical behavior. The crystalline phase is significantly stiffer along the x direction, parallel to which we have the maximum interdigitation of nearly all-*trans* side chains. In the liquid-crystalline phase, the direction along which the system responds in the stiffest manner is the columnar direction z, due to the repulsive vdW interactions of the cores; the herringbone pattern is now absent and the polyaromatic cores can no longer absorb compression as tilt reduction. This anisotropy is depicted in Figure 4.15, where the variation of the supercell parameters is plotted under a compressive ladder-like load.

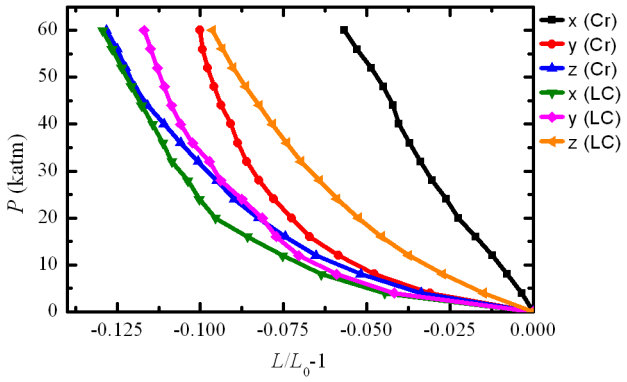

Figure 4.15: Variation of the supercell parameters of the crystalline and liquid-crystalline phases of the HBC-C12 molecular crystal under compressive load. All lengths are normalized with respect to their equilibrium values at 1 atm.

In order to focus in more detail on the impact of compression on the HBC-C12 system, the distributions of proper dihedral angles are examined at intermediate (32 katm) and full load (60 katm). The side chain conformation seems to absorb the applied pressure, not by changing the *trans-gauche* ratios dramatically but by broadening the distributions about their maxima. As far as the core sp^2 carbon dihedrals are concerned, the compression has literally no impact, meaning that the cores retain their original planarity. A diagrammatic representation of the findings outlined above can be seen in Figure 4.16, where the side chain backbone aliphatic (C2-C2-C2-C2), the linking aromatic-aliphatic (CH-CA-C2-C2)

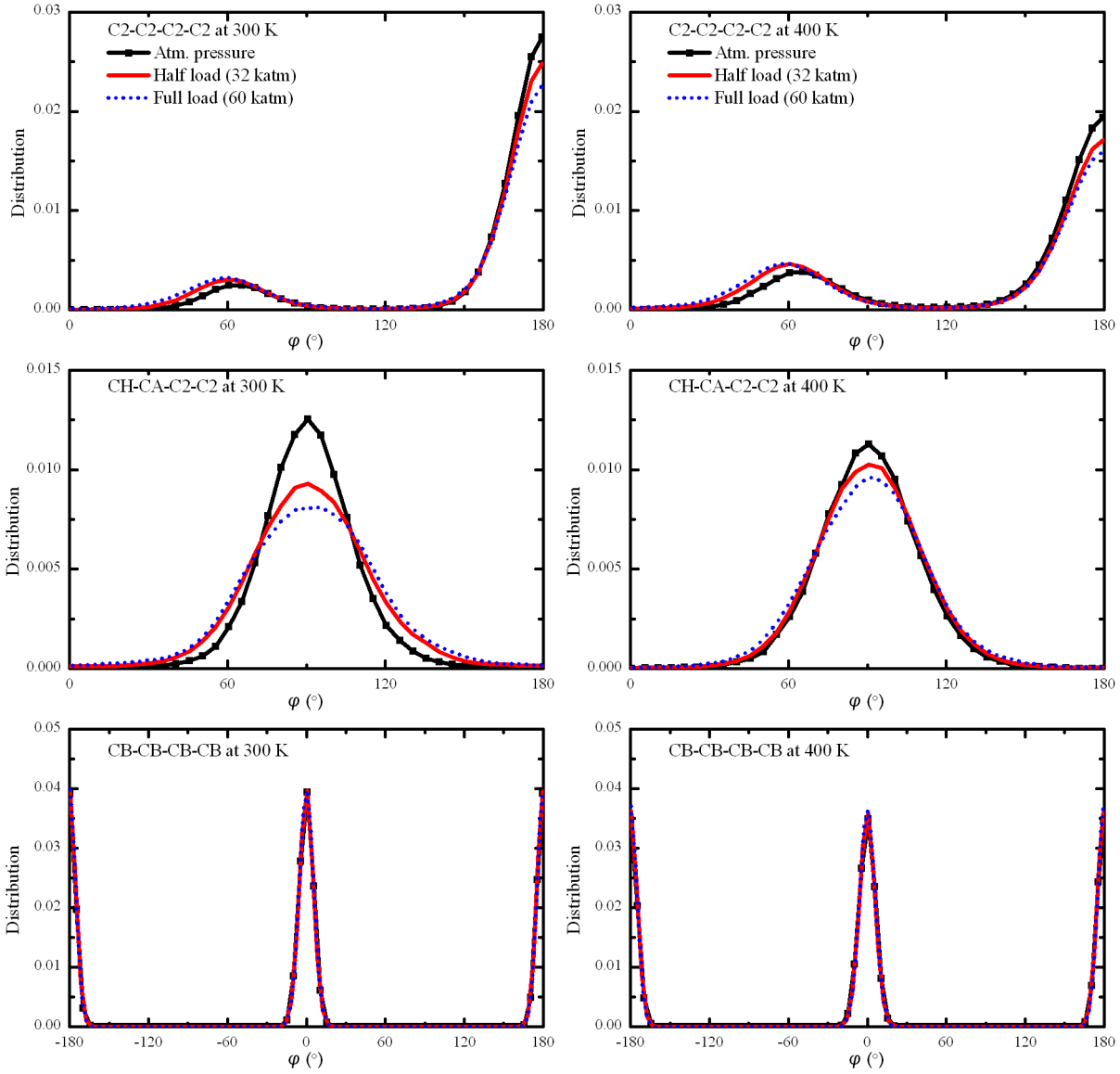

Figure 4.16: Dihedral angle distributions in the crystalline and liquid-crystalline phase, at atmospheric pressure and under intermediate and full load.

and the core (CB-CB-CB-CB) dihedral angle distributions are depicted.

Although virtual stress–strain simulations using orthogonal simulation cells provide a plethora of information concerning the mechanical behavior of the systems under study, their extension in order to calculate elastic moduli beyond the bulk modulus would require an enormous number of calculations with composite deformations along a series of high symmetry directions. Instead of following this time- and resource-consuming path, strain fluctuation theory is utilized, allowing us to extract the complete mechanical response. The bulk and shear moduli of the HBC-C12 system in its crystalline and liquid-crystalline phases, calculated via strain fluctuations, are depicted in Figure 4.17.

The value of the crystalline shear modulus obtained via the strain fluctuation theory is 380±3 MPa and its liquid-crystalline counterpart is equal to 13.0±0.1 MPa, roughly

30 times smaller. The convergence of the bulk moduli calculated with Equation 4.7 to the numerical values obtained by stress-strain simulations enhances the validity of the calculated results.

Examining the shear moduli obtained via the Reuss averaging scheme of Equation 4.8, one realizes that the crystalline phase is stiffer than the liquid-crystalline phase when subjected to shear stress, a behavior that should be attributed to the fact that the closely packed interdigitated side chains of the crystalline system enhance its mechanical robustness. In the liquid-crystalline phase, the elimination of molecular tilt in the core and the pronounced thermal motion of side chains, which introduces conformational defects, render the system more vulnerable to shearing deformations. The calculated values for G_{R} are in fair agreement with the experimental data of the dynamic storage modulus of such discotic materials in the limit of high frequencies.[39]

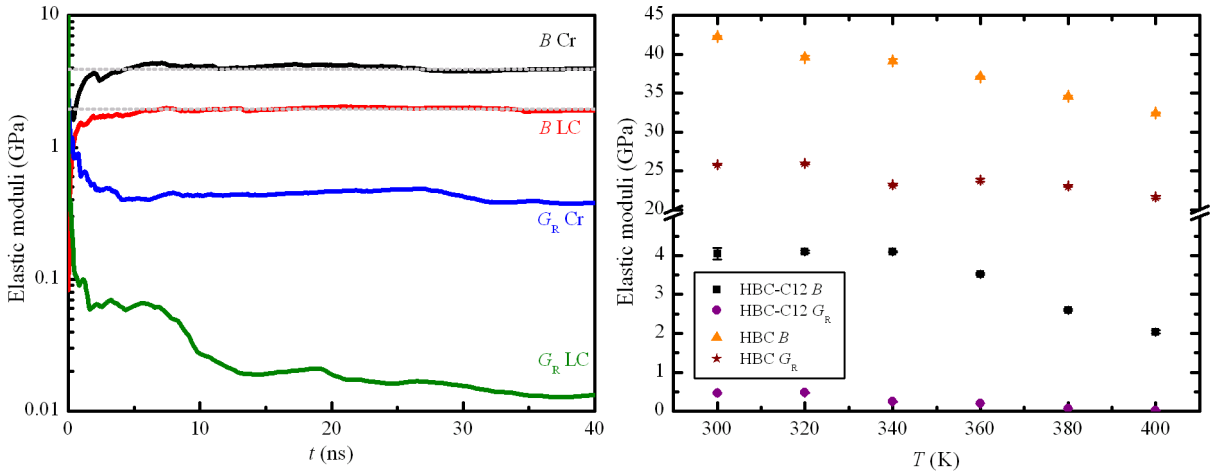

Figure 4.17: Left panel: time evolution of bulk B and shear moduli G_{R} calculated directly from the isothermal compliance tensor for the crystalline and liquid-crystalline phases of the HBC-C12 system. The dotted lines to which the bulk moduli converge correspond to the values obtained by stress-strain calculations using orthogonal simulation cells. Right panel: Temperature dependence of elastic moduli for pristine HBC and HBC-C12 molecular crystals.

A direct comparison between the elastic moduli of pristine and alkyl-substituted HBC molecular crystals over a temperature range between 300 K and 400 K clarifies the contribution of the aliphatic nanophase to mechanical properties: the soft alkyl mantle surrounding the molecular wires induces a decrease in both bulk and shear moduli by an order of magnitude compared to unsubstituted HBC. Furthermore, both materials exhibit a relative softening with temperature rise.

4.2.3 Dynamical Properties

The melting process from the two-dimensional orthogonal crystalline to the hexagonal liquid-crystalline phase can be monitored via the time evolution of the supercell parameters and the molecular MSD function. These quantities are depicted in Figure 4.18 for the HBC-C12 system. The tilt angle of the mesogens with respect to the columnar direction can also be regarded as a measure of phase transition; it is not shown here because it exhibits exactly the same trends as the z supercell component displayed in Figure 4.18.

Upon heating, the system initially exhibits a negative expansion along the x-direction, which is the direction of maximum all-*trans* interdigitation, simultaneously with an increase in the tilt angle. This phenomenon is highlighted in Figure 4.18 by the first shaded area from the left (grey rectangle) and is in good agreement with experimental findings.[39] This negative expansion is cancelled out by entropic contributions as the melting process continues, leading the system to a tilt-less tetragonal phase, which is highlighted by the second shaded area from the left (yellow rectangle). This metastable phase is gradually transformed into a hexagonal two-dimensional lattice, as is depicted by the fork-like separation of the x and y components and identified by theoretical XRD spectra calculated from the MD trajectories.

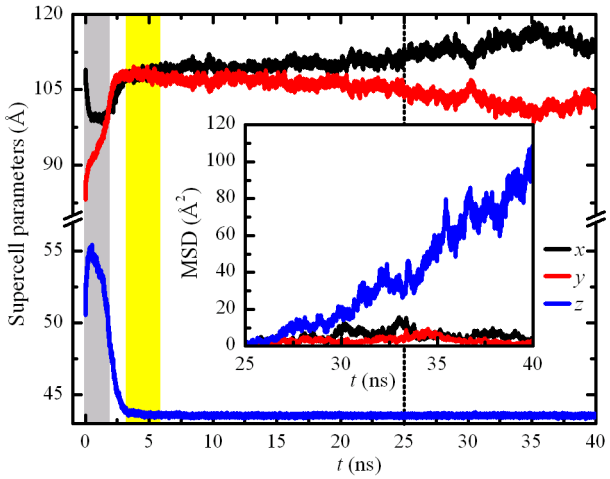

Figure 4.18: Time evolution of the supercell parameters of the HBC-C12 system upon introducing a step change in temperature at 400 K. The inset diagram depicts the mean square displacement components of the molecular centers of mass in the hexagonal phase.

Once the system reaches the hexagonal phase, the manifestation of liquid-crystalline behavior along the columnar direction arises progressively, as is shown in the inset diagram in Figure 4.18, where the MSD function along the three Cartesian components is plotted. The time origin for the MSD calculations is near 25 ns (pointed out by the grey dotted line in the diagram), situated well inside the hexagonal phase. The fact that the x and y components of the MSD saturate at a very low value shows that there is no significant mobility along these directions; on the other hand, along the columnar z-direction, a molecular nanowire translation is evident, since the MSD function increases gradually to values that are higher by orders of magnitude in comparison to the x-y plateau. It should be noted that this *en-masse* collective motion along the columnar direction has

been also identified in the case of the triphenylene molecule and has been explained as a drift motion of the columns rather than true diffusion.[189] The overall behavior due to the rise in temperature outlined above is exhibited by all studied systems and shows very little variation with substitution or side chain length reduction.

Moving on to the dynamical properties of the crystalline phase at equilibrium, both substitution and side chain length reduction seem to have a small effect on the mobility of molecular cores, as is quantified via the second-order Legendre polynomials of the perpendicular and coplanar vectors. The highly ordered crystalline phase of the hexa-dodecyl substituted system exhibits the smallest mobility, with the other systems showing a more pronounced core mobility as is depicted in Figure 4.19, where the Legendre polynomials of both core vectors and end-to-end side chain vectors are plotted.

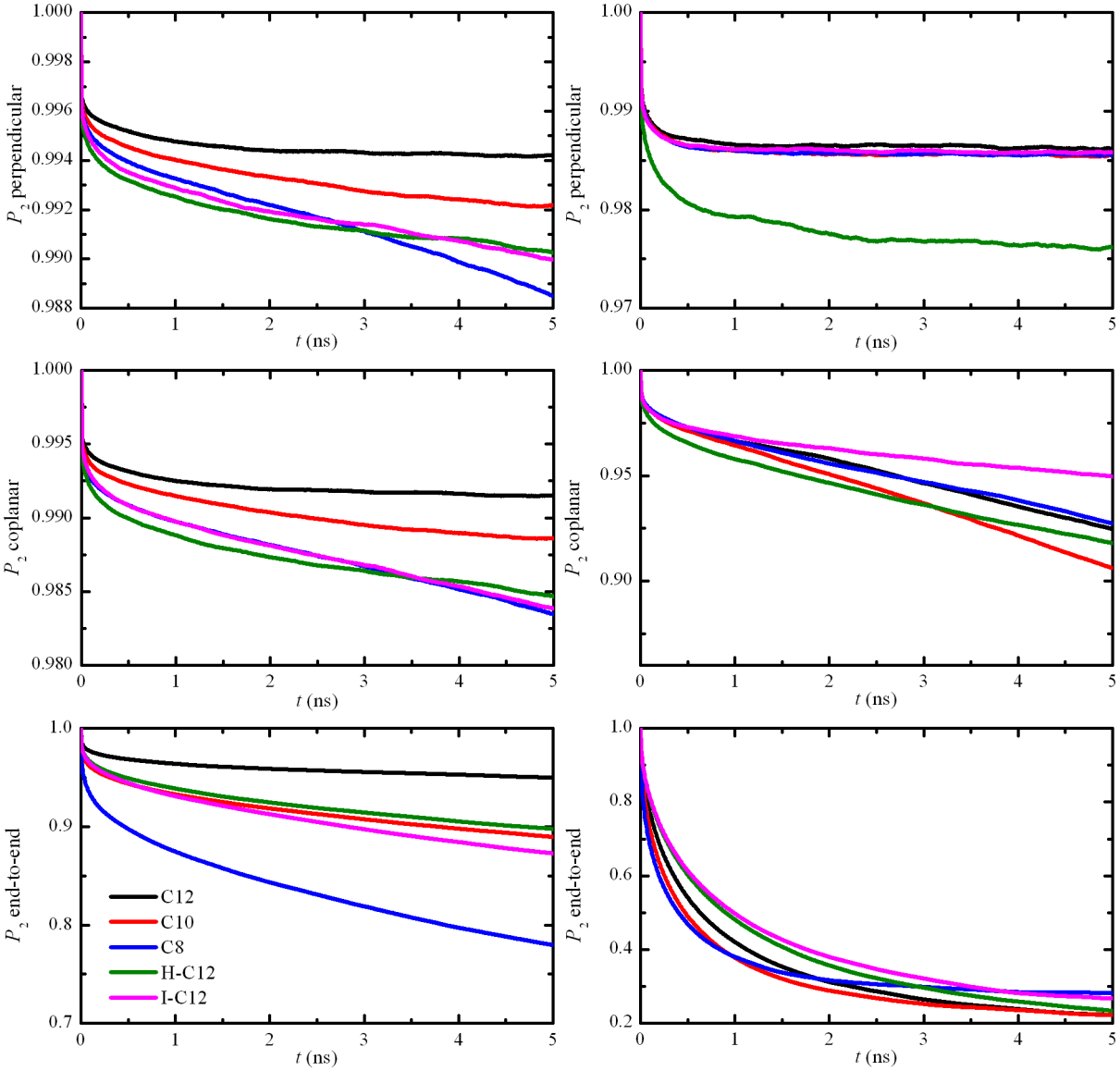

Figure 4.19: Second-order Legendre polynomial ACFs of the crystalline (left panel) and liquid-crystalline (right panel) phases for three vector quantities: the perpendicular and coplanar core vectors and the side chain end-to-end vectors.

In the liquid-crystalline phase, the perpendicular vector autocorrelation functions exhibit changes comparable to those in the crystalline phase, indicating that both phases tend to keep their mean tilt angle at its equilibrium values, near 30° for the crystalline and near zero for the liquid-crystalline phases. As far as the coplanar vector is concerned, the liquid-crystalline phase shows higher rotational mobility. It should be noted that the iodine substituted systems decorrelate at a slower rate than the hydrogen substituted counterparts, a phenomenon attributed to stronger electrostatic interactions. Finally, the side chain end-to-end vector autocorrelation functions manifest the expected behavior with a raise in temperature, exhibiting much faster decorrelation rates than in the orthogonal crystalline phase.

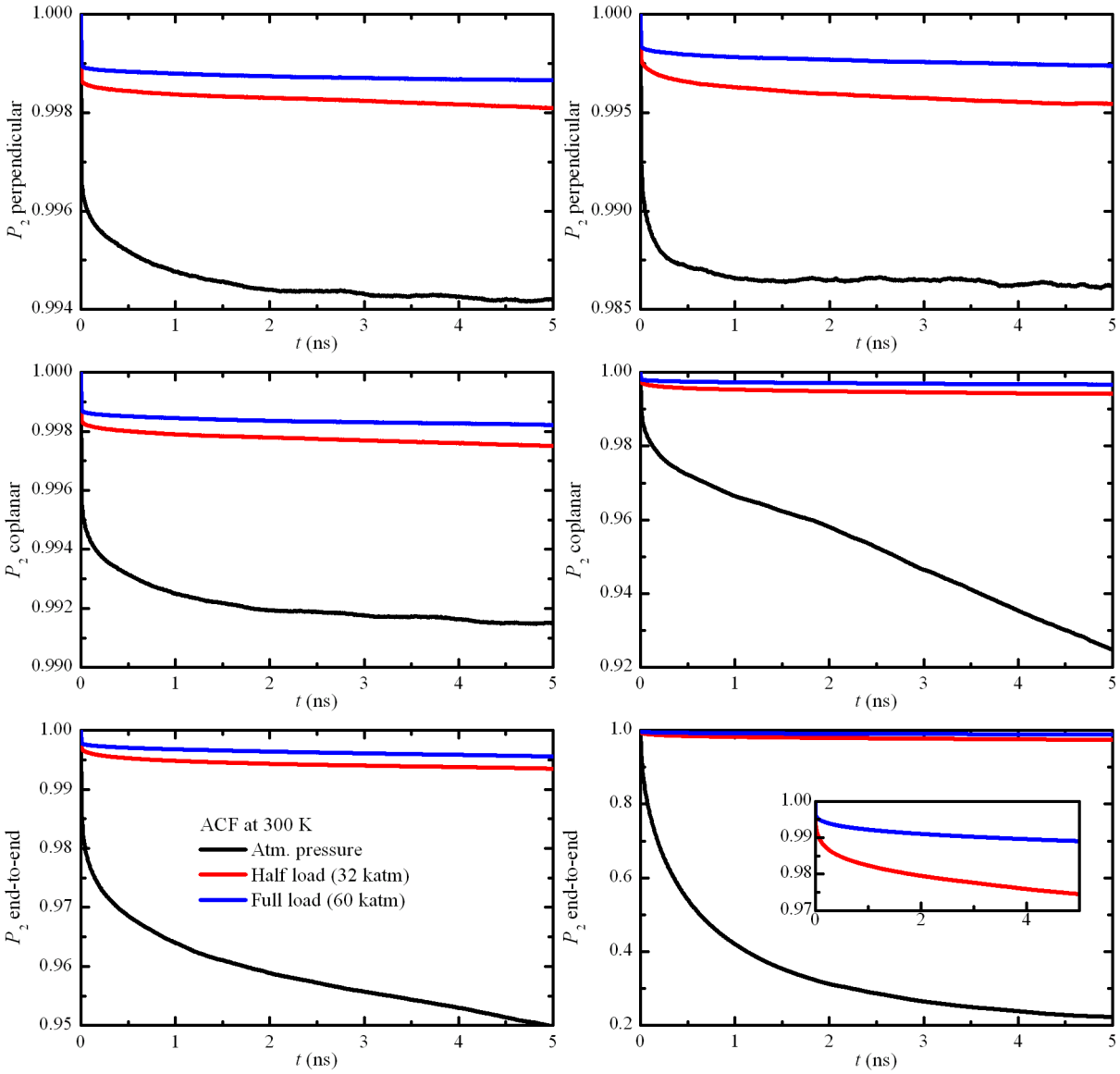

Figure 4.20: Impact of compressive load on the dynamical properties of the HBC-C12 system in the crystalline (left panel) and liquid-crystalline (right panel) phase. The inset in the bottom right diagram depicts the two uppermost curves of the figure in more detail.

Table 4.6: Relaxation times τ, stretching exponents β and correlation times t_C for the end-to-end spectra of the HBC-C12 system.

System	Fitting parameters
Cr at 1 atm	$\tau = 1.71 \times 10^7$ ns, $\beta = 0.20$, $t_C = 2.18 \times 10^9$ ns
LC at 1 atm	$\tau = 1.55$ ns, $\beta = 0.42$, $t_C = 4.61$ ns
LC at 32 katm	$\tau = 7.00 \times 10^7$ ns, $\beta = 0.22$, $t_C = 3.58 \times 10^9$ ns
LC at 60 katm	$\tau = 3.15 \times 10^{10}$ ns, $\beta = 0.20$, $t_C = 3.72 \times 10^{12}$ ns

Apart from dynamical properties at equilibrium, the effect of compressive stress on the aforementioned autocorrelation functions is also examined for the HBC-C12 system in both phases. As in the case of the dihedral angle distribution functions, the Legendre polynomials of the perpendicular, coplanar and side chain end-to-end vectors are studied at an intermediate and at full load. The time evolution of these orientational correlation functions is depicted in Figure 4.20.

Judging from the evolution of the autocorrelation functions at intermediate and full load, one can safely deduce that the compression of the system strongly slows down the dynamics, in fair agreement with experimental findings.[40] Upon examination of the core vector ACFs, one sees that the applied pressure limits the core mobility, while the end-to-end vector ACF shows a deceleration of the side chain entropic movement - a phenomenon more intense in the case of the liquid-crystalline phase.

To further quantify the effect of extreme compression on side chain mobility, a stretched exponential function of the form $\exp\left[-(t/\tau)^{\beta}\right]$ is fitted to the end-to-end correlation spectra of the HBC-C12 system. Apparently, this procedure is not applicable to the crystalline spectra under pressure, since the autocorrelation functions there saturate at a "hard" plateau near unity. The parameters obtained from the fitting procedure are listed in Table 4.6. Judging from the values of the correlation times t_C, the applied compression clearly slows down the side chain dynamics significantly.

4.3 Conclusions

A method for preparing initial configurations of columnar alkyl-substituted nanographene crystals with the herringbone symmetry has been presented, based on a so-called quasi-adiabatic procedure, where we keep the columnar pillars fixed, allowing the side chain aliphatic nanophase to adapt to such an environment. Using this methodology, HBC molecular crystals with alkyl side chains were studied employing MD simulations.

As far as the crystalline phase of the materials is concerned, a general structural robustness with respect to changes in the peripheral substitution was observed, as is reflected in the mean core-to-core distance of the mesogens, a vital parameter for charge transport applications. Although the side chain substitution and length reduction in-

duce a certain disorder in the systems, structural and dynamical studies showed that the herringbone pattern is retained with minimal core movement, the systems becoming slightly more mobile in comparison to the highly interdigitated HBC-C12 crystal. The liquid-crystalline phase obtained via melting simulations demonstrates an even more pronounced insensitivity to peripheral change: all systems form hexagonal columnar aggregates, with diffusive behavior along the columnar axis and a relatively constant core distance.

In the case of HBC-C12 molecular crystals, stacking patterns are acquired from equilibrium MD simulations, unveiling the existence of various graphitic-like motifs that are eventually eliminated upon melting to the liquid-crystalline phase, where the stacking adopts a clearly rotated, "daisy-like" pattern. Differentiations to the orientational characteristics of the side chain nanophase are also reported, with the dodecane functional groups exhibiting variable protrusion schemes upon transitioning from the crystalline to the liquid-crystalline phase.

Two characteristic mechanical anisotropies were found under compressive load via virtual stress-strain experiments. First, we report a spatial anisotropy, since the direction along which the material is harder switches from x in the crystalline phase (parallel to the all-*trans* side chain direction) to z in the liquid-crystalline phase (parallel to the columnar direction). Second, the volumetric response of the two distinct nanophases, the columnar and the aliphatic, is different, with the aliphatic nanophase putting up smaller resistance to compression. The application of compressive stress up to 60 katm results in a small (up to $\sim$1%) decrease in the core mean radius, and a small decrease in the tilt angle in the crystalline phase. In the case of the liquid-crystalline phase, the cores suffer the same radius reduction but no significant alteration to their perpendicular alignment with respect to the columnar axis.

Based on the calculated bulk moduli of both phases, the systems can be characterized as "soft waxes", with the crystalline phase being stiffer than the liquid-crystalline phase. A significant difference is seen in their response to shear stresses, since the liquid-crystalline phase exhibits a shear modulus smaller by one to two orders of magnitude than the crystalline phase. This behavior is attributed to conformational defects of the side chains, alongside their more pronounced entropic movement and the loss of molecular tilt of the cores with respect to the axial direction.

Proper dihedral angle distribution analyses indicate that strain is taken up primarily by the aliphatic nanophase by broadening the distribution of the dihedral angles about their respective trans and *gauche-gauche´* maxima. The same analysis yields no deviation from planarity in the polyaromatic cores in the liquid-crystalline state. Furthermore, the effect of compression on dynamical processes was examined, elucidating that the application of pressure slows down the kinetics of both columnar and the aliphatic nanophases.

The melting process was studied through monitoring the supercell parameters and the

MSD function. This study indicated the existence of a negative expansion region in the early stages of the melting process. The systems then pass from the herringbone crystalline orthogonal phase to an intermediate tilt-less tetragonal phase, ending up in the hexagonal liquid-crystalline phase. Diffusion along the columnar direction in the hexagonal phase is identified via the molecular MSD function, regardless of the substitution or of the side chain length.

The studied materials show a remarkable structural robustness, forming neatly packed molecular wires even in the presence of peripheral defects and ambient mechanical perturbations. This classifies them as strong candidates for organic electronic applications.

Chapter 5

Molecular Simulations of Amphiphilic Discotic Mesogens

This chapter contains empirical MD simulation results regarding bulk lamellar molecular crystals made up by amphiphilic discotic mesogens grafted with both hydrophobic and hydrophilic peripheral side chains. Properties are evaluated at equilibrium, at different temperatures, in order to access some fundamental insight on the effect of the hydrophilic nanophase morphology on structural features and the melting process.

5.1 Systems of Interest and Computational Details

5.1.1 Preliminaries

Empirical MD simulations are put to use for the examination of lamellar structures comprised of amphiphilic, "Janus-type" discotic mesogens. The mesogen under study is the C12-HBC-PhOTEG molecule (Figure 1.13: **46**) carrying both aliphatic C12 and TEG side chains.

Atomistic calculations are carried out in the isobaric-isostress statistical ensemble via the MTK EoMs[317], utilizing typical periodic boundary conditions. The integration step is set to 1 fs and the time constants for temperature and pressure control are equal to 100 fs and 2000 fs, respectively. Long-range electrostatic interactions are treated via the PPPM mesh-based method.[306] All simulations are carried out using the LAMMPS simulation package.[318]

5.1.2 Force Field

Due to the presence of oxygen-bearing side chains, the use of the hybrid all-atom/united-atom FF described in Table 4.1 cannot be extended to such mesogens. The description of particle interactions is quantified by means of the CHARMM Generalized Force Field

(CGenFF).[337;338] Atom type and partial charge assignment is carried out automatically via the CGenFF interface available over the World Wide Web at https://cgenff.paramchem.org.[339;340]

The functional form of the utilized FF is described by Equation 5.1 and employs typical harmonic energy expressions for bond stretching and bending, and out-of-plane motions. Torsional barriers are quantified via suitable superpositions of single cosine expressions. Moreover, superior quantitative accuracy is achieved through the utilization of UB "1-3" angle terms.

$$\begin{aligned} E = & \sum_{\text{bonds}} k_{\text{b}} \left(r - r_0\right)^2 + \sum_{\text{angles}} k_{\text{a}} \left(\theta - \theta_0\right)^2 + \sum_{\text{1-3 pairs}} k_{\text{UB}} \left(S - S_0\right)^2 + \\ & + \sum_{\text{dihedrals}} \sum_{m} k_{\text{d},m} \left[1 + \cos\left(n_m \varphi - d_m\right)\right] + \sum_{\text{impropers}} k_{\text{i}} \left(\chi - \chi_0\right)^2 + \\ & + \sum_{i<j} \frac{1}{4\pi\varepsilon_{\text{r}}\varepsilon_0} \frac{q_i q_j}{r_{ij}} + \sum_{i<j} 4\varepsilon_{ij} \left[\left(\frac{\sigma_{ij}}{r_{ij}}\right)^{12} - \left(\frac{\sigma_{ij}}{r_{ij}}\right)^{6}\right] \end{aligned} \tag{5.1}$$

Non-bonded interactions are quantified via the Coulomb and LJ potentials, with the latter obeying a smooth truncation scheme based on Equations 2.92 and 2.93, using an inner and outer cut-off radius of 10 Å and 12 Å respectively. Typical geometric and arithmetic combining rules apply for ε_{ij} and σ_{ij} parameters, respectively. Furthermore, intramolecular LJ interactions are omitted for "1-2" and "1-3" atom pairs and alternative ε and σ values are used for "1-4" atom pairs situated on the ends of a proper dihedral angle.

5.1.3 Initial Configurations

As regards initial configurations of lamellar molecular crystals comprised of C12-HBC-PhOTEG mesogens, valuable insight has been drawn from experimental information on similar discotic materials. To be more precise, Chen *et al.*[341] have demonstrated that amphiphilic hexathienocoronene molecules can self-organize into various forms, including tubular structures, monolayer assemblies, and well-defined bulk lamellar molecular crystals. In the latter form, discotic cores are arranged in a tilted fashion, with the hydrophobic dodecane nanophase in full interdigitation. This very structural profile is chosen for the C12-HBC-PhOTEG lamellae under study, leaving as an undetermined factor the morphology of the hydrophilic TEG nanophase.

Bearing in mind the aforementioned structural profile, two lamellar polymorphs are taken into consideration: one with the TEG nanophase in full interdigitation and a second one with the TEG side chains folded away from adjacent lamellae, thus resulting in a non-interdigitated variant. Graphical depictions of the two utilized polymorphs are illustrated in Figure 5.1.

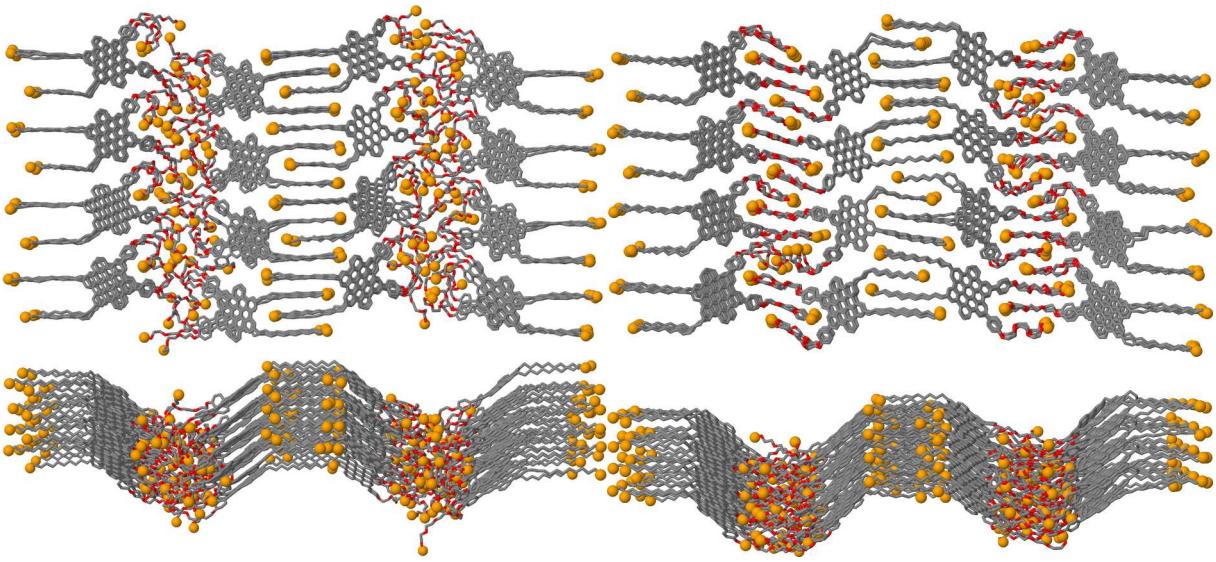

Figure 5.1: Top and side views of the folded (left) and interdigitated (right) polymorphs of C12-HBC-PhOTEG. The orange spheres correspond to the terminal -CH_3 units of every side chain and are used as a visual aid to show the level of interdigitation.

5.1.4 Properties Under Study

Structural characterization of the two polymorphs at different temperatures is accomplished through various complementary methods, aiming at the examination of features linked to both the discotic and side chain parts of the mesogens.

Interlamellar separation is extracted by means of ODR plane calculations: molecular CoMs belonging to the same lamella are used to define an ODR plane that describes in an optimal manner their spatial distribution. Provided that all lamellar planes are near-parallel, their separation is calculated in a geometric fashion. Intralamellar structure is probed via CoM distance calculations, thus quantifying both intra- and inter-columnar structural features for a given lamella.

Moreover, stacking patterns are extracted from equilibrated trajectories using methodologies already described in the previous chapter and side chain end-to-end vector and proper dihedral angle analyses are carried out for the determination of the structural characteristics of the hydrophobic C12 and hydrophilic TEG nanophases.

As regards the orientational state of HBC cores, perpendicular discotic core vectors are derived for the quantification of the tilt angle and coplanar vectors are put to use in order to quantify the twist angle between neighboring mesogens belonging to the same molecular wire. In the case of perpendicular core vectors, the notion of the orientational order parameter Q is introduced as a measure of molecular directionality and spatial homogeneity. In more detail, given the normalized perpendicular vectors $\hat{u}$, the orientational order tensor $\mathbf{Q}$ is derived for every molecular wire via the expression

$$Q_{ab} = \left\langle \frac{1}{N_{\mathrm{col}}} \sum_{i=1}^{N_{\mathrm{col}}} \left(\frac{3}{2} u_a^{(i)} u_b^{(i)} - \frac{1}{2} \delta_{ab} \right) \right\rangle_t \tag{5.2}$$

where N_{col} is the number of molecules per column, δ_{ab} the Kronecker delta and a and b the Cartesian indices with values x, y and z. The outer brackets symbolize a time averaging calculation scheme.

The diagonalization of $\mathbf{Q}$ returns the orientational director $\hat{n}$, which is the eigenvector corresponding to the largest eigenvalue of $\mathbf{Q}$. This largest eigenvalue corresponds to the orientational order parameter Q, which is a measure of alignment of vectors $\hat{u}$ with respect to the director $\hat{n}$: a value close to unity corresponds to strong orientational correlation, whereas values close to zero indicate random, uncorrelated orientation.

As far as dynamical properties are concerned, CoM MSD functions are used to quantify translational motion and vector ACFs are put to use for the examination of core and side chain movement.

5.2 Results and Discussion

5.2.1 Structural Properties

Both polymorphs retain their lamellar structure in the temperature interval between 300 K and 450 K, with pronounced structural variations taking place at the elevated temperature of 450 K. As far as the lamellar separation is concerned, minuscule differences occur up to the temperature of 400K. Upon temperature rise at 450 K, interlamellar distances are further augmented, mostly due to the loss of C12 side chain interdigitation. In the case of intercolumnar separation inside every lamella, vertical ODR CoM distance histograms indicate that temperature rise leads to a degree of misalignment but with the lamellar morphology still generally intact.

Interlamellar separation and intralamellar molecular wire distance histograms are depicted in Figure 5.2 for both polymorphs and all examined temperatures. Moreover, Figure 5.3 depicts the C12 nanophase interdigitation loss at 450 K for the interdigitated polymorph that results in a pronounced expansion along the normal to the lamellar direction. In this very illustration, pictorial evidence of intralamellar molecular wire misalignment is also shown.

Information regarding core tilt angle and possible spatial tilt correlations is gained via orientational tensor analyses that result in time-series of orientational director $\hat{n}$ components. Given the fact that CoM directors for all systems have been found aligned with $+\hat{z}$, the inverse cosine of the time average of the z component $\hat{n}_z$ is practically the core tilt angle. Furthermore, sign relationships between other $\hat{n}$ components reveal details on how the tilted molecules arrange themselves in the bulk lamellar structure.

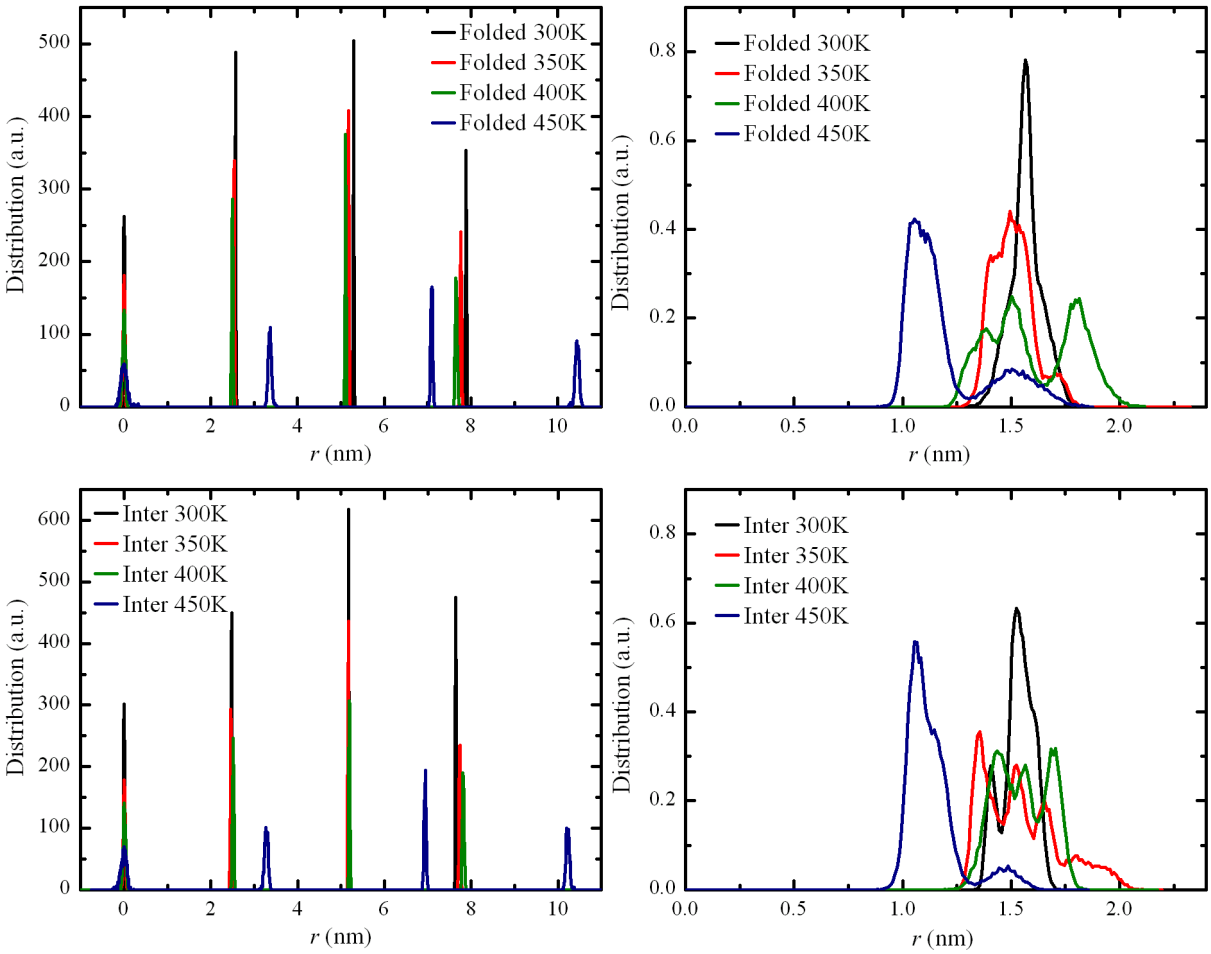

Figure 5.2: Interlamellar (left panels) and intercolumnar (right panels) distance histograms for the folded (top) and interdigitated (bottom) polymorphs at different temperatures.

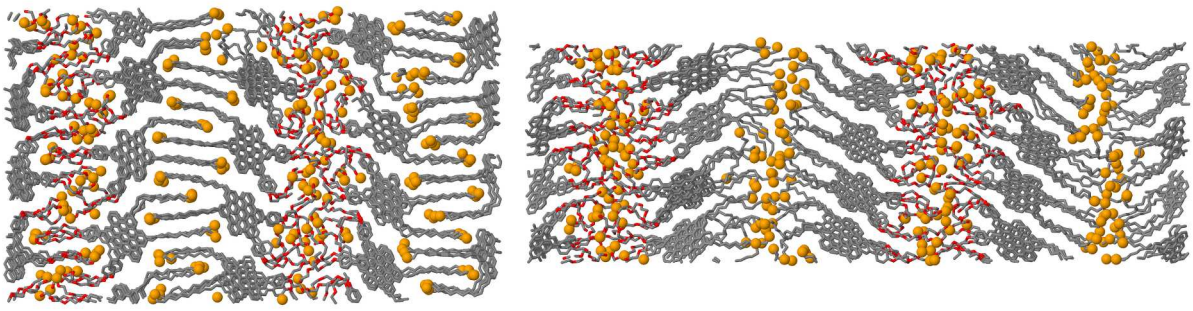

Figure 5.3: Top view periodic representations of the so-called interdigitated C12-HBC-PhOTEG polymorph at 400 K (left) and 450 K (right). The orange spheres correspond to the terminal -CH_3 units and are used as a visual aid to elucidate side chain interdigitation state.

A characteristic example of orientational director component time-series per lamella is shown in Figure 5.4 for the folded polymorph at 300 K and 450 K, respectively. Analogous

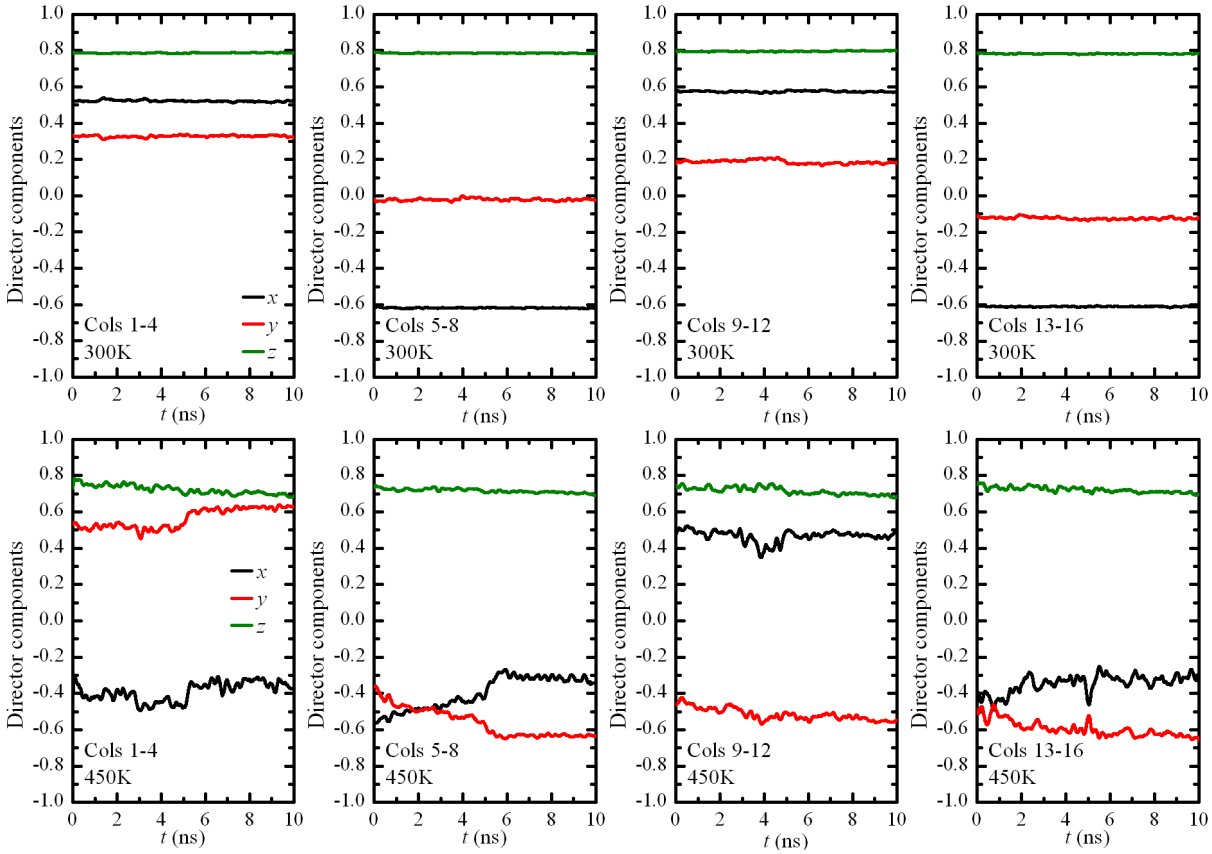

Figure 5.4: Characteristic orientational director components time-series per lamella.

temporal behavior is manifested by the interdigitated polymorph. At room temperature, the alternating sign of the x component recorded per lamella is an evidence of an alternating, herringbone-like tilt pattern when moving from one lamella to another. The same behavior holds for the elevated temperatures of 350 K and 400 K. A change to tilt spatial correlation occurs upon heating at 450 K. Analyses per lamella show a relative disruption to the alternating tilt pattern; proper quantitative results are gained by means of tilt analyses per molecular wire. Representative results from the latter procedure are shown in Figure 5.5 for the x and y components of $\hat{n}$, elucidating that temperature rise to 450 K induces an intralamellar distress with respect to the projection of the orientational director: the herringbone-like interlamellar feature is forfeited, since the orientational directors per column are facing away from the normal to lamellae direction. Nevertheless, the tilt of the mesogens is further fortified at approximately 45°. This very phenomenon, i.e. the intralamellar selective *en-masse* molecular nanowire rotation, coupled to the tilt angle augmentation, leads to a contraction at 450 K along the y direction which is normal to the stacking direction and the perpendicular to lamellar planes direction as well. Average tilt angle values for both polymorphs and all examined temperatures, along with intracolumnar CoM distance and geometrically derived core-to-core distances are gathered in Table 5.1.

Amphiphilic C12-HBC-PhOTEG mesogens self-organized into lamellar supramolecu-

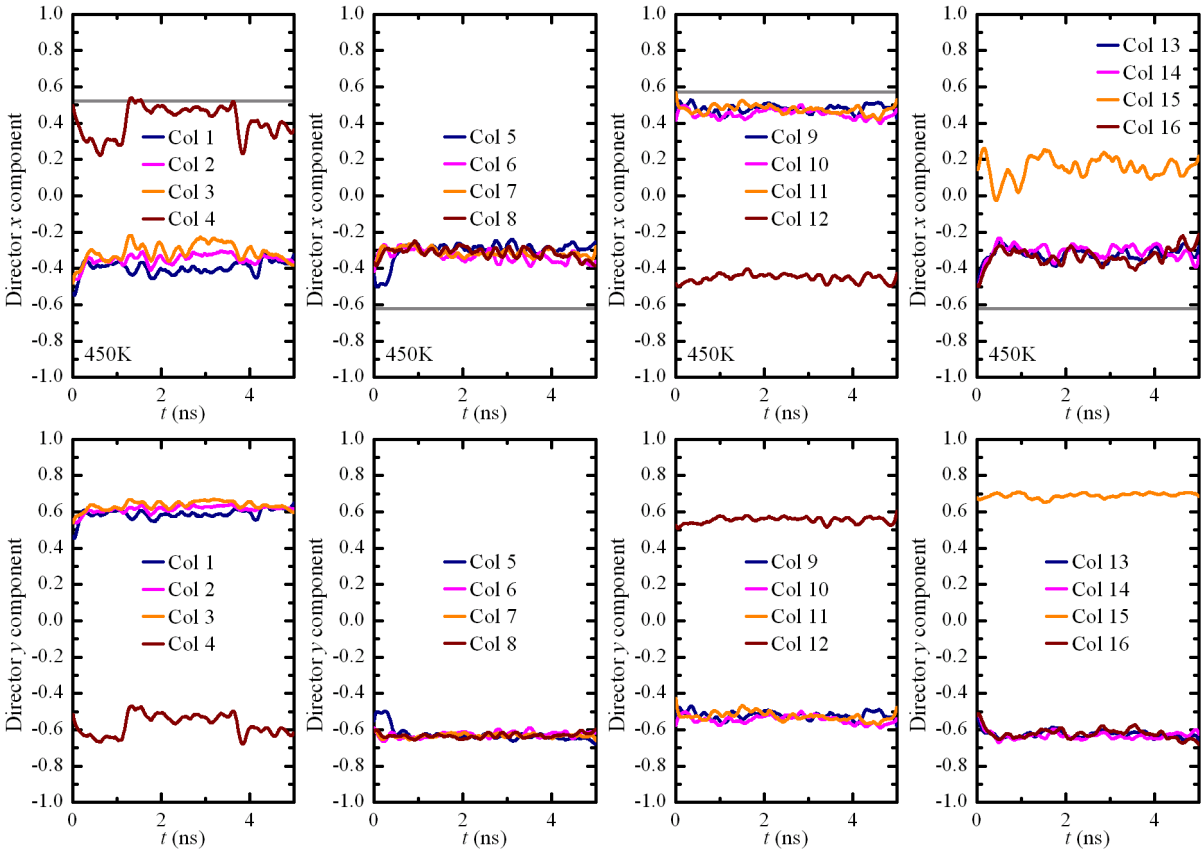

Figure 5.5: Time-series of the x and y orientational director components per column at 450 K. The gray straight lines in the upper diagrams correspond to the average x component at room temperature.

lar assemblies exhibit a pronounced structural robustness with respect to features of the discotic nano-separated phase. Except for the conservation of the tilted profile - although relatively frustrated at 450 K - the twist angle between neighboring discs belonging to the same molecular pillar is drastically limited below 10° for both polymorphs and temperatures examined, except for the folded polymorph at 450 K which manifests a quite diffuse peak situated near 25°. Twist angle distributions are depicted in Figure 5.6.

Table 5.1: Average tilt angle, intracolumnar CoM separation c, and geometrically derived core-to-core distance d per polymorph and temperature.

	Folded			Interdigitated		
T (K)	Tilt (°)	c (Å)	d (Å)	Tilt (°)	c (Å)	d (Å)
300	37.95	4.64	3.67	40.55	4.80	3.65
350	41.28	4.87	3.66	41.22	4.85	3.65
400	40.53	4.86	3.69	41.27	4.89	3.68
450	45.14	5.20	3.67	45.36	5.20	3.65

This tendency towards small twist angles is a characteristic trait of graphitic-like core stacking. As in the case of symmetrically alkyl-substituted HBC cores, CoM projection

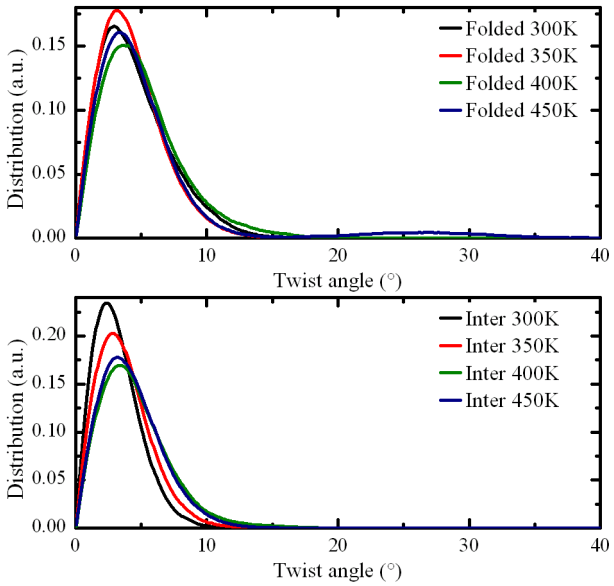

Figure 5.6: Intracolumnar neighboring core twist angle distributions for both polymorphs and at all examined temperatures.

analyses are put to use in order to quantify most probable stacking patterns emerging at different temperatures. Two-dimensional contour plots for both polymorphs are depicted in Figures 5.7 and 5.8 where wireframe representations of the HBC core on which the CoM projection takes place are embedded.

The projected CoM density profiles for both polymorphs at 300 K, 350 K, and 400 K, in conjunction with twist angle maxima located near 3°, suggest a well-defined graphitic-like stacking pattern. The manifestation of contour features away from a single dominant peak is characteristic of parallel sliding movement inside each molecular wire. The rise in temperature seems to assist energy barrier crossing for this localized, trapped sliding motion, leading to the formation of multiple contour areas with significant statistical weight located in areas with 6-fold rotational symmetry with respect to the axes origin.

The fact that the full 6-fold symmetry is not present in the associated contour plots is due to the algorithmic approach for the calculation of projected CoM density profiles. In order to be able to extract consistent results, given a neighboring core pair inside a molecular wire, a reference atom on the core periphery is selected in defining a coplanar core vector for bottom core alignment purposes (see right panel of Figure 4.8). During the crystallographic creation of C12-HBC-PhOTEG lamellar molecular crystals, mesogens belonging to adjacent lamellae were initially rotated about the stacking direction by 180°. As a result, this "symmetry" in atom numbering affects the appearance of projected CoM contour plots.

Upon temperature rise to 450K, the morphology of the projected CoM contours is altered, exhibiting two major peaks at positions consistent again with graphitic-like stacking patterns. In this case, the stacking motifs are similar to the AA graphitic pattern, while at lower temperatures, the most dominant pattern is of the so-called AA' type. Selected molecular representations of dominant stacking patterns are shown as insets in both Figures 5.7 and 5.8.

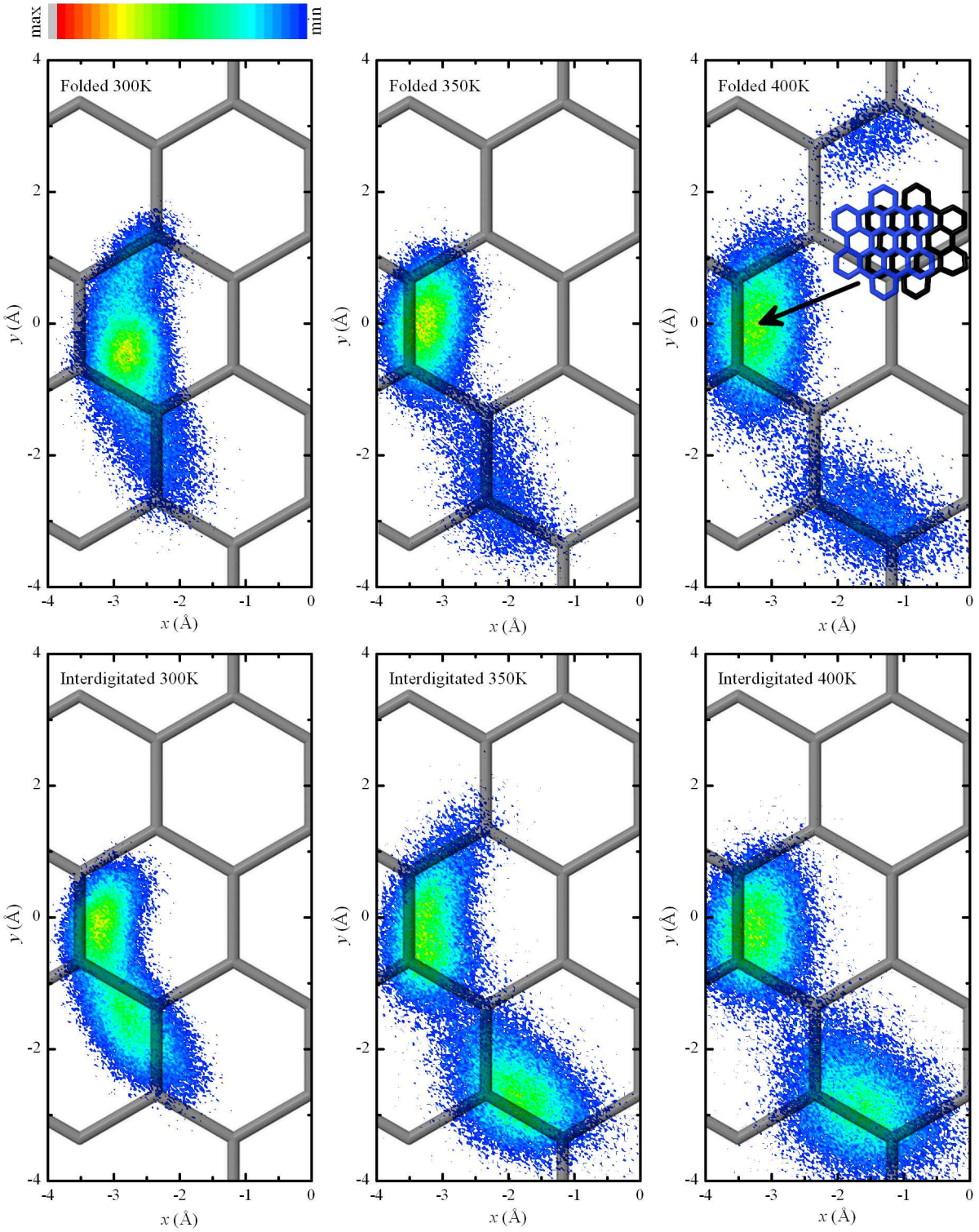

Figure 5.7: Projected core CoM contour plots for C12-HBC-PhOTEG lamellar molecular crystals at three different temperatures and for both polymorphs under study.

As far as structural properties of C12 and TEG side chain nanophases are concerned, a first measure relies on side chain end-to-end vector length distributions. Characteristic histograms for both side chain types and polymorphs are depicted in Figure 5.9 with the TEG curves plotted inside each inset. In the case of the aliphatic C12 nanophase, two

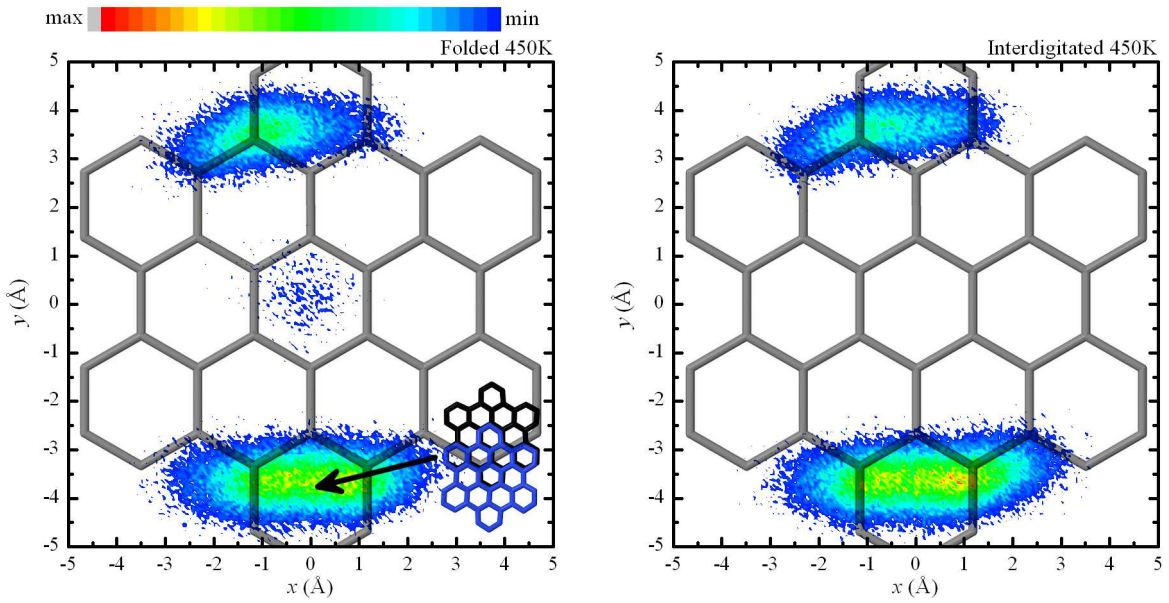

Figure 5.8: Projected core CoM contour plots for C12-HBC-PhOTEG lamellar molecular crystals at 450 K for both polymorphs under study.

dominant peaks are present at room temperature, indicating two distinct ways of C12 side chain protrusion for the lamellar configurations at hand. This characteristic vanishes upon heating at 450 K, resulting in a broader but single maximum peak that is linked to a liquid-like behavior.

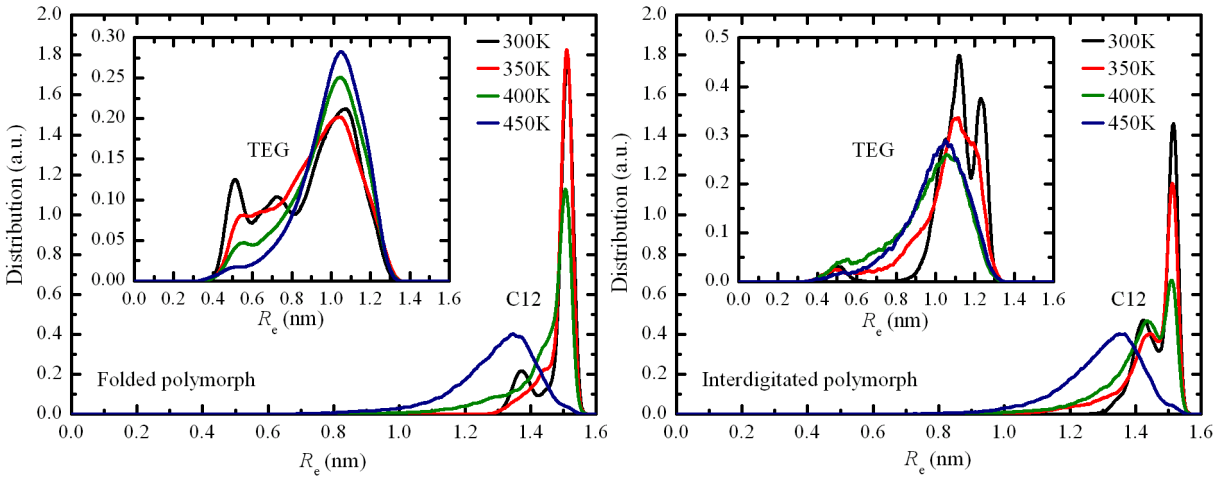

Figure 5.9: C12 and TEG side chain end-to-end vector length distributions for the folded (left) and interdigitated (right) polymorphs for all examined temperatures. Host and inset diagrams correspond to the C12 and TEG nanophases, respectively.

End-to-end vector length distributions for TEG side chains exhibit different profiles at low temperatures, as is expected due to the two different interdigitation schemes. The fact that TEG distributions lose sharp peak characteristics even from the temperature of 350 K is a direct indication of the tendency of the TEG nanophase to melt at a lower temperature compared to the C12 side chain nanophase, even in the case of the interdigitated

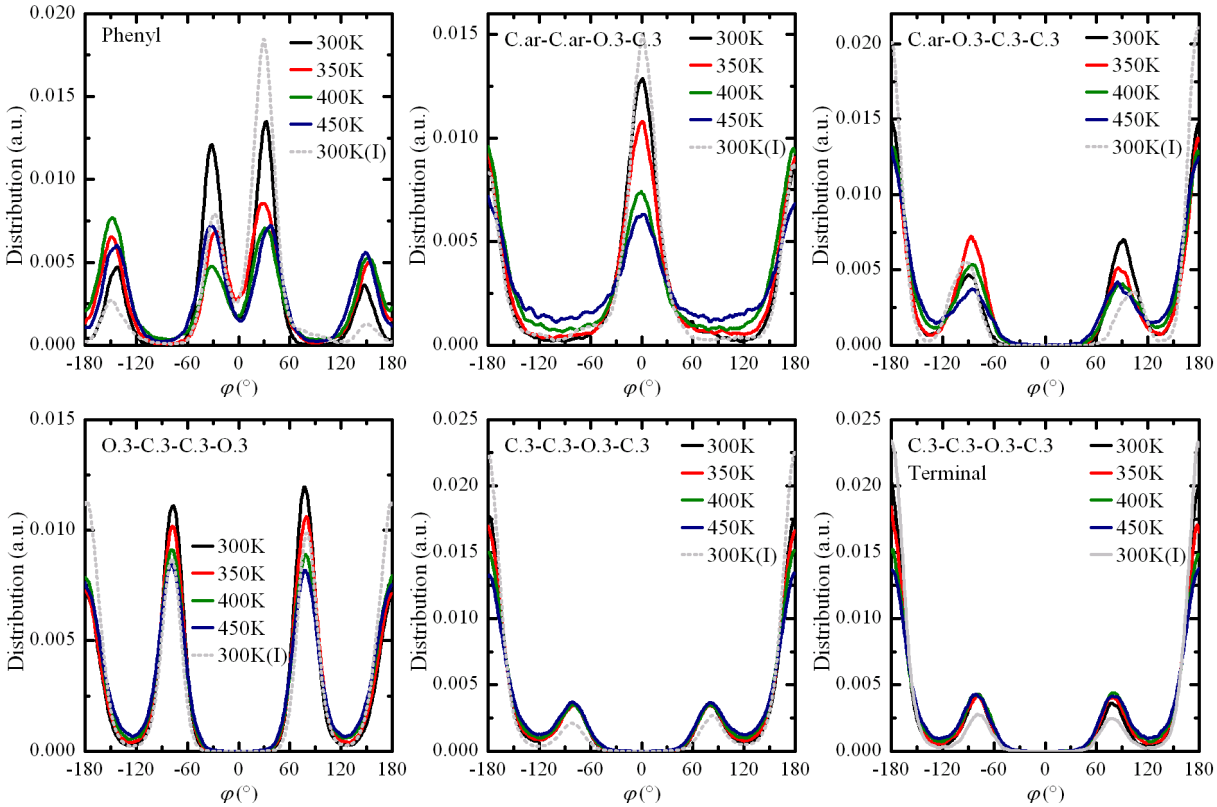

Figure 5.10: TEG side chain dihedral angle distributions for the folded polymorph. The dotted curves correspond to distributions taken from the interdigitated (I) polymorph at room temperature.

polymorph. The reason for this behavior is due to the presence of oxygen backbone atoms that are linked with more easily temperature triggered torsional movement compared to linear alkanes.

A more detailed picture regarding the structural characteristics of the soft, side chain nanophases that insulate the discotic lamellae is gained through backbone dihedral angle conformational statistics should one examine torsional distributions at equilibrium per dihedral type. TEG side chain distributions for the folded polymorph are depicted in Figure 5.10, with the proper dihedral type denoted in each diagram (C.ar, C.3, and O.3 stand for aromatic and aliphatic carbon, and sp^3 oxygen, respectively), along with room temperature curves for the same torsional types for the interdigitated polymorph.

The differences between the two polymorphs at 300 K are evident: *trans* populations for trimodal *trans-gauche-gauche'* (TGG') dihedral types contain higher populations for the interdigitated polymorph compared to the folded one, a behavior consistent with the associated protrusion schemes. Backbone conformational statistics are affected by temperature rise: TGG' types suffer from a decrease in *trans* populations, whereas the other two types show such variations that result in near-equal symmetrical populations at 450 K. The interdigitated polymorph exhibits the same trends with temperature rise as with the folded polymorph.

Dihedral distributions for the aliphatic C12 nanophase are depicted in Figure 5.11 for the folded polymorph. Distributions of the interdigitated polymorph show analogous features and behavior upon temperature rise.

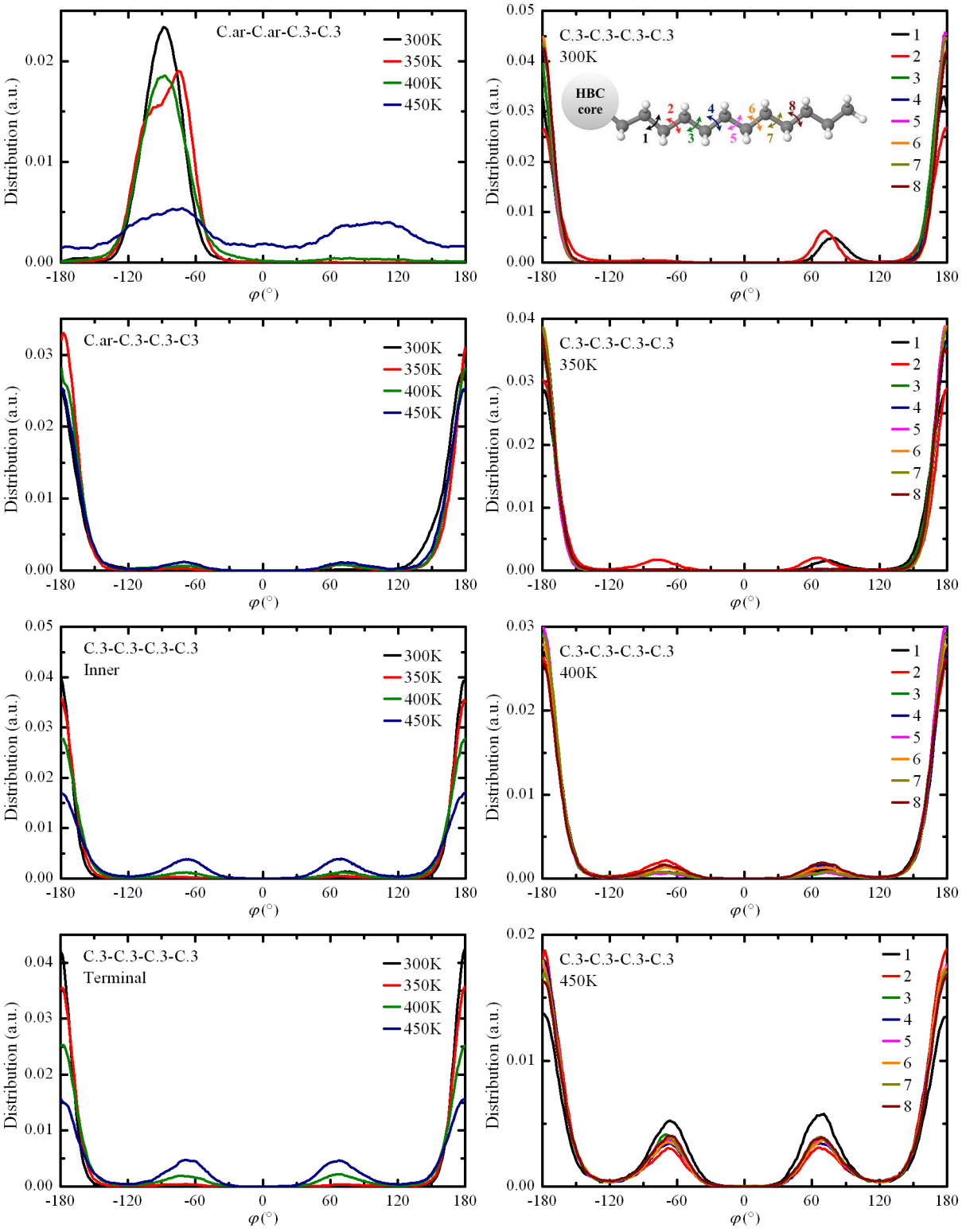

Figure 5.11: C12 side chain dihedral angle distributions for the folded polymorph. The right panel contains detailed distributions of all inner aliphatic torsion types.

The effect of temperature variations are evident: the linking dihedral type C.ar – C.ar – C.3 – C.3 surpasses the torsional energy barrier at 450 K, a strong evidence for C12 side chain melting, and TGG' torsion types generally follow the rule of *gauche* population augmentation upon temperature rise. The right panel of 5.11 contains the sequence of dihedral angle distributions belonging to the inner C.3 – C.3 – C.3 – C.3 type, as is shown in the inset of the top right diagram. The *gauche* defects for types (1) and (2) account for the dual peak of C12 side chain end-to-end vector length distributions depicted in Figure 5.9.

5.2.2 Dynamical Properties

Discotic core movement is quantified through two basic time autocorrelation functions: one is based on second order Legendre polynomial orientational correlation of selected PAH core vectors by means of Equation 4.10, while the other characterizes translational discotic CoM motion via MSD calculations using Equation 4.9.

In the case of vector orientational ACF, two characteristic vectors are taken into consideration: the perpendicular and the coplanar to the discotic core vectors. ACF spectra of the aforementioned vectors for both polymorphs and for all examined temperatures are shown in Figure 5.12.

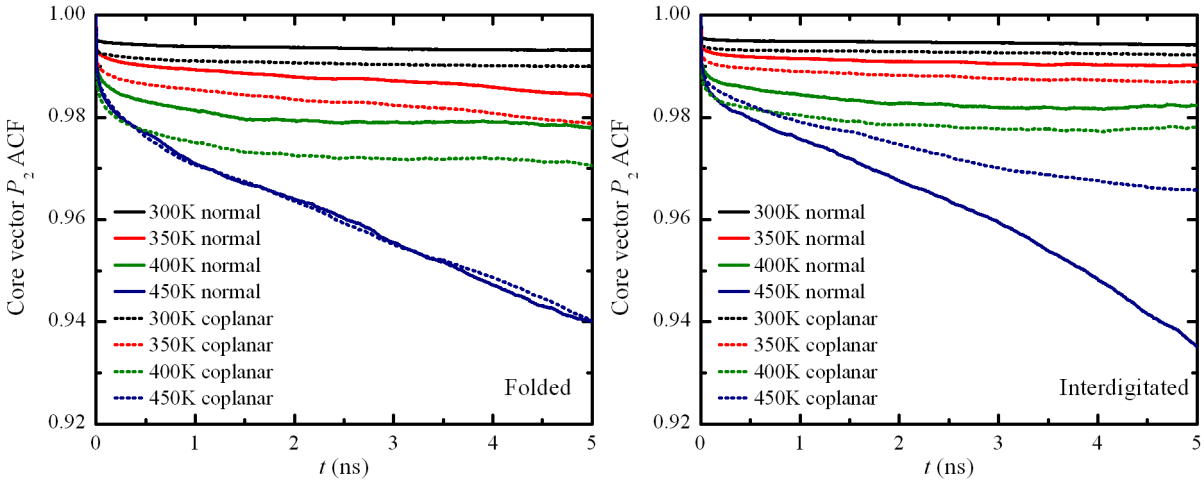

Figure 5.12: Second-order Legendre polynomial ACFs of the normal and coplanar core vectors for the folded (left) and interdigitated (right) polymorphs.

The saturation of vector ACF functions at relatively hard plateaus above 0.97 for temperatures ranging between 300 K and 400 K suggests minimal core librational movement. As regards the comparison between the movement of the normal and coplanar core vectors, the latter is manifested at lower plateaus with respect to the former, concluding that the rotational motion about the normal vector is more pronounced than the rocking motion of the normal vector itself. At the temperature of 450 K, vector movement is

further augmented, nevertheless without reaching low values that are linked with partial or total memory loss of the initial state and randomization of core vector movement.

Vector ACF analyses are also carried out for side chain end-to-end vectors as a measure of the mobility of the very factors that induce thermotropic variations due to the pronounced thermal motion of articulated functional groups. Relevant ACF spectra for both C12 and TEG side chains are illustrated in Figure 5.13.

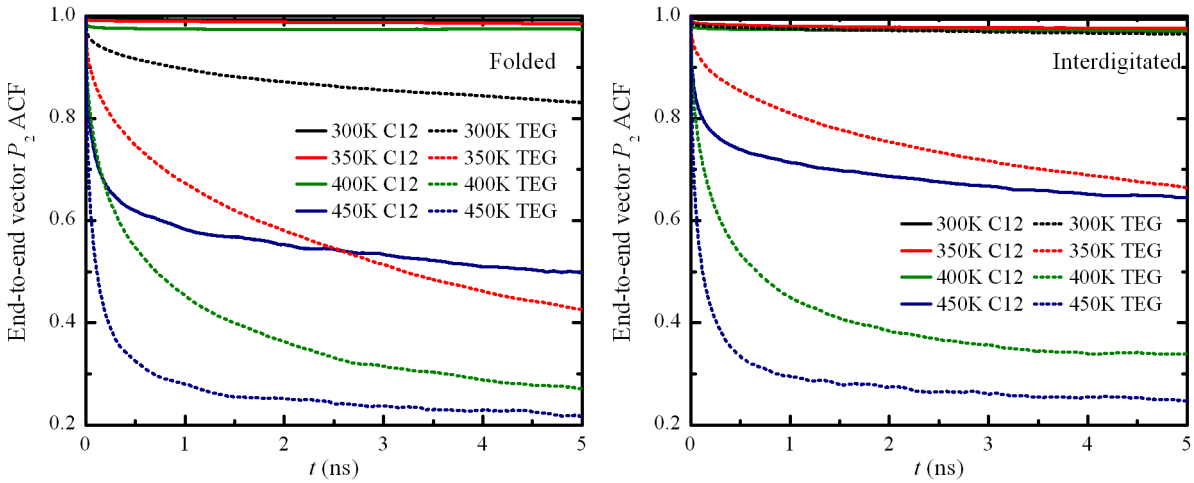

Figure 5.13: Second-order Legendre polynomial ACFs of the side chain end-to-end vectors for the folded (left) and interdigitated (right) polymorphs.

The solid curves in both panels of Figure 5.13 describe the orientational autocorrelation mechanism of the initially interdigitated C12 side chains of both polymorphs. The fact that for temperatures ranging between 300 K and 400 K, C12 side chain ACFs are saturated near unity suggests that this molecular motion is very limited, with the aliphatic C12 functional groups at full interdigitation serving as near-rigid hydrophobic spacers between lamellae.

TEG side chain orientational autocorrelation is shown by the dotted curves in Figure 5.13. As regards the interdigitated polymorph (right panel), the movement of TEG groups is limited at room temperature as a result of the interdigitated nature of the side chains. The thermal activation of this particular movement is accomplished at temperatures above 350 K. For the folded polymorph, even at 300 K, TEG side chain movement is pronounced and further augmented at elevated temperatures.

In the case of molecular translation motion, CoM MSD functions are evaluated for both systems for all examined temperatures, taking into consideration only discotic core atoms for the derivation of molecular CoMs in order to factor out artefacts due to the variable side chain arrangements. MSD components along the three Cartesian directions of the orthogonal supercell enclosing all atoms are depicted in Figures 5.14 and 5.15, with the solid, dotted, and dashed curves corresponding to MSD components at 300 K, 350 K, and 400 K, respectively, in Figure 5.14.

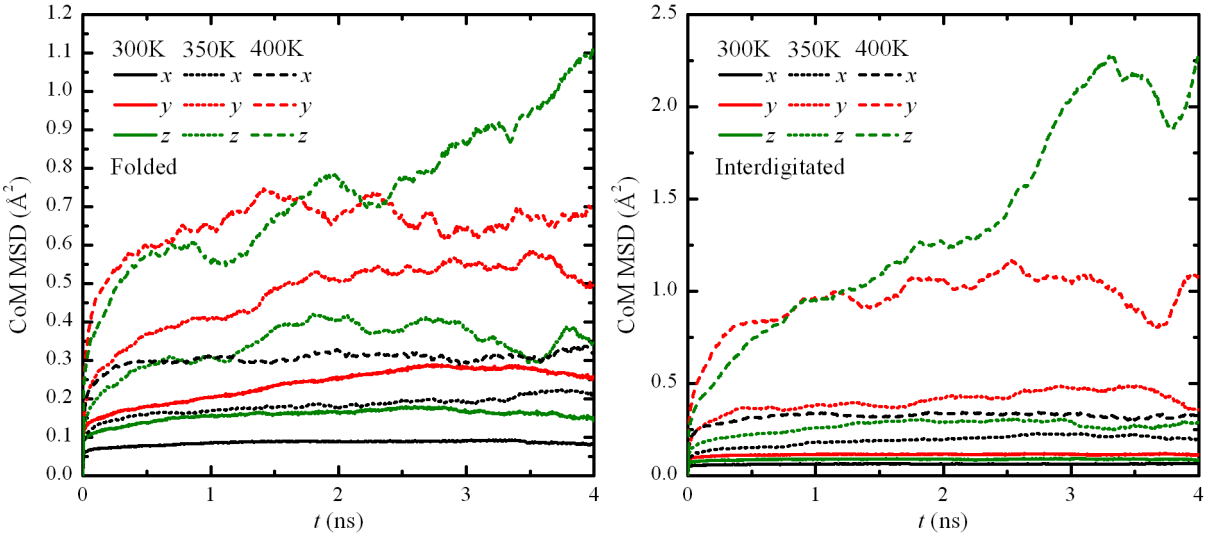

Figure 5.14: Discotic CoM MSD functions for the folded (left) and interdigitated (right) polymorph at the three temperatures of 300 K, 350 K, and 400 K.

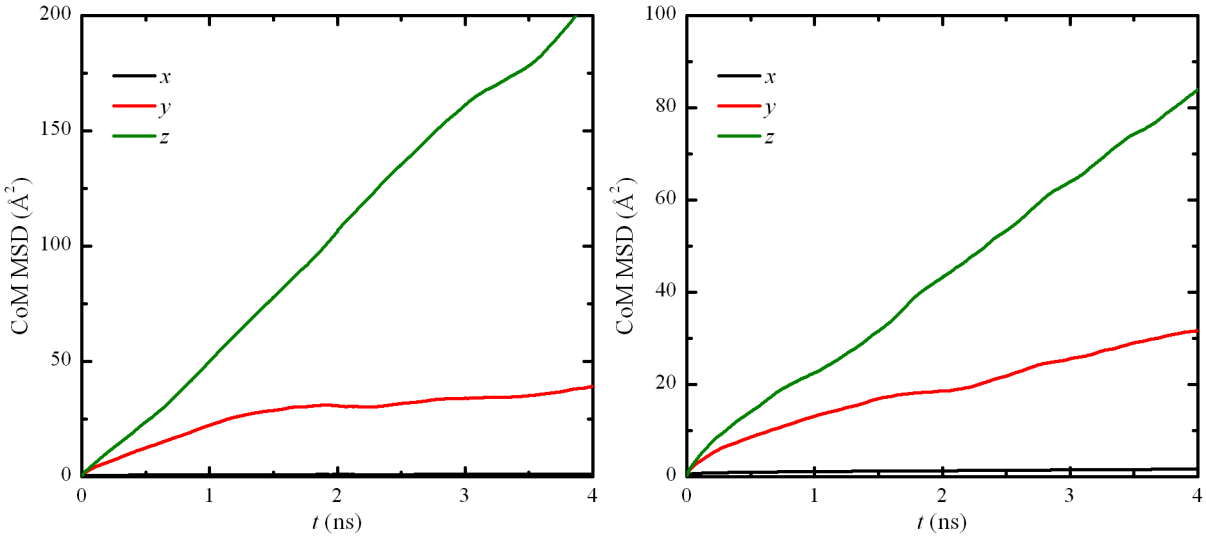

Figure 5.15: Discotic CoM MSD functions for the folded (left) and interdigitated (right) polymorph at 450 K.

Both polymorphs form neatly stacked lamellar supramolecular assemblies with minimal molecular translational movement, as is indicated by the small values of CoM MSD below 2.5 Å^2. A thermotropic liquid-crystalline behavior is triggered at the temperature of 450 K by means of two distinct motion types: a moderate lamellar movement along the y direction and a pronounced movement along the z direction which is aligned with the stacking direction of the discotic molecular wires.

The two polymorphs exhibit differentiated translational motion with respect to the original interdigitation state of the TEG nanophase, with the folded polymorph showing faster translational motion. This behavior is consistent with dynamical findings regarding

core and side chain vectors, since the folded polymorph manifests faster decorrelation for all vectorial mechanisms examined compared to the interdigitated polymorph.

It should be noted that the compound lamellar movement decomposed onto the y and z directions is identified as an *en-masse* motion without breaking apart the lamellar morphology and exhibiting oscillatory-like effects without the existence of a dominant direction of constant flow diffusion.

5.3 Conclusions

Lamellar molecular crystals comprised of amphiphilic C12-HBC-PhOTEG mesogens have been studied be means of MD simulations. Initial configurations involved two candidate room temperature polymorphs differentiated with respect to the morphology of the TEG nanophase. Molecular crystals under study retain their lamellar organization, exhibiting thermotropic liquid-crystalline behavior triggered at the temperature of 450 K while maintaining crystalline characteristics up to the temperature of 400 K.

Upon heating to 450 K, sizable expansion along the direction normal to the lamellae (x) is noticed, a phenomenon attributed to the disengagement of originally interdigitated C12 side chains. At the same time, negative thermal expansion is taking place along the y direction, that is parallel to the lamellar planes and normal to the molecular wire stacking direction. The mechanism behind this behavior involves different collective motions, such as rotations of the columnar orientational directors describing the core tilt state, resulting in configurations where the orientational directors are arranged in a near-parallel way with respect to the lamellar planes, followed by a tilt increase and minor molecular wire misalignment. CoM distances along the stacking direction z varies accordingly in order to maintain a core-to-core distance near the nominal values of 3.65 Å.

Discotic core stacking analyses indicate that up to the temperature of 400 K, i.e. before the melting point, HBC cores are arranged in a tilted fashion inside each lamella, exhibiting graphitic-like stacking patterns, with the AA' motif carrying significant statistical weight. Upon entering the liquid-crystalline phase at 450 K, the stacking pattern is transformed to an AA graphitic-like motif. This stacking pattern transition should be attributed to the rotation of the orientational directors facing away from the normal to the lamellae direction.

The melting point towards the liquid-crystalline phase is firmly located above 400 K. The TEG nanophase begins melting at relatively lower temperatures, as is shown by side chain end-to-end vector analyses. At the temperature of 450 K, strong evidence of liquid-crystalline behavior is identified via molecular core MSD analyses, unveiling a compound lamellar, *en-masse* motion along both y and z directions, with more pronounced movement along the stacking direction z. Nevertheless, lamellae slide with respect to one another without compromising their integrity and tilted nature. The reason behind

this behavior should be attributed to the layered, ternary nature of the supramolecular assembly, with the three nanophases (C12, HBC, TEG) kept separated over the examined temperature range, well below the isotropization temperature. Furthermore, the two "missing" side chains compared to hexa-substituted HBC derivatives serve two major purposes: better discotic aggregation inside each lamella and a diminished entropic effect.

The conservation of tilted discotic arrangements with graphitic-like stacking patterns is of major importance regarding possible organic electronics applications, since such molecular arrangements are linked to effective charge transfer rates. Another highly intriguing aspect is the possibility of lamellar immobilization by means of partial side chain polymerization. Should appropriate terminal side chain groups be used[47], a thermal activated cross-linking can effectively "lock" lamellar motion, while trapping the discotic cores in fine arrangement inside each lamella at highly sought graphitic-like stacking patterns, thus resulting to structurally and mechanically robust cross-linked discotic lamellas with high conducting capabilities.

Chapter 6

Molecular Simulations of Extended and Covalently Linked Discotics

This chapter focuses on the examination of molecular assemblies comprised of functionalized extended PAHs and discotic "super-molecules" resulting from the covalent linking of various cores. A hierarchical approach is adopted for the construction of plausible initial configurations, starting from the level of molecular dimers, to isolated molecular wires and, finally, to molecular crystals, utilizing a hybrid MC growth scheme for the generation of the side chain nanophase. Connections with single molecule QM results are established towards the evaluation of charge transfer capabilities in conjunction with information gained from empirical atomistic simulations.

6.1 Systems of Interest and Computational Details

6.1.1 Preliminaries

In this chapter, systems under study include soluble nanographene molecules based on HBC, C96, and C132 discotic cores (Figure 1.2: **16**, Figure 1.15: **53**, and Figure 1.15: **55**, respectively) with appropriate side chain functionalization. The present study focuses on the so-called hexagonal mesophase, in which molecular wires made up by stacked discotic mesogens self-organize into a hexagonal arrangement. In order to carry out a sound comparative study with respect to the surrounding alkyl nanophase, all systems are grafted with phytane ($C_{20}H_{43}$, also referred to as C16,4; see Figure 1.6: **c**) side groups. For comparative purposes, dodecane (C12) groups are utilized in the case of the C96 discotic core.

Along with single PAH core molecules, a series of covalently linked "super-molecules" grafted with C16,4 side chains are also considered. The first kind of "super-molecule" is the dumbbell-like HBC-DB molecule. (Figure 1.16: **57**) The rest are star-shaped tri-arm assemblies (Figure 3.2) utilizing a TPB linker and HBC, C96, and C132 peripheral

cores, also carrying C16,4 groups on specific grafting sites. Furthermore, in the case of TPB-linked molecules, a special case of asymmetrically functionalized cores is examined where two out of three core molecules bear C16,4 side groups and the third is kept in its pristine form.

Empirical MD simulations are utilized for the equilibration and the examination of structural and dynamical properties. Calculations in the isothermal-isostress statistical ensemble are carried out by means of the MTK EoMs[317] using a time constant of 100 fs for temperature control and 2500 fs for pressure control. A time step of 1 fs is used for all simulations and periodic boundary conditions are applied. Long range interactions are treated in the reciprocal space via PPPM mesh-based methods.[306;326] All empirical atomistic simulations are carried out using the open-source software LAMMPS.[318]

6.1.2 Force Field and Initial Configurations

As regards the utilized FFs, atomistic simulations are carried out employing two different force fields. To be more precise, for all-atom MM dimer simulations, the CGenFF[337;338] force field is used and for hybrid all-atom/united-atom MM and MD simulations, a combination of GAFF[327], OPLS[328;329] and GROMOS[342] force fields is utilized (see Table 4.1). Appropriate force field terms missing from the aforementioned compilation are taken from the work of Marcon *et al.*[195]

Two extra terms for bonded interactions are not included in Table 4.1: the proper dihedral angle describing the torsional barrier for covalently linked phenyl rings via a single bond and the improper dihedral angle regulating the out-of-plane tetrahedral arrangement pertinent to C16,4 side chains for the backbone sites where pendant methyl groups are attached. The former is quantified via a cosine expansion described by Equation 2.82 with $V_1 = 0.00$, $V_2 = -8.85$, $V_3 = 0.00$, and $V_4 = 5.52$, all expressed in $\mathrm{kcal\,mol^{-1}}$, and the latter through a simple harmonic expression with a force constant of $80.02\,\mathrm{kcal\,mol^{-1}\,rad^{-2}}$ and an equilibrium improper torsion value of 35.26°.

A challenging aspect of computational studies of soft matter systems is the construction of realistic initial configurations for atomistic simulations. In order to address this issue, all flexible side groups protruding from discotic columnar assemblies, either in the bulk or in isolated wires with one-dimensional periodicity, are grown following a bond-by-bond MC growth scheme[343], combined with geometry optimizations for the alleviation of unwanted atomic overlaps.

A key factor inherent to the growth mechanism of linear oligomeric molecular segments involves backbone conformational statistics. Once the statistical profile of backbone proper dihedral angles is defined by means of a probability density function (PDF) $\rho(\phi_i)$, the growth procedure selects a predefined number of candidate dihedral angles N_{trial} weighted according to the *a-priori* PDF. Out of all trial growth moves, one is selected

with a probability

$$p\left(\phi_i\right) = \frac{w\left(\phi_i\right)}{\sum_{j=1}^{N_{\text{trial}}} w\left(\phi_j\right)} \tag{6.1}$$

where $w\left(\phi_i\right)$ is the Boltzmann weight for an i-th growth move:

$$w\left(\phi_i\right) = \rho\left(\phi_i\right) \exp\left(-\frac{\Delta U_i}{k_{\text{B}} T}\right) \tag{6.2}$$

In the above equation, ΔU_i stands for the non-bonded energy difference between the trial growth move and the previous to the growth step state and T is the temperature at which the MC growth scheme is attempted.

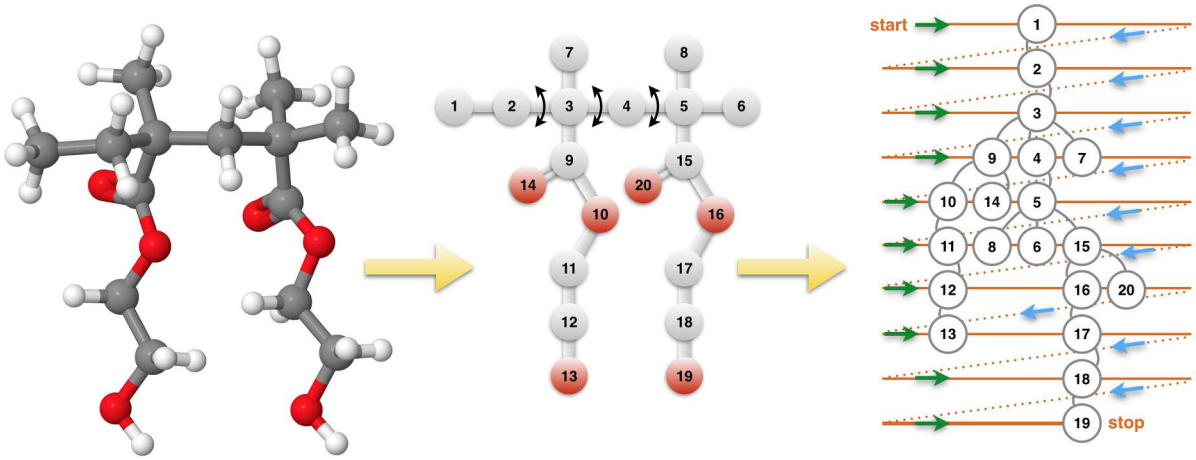

Figure 6.1: The reduction of an acyclic, branched molecular segment (left) to an algebraic tree structure (middle), that is eventually traversed via a level-order tree search algorithm (right). The black, double-ended curved arrows in the central depiction symbolize backbone dihedral angles subject to the MC biasing scheme. The "attacking" atom that is to be grafted first to a predefined growth site on a "seed" molecule is the atom labeled "1".

As far as some critical algorithmic issues are concerned, the bond-by-bond building scheme relies on a topological reduction of given acyclic macromolecular chains having fixed first-neighboring topology, with arbitrary branching, to tree structures. A detailed description of the building process is as follows: given a periodic supercell, "seed" molecules are placed on fixed positions, either on periodic sites or at random, optionally obeying certain orientation profiles enforced via Euler rigid rotations about molecular CoMs. "Seed" molecules are categorized into certain types according to their molecular identity, the kind of articulatedr molecular segments that are to be grown from them, and the so-called growth sites on them, i.e. predefined atoms from which the growth sequence is to commence. Every macromolecular segment that is to be grown from a given growth site is reduced to an algebraic tree which is eventually sequenced via a level-order

tree traversal scheme, thus dictating the order of addition of molecular segments. Growth sites are topologically updated during the bond-by-bond chain generation procedure, until the whole macromolecular segment is fully grown. An illustration of the aforementioned procedure is shown in Figure 6.1 for a hydroxyethyl methacrylate (HEMA) dimer.

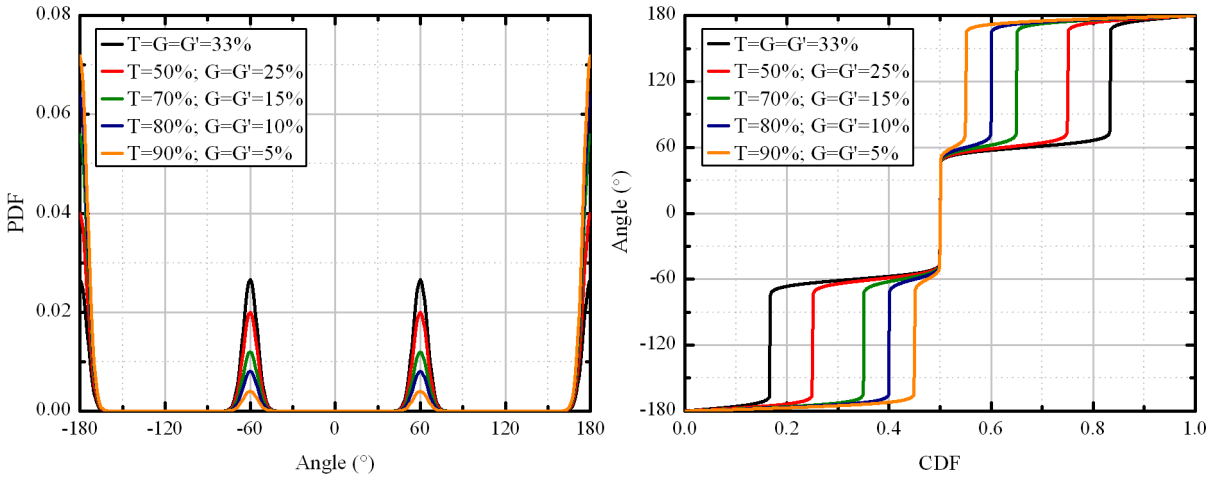

Figure 6.2: Probability density functions (left) and inverse cumulative probability density functions (right) for a *trans-gauche* system with variable population percentages and symmetric *gauche* states.

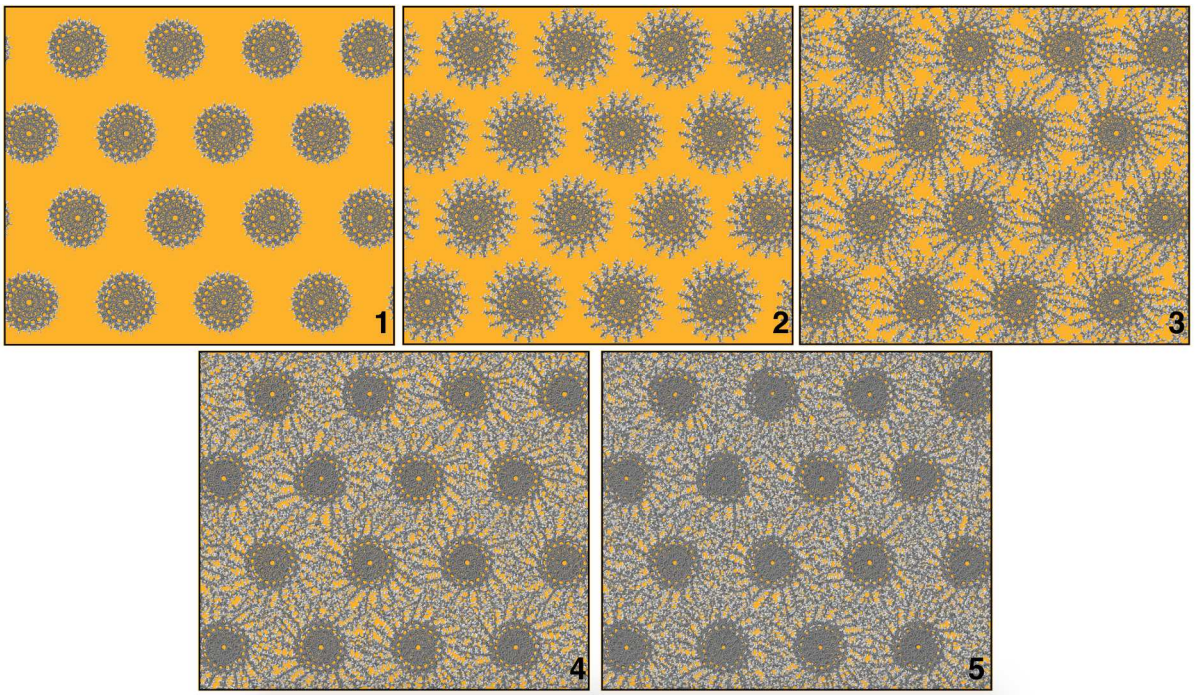

Figure 6.3: Illustration of the aliphatic nanophase growth procedure from molecular wires comprised of pristine discotic molecules.

Backbone atoms are explicitly defined through appropriate labeling, hence enabling the statistical biasing scheme described by Equations 6.1 and 6.2. This very torsional

biasing is accomplished by defining a specific PDF for every backbone dihedral type, using distributions relevant to the hybridization state of backbone atom types. A typical *trans-gauche* trimodal PDF is depicted in Figure 6.2. Once a torsional PDF is given, the cumulative PDF is resolved (CDF) and is used in conjunction to a uniform random number generator in order to produced structurally biased dihedral angle values. Characteristic CDFs for a *trans-gauche* system, with variable *trans* percentages and considering that *gauche* and *gauche'* states are equally probable, are illustrated in Figure 6.2.

The stereochemical biasing is further weighted using energetic criteria by means of Equation 6.2, resulting in structures with minimal geometric overlap. It should be noted that a linked-list cell spatial discretization method is utilized, centered on every growth site, resulting in a system size scale-free performance for the evaluation of non-bonded interactions. Severe molecular overlaps are avoided, even at high densities, by means of frequent energy minimization steps.

This combination of geometric optimizations by means of static energy minimization algorithms (typically a Conjugate-Gradient scheme) and the stereochemically and energetically biased MC sequential growth scheme constitutes a hybrid MC macromolecular growth algorithmic paradigm, resulting in structures with minuscule atomic overlaps. This approach allows the relatively easy growth of articulated molecular segments in the vicinity of non-accessible domains (nanoparticles or interfaces) while utilizing the benefits of the applied, well-established, MC growth methodology[343].

The hybrid MC growth methodology is applied for discotic systems in a core-shell manner: stacked discotics constitute "hard" molecular wires that play the role of a core phase and protruding side chains emerge as elements of the soft shell phase that surrounds every wire, allowing variable interdigitation levels according to the proximity of discotic nanowires with respect to one another. A straightforward utilization of this procedure can result in the creation of oligomeric and polymeric systems, either in pure state or in mixtures (random or nanostructured), and even in the presence of nano-inclusions. For example, initial configurations of polymer matrix nanocomposites can be created with this algorithm.

A pictorial example of the growth methodology is illustrated in Figure 6.3 for a system of stacked discotics forming molecular wires, from which the aliphatic nanophase is subsequently grown.

For the generation of C12 and C16,4 side groups, the hybrid MC growth method described above is employed, utilizing an 80% *trans* backbone dihedral angle profile.[344] The results of the bond-by-bond building process were validated for C12 melts, for which the original *trans* ratio imposed during the growth procedure was conserved. From a structural point of view, the applied building procedure for C12 systems reproduces the reported end-to-end distance of $\sim$1.23nm at room temperature.[344] Explicit hydrogen configurations are subsequently mapped onto a well-tested for discotic systems hybrid

united-atom/all-atom representation via the unification of aliphatic hydrogen atoms with their first neighboring sp^3 carbon atoms.

6.1.3 Properties Under Study

As regards the structural characterization of the examined systems, distributions of CoM separations are employed for the quantification of intra- and inter-molecular structure. In-plane core vectors are used for the evaluation of the twist angle between neighboring mesogens and perpendicular core vectors are utilized for the determination of the orientational order tensor $\mathbf{Q}$ (Equation 5.2). The tilt angle is resolved relying on the evaluation of the angle between the orientational director $\hat{n}$ - accessible through the diagonalization of $\mathbf{Q}$ - and the CoM director $\hat{n}_{\mathrm{CoM}}$ for each molecular column. Furthermore, structural features of the aliphatic nanophase are probed via typical proper dihedral angle distributions and side chain end-to-end vector analyses on both magnitude and orientation via the local tangential Cartesian system utilized for HBC derivatives (Figure 4.4).

Dynamical properties are calculated via the examination of the temporal behavior of vector orientation, while translational motion is dynamically probed through CoM MSD calculations. A multiple time origin calculation scheme is applied for all of the aforementioned dynamical features.

6.2 Results and Discussion

6.2.1 From Molecular Dimers to Molecular Wires

Discotic dimers comprised of HBC, C96, and C132 cores with short side chain functionalization are geometrically constructed and structurally optimized, in order to gain insight regarding favorable stacking patterns. The HBC derivative is used for FF validation purposes. Dimer construction is illustrated in Figure 6.4: (1) a discotic molecule is replicated and displaced along the perpendicular vector $\vec{p}$ by a distance d, (2) the "upper" molecule is rotated by a given twist angle, (3) a parallel displacement direction is chosen, and (4) the "upper" core is displaced by d_{off}.

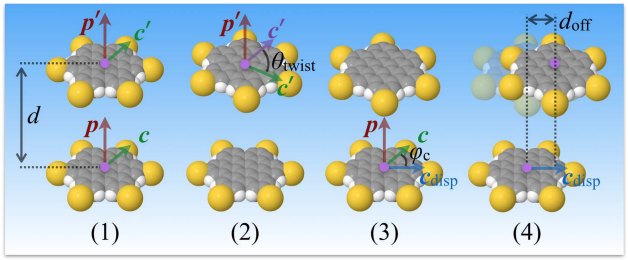

Figure 6.4: The geometric procedure for the creation of a discotic dimer. The bulkier gold spheres correspond to the side chain grafting sites.

For every molecular dimer constructed, a static geometry minimization is utilized in order to obtain a relaxed structure associated with a potential energy minimum. The

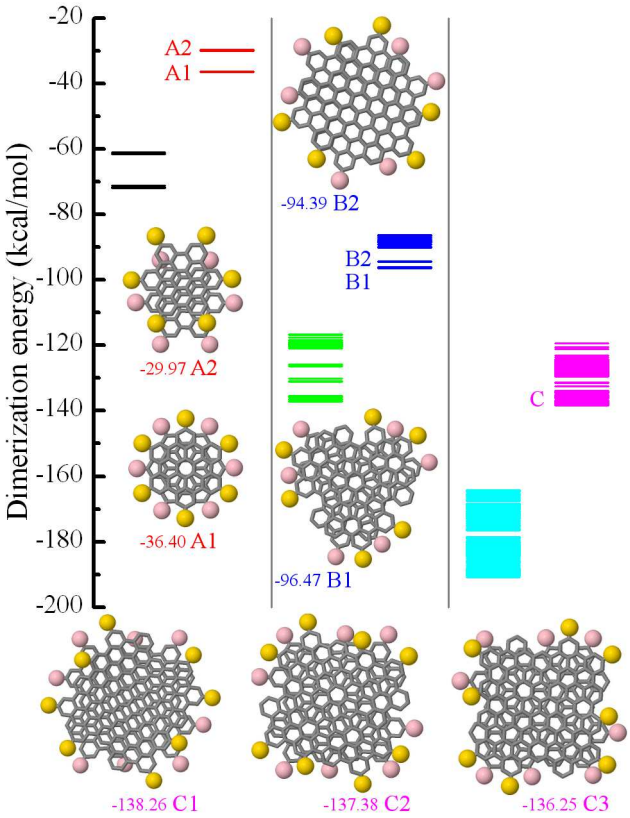

Figure 6.5: Dimerization energy minima and associated stacking patterns for HBC-C6 (left), C96-C6 (middle) and C132-C6 (right). In each panel, the left states register the total dimerization energy and the right states the core atoms dimerization energy. The pink and yellow spheres represent the linking side chain sites for the lower and upper molecule, respectively. Every low energy stacking pattern is shown alongside its core energy.

dimerization energy minima evaluated for every configuration are reported in Figure 6.5. The dimerization energy is calculated as the sum of all non-bonded intermolecular interactions. The left, middle and right diagram panels correspond to energy data for hexa-*n*-hexyl substituted HBC (HBC-C6) and C96 (C96-C6) and octa-*n*-hexyl substituted C132 (C132-C6) cores, respectively. Furthermore, each panel contains two data categories: the ones situated on the left (black, green and cyan) correspond to the total dimerization energy of the system, while the ones situated on the right (red, blue and magenta) to the core atoms dimerization energy. This refinement was deemed necessary in order to clarify the lowest core energy states and the associated stacking patterns. In the same figure, illustrations of these low energy stacking patterns are shown for every system.

For HBC-C6, there are two core energy minima: the global minimum A1 (see Figure 6.5) corresponds to a "daisy-like" stacking pattern with a twist angle of 30° and the local minimum A2 to a parallel displaced dimer configuration. The lowest energy structural results are in agreement with *ab-initio* findings from the literature[151] while the geometry of the A2 minimum is similar to the stacking pattern proposed by experimentalists for crystalline HBC-C12[26] and recently identified[345] as the metastable AA' graphitic stacking pattern.

In addition, to support the validity of the utilized hybrid force field, the same dimer calculations were carried out using the CGenFF force field with explicit hydrogen atoms.[337;338]

The minimum energy structures obtained coincide with the ones reached via the simpler FF, strengthening confidence in its predictive power.

As far as the stacking patterns of the other two mesogens are concerned, C96-C6 exhibits two refined minima: the global minimum B1 that is inherent to a daisy-like stacking pattern of a 20° twist angle and the local minimum B2 which corresponds to a graphitic AA stacking resulting after a 60° core rotation. For C132-C6, the stacking energetics appear more complicated, even after the core atoms energy refinement. This system exhibits a wide band of low energy states (labeled C in Figure 6.5). Upon careful inspection, this band supports three dominant stacking patterns: a graphitic-like pattern C1 that results after a 60° twist angle, and two daisy-like patterns, C2 and C3, with a twist angle of 20° and 90°, respectively, all listed in an ascending order with respect to the core atoms dimerization energy.

Information regarding minimum energy stacking patterns for C96 and C132 PAHs is used in order to create molecular wires with plausible internal stacking substructure. In the case of C96 based systems, the existence of minima B1 (20° twist angle) and B2 (60° twist angle) prompts the utilization of three symmetric stacking motifs: a 60° twist angle profile that corresponds to a graphitic-like AA stacking, an alternating 20° twist angle profile and a helical 20° twist angle stacking profile.

Once the internal molecular wire structure is determined, side chains are created using a MC growth scheme and the resulting systems are equilibrated via MD simulations. An interesting characteristic of non-chiral dodecyl substituted C96 molecular wires is the transition to the helical 20° twist angle stacking profile upon heating to 400 K. Twist angle time series of a periodic C96-C12 molecular wire initialized with a graphitic stacking pattern are shown in Figure 6.6 alongside molecular representations of the initial and final structures with lifted periodic boundary conditions for clarity. In the following molecular depictions, bulky green spheres correspond to aromatic linking carbon atoms where side chains are grafted, blue graphical elements are assigned to aliphatic -CH_2- units and the red ones to terminal -CH_3 units.

The utilization of heavier and bulkier C16,4 side chains decelerates the transition between different stacking patterns. To overcome this obstacle, MD simulations at higher temperatures were employed. During these simulations, the 60° stacking pattern gradually transforms to patterns with 20° twist angle, with the temperature rise expediting the transition. Similarly to C96-C12 molecular wires, the most stable stacking pattern arising from MD simulations is the chiral arrangement with a 20° twist angle.

In the case of C132 cores, the three low energy stacking patterns of 20°, 60° (graphitic) and 90° twist angle identified via MM dimer calculations lead to five molecular wire stacking profiles. Four of them correspond to alternating and helical arrangement bearing 20° and 60° twist angles, while the fifth is constructed considering a 90° twist angle. It should be noted that the 2-fold symmetry of C132 can support a 60° helical motif, as

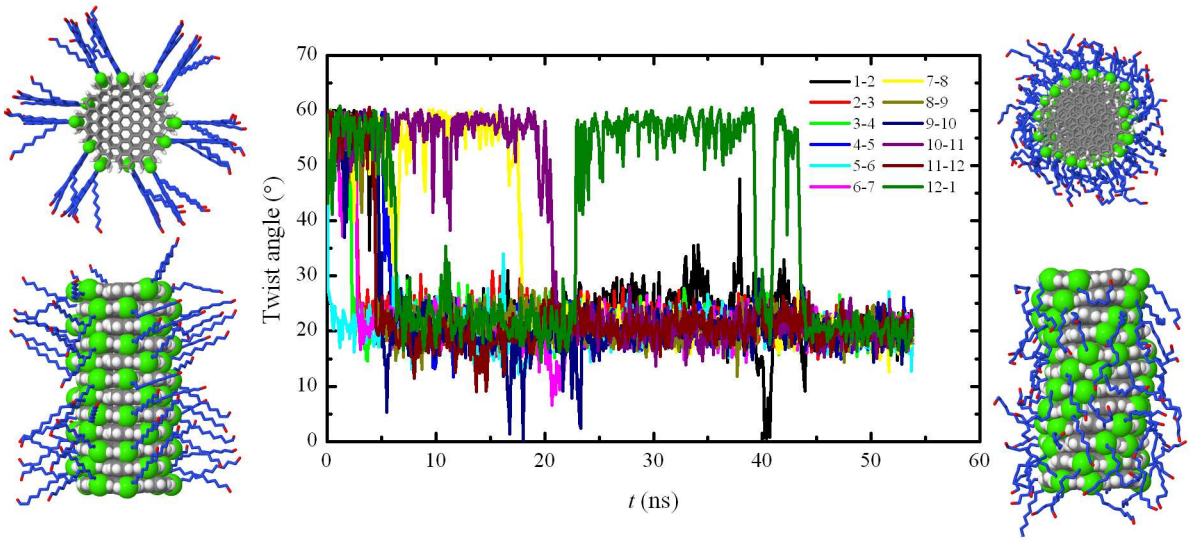

Figure 6.6: Twist angle time series at 400 K of a periodic C96-C12 molecular wire comprised of twelve molecules and initialized to a graphitic-like stacking pattern. Molecular representations on the left and on the right side of the diagram correspond to top and side views of the initial and final states, respectively.

opposed to C96 where the 3-fold molecular symmetry cannot discriminate between a possible alternating or chiral nature for the 60° twist angle stacking pattern.

Simulations of C132-C16,4 molecular wires exhibit a slower temporal evolution due to the augmented molecular weight of the mesogens. Graphitic stacking patterns with both alternating and helical arrangements transform at elevated temperatures to mixed stacking patterns with both 20° and 90° twist angles. Twist angle time series and molecular snapshots for a chiral 60° C132-C16,4 periodic nanowire with initial graphitic arrangement are depicted in Figure 6.7.

From the initial five stacking configurations examined for C132-C16,4 molecular wires, both alternating and helical graphitic-like profiles were found metastable, since transitions to mixed 20°/90° stacking profiles were manifested upon sufficient temperature rise. On the other hand, both alternating and helical 20° patterns and the 90° twist angle stacking pattern remain structurally invariant.

Based on all aforementioned findings, for bulk simulations we choose to examine pristine helices of 20° twist angle for C96 based systems and four different stacking variants for C132-C16,4: the alternating 20° and 90° profiles, the helical 20° profile and the mixed 20°/90° stacking motif.

6.2.2 Molecular Crystals of Extended Discotics

Preliminaries

Periodic molecular crystals comprised of grafted discotic molecules with intracolum-

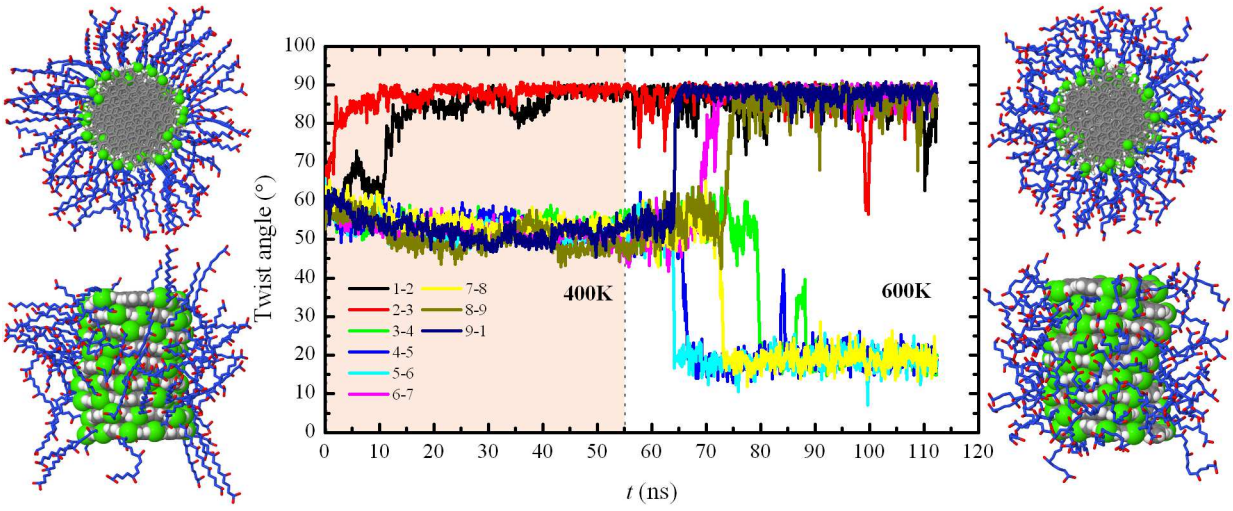

Figure 6.7: Twist angle time series at 400 K and 600 K of a periodic C132-C16,4 molecular wire comprised by nine molecules and initialized to a graphitic-like stacking pattern. Molecular representations on the left and on the right side of the diagram correspond to top and side views of the initial and final states, respectively.

nar structure in accordance to single column simulations findings are generated via the application of the hybrid MC growth methodology. Initially, nanographene pillars of stacked pristine PAH molecules with predefined twist angle profiles are placed on a two dimensional hexagonal lattice, with lattice constants taken from experimental data.[61] The aliphatic nanophase is subsequently grown, avoiding this way any possible structural artefacts that could arise should pre-grown isolated molecular wires be brought into proximity for the creation of the molecular crystal.

All bulk systems are made up of sixteen supramolecular columns, with each column bearing a variable number of molecules in order to adhere to the applied periodic conditions. To be more precise, HBC and C96 based molecular crystals contain twelve molecules per column. C132 based systems with alternating 20° and 90° twist angle have ten molecules in each column and the remaining chiral system with a twist angle of 20° and the mixed 20°/90° stacking system have both nine molecules in every molecular pillar. Molecular crystals are equilibrated via MD simulations in the isobaric-isostress statistical ensemble at six different temperatures, ranging from 300 K to 400 K with an interval of 20 K. Triclinic periodic simulation boxes are utilized, with an anisotropic barostat maintaining the pressure at 1 atm.

Structural Properties

Systems under study retain the two dimensional hexagonal symmetry of the columnar lattice in the examined temperature range. Molecular pillars remain highly ordered, since orientational order parameter studies on both CoM directors and perpendicular

Table 6.1: Intercolumnar distances (left of the slash; expressed in Å) and core tilt angles (right of the slash; expressed in °) with respect to temperature for systems (each system's twist angle profile is noted inside parentheses): a. HBC-C16,4(30°), b. C96-C16(20°), c. C96-C16,4(20°), d. C132-C16,4(20°), e. C132-C16,4(20°alt), f. C132-C16,4(90°alt), g. C132-C16,4(mixed 20°/90°).

	T (K)					
ID	300	320	340	360	380	400
a.	34.08/2.36	34.38/1.72	34.42/1.64	34.49/1.56	34.60/1.35	34.88/1.12
b.	31.47/1.68	31.56/1.72	31.60/1.43	31.76/0.72	31.90/0.41	31.94/0.56
c.	37.07/2.56	37.14/2.68	37.32/2.12	37.38/1.43	37.82/1.76	37.87/1.41
d.	41.91/3.56	42.22/4.48	42.25/4.70	42.46/3.84	42.43/4.27	42.87/4.58
e.	42.23/6.87	42.43/7.90	42.53/11.06	42.50/11.20	42.44/13.75	42.18/17.46
f.	42.04/5.65	42.19/4.27	42.20/5.15	42.41/4.31	42.34/4.22	42.62/3.57
g.	42.44/3.67	41.75/3.01	42.26/3.23	42.39/3.93	42.60/3.42	42.79/3.04

core vectors yield upon diagonalization single maximum eigenvalues above 0.99, indicating strong alignment. For all cases, CoM directors are practically aligned with the $\hat{z}$ vector in space. Furthermore, initial twist angle profiles remain unaffected, except in the case of C132-C16,4 molecular crystals with alternating 20° profile, for which twist angles are slightly shifted to ∼17°.

Structural information regarding distances between molecular pillar and core-to-core distances inside each column can be extracted from CoM distance histograms $h(r)$. For the calculation of intercolumnar distances, an alternative approach is also considered: besides typical distances between core CoMs, a more elaborate method is utilized that results in vertical intercolumnar distances. To be more precise, should a specific molecular column be taken into consideration, we calculate the perpendicular distance of each CoM belonging to this column from the ODR lines of neighboring columns.

Both $h(r)$ and vertical CoM distance from neighboring ODR lines histograms $h_{\perp}(r)$ are depicted in Figure 6.8 for all examined molecular crystals at 400 K. The dotted gray lines correspond to available experimental data regarding intercolumnar distances.[61] The inset graph for HBC-C16,4 shows all peaks compliant to the hexagonal symmetry, including peak position ratios. Small distance peaks of the C96-C12 system are eclipsed by the peaks of the C96-C16,4 system.

The effect of temperature rise on selected structural properties is outlined in Table 6.1, where two basic parameters are included in the form of a dyad containing the intercolumnar distance calculated using the vertical CoM distance from neighboring ODR lines method and the molecular tilt separated by a slash.

As far as the hexagonal lattice constants and the core tilt are concerned, a general trend is evident for all molecular crystals examined except the C132-C16,4(20°alt) system: the rise in temperature leads to positive thermal expansion accompanied by a tilt reduction. A characteristic example of the effect of the stacking pattern on the structure

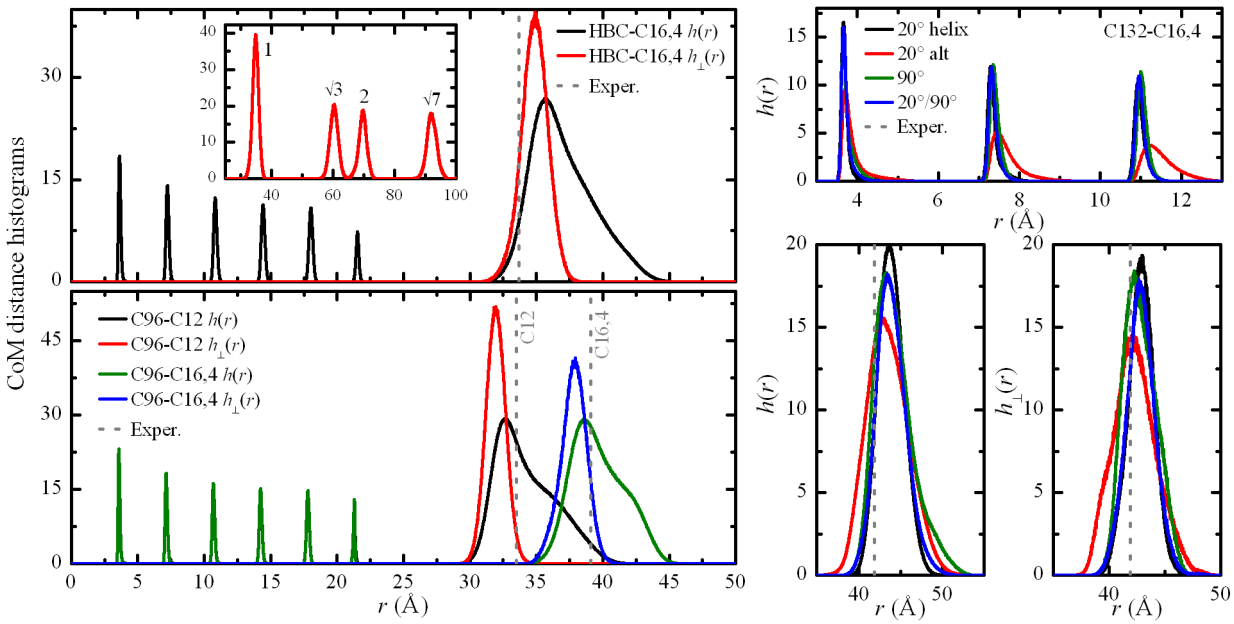

Figure 6.8: Molecular core CoM distance histograms $h(r)$ alongside vertical CoM distance from neighboring ODR lines histograms $h_{\perp}(r)$ for functionalized discotic molecules in the bulk at 400 K.

of such materials is found in the excluded system. The alternating 20° stacking profile for C132-C16,4 results in relatively highly tilted systems that exhibit an out of the ordinary response to temperature rise: the core-to-core distance decreases upon heating, the tilt angle follows an increasing trend and the lateral with respect to the columnar direction lattice expansion shows a maximum, resulting in a molecular crystal with smaller lattice constants at 400 K in comparison to the room temperature analogue.

A similar negative thermal expansion manifestation has already been pointed out in the literature via experimental[39] and theoretical[346] investigations of discotic materials. It should be noted that tilted C132-C16,4(20°alt) molecular crystals lack any specific tilt motif like the "herringbone" tilt pattern inherent to HBC derivatives.[195;346]

In the case of the side chain *trans* population upon heating, all phytyl substituted systems converge to a ∼64% trans population, while the dodecyl substituted C96 molecular crystal shows a clear decrease towards ∼58%. This difference is expected since the pendant methyl groups of C16,4 should relatively hinder side chain coiling. It should be noted that the original 80% *trans* population is not conserved by any studied system, indicating that the aliphatic nanophase is equilibrated to a state where the side chains are not overextended towards an all-*trans* configuration, characteristic of highly crystalline systems. The evolution of the vertical PAH core distance and of the C12 and C16,4 side chain trans population is depicted in Figure 6.9, where all systems are labeled using the notation described in Table 6.1.

A more comprehensive view on the structural properties of the soft aliphatic nanophase can be obtained via side chain end-to-end vector analyses. The most straightforward con-

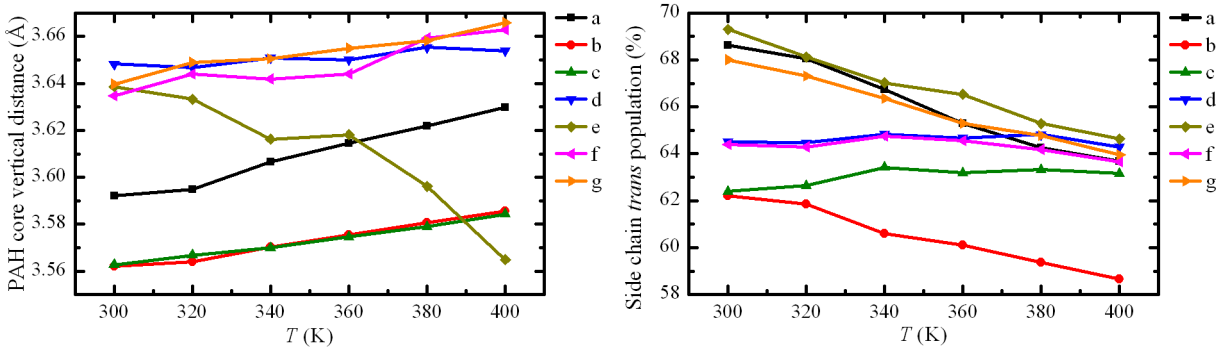

Figure 6.9: Vertical core distances (left) and side chain *trans* population (right) with respect to temperature for all studied systems. System labeling: a. HBC-C16,4(30°), b. C96-C16(20°), c. C96-C16,4(20°), d. C132-C16,4(20°), e. C132-C16,4(20°alt), f. C132-C16,4(90°alt), g. C132-C16,4(mixed 20°/90°).

sideration rests on the examination of the statistical distributions of end-to-end vector length with respect to temperature. For C96-C12 molecular crystals, a broad dominant peak is situated near approximately 13 Å, while a smaller peak is manifested at ∼15 Å. As temperature rises, end-to-end vector length distributions are slightly shifted towards smaller length values and the small peak near 15 Å gradually diminishes - a behavior consistent with the drop of trans side chain proper dihedral angle population for this system.

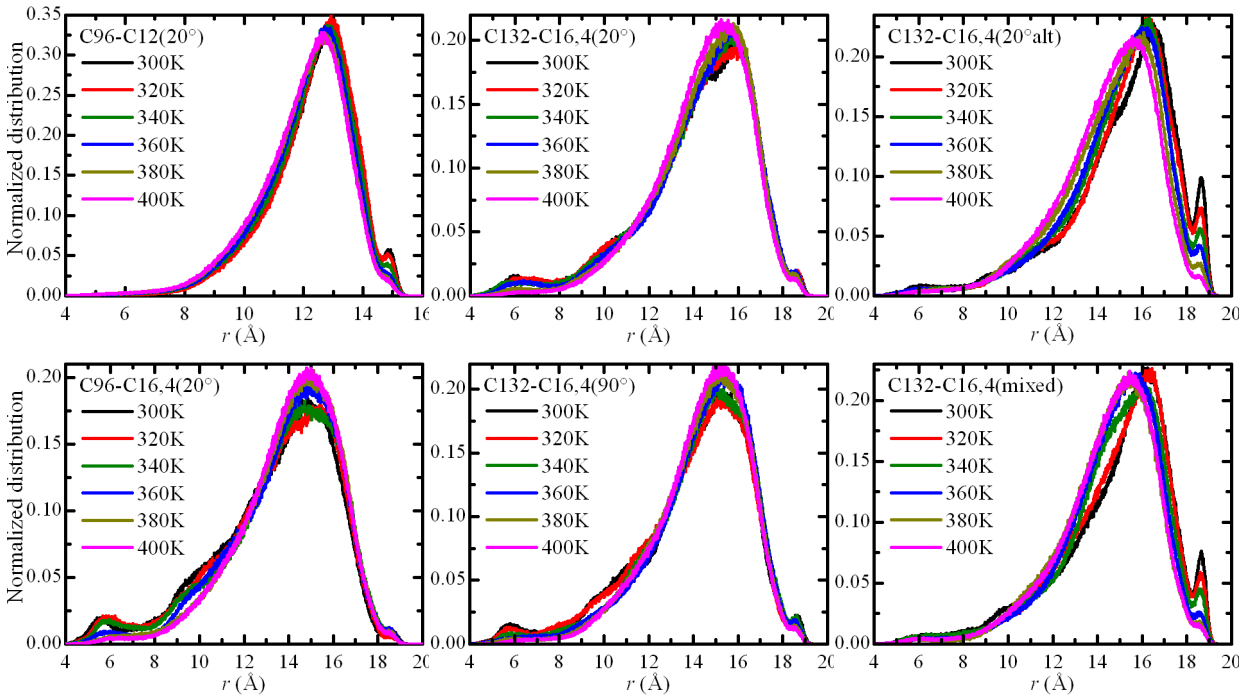

Figure 6.10: Side chain end-to-end vector length distributions of C96 and C132 based systems for all examined temperatures.

In the case of phytyl substituted discotics, the length distributions are more diverse, exhibiting more features - especially at low temperatures – which are eventually smeared

by temperature rise for all systems. At low temperatures, the extended side chain length peak at ∼15 Å is well-pronounced for C132-C16,4 with alternating 20° twist angle profile, as well as for HBC-C16,4 and for the mixed 20°/90° stacking pattern of C132-C16,4. Nevertheless, well within the mesophase at 400 K, this peak is diminished down to a discrete shoulder-like feature. Characteristic end-to-end vector length distribution families are depicted in Figure 6.10.

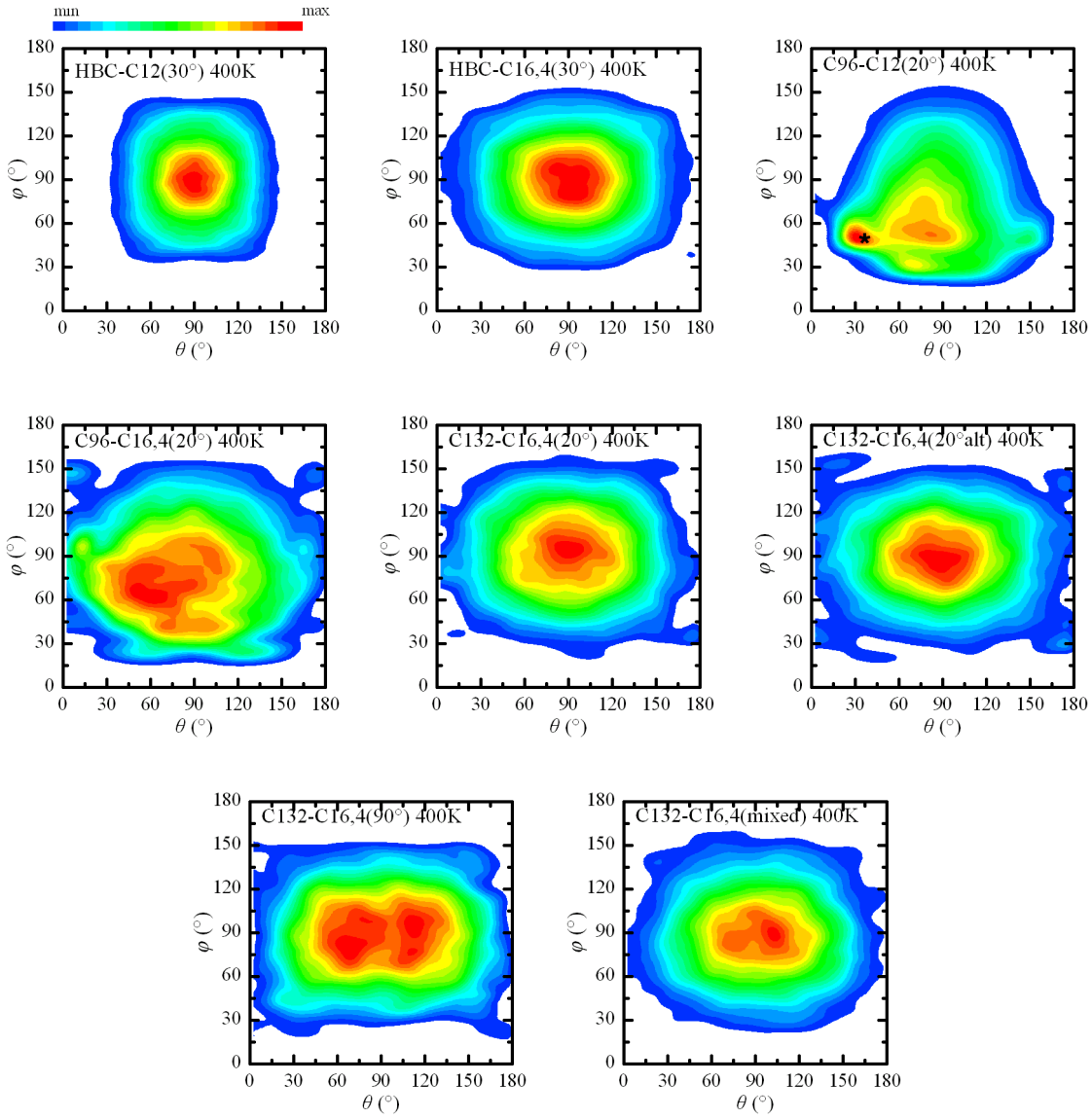

Figure 6.11: Side chain end-to-end vector orientation contours via the utilization of a local tangential coordinate system for C12 and C16,4 side chains in the length intervals of 12-14 Å and 12-16 Å respectively. The black asterisk on the contour plot of C96-C12 corresponds to the single column orientational maximum.

The orientational characteristics of side chain end-to-end vectors are probed via the application of projection analyses using local tangential coordinates systems. The aforementioned procedure returns the azimuthal angle θ and the polar angle φ for each vector,

thus quantifying any orientational preferences of the aliphatic nanophase. Time averaged contour plots of these angles for end-to-end vectors with lengths of high statistical merit at 400 K are plotted in Figure 6.11 for all systems. For C12 substituted molecular crystals, the vector length range is from 12 Å to 14 Å while for C16,4 substituted systems this range is taken from 12 Å to 16 Å.

The almost-perfect symmetry around 90° for both angles of the contour plot belonging to HBC-C12 molecular crystals with a 30° twist angle profile is indicative of a radial side chain protrusion profile. This motif is slightly altered when bulkier C16,4 side chains are utilized with the distribution being broadened along the azimuthal angle θ direction. An immediate effect of different discotic core geometry and size is evident for C96 based systems. For both dodecyl and phytyl substituted C96 molecular crystals, orientation distribution maxima are shifted to smaller angles. This behavior is consistent with a tendency of the side chains to collapse about the discotic molecular wire. This assumption is further supported by the proximity of the pronounced global maximum to the angle dyad (36°,46°) at which single column MD simulations exhibit the side chain orientational peak that corresponds to a collapsed alkyl mantle as depicted in Figure 6.6.

C132 based systems exhibit a symmetry similar to HBC-C16,4 of a radial side chain arrangement with a small differentiation for C132-C16,4 with a 90° twist angle profile for which the maximum at (90°,90°) seems to be evolving into two maxima that correspond to a fork-like protrusion scheme. This bimodal behavior seems to emerge in the case of the mixed stacking pattern molecular crystal as well. Side chain orientation contour plots for every examined temperature are included in the Appendices in Figures from III.1 to III.8.

Dynamical Properties

The effect of temperature on core dynamics is examined via ACF analyses through second order Legendre polynomial orientational correlation measurements. Two basic core vectors are considered: a normal to the PAH core and a coplanar one. Selected ACFs are depicted in Figure 6.12.

According to vector ACF analyses, the rise in temperature leads to increased core mobility. Nevertheless, ACF curves exhibit a saturative behavior towards hard plateaus situated above 0.985 and 0.97 for normal and in-plane vectors, respectively. The effect of different substitution is depicted in Figure 6.12 for C96 based molecular crystals where the mesophase plateaus are drawn with dotted lines, leading to the conclusion that lighter C12 side chains lead to more pronounced thermal motion, retaining, however, the saturative behavior. Polymorphs of C132-C16,4 show similar vector dynamical response to C132-C16,4(20°), indicating that the stacking pattern has a minuscule effect.

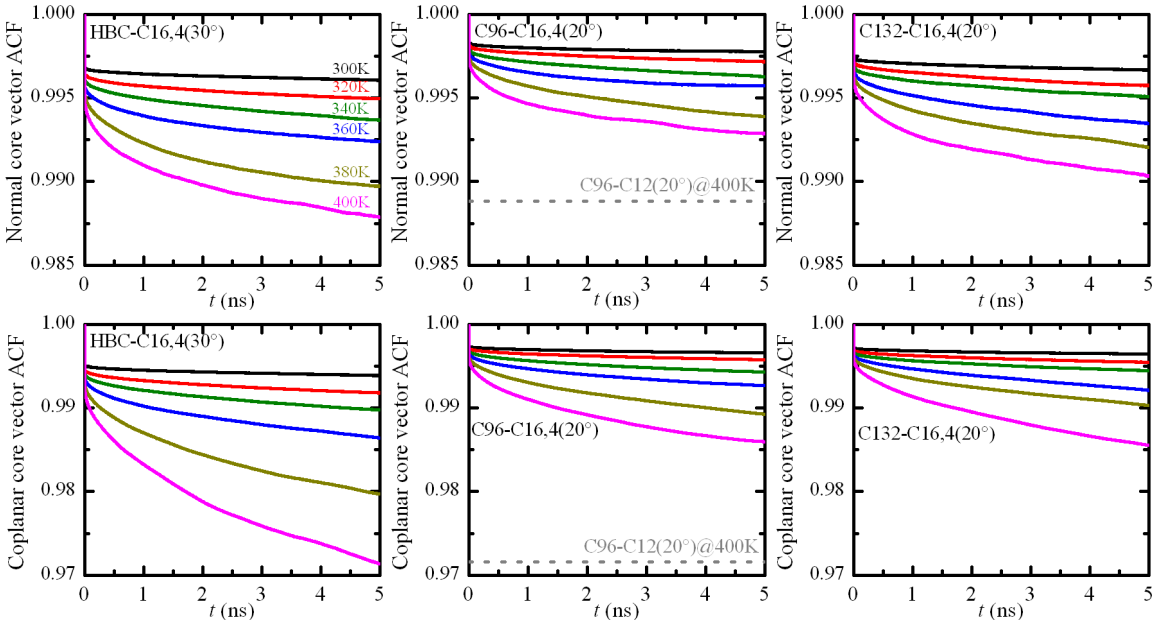

Figure 6.12: Normal and coplanar to the PAH core vector autocorrelation spectra. The temperature color labeling of the upper left diagram applies to all others. Dashed lines correspond to C96-C12 plateaus at 400 K.

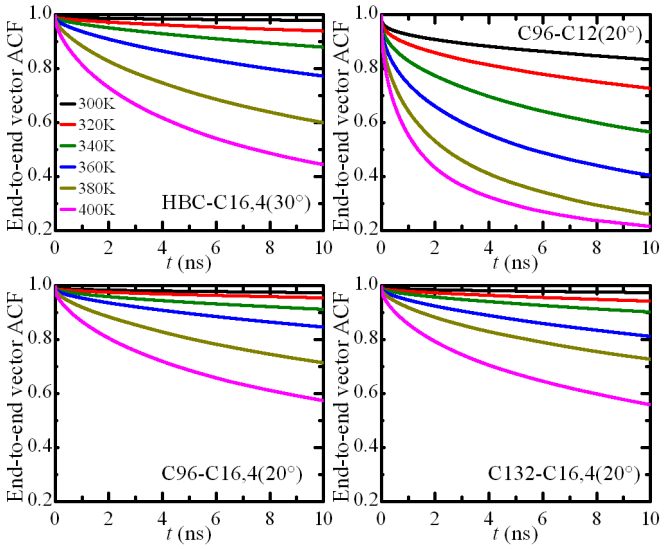

Figure 6.13: End-to-end side chain vector autocorrelation spectra. The temperature color labeling of the upper left diagram applies to all others.

Side chain dynamics are also examined via an analogous vector ACF procedure. Characteristic autocorrelation functions are plotted in Figure 6.13. Side chain dynamics shows a differentiation with respect to side chain and PAH core type. For C96 based molecular crystals, lighter C12 functional groups decorrelate faster with rising temperature when compared to their C16,4 counterparts. When comparing results of phytyl substituted systems, HBC-C16,4 side chains appear more mobile than in the case of C96 and C132, a feature which should be attributed to the smaller core molecular weight that allows a

more vibrant core movement. The remaining polymorphs of C132-C16,4 have the same side chain orientational temporal behavior with C132-C16,4(20°).

Translational dynamical phenomena are quantified by means of core CoM MSD calculations. Given the fact that all director vectors of the systems under study are practically aligned along the z Cartesian component, the MSD along this particular direction can be used to probe molecular movement along the stacking direction. The temporal evolution of the aforementioned property for all molecular crystals at 400 K is shown in Figure 6.14.

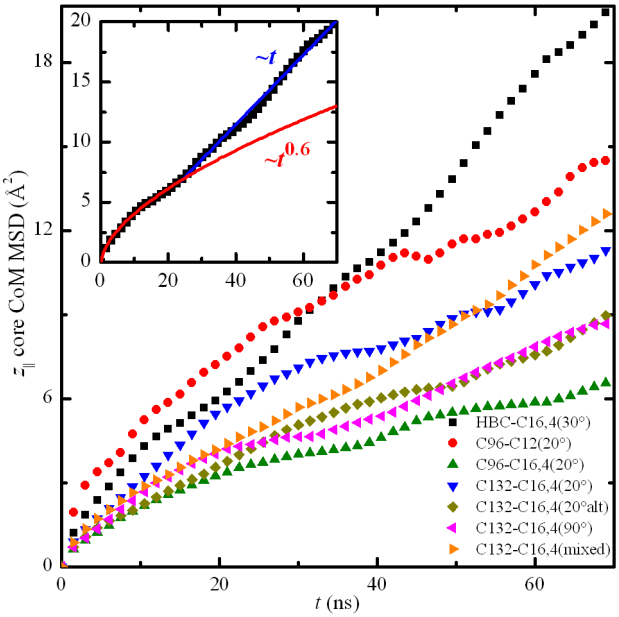

Figure 6.14: Discotic core CoM MSD functions along the columnar director for all molecular crystals at 400 K. The inset diagram depicts the columnar MSD for HBC-C16,4 alongside two characteristic power law trend lines.

All systems exhibit a sub-diffusive behavior at small time scales, followed - on occasion - by a linear diffusive regime, as is clearly shown in Figure 6.14 for HBC-C16,4. A power law behavior has been identified for the sub-diffusive translational mechanism with exponents ranging from 0.53 to 0.67. In particular for HBC-C16,4, a crossover is identified near ∼25 ns, in agreement to similar dynamical studies of HBC derivatives.[194]

The lack of a discrete linear diffusive regime for some systems should be attributed to the inability of MD simulations to properly yield such results for high molecular weight systems within the examined time range (∼100 ns). Temperature elevation has been found to increase the translational motion for all discotic materials under study.

The fact that heavier C96 and C132 based systems show a dynamical deceleration suggests that molecular core translational thermal motion is suppressed in comparison to HBC derivatives, resulting in slower temporal evolution. This attribute can be in advantage for molecular electronic applications, since a diminished motion - both translational and librational - causes less structural defects. On the other hand, this very phenomenon

could hinder the synthesis, purification and processing procedures via "wet chemistry" methods, as already pointed out in the literature.[29]

6.2.3 Molecular Crystals of Tri-arm Discotics

Preliminaries

Isolated molecular wires and molecular crystals comprised of functionalized "super-molecules" with tri-arm symmetry and TPB linkage are examined via MD simulations, utilizing HBC, C96 and C132 cores. The role of the linking TPB unit is evident: the non-coplanar arrangement of the outer phenyl rings with respect to the inner ring prompts the attached discotic molecules to align parallel to the plane of the inner phenyl ring. This planar configuration cannot be achieved with stiffer, less articulated linking units, like a nitrogen atom or a single phenyl ring, since such linkanges form propeller-like geometries due to steric hindrance.

As far as the peripheral substitution is concerned, all molecules are functionalized with phytyl side chains through the introduction of two distinct grafting variants. The first variant relies on symmetric substitution, with every discotic sub-unit bearing the same number of side chains, while the second on an asymmetric substitution scheme that leaves a discotic molecular fragment in its pristine, unsubstituted form.

Structural and Dynamical Properties

For the description of the overall orientation of stacked "super-molecules", the notion of the linkage twist angle is introduced. For tri-arm geometries with TPB linking units, the vector that connects the geometric centers of the inner and a predefined external TPB phenyl ring is used for the calculation of the linkage twist angle between neighboring "super-molecules". Having in mind the definition of the linkage twist angle, a series of single column initial configurations with different linkage twist angles of 0° (cofacial alignment) and 10°, 20° and 30° are generated and equilibrated via MD simulations.

In order to comprehend the structure of the examined tri-arm supramolecular pillars, two characteristic molecular wires made up of symmetrically and asymmetrically substituted TPB-linked C132 "super-molecules" are depicted in the following figure, alongside single molecule representations. The blue spheres correspond to side chain -CH_2- units and the red spheres to pendant and terminal -CH_3 units. Inner discotic carbon atoms are colored grey, outer linking atoms to which side chains are grafted are depicted with enlarged green spheres and sp^2 hybridized carbon atoms bearing hydrogen atoms on the core periphery are colored orange. Finally, TPB carbon atoms linked only to other carbon atoms are shown using pink spheres. For both molecular wires in Figure 6.15, a

three-stage rendering is chosen: the first stage utilizes all simulation atoms, showing this way the surrounding aliphatic mantle; the second stage depicts only core atoms, while the third reduces core atoms from spheres to sticks in order to show the inner structure of the TPB supramolecular cord.

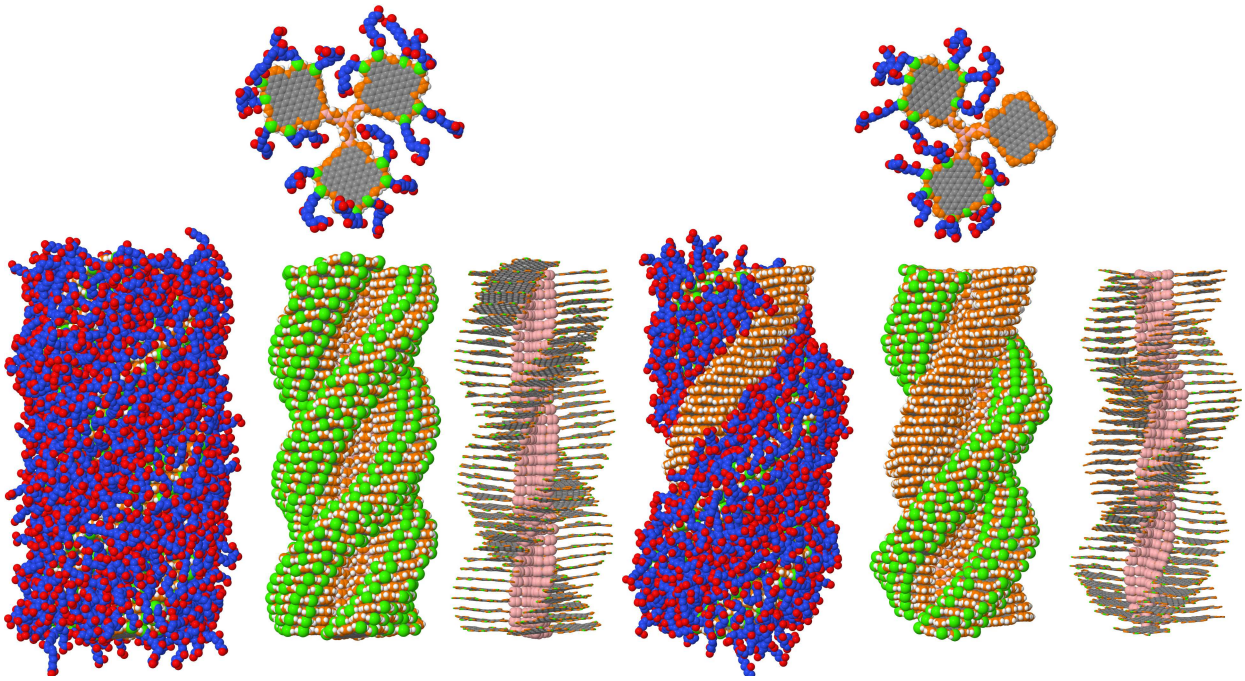

Figure 6.15: Single molecule representations of symmetrically (top left) and asymmetrically (top right) substituted TPB-linked C132 "super-molecules". The bottom depictions constitute three-stage renderings of molecular wires with a chiral 10° linkage twist angle profile.

For all tri-arm single column systems under study, the lowest energy corresponds to chiral configurations with a linkage twist angle of 10°. Having this information at hand, periodic molecular crystals in compliance with the aforementioned supramolecular stacking profile are created by placing unsubstituted molecular pillars on a hexagonal lattice of predefined spacing and subsequently growing the aliphatic nanophase utilizing the hybrid MC growth method.

The initial lattice constants normal to the columnar direction of the hexagonal lattice on which the pristine molecular pillars are placed prior to the alkyl nanophase MC growth are deduced from information concerning the structural properties of non-covalently linked molecular crystals. If one denotes the distance between the CoMs of the TPB linker and the PAH as a_1, the effective radius of the PAH as a_2, and the intercolumnar distance in the alkyl nanophase parallel to the line segment that connects the CoMs of two neighboring pillars as a_3 , the resulting spacing is expressed as $a = 2a_1 + 2a_2 + a_3$. Assuming that the side chain domain has the same spatial characteristics as non-linked molecular crystals, the intercolumnar distance for the non-linked systems can be written

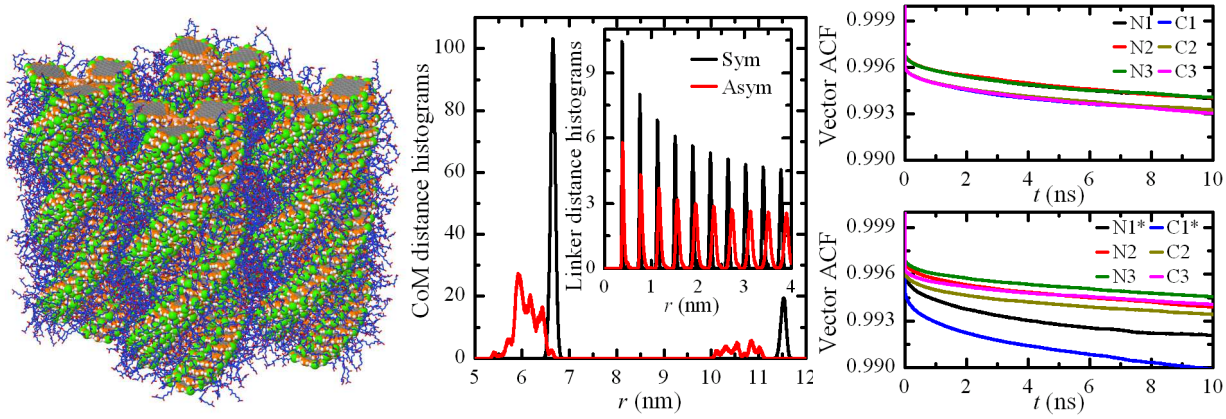

Figure 6.16: Graphical depiction of a molecular crystal of symmetrically substituted TPB-linked C132 "super-molecules" with lifted periodic boundary conditions (left panel), CoM distance histograms (central panel) and normal (N) and coplanar (C) vector orientational ACF functions (right panel) with respect to the substitution scheme.

as $a_i = 2a_2 + a_3$. Having this assumption in mind, the initial spacing for the "super-molecules" systems can be expressed as $a = 2a_1 + a_i$. By assigning for HBC, C96 and C132 linker-to-PAH CoM distances a_1 of 14.0 Å, 17.5 Å and 20.0 Å (derived from *in-vacuo* optimized single tri-arm molecules) and using for a_i values from Table 6.1 at 400 K, we end up with initial lattice constants of 63 Å, 73 Å and 82 Å for the three under study systems. The initial spacing along the stacking direction is set to 3.6 Å.

As far as the substitution scheme is concerned, symmetrically substituted systems of HBC, C96 and C132 cores bear three, four and six phytyl side chains per discotic unit. The initial substitution scheme relied on the convention to use as many side chains per core as were utilized for non-linked systems minus two. This way, one grafting site is reserved for the TPB linker and its nearest site is ignored in order to minimize the probability of TPB cord perforation by the side chains. This scheme leads to nicely stacked TPB-linked C96 and C132 systems but not for HBC based pillars, since the utilization of four side chains per core resulted in severe side chain penetration into the TPB cord during the MC side chain growth step. For this reason, the number of three side chains per core is chosen for TPB-linked HBC systems. In the case of asymmetrically substituted tri-arm "super-molecules", for HBC-based systems the same number of side chains per disk is maintained, whereas for C96 and C132 based systems the maximum number of five and seven functional groups per core is chosen in order to enhance their potential solubility.

After the creation of the side chain nanophase, all systems are equilibrated via MD simulations at 400 K utilizing triclinic periodic supercells. Symmetrically substituted molecular crystals exhibit lateral hexagonal lattice constants of 46.4 Å, 58.3 Å and 66.5 Å for HBC, C96 and C132 tri-arm systems respectively and the vertical distance along the

stacking direction of TPB CoM is near 3.7 Å for all studied molecular crystals. The linkage twist angle exhibits a unique maximum situated at 10°. As far as discotic core structural features are concerned, the tilt angle with respect to TPB cord directors is found at 4.5°, 5.5° and 9.0° for HBC, C96 and C132 based systems. Another angular quantity measured from equilibrated MD trajectories is the pitch angle of each protruding disk in reference to the TPB cord director. Calculated pitch angles are situated slightly above 90° for all molecular crystals. Core mobility is also quantified via normal and coplanar vector orientational ACF functions. Characteristic results for both symmetrically and asymmetrically substituted C132-based tri-arm systems are shown in the following figures. HBC and C96 based tri-arm systems exhibit analogous properties.

The effect of the substitution scheme shows a rather counterintuitive behavior. One would suspect that the lack of side chains on one of the three linked discotic cores should lead to more pronounced structural and dynamical order, since in the asymmetrically substituted systems, the entropic contributions are reduced in comparison to fully substituted molecules. Analyses at equilibrium indicate that the exact opposite phenomenon takes place: the partial absence of grafted side chains results in structural disorder and more pronounced disk mobility, indicating that the amorphous side chain nanophase acts as a stabilizing medium for such systems.

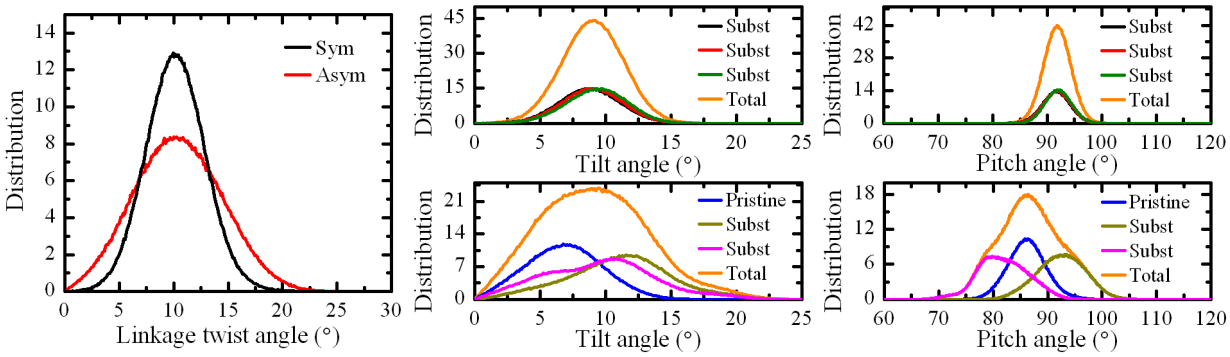

Figure 6.17: Angular quantities characteristic of the intracolumnar structure for the TPB-linked C132 molecular crystal with respect to the substitution scheme.

Upon careful inspection of the structural quantities plotted in Figures 6.16 and 6.17, the induced asymmetry to the substitution scheme leads to smaller intercolumnar distances and to discrepancies in core tilt and pitch angles. Furthermore, dynamical studies indicate that pristine cores ($N1^*$ and $C1^*$ in the right panel of Figure 6.16) are more mobile compared to substituted cores, a behavior showing that tangential core interactions are not adequate to stabilize discotic movement. Should all aforementioned findings be taken into consideration, the role of the soft, amorphous aliphatic nanophase is to be revised: instead of attributing only entropic characteristics to the side chain mantle, one needs to also consider this very nanophase as a stabilizing agent with "gluing" properties with respect to structural and dynamical uniformity.

6.2.4 Molecular Crystals of Dumbbell Discotics

Preliminaries

Molecular crystals of functionalized HBC-DB dumbbell mesogens are examined by means of MD simulations. As far as the functional groups are concerned, 2,6-dimethyloctane (C8,2) side chains are utilized, grafted onto 10 peripheral sites, hence resulting in the HBC-DB-C8,2 mesogen depicted in Figure 6.18, along with an illustration of a molecular crystal comprised of such molecules.

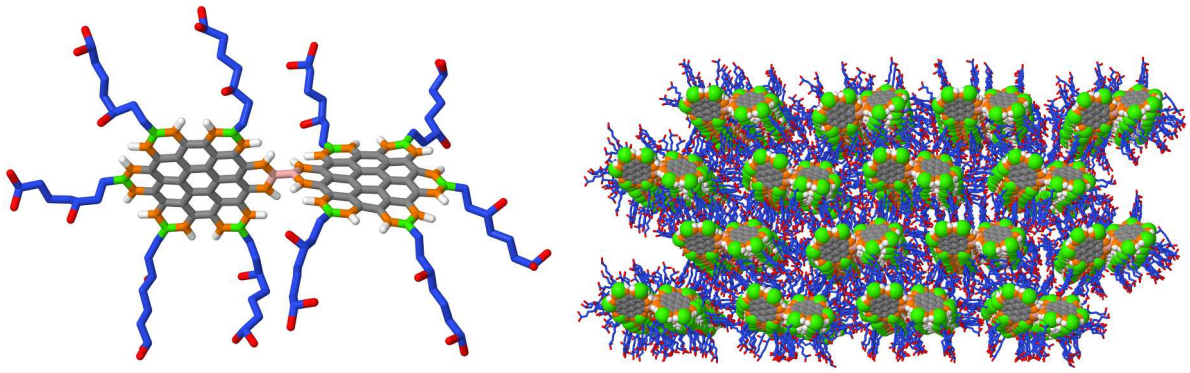

Figure 6.18: A single HBC-DB-C8,2 mesogen (left) and a top view of a molecular crystal made up by such molecules (right).

Due to the suspected crystalline nature of the surrounding side chain nanophase, mesogens are initially placed on lattice positions derived from experimental information.[83] Should a major molecular axis be defined by the two linking atoms forming the covalent linkage, all eight C8,2 side chains protruding in a perpendicular manner with respect to the aforementioned axis are explicitly considered during the crystallographic packing of the molecules in order to achieve maximum interdigitation. The remaining two side chains with their grafting sites situated on the major axis are grown using the hybrid MC growth scheme.

Periodic HBC-DB-C8,2 molecular crystals are equilibrated via MD simulations at a temperature of 300 K and pressure of 1 atm. In order to examine the response of such soluble discotic dumbbell systems to temperature rise, simulations at elevated temperatures of 400 K and 500 K are also conducted.

Structural and Dynamical Properties

This particular mesogen is characterized by a major structural deviation when moving from the *in-vacuo* to the condensed state description: the torsional angle about the linking covalent bond is raised from approximately 40° according to isolated molecule DFT calculations to ∼90° at the molecular crystal level.[83] This difference should be at-

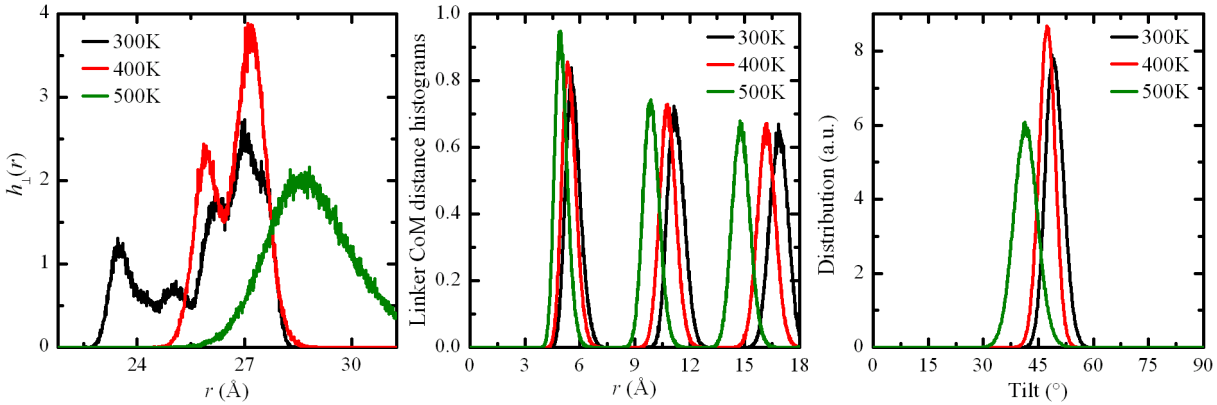

Figure 6.19: Temperature dependence of key structural features of HBC-DB-C8,2 molecular crystals: intercolumnar (left) and intracolumnar (center) distance distributions, along with core tilt angle histograms.

tributed to the compound effect of both π-π interactions and side chain packing; two factors missing from the single molecule level of description.

In order to account for the aforementioned torsional structural discrepancy, modifications to the utilized FF are in order. For this current study, an *ad-hoc* torsion barrier of $1\,\mathrm{kcal\,mol^{-1}}$ with minima at $\pm 90°$ is imposed instead of the dihedral angle term proposed by Marcon *et al.*[195]. This modification reproduces in a successful manner the $\sim 45°$ tilt angle of each HBC core with respect to the stacking direction reported by experimentalists.[83]

The dumbbell form of the examined mesogens seems to provide further structural stability upon temperature rise, with a significant degree of crystallinity and ordered stacking prevailing at the elevated temperature of 400 K. It should be noted that most single core HBC derivatives melt to the hexagonal mesophase around 400 K.[61] The dimerization to dumbbell structures is a route towards raising this melting point to higher values. The variation of major structural features upon temperature rise is depicted in Figure 6.19. Major structural changes with respect to the two dimensional columnar lattice take place at 500 K, with the orthorhombic arrangement melting to a hexagonal one, nevertheless without losing the characteristic tilted nature of the stacked mesogens.

Stacking patterns of HBC-DB-C8,2 mesogens are more resilient to temperature rise, with graphitic-like motifs still present even at 400 K. A statistical analysis of stacking patterns using the CoM projection method described in Figure 4.8 (but without any further differentiation with respect to the twist angle) is utilized for the examination of intracolumnar core stacking. The contour plots of projected CoMs are depicted in Figure 6.20, along with representative inset illustrations of most probable stacking patterns.

The unimodal nature of the projected CoM distributions at 300 K and 400 K points to a robust graphitic-like stacking motif, tightly linked to the tilted nature of the mesogens. Upon temperature rise at 500 K, the distribution exhibits a second, yet shallow, peak

that corresponds to "daisy-like" stacking, but without giving away the tilted nature of the core packing, as it can be seen in the tilt angle distribution in Figure 6.19.

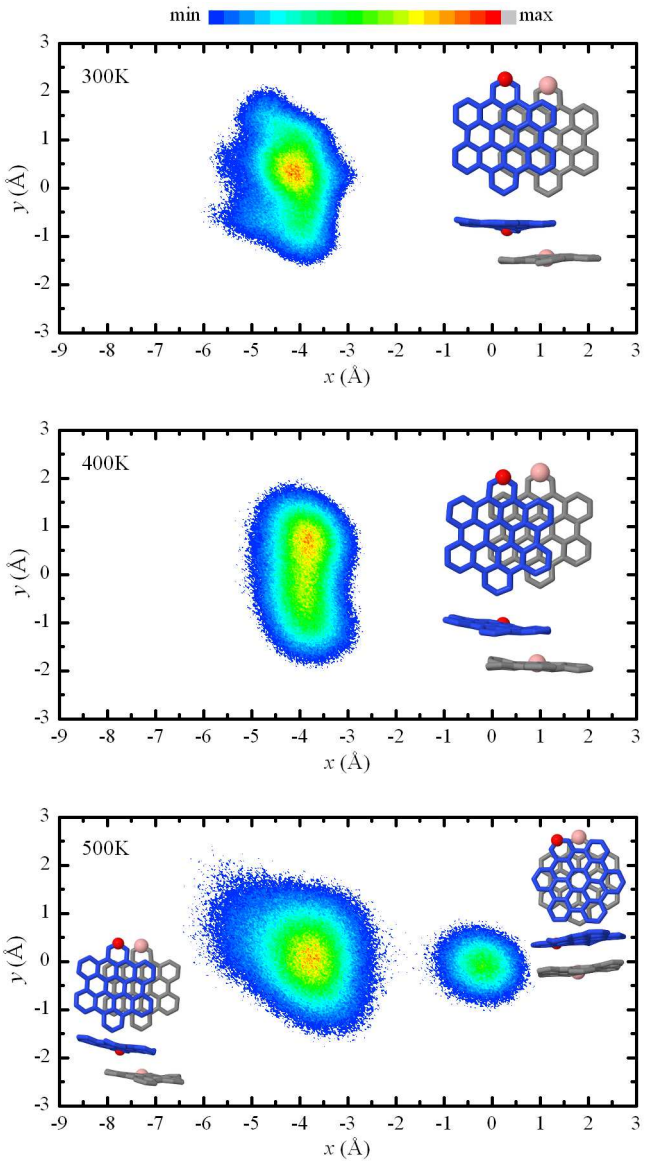

Figure 6.20: Contour plots of projected upper core CoMs to the plane defined by the lower core for every discotic dimer. The lower molecule CoM is centered at (0.0,0.0). Insets correspond to stacking patterns with high statistical merit. Red and pink spheres correspond to linking sites.

As far as core dynamics are concerned, the covalent dimerization provides further dynamic stability to the self-organized tilted pillars, with sizable decorrelation to both normal and coplanar core vectors occurring at the temperature of 500 K. Characteristic vector ACF spectra are illustrated in Figure 6.21.

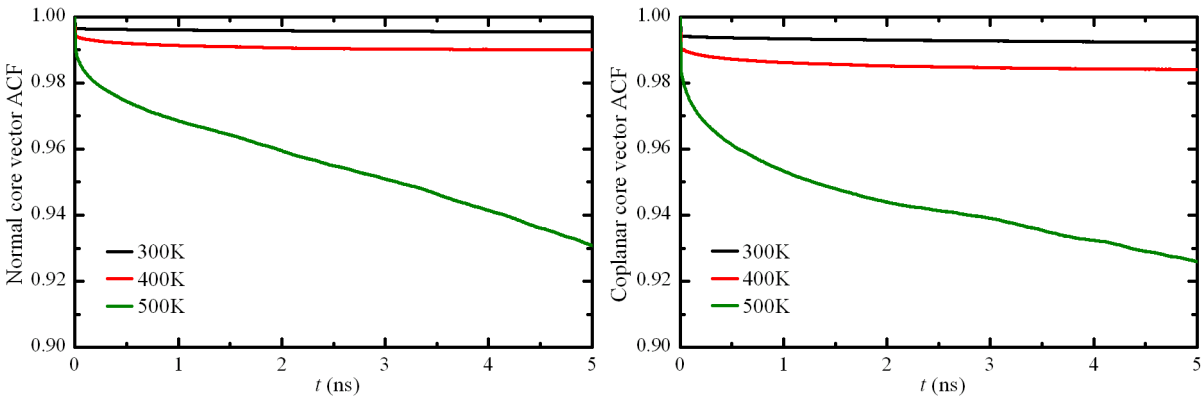

Figure 6.21: Normal and coplanar to the PAH core vector autocorrelation spectra for HBC-DB-C8,2 molecular crystals.

6.2.5 Charge Transfer Properties

Equilibrium MD trajectories of functionalized single and covalently linked discotics can be used in order to examine charge transfer capabilities. Due to the large extent of PAH cores, a direct evaluation of CTIs would be extremely demanding from a computational point of view. To alleviate this technical obstacle, a statistical approach is adopted, based on most probable core stacking profiles derived from atomistic system snapshots at equilibrium.

In the case of the mesophases of grafted C96 and C132 mesogens, an estimation of an upper boundary for charge mobility is straightforward through Equations 2.68 to 2.70. For C96, electron and hole CTI values are found at 34.47 meV and 23.66 meV. Based on reorganization energy and CTI calculations, in the case of C96 discotic cores with a twist angle of 20° and an average core-to-core distance of 3.6 Å at 300 K, electron and hole mobilities are found as 0.89 $cm^2\,V^{-1}\,s^{-1}$ and 0.53 $cm^2\,V^{-1}\,s^{-1}$, respectively, resulting in a total value of 1.42 $cm^2\,V^{-1}\,s^{-1}$. Experimental findings from room temperature measurements report a compound mobility ∼0.2 $cm^2\,V^{-1}\,s^{-1}$. This overestimation is to be expected due to the static nature of our calculations. In the case of C132, electron and hole CTI values for a twist angle of 20° are equal to 17.89 meV and 19.68 meV respectively, leading to an electron mobility of 0.35 $cm^2\,V^{-1}\,s^{-1}$ and a hole mobility of 0.49 $cm^2\,V^{-1}\,s^{-1}$. The 90° stacking pattern of C132 yields CTI values for electrons and holes equal to 2.10 meV and 0.73 meV that, in turn, correspond to room temperature mobility of 0.005 $cm^2\,V^{-1}\,s^{-1}$ and 0.001 $cm^2\,V^{-1}\,s^{-1}$ respectively, elucidating the dramatic effect of core stacking patterns on charge transport.

Symmetrically substituted C96 and C132 based tri-arm bulk molecular crystals are also examined with respect to the manifested discotic stacking patterns inside each 3-fold chiral molecular pillar. To this end, a more intricate method for the determination of stacking profiles is utilized, since a simple core twist angle analysis cannot be applied

due to the fact that discotic CoMs are out of alignment. Discotic segments are grouped and examined into dimeric first neighboring dyads. For each dyad, the lower core CoM is considered as the origin of a local two-dimensional coordinate system. In this system of coordinates, the vertical projection of the position of the upper CoM is recorded, alongside the dimer core twist angle. By applying a binning procedure with respect to twist angles, two-dimensional distributions of upper CoM projections are accumulated. Representative diagrams of this procedure are depicted in Figures 6.22 and 6.23.

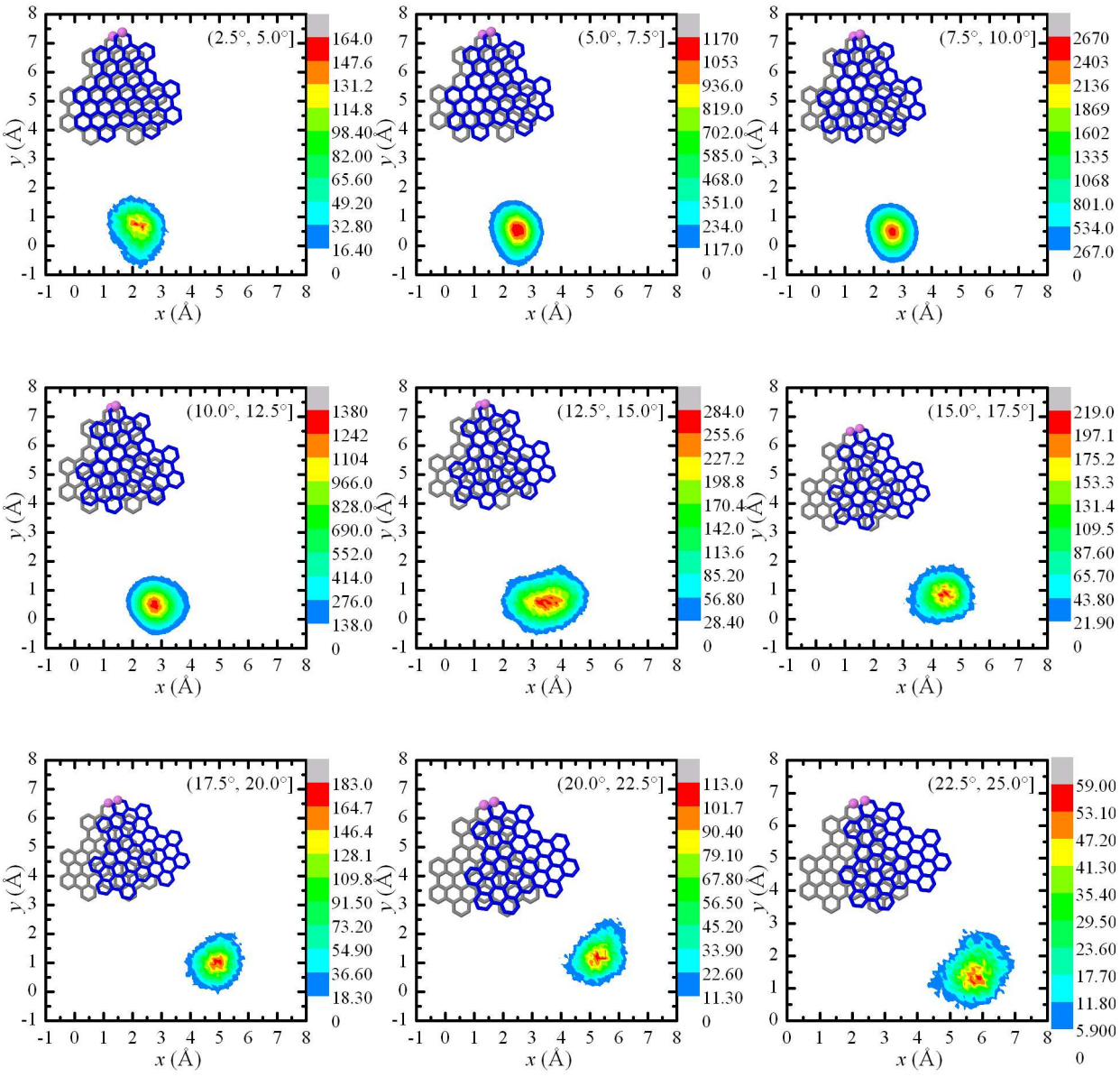

Figure 6.22: Upper molecule projected CoM contours for given core twist angle binning interval for TPB-linked symmetrically substituted C96 tri-arm molecular crystals. The lower molecule CoM is centered at (0.0,0.0). Insets correspond to most probable dimer configuration. Violet spheres represent the PAH atom connected to the TPB linker.

For all examined systems and twist angle bins, CoM projection contours exhibit a

unimodal nature, enabling thus a straightforward determination of statistically significant stacking patterns derived from MD trajectories. The population of the dominant stacking pattern with respect to the core twist angle for tri-arm C96 and C132 molecular crystals is shown in Figure 6.24. Inset dimer depictions correspond to most probable stacking patterns, with the violet spheres indicating the PAH carbon atom connected to the TPB covalent linker.

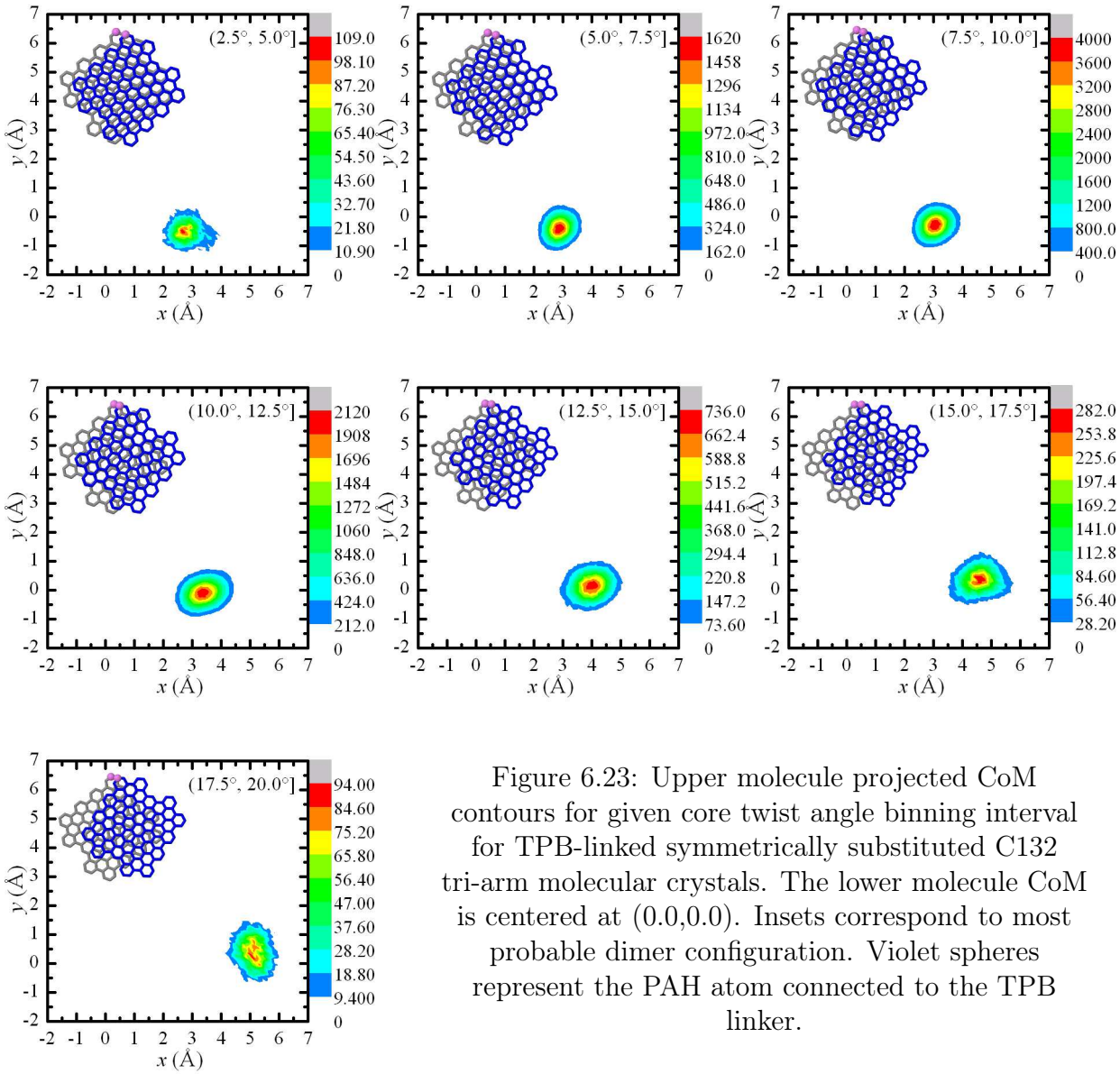

Figure 6.23: Upper molecule projected CoM contours for given core twist angle binning interval for TPB-linked symmetrically substituted C132 tri-arm molecular crystals. The lower molecule CoM is centered at (0.0,0.0). Insets correspond to most probable dimer configuration. Violet spheres represent the PAH atom connected to the TPB linker.

The stacking pattern statistical analysis can be utilized in order to extract valuable information regarding charge transfer properties. DFT calculations on single tri-arm molecules on the B3LYP-D3/6-31G** level of theory show that the electronic density attributed to states from the HOMO-8 to the HOMO level is localized on the discotic segments. Having this information at hand, a first approach for hole transport CTI calculations can be established on the basis of the HOMO and HOMO-1 levels, in full

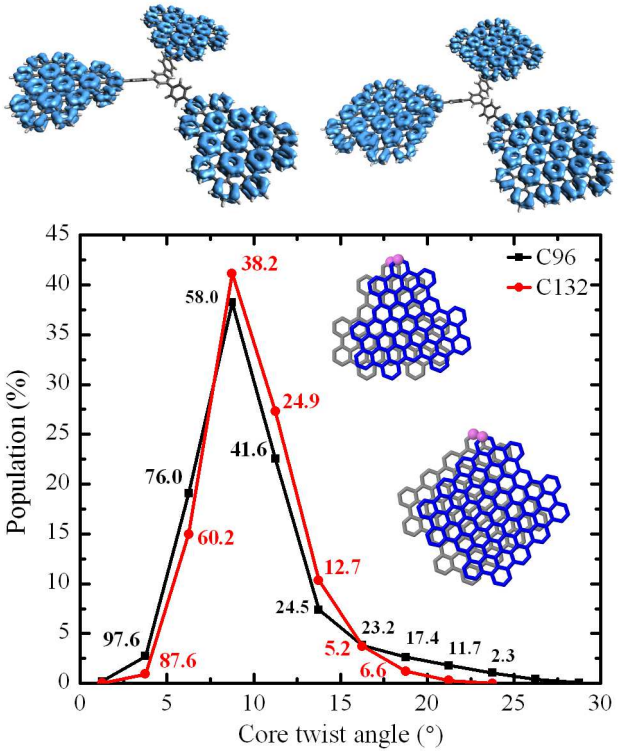

Figure 6.24: Partial electronic density contour plots near the HOMO state of TPB-linked C96 and C132 molecules (top) and the statistical distribution of dominant stacking patterns with discrete core twist angle (bottom). The numbers next to statistically significant points correspond to CTI values (expressed in meV) for hole transfer and the inset depictions correspond to the most probable dimer stacking patterns.

analogy with the case of isolated dimers. All calculated values are listed in Figure 6.24 next to each stacking pattern point. A decreasing trend with respect to the core twist angle is evident for hole CTI values. Nevertheless, the values of most probable stacking profiles indicate the suitability of such supramolecular chiral structures for charge transfer applications. For C132-based tri-arm geometries in particular, the utilization of the TPB linker prohibits C132 discotic cores from forming 90° stacking patterns, thus improving the potential charge transfer mechanism.

Although asymmetrically substituted "super-molecules" failed as more structurally robust bulk candidates, their application as cofacially stacked molecular monolayers is found to be quite promising. To this end, an interfacial system of cofacial TPB-linked C132 tri-arm molecules with asymmetric phytyl substitution is created by placing the monolayer on top of a silicon substrate. A characteristic depiction of such a prototype system is shown in Figure 6.25.

In this interfacial arrangement, substituted C132 discotic cores adopt the typical stacking profile with core twist angles near 20°. On the other hand, pristine segments exhibit near-graphitic stacking patterns, with core twist angle values limited below 10°. A selection of statistically significant stacking motifs of unsubstituted cores is depicted in Figure 6.25, together with their associated hole CTI values. The aforementioned values make this type of self-organization appealing for charge transfer applications. Furthermore, the exposed pristine graphitic segments can - in principle - serve as nanopatterned intercalation arrays for either hydrogen or ion storage and as firmly aligned nanographene edges for a plethora of applications.[347]

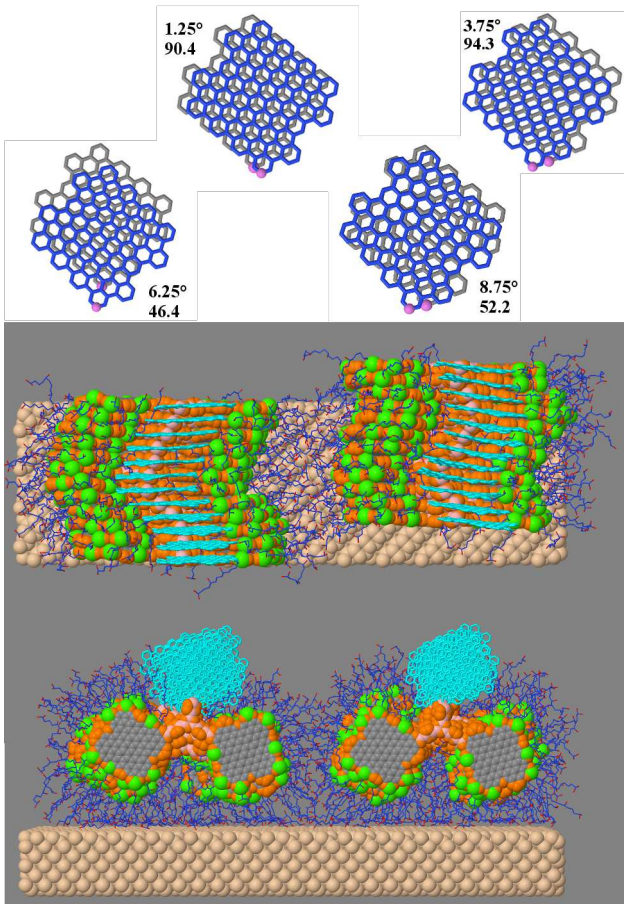

Figure 6.25: Graphical depiction of an interfacial system comprised by a cofacially aligned monolayer of asymmetrically substituted TPB-linked C132 molecules on top of a silicon substrate. Hydrogens are omitted for clarity. Dominant stacking patterns of pristine C132 cores (colored cyan in the slab representation) are also shown, alongside core twist angle and hole CTI values in meV.

6.3 Conclusions

A hierarchical approach for the creation of initial configurations from the level of a molecular dimer to an isolated molecular wire and to a molecular crystal is proposed and utilized in the case of alkyl substituted discotic molecules. The methodology relies on predicting favorable stacking patterns at the dimer level using empirical force fields; creating single column systems according to findings from dimer calculations; and studying the energetic and the evolution of the structural features using MD simulations. Results from single column simulations are used in order to select energetically more favorable structures to create molecular crystals.

Molecular crystal creation for systems with disordered alkyl nanophase is based on a hybrid MC growth scheme that minimizes artefacts due to side chain collapse should equilibrated single columns be used. Structural studies on functionalized HBC, C96 and C132 based molecular crystals suggest that these particular mesogens form robust bulk assemblies at the examined temperature range from 300 K to 400 K. In particular for C96-C12 and C96-C16,4, a chiral stacking pattern with a core twist angle of 20° is proposed, in fine agreement with experimental structural findings. For C132-C16,4 molecular crystals, four polymorphs are examined with various stacking motifs. Graphitic-like stacking patterns have been proven not to be preferable. Furthermore, the manifestation of 90°

twist angle stacking patterns is plausible for this system, thus hindering its charge transport capabilities due to extremely low CTI values associated with this stacking motif. In addition, should an alternating 20° twist angle pattern be adopted, this particular arrangement results in molecular crystals with finite tilt with respect to the stacking direction - a feature that is not inherent to all other stacking patterns at the level of the molecular crystals.

A detailed structural analysis of the soft, aliphatic nanophase is carried out, elucidating the effect of the functionalization type and discotic core stacking on the orientational characteristics of the side chain nanophase. The utilization of C16,4 functional groups results in radially protruding side chains due to the presence of pendant methyl units along the side chain body, while dodecane side chains show a coiling preference. This preference is also evident in the case of C96-C16,4 molecular crystals, in a less pronounced fashion. This behavior suggests that core geometry and stacking motifs affect structural characteristics of the side chain mantle.

Dynamical studies indicate that core movement quantified via vectors normal and coplanar to the cores is minimal in the nanosecond regime, a finding suggesting reduced spatial defects - a pivotal characteristic for charge transport applications. Diffusion studies along the columnar direction via MSD calculations were proven inadequate to characterize the translational dynamics due to augmented molecular weight. Nevertheless, again in the nanosecond regime, systems appear to be on the verge between a columnar plastic and liquid-crystalline phase.

Discotic tri-arm "super-molecules" with C16,4 side groups and TPB covalent linking are examined at the bulk molecular crystal level. A chiral stacking pattern of a linkage twist angle of 10° is found to be most preferable for all examined systems. In the case of C96 and C132 based tri-arm molecules, a detailed stacking pattern analysis is performed, showing that PAH segments adopt different stacking patterns compared to discotic single crystals. The compound stacking motifs inherit to tri-arm systems yield larger CTI values, indicating that the formed discotic triple helices can serve as an alternative charge transport system. Especially for C132 tri-arm systems, the "notorious" 90° stacking pattern is altogether avoided, suggesting potential applications of this extended PAH for organic electronic applications.

Furthermore, the overall effect of the side chain nanophase features on the structure and dynamics of tri-arm bulk systems is examined via an asymmetric substitution scheme that relies on leaving one of the three cores in its pristine form. A counterintuitive behavior is manifested, showing that symmetrically substituted systems are more robust. The aforementioned findings suggest that the side chain nanophase is not only a means of solubilization, but a cohesive agent as well that minimizes core libration and stabilizes the supramolecular assembly. Although the asymmetric substitution failed to yield a more stable candidate for bulk assembly, its utilization in the form of an interfacial system is

a promising alternative application of tri-arm "super-molecules". In such a form, pristine discotic cores adopt near graphitic-like stacking patterns, capable of exhibiting viable charge transfer. Moreover, monolayers of asymmetrically substituted tri-arm systems can serve as exposed nanopatterned nanographene arrays with a plethora of applications.

In the case of soluble HBC dumbbell mesogens, a torsional discrepancy is identified when moving from the single molecule description to molecular crystals of stacked, covalently linked discotics. A force field modification is implemented in order to account for this behavior, thus allowing the examination of structural and dynamical properties via equilibrium MD simulations. The direct dimerization via a single covalent bond raises the melting point above 400 K, hence prompting the usage of such materials as stable conducting media at elevated temperatures.

General Conclusions

DFT Studies of Discotic Molecules

The utilization of ground-state DFT calculations has been proven an effective way for probing single molecule electronic and charge transfer properties. In the case of single core mesogens, core extent, degree of planarization and overall morphology affect both electronic properties - quantified via FMO energy levels and spatial distribution - and reorganization energies. Peripheral HBC functionalization using atomic species or molecular fragments with electronegativity differences compared to sp^2 carbon atoms is found to induce permanent electric dipole moment to the otherwise non-polar HBC core, in a controllable manner via the choice of appropriate substituents, without interfering significantly with pristine core electronic properties, although some changes to charge reorganization energies are reported due to complex relaxation mechanisms upon ionization when articulated substituents are utilized.

Besides single core molecules, DFT examinations of covalently linked discotics by means of variable articulated linking units indicate that such drastic morphological interventions result in new mesogens with diverse and optimized properties. As far as HBC cores are concerned, the utilization of 3-fold central linkers, such as benzene, TPB, nitrogen, and TPA, and the direct covalent dimerization resulting in a dumbbell geometry, lead to the formation of molecules with controllable HOMO-LUMO gap and absolute FMO energy level positions, while exhibiting lower reorganization energy for both electrons and holes. Detailed analyses suggest that such discotic "super-molecules" obtain low reorganization energies due to more easily followed geometric relaxation in the ionic state, manifested primarily through torsional variations on the linking units and the terminal HBC cores as out-of-plane peripheral distortion.

A sub-category of star-shaped discotic "super-molecules" is also considered, with variable terminal core units such as benzene, pyrene, peropyrene, and HBC, and nitrogen-containing linking units like atomic nitrogen and TPA. Some of the examined mesogens of the aforementioned class exhibit morphological sensitivity of electronic properties and low reorganization energies compared to pristine HBC, thus proving their suitability for organic electronics applications for hole conducting devices. Moreover, some nitrogen-containing star-shaped molecules are characterized by near-equal electron and hole re-

organization energy values, hence prompting possible utilization as ambipolar organic active media.

In the case of coronene, HBC, C96, and C132 cores, dimer studies on the basis of FMO charge transfer elucidate the effect of relative position and orientation to the CTI values. Upon rotating initially cofacial discs about the direction normal to the cores by a prescribed twist angle, CTI variations indicate that maxima are gained on graphitic-like AA stacking profiles. Of particular interest is the extended tetragonal C132 core, for which the CTI is effectively diminished to zero for a twist angle of 90°. Calculations on dimers resulting from parallel displacements along high symmetry directions suggest high CTI values for all graphitic-like stacking patterns, namely AA, AA' and AB, although for small displacements the AB stacking motif is linked with relatively small values compared to the other two patterns.

Molecular Simulations of Alkyl-substituted HBC Molecular Crystals

MD simulations of alkyl-functionalized HBC cores with aliphatic side chains with variable length and hydrogen and iodine mono-substitution by means of side chain replacement allow the determination of structural, mechanical, and dynamical properties at equilibrium, with fine agreement compared to available experimental data. Stacking pattern analyses indicate a variety of graphitic-like packing motifs for HBC-C12 molecular crystals at room temperature, coexisting with a small fraction of twisted, "daisy-like" patterns. The melting process towards the hexagonal liquid-crystalline phase is identified and probed at the temperature of 400 K, suggesting a complete domination of the "daisy-like" pattern, that subsequently hinders charge transfer due to lower CTI values.

Analyses of the effect of the peripheral substitution status indicate that side chain length alterations and replacement with a hydrogen or iodine atoms induce a certain dynamical disorder to the aliphatic nanophase, leading to more pronounced core libration in the crystalline phase. On the other hand, liquid-crystalline phases exhibit a relative insensitivity to peripheral alterations except for the case of iodine substitution: HBC-I-C12 columnar liquid crystals manifest a dynamical retardation in both core and side chain movement.

The elastic response is quantified by means of two complementary methods: virtual stress-strain experiments and the strain fluctuation theory, yielding a characteristic to the melting process thermotropic dependence for calculated elastic moduli. The effect of compressive load on both structural and dynamical features of HBC-C12 molecular crystals suggests a highly elastic response, even for extreme compression. A pronounced dynamical deceleration is identified upon loading and a differentiation on which nanophase exhibits higher resistance to compression is identified, with the crystalline and liquid-crystalline phases being stiffer due to side chain crystallization and core planarization,

respectively.

Molecular Simulations of Amphiphilic Discotic Mesogens

Atomistic simulations by means of an all-atom FF of amphiphilic, "Janus-type" C12-HBC-PhOTEG mesogens in lamellar molecular arrangements have been carried out for the first time in the literature. Findings indicate a pronounced structural robustness upon temperature rise, with the lamellae retaining their morphological integrity even up to the temperature of 450 K. A novel characteristic of this prototype system is the ability of the HBC cores to maintain graphitic-like stacking patterns at all examined temperatures. Complete structural and dynamical profiling of core and side chain movement give information regarding the degree of interdigitation and crystallization of the hydrophilic TEG and hydrophobic C12 side chain nanophases upon temperature rise, while at the same time reporting a tilt direction differentiation in the liquid-crystalline phase.

The melting process has been identified to be fully activated at the temperature of 450 K. In contrast to hexa-substituted HBC mesogens, translational motion, characteristic of the liquid-crystalline phase, is manifested along two different directions: along the stacking direction and relatively slower along the direction perpendicular to the stacking and the normal to the lamellae directions, hence leading to a composite, *en-masse*, lamellar movement, with characteristic palindromic features.

Molecular Simulations of Extended and Covalently Linked Discotics

A hierarchical approach from the level of a molecular dimer, to molecular pillar and, finally, to bulk molecular crystals has been found quite efficient for the creation of plausible initial configurations when minimal structural information is available. A bond-by-bond hybrid MC growth methodology is utilized for the creation of the surrounding side chain nanophase, returning structurally non-frustrated configurations, with targeted macromolecular properties with respect to side chain features. This method for the efficient creation of core-shell nanostructures in the context of discotic materials modeling is first reported in this work.

MD simulation results of extended core discotics based on phytane-substituted C96 and C132 cores are in fine agreement with experimental structural data. The stacking of such cores in the bulk is quantified, elucidating the core tendency towards twisted, non-graphitic conformations. A subtle, but present, effect of the stacking pattern and intracolumnar symmetry (chiral or non-chiral) is identified on side chain orientational characteristics. Furthermore, C132-C16,4 molecular crystals with alternating 20° stacking profile seem to form slightly tilted supramolecular assemblies, in contrast to all other stacking motifs under study.

As regards translational dynamical properties, C96 and C132 based molecular crystals seem to lie on the very edge of the capability of atomistic simulations to yield satisfactory MSD results in reasonable simulation time limited under 100 ns. The sheer molecular weight and spatial correlations encountered in such systems require significantly longer simulations in order to differentiate a possible columnar plastic and liquid crystalline phase manifestation.

In the field of discotic "super-molecules", HBC dumbbells grafted with 2,6-dimethyloctane side groups required a force field calibration in order to account for a different linking twist angle suggested by experimental findings. Upon this modification, MD simulations have been utilized in fair agreement with available experimental data, revealing a relative structural and dynamical robustness upon temperature rise, with the cores adopting AA' graphitic-like stacking patterns at the elevated temperatures of 400 K and minimal core libration, hence prompting their utilization for stable charge transfer at elevated temperatures compared to hexa-substituted HBC derivatives.

Thee discotic tri-arm mesogens have been examined by means of MD simulations, all having a TPB linker, with HBC, C96, and C132 peripheral cores, all grafted with phytane side groups. Isolated molecular wire simulations suggest that the most stable arrangement is the one of a triple-helix with a linkage twist angle of 10°. Molecular crystals of such mesogens in chiral pillar arrangements are studied. Stacking patterns inherent to such supramolecular arrangements are found to be combinations of small parallel displacements and core twist angles limited at approximately 10°, hence avoiding CTI minima at 20° for C96 and at 20° an 90° for C132 cores, respectively.

A multiscale methodology based on statistical analyses of stacking patterns derived from atomistic simulations in the bulk of phytane-substituted discotic tri-arm molecules and CTI calculations on the basis of the FMO approach suggest superior CTI values compared to single core molecular crystals, in chiral molecular arrangement and possible substrate-assisted cofacial packing. The aforementioned findings regarding CTI, coupled to record-low reported reorganization energies for such tri-arm discotic molecules, render them highly promising candidates for organic electronics applications.

Software Development and Dissemination of Research

For the purposes of this work the following noteworthy software solutions were deemed necessary and developed:

- A generic molecular topology derivation software, capable of reading Tripos mol2 files containing molecular coordinates and bond connectivity of a single or multiple macromolecules, and providing fixed-topology information regarding bonds, angles, and proper and improper dihedral angles, while carrying out automatic type identifications. This particular software, coupled with appropriate utilities for the creation of periodic molecular crystals by means of CoM translations and rotations was put to use for the creation of initial LAMMPS configuration files for the majority of the studied systems.

- A macromolecular building software capable of creating amorphous assemblies of user-defined chain-like molecules of arbitrary length, chemical composition, and branching, either in pristine molecular forms of grafted onto nanostructures already embedded into a predefined simulation supercell. The core of this approach for the creation of initial configurations is based on bond-by-bond sequential chain creation using MC criteria, coupled to geometric biasing, independent from the utilized force fields, and frequent, on-the-fly geometry optimization for the alleviation of atomic overlaps. This hybrid methodology is suited for growing soft nanophases out of hard nanostructures and for the generation of amorphous soft matrices of arbitrary polymerization degree in the presence of nano-inclusions and interfaces.

- A converter of ParamChem CGenFF input stream files into LAMMPS input files, generating both the required topological information and the force field information script file for direct usage as input to the LAMMPS simulation package.

- A post-process utility for the determination of theoretical XRD spectra from equilibrium MD simulation trajectories, based on the calculation of the form factor on nodes of the reciprocal space, also parallelized for optimal performance.

- A generic multiple time origin correlation software, parallelized for optimal performance, capable of producing ACF spectra of densely written data files.

As far as the dissemination of the research carried out for the purposes of this dissertation, the following actions have been followed:

Peer-reviewed journals

1. Ziogos, O.G.; Theodorou, D.N. "Molecular dynamics simulations of alkyl substituted nanographene crystals" *Mol. Phys.* **2015**, *113*, 2776-2790.

Peer-reviewed conference proceedings

1. Ziogos, O.G.; Theodorou, D.N. "Molecular Simulations of Nanographene Systems" *Materials Today: Proceedings* **2017**, in press.

2. Ziogos, O.G.; Megariotis, G.; Theodorou, D.N. "Atomistic and Coarse-grained Simulations of Hexabenzocoronene Crystals" *Journal of Physics: Conference Series* **2016**, *738*, 012019.

3. Ziogos, O.G.; Theodorou, D.N. "Structural and dynamical properties of nanographene molecular wires: A Molecular Dynamics study" Nanotechnology (IEEE-NANO), 2015 IEEE 15th International Conference on, 817-820.

4. Megariotis, G.; Ziogos, O.G.; Theodorou, D.N. "Multiscale simulations of hexa-peri-hexabenzocoronene and hexa-n-dodecyl-hexa-peri-hexabenzocoronene" *AIP Conference Proceedings* **2015**, *1702*, 190010.

International conferences

1. Bardas, C.G.; Ziogos, O.G.; Theodorou, D.N. "Atomistic Simulations of Carbon Nanotube-Polymer Matrix Nanocomposites", SciMeeting-Europe, 21-23 June 2017, Athens, Greece.

2. Ziogos, O.G.; Megariotis, G.; Theodorou, D.N. "Atomistic and Coarse-grained Simulations of Hexabenzocoronene Crystals", 5th International Conference on Mathematical Modeling in Physical Sciences (IC-MSquare 2016), 23-26 May 2016, Athens, Greece.

3. Ziogos, O.G.; Theodorou, D.N. "Structural and dynamical properties of nanographene molecular wires: A Molecular Dynamics study", IEEE 15th International Conference on Nanotechnology, 27-30 July 2015, Rome, Italy.

4. Ziogos, O.G.; Theodorou, D.N. "Atomistic Simulations of Nanographene Crystals", EUROMAT 2015, 20-24 September 2015, Warsaw, Poland.

5. Megariotis, G.; Ziogos, O.G.; Theodorou, D.N. "Multiscale simulations of hexa-peri-hexabenzocoronene and hexa-n-dodecyl-hexa-peri-hexabenzocoronene", 11th International Conference of Computational Methods in Sciences and Engineering (ICCMSE 2015), 20-23 March 2015, Athens, Greece.

6. Ziogos, O.G.; Theodorou, D.N. "Mechanical properties of pristine and mono-substituted hexa-n-dodecyl-hexa-peri-hexabenzocoronene (HBC-C12) crystals: A Molecular Dynamics study", E-MRS 2014 Spring Meeting, 26-30 May 2014, Lille, France.

Regional conferences

1. Ziogos, O.G.; Theodorou, D.N. "Molecular Simulations of Nanographene Systems", 11th Panhellenic Scientific Conference in Chemical Engineering, 25-27 May 2017, Thessaloniki, Greece.

2. Konstantinopoulos, S.; Ziogos, O.G.; Theodorou, D.N. "Atomistic Simulations of Nanographene Discotic Liquid Crystals ", 11th Panhellenic Scientific Conference in Chemical Engineering, 25-27 May 2017, Thessaloniki, Greece.

3. Bardas, C.G.; Ziogos, O.G.; Theodorou, D.N. "Atomistic Simulations of Carbon Nanotube-Polymer Matrix Nanocomposites", 11th Panhellenic Scientific Conference in Chemical Engineering, 25-27 May 2017, Thessaloniki, Greece.

4. Perdikari, T.M.; Ziogos, O.G.; Theodorou, D.N. "Atomistic Simulations of Lamellar Nanostructures of Amphiphilic Disclike Molecules", 11th Panhellenic Scientific Conference in Chemical Engineering, 25-27 May 2017, Thessaloniki, Greece.

5. Megariotis, G.; Ziogos, O.G.; Theodorou, D.N. "Coarse-grained Computer Simulations of Hexa-peri-hexabenzocoronene (HBC) and Hexa-n-dodecyl-hexa-peri-hexabenzocoronene (HBC-C12)", 31st Panhellenic Conference on Solid State Physics & Materials Science, 20-23 September 2015, Thessaloniki, Greece.

6. Ziogos, O.G.; Theodorou, D.N. "Elastic properties of soluble nanographene crystals via molecular dynamics simulations", 10th Hellenic Polymer Society Conference, 4-6 December 2014, Patras, Greece.

7. Ziogos, O.G.; Tsetseris, L., Theodorou, D.N. "Atomistic Simulations of Dipole Substituted peri-Hexabenzocoronene Molecular Crystals", 29th Panhellenic Conference on Solid State Physics & Materials Science, 22-25 September 2013, Athens, Greece.

Diploma and Master thesis co-supervision

1. 2016-2017: M.Sc. Thesis co-supervision: "Atomistic Simulations of Carbon Nanotube-Polymer Matrix Nanocomposites", C. Bardas.

2. 2016-2017: M.Sc. Thesis co-supervision: "Molecular Simulations of Graphene-based Materials for Organic Electronics", S. Konstantinopoulos.

3. 2016-2017: B.Sc. Thesis co-supervision: "Atomistic Simulations of Lamellar Nanostructures of Amphiphilic Disc-like Molecules", M. Perdikari.

4. 2014-2015: B.Sc. Thesis co-supervision: "Atomistic Simulations of Nanographene Discotic Liquid Crystals", S. Konstantinopoulos.

Research Perspectives

As regards *ab-initio* DFT studies of discotic mesogens, either single-core or articulated, multi-core, with variable parameters the peripheral substitution and the very morphology of the mesogen, respectively, a further step towards the understanding of quantum-based properties involves excited-state calculations. Equilibrated ground-state geometries can be put to use as input for time-dependent DFT calculations for the determination of absorption and emittance spectra, thus providing crucial information regarding optoelectronic properties of discotic molecules.

Moreover, the reported findings on star-shaped discotic tri-arm molecules can serve as the foundation of multiscale analyses on different levels of molecular organization. To be more precise, should one take into consideration a tri-arm mesogen, the next foremost structural level is the dumbbell molecule via appropriate linkage. A characteristic geometric feature of molecules with 3-fold symmetry is their potential ability to form macrocycles as the next level of structural arrangement which can be envisioned as precursor states of two- or three-dimensional covalent organic frameworks. Of particular importance are the variations in morphological, electronic and charge transfer properties while crossing from one level of structural organization to the next, along with possible property tuning via permanent functionalization on specific peripheral sites.

In the case of amphiphilic HBC derivatives, the fundamental work on the C12-HBC-PhOTEG mesogen can be easily extended on amphiphilic discogens with variable side chain types, with variations to side chain length, topology, and chemical composition, aiming to elucidate possible effects on the melting process and on the structural and dynamical features for given temperature conditions. The fact that the lamellar system under study has a proven structural robustness at elevated temperatures, hence enabling thermal side chain polymerization should appropriate functional groups be utilized, prompts a variety of possible computational examinations by means of on-the-fly oligomeric cross-linking towards the creation of interlocked lamellae for organic electronics applications.

Appendices

Appendix I: Frontier Molecular Orbitals of Covalently Linked Discotics

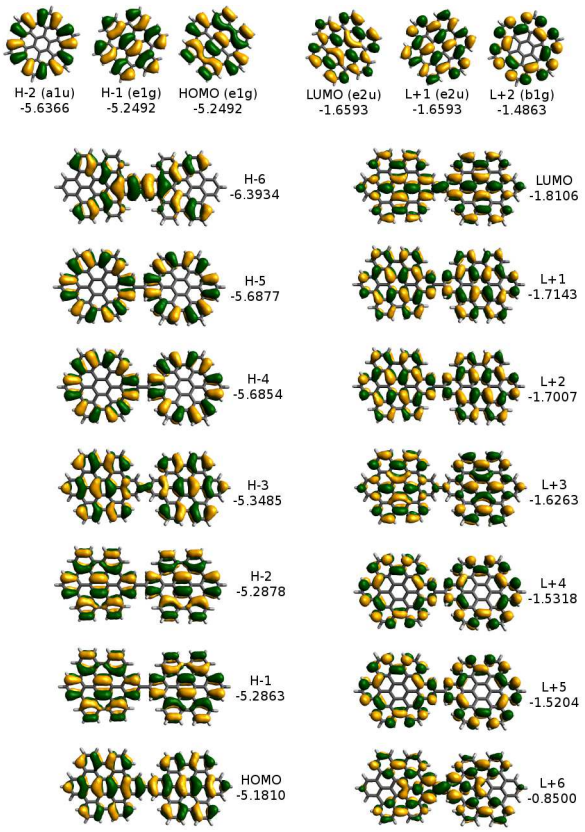

Figure I.1: Selected frontier molecular orbitals of the HBC dumbbell at the B3LYP/6-31G** level of theory alongside the HOMO-2, HOMO-1, HOMO, LUMO, LUMO+1 and LUMO+2 orbitals of HBC. Energy levels are expressed in eV.

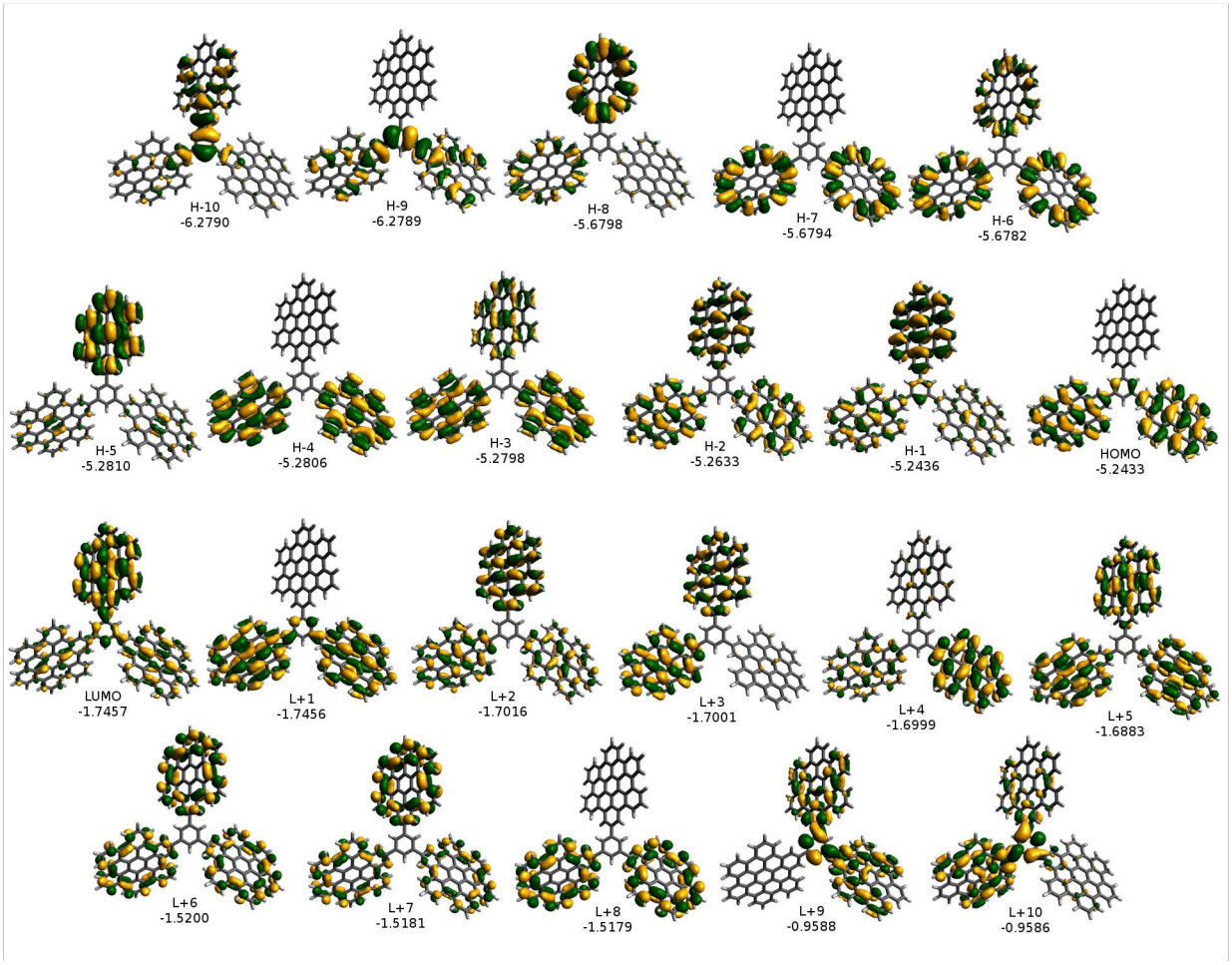

Figure I.2: Selected frontier molecular orbitals of the benzene tri-arm HBC "super-molecule" at the B3LYP/6-31G** level of theory. Energy levels are expressed in eV.

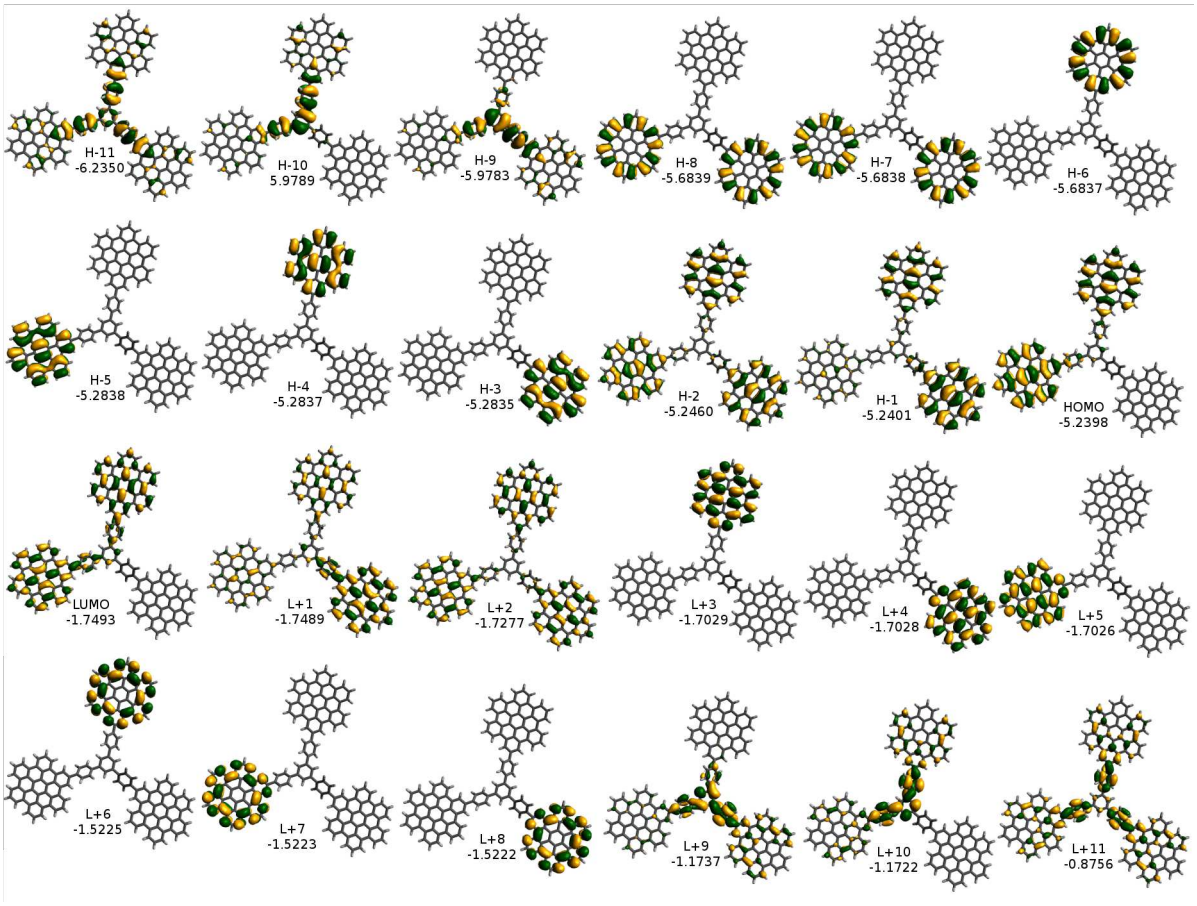

Figure I.3: Selected frontier molecular orbitals of the TPB tri-arm HBC "super-molecule" at the B3LYP/6-31G** level of theory. Energy levels are expressed in eV.

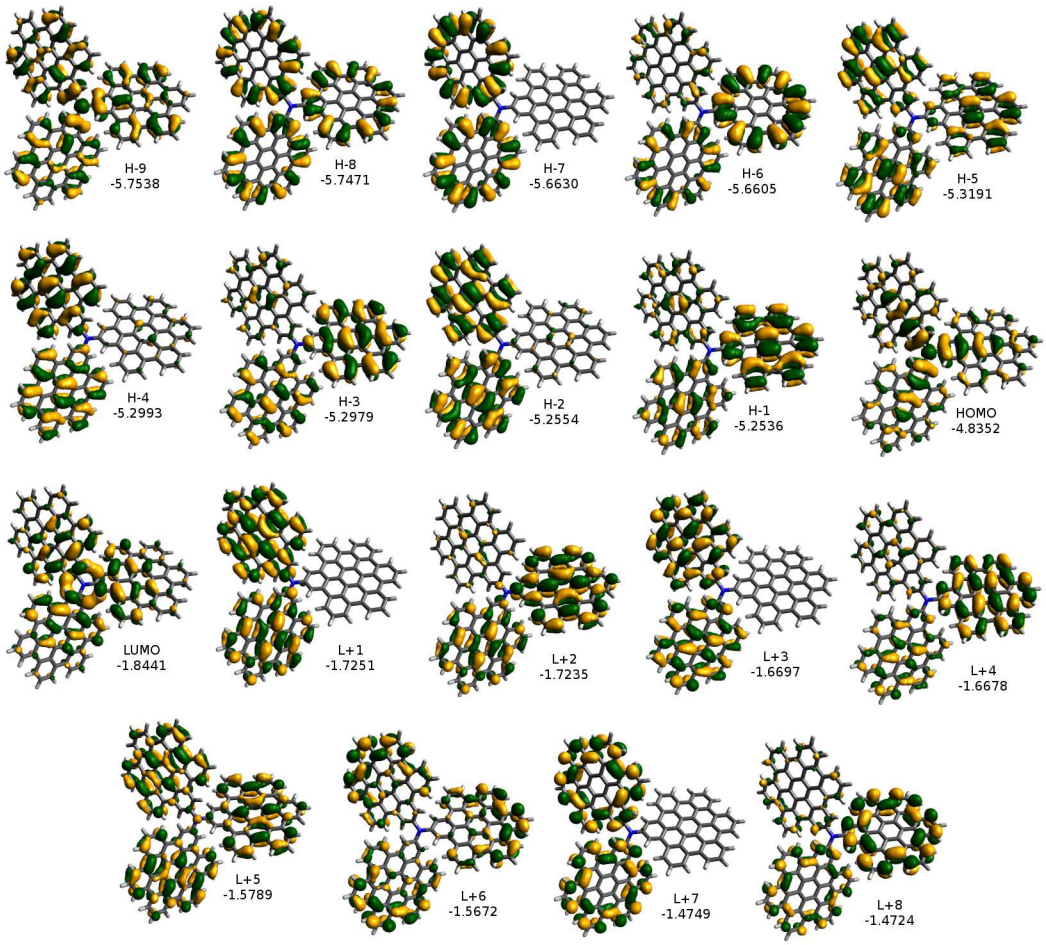

Figure I.4: Selected frontier molecular orbitals of the nitrogen tri-arm HBC "super-molecule" at the B3LYP/6-31G** level of theory. Energy levels are expressed in eV.

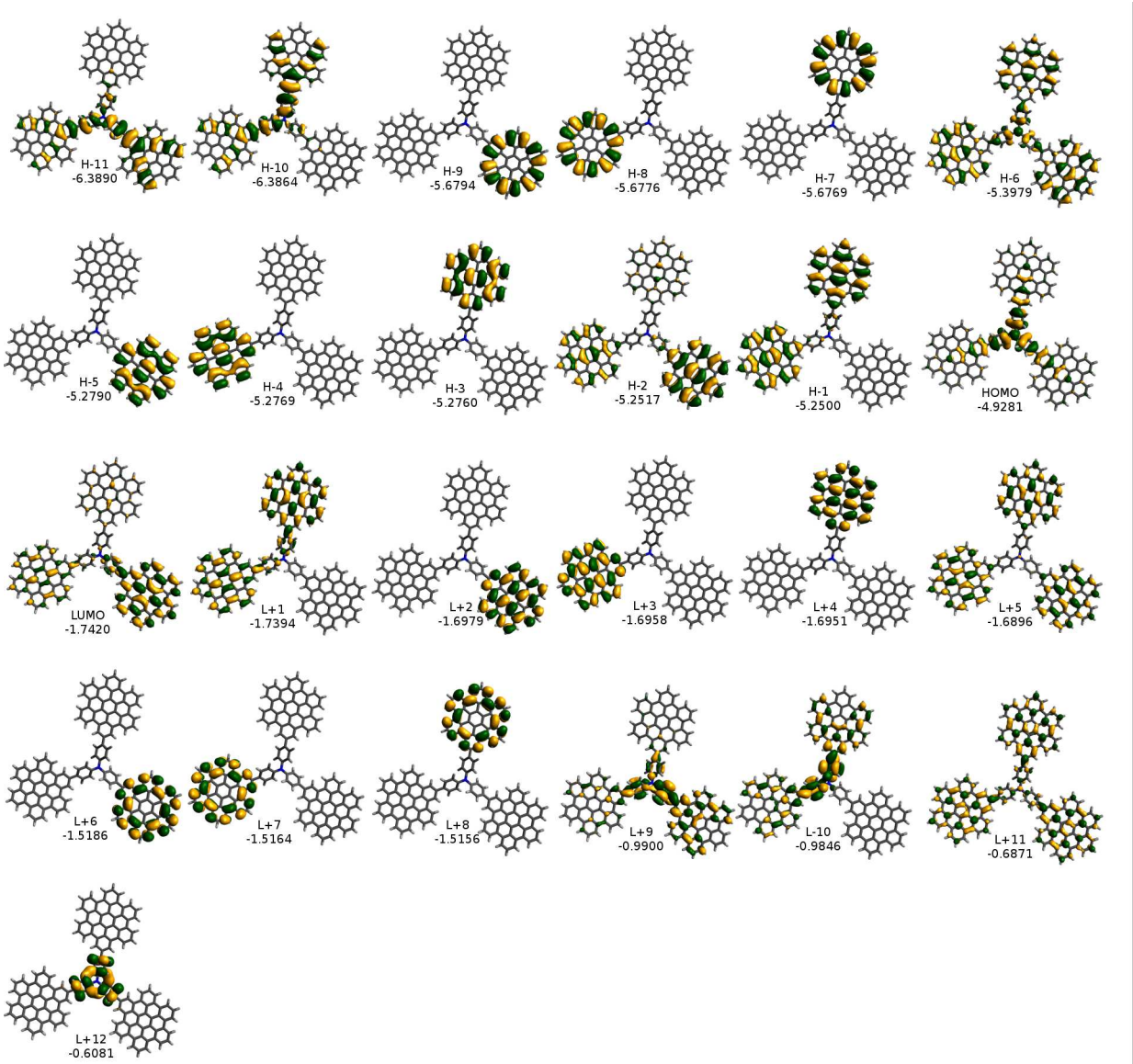

Figure I.5: Selected frontier molecular orbitals of the TPA tri-arm HBC "super-molecule" at the B3LYP/6-31G** level of theory. Energy levels are expressed in eV.

Appendix II: Orthogonal Distance Regression Line and Plane Geometric Calculations

Given a selection of points in three-dimensional Euclidean space, the orthogonal distance regression (ODR) method constitutes a geometric tool for the derivation of a line or a plane that describes the given point distribution in the most suited way.

The ODR method for the calculation of a plane that best fits a selection of points is as follows. Suppose that the ODR plane is expressed as $ax+by+cz+d=0$. If a selection of N points is denoted as (x_i, y_i, z_i), the distance of a given point i from the ODR plane is expressed as

$$D_i = \frac{|ax_i + by_i + cz_i + d|}{\sqrt{a^2 + b^2 + c^2}}$$

The derivation of the ODR plane can be seen as an optimization problem aiming at the minimization of the following objective function:

$$f(a,b,c,d) = \sum_{i=1}^{N} D_i^2 = \sum_{i=1}^{N} \frac{(ax_i + by_i + cz_i + d)^2}{a^2 + b^2 + c^2}$$

The condition $\frac{\partial f}{\vartheta d} = 0$ that must hold for a potential critical point leads to the following expression for the plane parameter d:

$$d = -(aX + bY + cZ)$$

where (X, Y, Z) the centroid of the collection of points. Upon back-substitution, the plane equation is rewritten as:

$$a(x - X) + b(y - Y) + c(z - Z) = 0$$

and the objective function is expressed as

$$f = f(a,b,c) = \sum_{i=1}^{N} \frac{[a(x_i - X) + b(y_i - Y) + c(z_i - Z)]^2}{a^2 + b^2 + c^2}$$

Should a matrix notation be used, defining the column vector

$$v = \begin{pmatrix} a \\ b \\ c \end{pmatrix}$$

and the matrix

$$M = \begin{pmatrix} x_1 - X & y_1 - Y & z_1 - Z \\ x_2 - X & y_2 - Y & z_2 - Z \\ \vdots & \vdots & \vdots \\ x_N - X & y_N - Y & z_N - Z \end{pmatrix}$$

help rewriting the objective function in the form of a Rayleigh Quotient:

$$f = f(u) = \frac{u^{\mathrm{T}} \left(M^{\mathrm{T}} M\right) u}{u^{\mathrm{T}} u} = \frac{u^{\mathrm{T}} A u}{u^{\mathrm{T}} u}$$

where $A = M^{\mathrm{T}} M$. In this matrix notation, f is minimized by the eigenvector of A corresponding to the smallest eigenvalue.

To sum up, in order to calculate the ODR plane, one needs only to find the centroid of the selection of points and then form matrix A, whose eigenvector linked to the smallest eigenvalue is practically the normal to the plane vector.

For the calculation of the ODR line, an analogous optimization problem to the ODR plane analysis is formulated and solved via matrix manipulations. Suppose that the ODR line is expressed in the following parametric form:

$$\begin{aligned} x &= x_0 + \lambda e_x \\ y &= y_0 + \lambda e_y \\ z &= z_0 + \lambda e_z \end{aligned}$$

where (x_0, y_0, z_0) a point belonging to the ODR line and $\hat{e} = (e_x, e_y, e_z)$ the unit vector defining the direction of the ODR line in the three-dimensional space.

A suitable objective function g whose minimization results in the ODR line best fitting the collection of N points is deduced using the point-to-line distance equation, resulting to the following expression:

$$\begin{aligned} &g = g(x_0, y_0, z_0, e_x, e_y, e_z) = \\ &= \sum_{i=1}^{N} \left\{ \left[e_z (y_i - y_0) - e_y (z_i - z_0) \right]^2 + \left[e_x (z_i - z_0) - e_z (x_i - x_0) \right]^2 + \left[e_y (x_i - x_0) - e_x (y_i - y_0) \right]^2 \right\} \end{aligned}$$

The critical point criterium with respect to the x_0, y_0, z_0 variables gives the following condition:

$$\frac{x_0 - X}{e_x} = \frac{y - Y}{e_y} = \frac{z_0 - X}{e_z}$$

proving that the ODR line passes through the centroid (X, Y, Z), hence in can be used

as an acceptable parametrization for x_0, y_0, z_0.

For the determination of the rest parameters, a geometric decomposition is in order. Should we denote the centroid as (C), the ODR line as (L) and a plane passing from (C) in a perpendicular manner with respect to (L) as (P), by means of the Pythagorean theorem, the vertical distance of a point i from (L) can be written as:

$$[\text{dist}\,(i,L)]^2 = [\text{dist}\,(i,C)]^2 - [\text{dist}\,(i,P)]^2$$

Since $[\text{dist}\,(i,C)]^2$ is constant for all points, the aforementioned expression prompts the reformulation of the minimization problem in the basis of maximizing the following familiar expression:

$$f\,(a,b,c,d) = \sum_{i=1}^{N} D_i^2 = \sum_{i=1}^{N} [\text{dist}\,(i,P)]^2$$

This maximization is achieved by the eigenvector of A that corresponds to its largest eigenvalue.

Appendix III: Single Core Discotics Side Chain Orientation Contour Plots

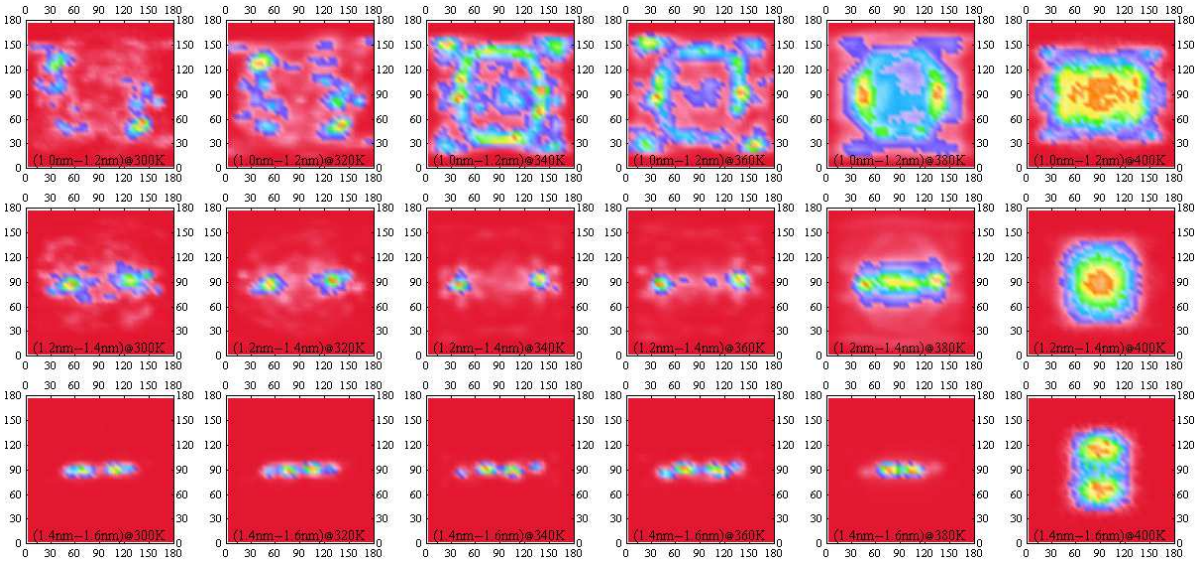

Figure III.1: Side chain end-to-end vector orientation contours for HBC-C12 molecular crystals. Horizontal and vertical axes correspond to the azimuthal angle ϑ and polar angle φ respectively. Vector length interval is written inside parentheses, followed by the temperature. Same description applies to the following figures.

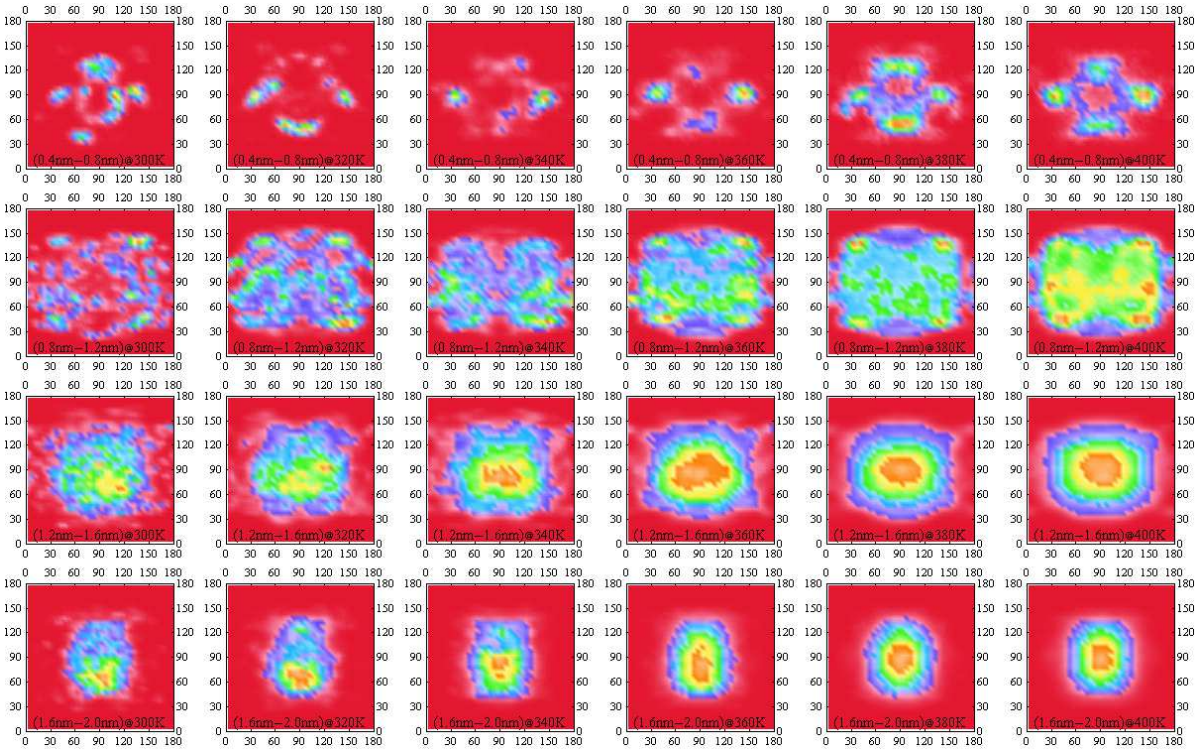

Figure III.2: Side chain end-to-end vector orientation contours for HBC-C16,4 molecular crystals.

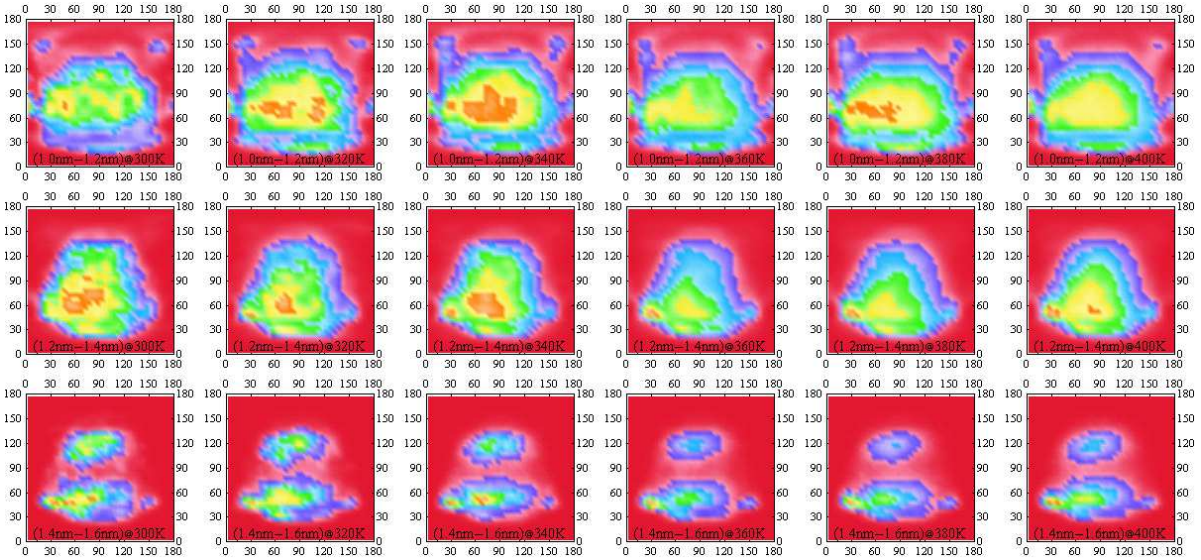

Figure III.3: Side chain end-to-end vector orientation contours for C96-C12 molecular crystals.

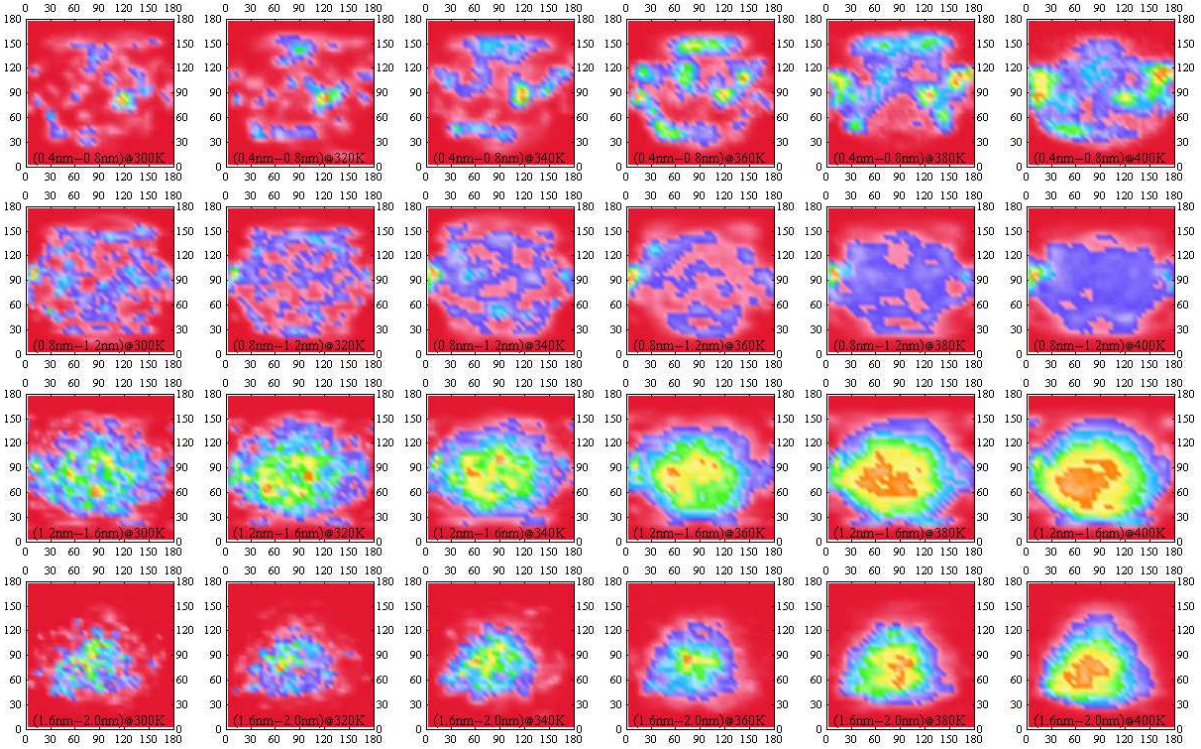

Figure III.4: Side chain end-to-end vector orientation contours for C96-C16,4 molecular crystals.

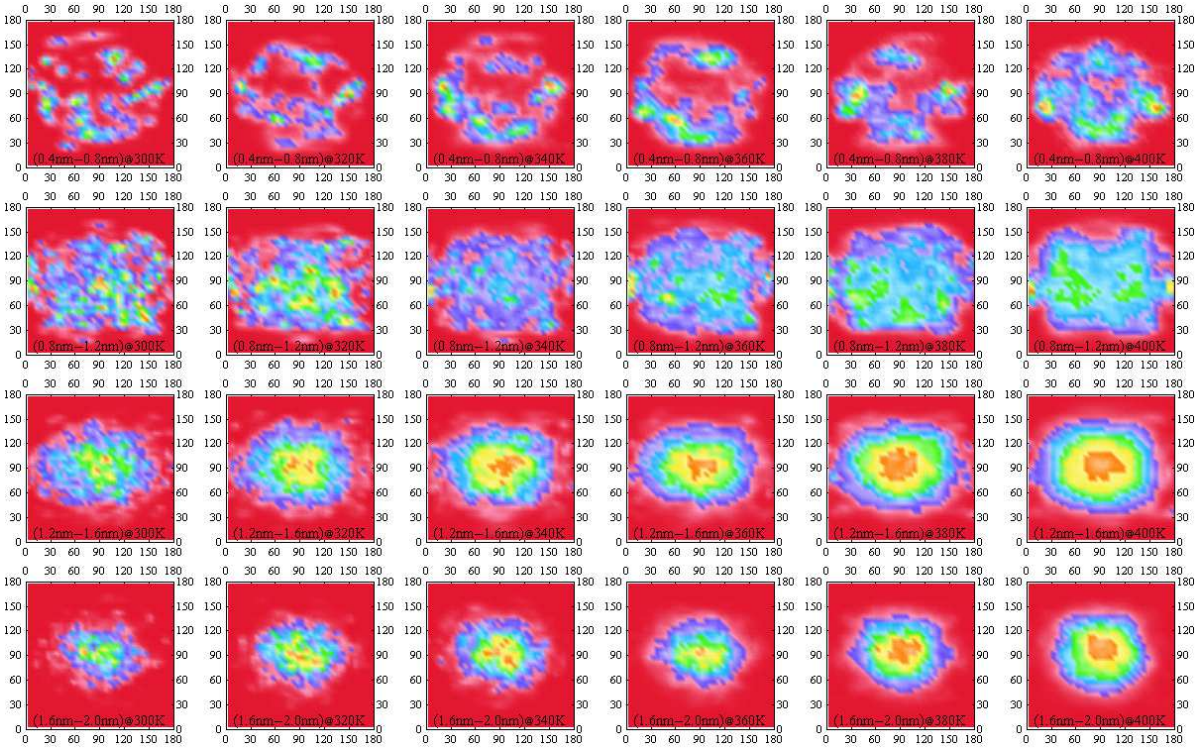

Figure III.5: Side chain end-to-end vector orientation contours for C132-C16,4(20°) molecular crystals.

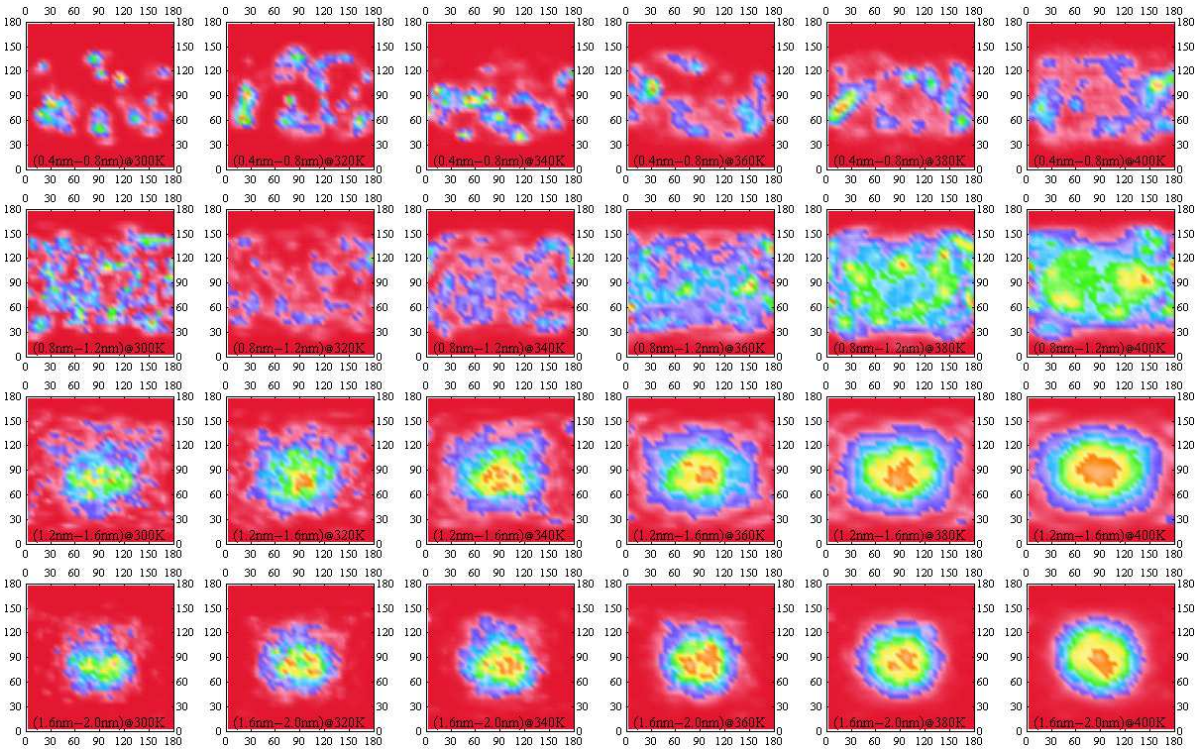

Figure III.6: Side chain end-to-end vector orientation contours for C132-C16,4(20°alt).

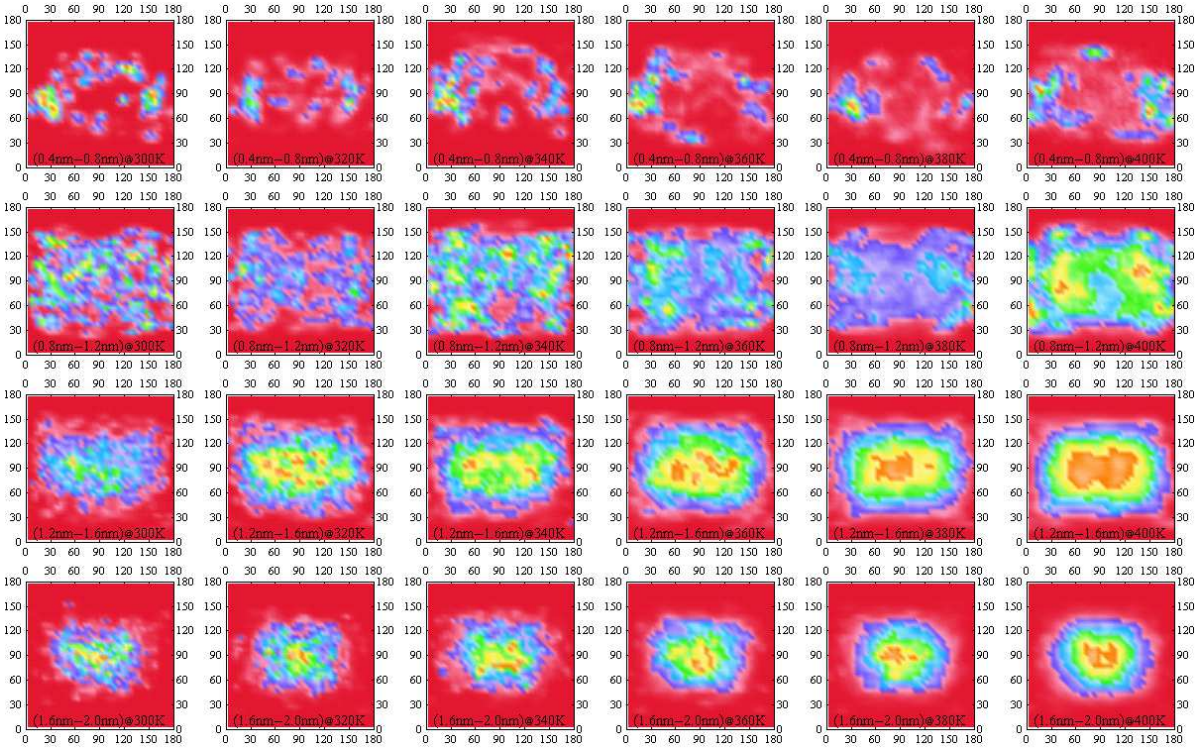

Figure III.7: Side chain end-to-end vector orientation contours for C132-C16,4(90°).

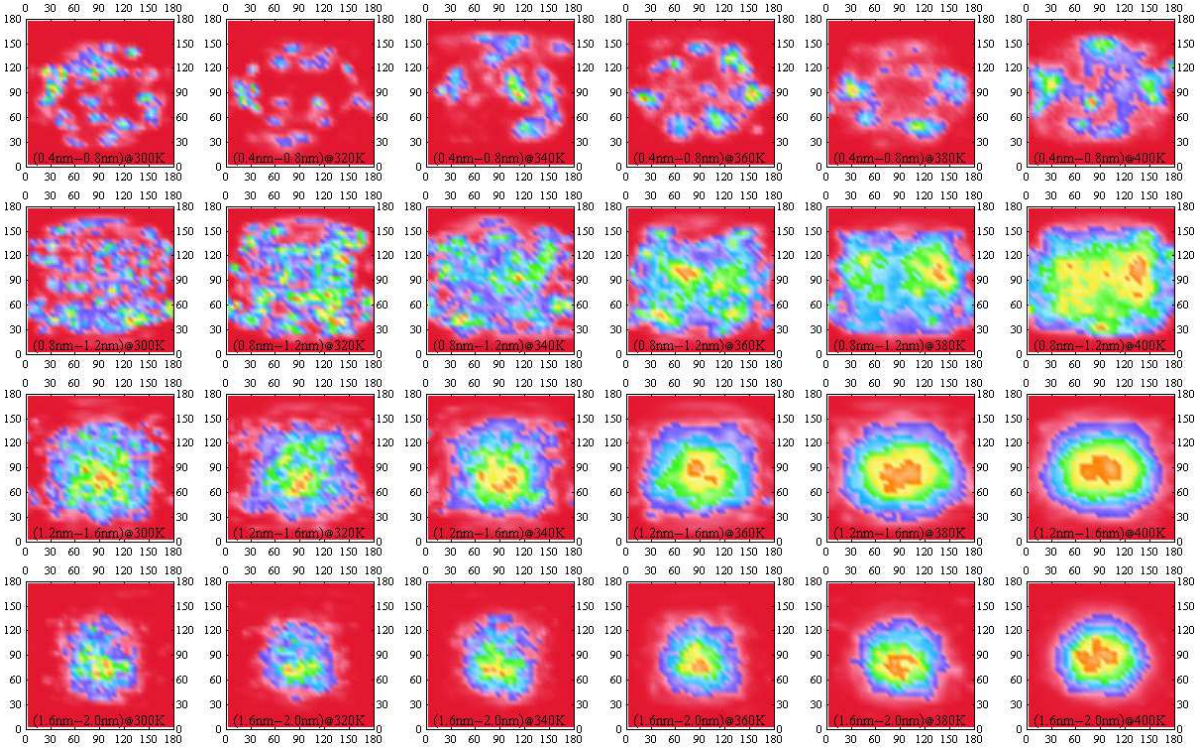

Figure III.8: Side chain end-to-end vector orientation contours for C132-C16,4(mixed 20°/90°).

Bibliography

[1] Cyvin, S. J.; Gutmain, I. *Kekulé Structures in Benzonoid Hydrocarbons*; Springer-Verlag, 1988.

[2] Coulson, C. A.; O'Leary, B.; Mallion, R. B. *Hückel Theory of Organic Chemists*; Academic Press, 1978.

[3] Balaban, A.; Harary, F. *Tetrahedron* **1968**, *24*, 2505–2516.

[4] Haley, M. M.; Tykwinski, R. R. *Carbon-Rich Compounds*; Wiley-VCH, 2006.

[5] Wöll, C. *Organic Electronics*; Wiley-VCH, 2009.

[6] Desiraju, G. R.; Gavezzotti, A. *Acta Cryst. B* **1989**, *45*, 473–482.

[7] Demus, D.; Goodby, J.; Gray, G. W.; Spiess, H.-W.; Vill, V. *Handbook of Liquid Crystals*; Wiley-VCH, 1998.

[8] Kumar, S. *Chemistry of Discotic Liquid Crystals*; CRC Press, 2016.

[9] Chandrasekhar, S.; Sadashiva, B. K.; Suresh, K. A. *Pramana* **1977**, *9*, 471–480.

[10] Kumar, S. *Chem. Soc. Rev.* **2006**, *35*, 83–109.

[11] Simpson, C. D.; Wu, J.; Watson, M. D.; Müllen, K. *J. Mater. Chem.* **2004**, *14*, 494–504.

[12] Wu, J.; Pisula, W.; Müllen, K. *Chem. Rev.* **2007**, *107*, 718–747.

[13] Jiang, J. *Functional Phthalocyanine Molecular Materials*; Springer, 2010.

[14] Goddard, R.; Haenel, M. W.; Herndon, W. C.; Krüger, C.; Zander, M. *J. Am. Chem. Soc.* **1995**, *117*, 30–41.

[15] Fischbach, I.; Pakula, T.; Minkin, P.; Fechtenkötter, A.; Müllen, K.; Spiess, H. W.; Saalwächter, K. *J. Phys. Chem. B* **2002**, *106*, 6408–6418.

[16] Clar, E.; Ironside, C. T.; Zander, M. *J. Chem. Soc.* **1959**, 142.

[17] Halleux, A.; Martin, R. H.; King, G. S. D. *Helv. Chim. Acta* **1958**, *41*, 1177–1183.

[18] Hendel, W.; Khan, Z. H.; Schmidt, W. *Tetrahedron* **1986**, *42*, 1127–1134.

[19] Herwig, P.; Kayser, C. W.; Müllen, K.; Spiess, H. W. *Adv. Mater.* **1996**, *8*, 510–513.

[20] Stabel, A.; Herwig, P.; Müllen, K.; Rabe, J. P. *Angew. Chem. Int. Ed. Engl.* **1995**, *34*, 1609–1611.

[21] Iyer, V. S.; Wehmeier, M.; Brand, J. D.; Keegstra, M. A.; Müllen, K. *Angew. Chem. Int. Ed. Engl.* **1997**, *36*, 1604–1607.

[22] Müller, M.; Iyer, V. S.; Kübel, C.; Enkelmann, V.; Müllen, K. *Angew. Chem. Int. Ed. Engl.* **1997**, *36*, 1607–1610.

[23] Müller, M.; Kübel, C.; Morgenroth, F.; Iyer, V. S.; Müllen, K. *Carbon* **1998**, *36*, 827–831.

[24] Fechtenkötter, A.; Tchebotareva, N.; Watson, M.; Müllen, K. *Tetrahedron* **2001**, *57*, 3769–3783.

[25] Carminati, M.; Brambilla, L.; Zerbi, G.; Müllen, K.; Wu, J. *J. Chem. Phys.* **2005**, *123*, 144706.

[26] Brown, S. P.; Schnell, I.; Brand, J. D.; Müllen, K.; Spiess, H. W. *J. Am. Chem. Soc.* **1999**, *121*, 6712–6718.

[27] van de Craats, A. M.; Warman, J. M. *Adv. Mater.* **2001**, *13*, 130–133.

[28] van de Craats, A. M.; Warman, J. M.; Fechtenkötter, A.; Brand, J. D.; Harbison, M. A.; Müllen, K. *Adv. Mater.* **1999**, *11*, 1469–1472.

[29] Debije, M. G.; Piris, J.; de Haas, M. P.; Warman, J. M.; Tomović, Ž.; Simpson, C. D.; Watson, M. D.; Müllen, K. *J. Am. Chem. Soc.* **2004**, *126*, 4641–4645.

[30] Pisula, W.; Menon, A.; Stepputat, M.; Lieberwirth, I.; Kolb, U.; Tracz, A.; Sirringhaus, H.; Pakula, T.; Müllen, K. *Adv. Mater.* **2005**, *17*, 684–689.

[31] Xiao, S.; Myers, M.; Miao, Q.; Sanaur, S.; Pang, K.; Steigerwald, M. L.; Nuckolls, C. *Angew. Chem. Int. Ed.* **2005**, *44*, 7390–7394.

[32] Elmahdy, M. M.; Floudas, G.; Kastler, M.; Müllen, K. *J. Phys.: Condens. Matter* **2008**, *20*, 244105.

[33] Ito, S.; Wehmeier, M.; Brand, J. D.; Kübel, C.; Epsch, R.; Rabe, J. P.; Müllen, K. *Chem. Eur. J.* **2000**, *6*, 4327–4342.

[34] Pisula, W.; Feng, X.; Müllen, K. *Adv. Mater.* **2010**, *22*, 3634–3649.

[35] Elmahdy, M. M.; Dou, X.; Mondeshki, M.; Floudas, G.; Butt, H.-J.; Spiess, H. W.; Müllen, K. *J. Am. Chem. Soc.* **2008**, *130*, 5311–5319.

[36] Elmahdy, M. M.; Floudas, G.; Mondeshki, M.; Spiess, H. W.; Dou, X.; Müllen, K. *Phys. Rev. Lett.* **2008**, *100*, 107801.

[37] Elmahdy, M. M.; Mondeshki, M.; Dou, X.; Butt, H.-J.; Spiess, H. W.; Müllen, K.; Floudas, G. *J. Chem. Phys.* **2009**, *131*, 114704.

[38] Grigoriadis, C.; Haase, N.; Butt, H.-J.; Müllen, K.; Floudas, G. *Adv. Mater.* **2010**, *22*, 1403–1406.

[39] Grigoriadis, C.; Haase, N.; Butt, H.-J.; Müllen, K.; Floudas, G. *Soft Matter* **2011**, *7*, 4680.

[40] Haase, N.; Grigoriadis, C.; Butt, H.-J.; Müllen, K.; Floudas, G. *J. Phys. Chem. B* **2011**, *115*, 5807–5814.

[41] Papadopoulos, P.; Grigoriadis, C.; Haase, N.; Butt, H.-J.; Müllen, K.; Floudas, G. *J. Phys. Chem. B* **2011**, *115*, 14919–14927.

[42] Wu, J.; Li, J.; Kolb, U.; Müllen, K. *Chem. Commun.* **2006**, 48–50.

[43] Hill, J. P.; Jin, W.; Kosaka, A.; Fukushima, T.; Ichihara, H.; Shimomura, T.; Ito, K.; Hashizume, T.; Ishii, N.; Aida, T. *Science* **2004**, *304*, 1481–1483.

[44] Aida, T.; Fukushima, T. *Phil. Trans. R. Soc. A* **2007**, *365*, 1539–1552.

[45] Wu, J.; Baumgarten, M.; Debije, M. G.; Warman, J. M.; Müllen, K. *Angew. Chem.* **2004**, *116*, 5445–5449.

[46] Brand, J. D.; Kübel, C.; Ito, S.; Müllen, K. *Chem. Mater.* **2000**, *12*, 1638–1647.

[47] Spraul, B. K.; Suresh, S.; Glaser, S.; Perahia, D.; Ballato, J.; Smith, D. W. *J. Am. Chem. Soc.* **2004**, *126*, 12772–12773.

[48] Wang, Z.; Dötz, F.; Enkelmann, V.; Müllen, K. *Angew. Chem. Int. Ed.* **2005**, *44*, 1247–1250.

[49] Zhang, Y.; Zhang, Y.; Li, G.; Lu, J.; Lin, X.; Tan, Y.; Feng, X.; Du, S.; Müllen, K.; Gao, H.-J. *J. Chem. Phys.* **2015**, *142*, 101911.

[50] Kratzer, A.; Englert, J. M.; Lungerich, D.; Heinemann, F. W.; Jux, N.; Hirsch, A. *Faraday Discuss.* **2014**, *173*, 297–310.

[51] Yamamoto, Y.; Fukushima, T.; Suna, Y.; Ishii, N.; Saeki, A.; Seki, S.; Tagawa, S.; Taniguchi, M.; Kawai, T.; Aida, T. *Science* **2006**, *314*, 1761–1764.

[52] Yamamoto, Y.; Zhang, G.; Jin, W.; Fukushima, T.; Ishii, N.; Saeki, A.; Seki, S.; Tagawa, S.; Minari, T.; Tsukagoshi, K.; Aida, T. *PNAS* **2009**, *106*, 21051–21056.

[53] Pipertzis, A.; Zardalidis, G.; Wunderlich, K.; Klapper, M.; Müllen, K.; Floudas, G. *Macromolecules* **2017**, *50*, 1981–1990.

[54] Lim, Y.; Lee, S.; Jang, H.; Yoo, J.; Ha, J.; Ju, H.; Hong, T.; Kim, W. *Int. J. Hydrogen Energy* **2015**, *40*, 1316–1323.

[55] Wang, P.-I.; Pisula, W.; Müllen, K.; Liaw, D.-J. *Polym. Chem.* **2016**, *7*, 6211–6219.

[56] Gao, C.; Qiao, Z.; Shi, K.; Chen, S.; Li, Y.; Yu, G.; Li, X.; Wang, H. *Org. Electron.* **2016**, *38*, 245–255.

[57] Thompson, C. M.; McCandless, G. T.; Wijenayake, S. N.; Alfarawati, O.; Jahangiri, M.; Kokash, A.; Tran, Z.; Smaldone, R. A. *Macromolecules* **2014**, *47*, 8645–8652.

[58] Karunathilake, A. A. K.; Chang, J.; Thompson, C. M.; Nguyen, C. U.; Nguyen, D. Q.; Rajan, A.; Sridharan, A.; Vyakaranam, M.; Adegboyega, N.; Kim, S. J.; Smaldone, R. A. *RSC Adv.* **2016**, *6*, 65763–65769.

[59] Duran, H.; Hartmann-Azanza, B.; Steinhart, M.; Gehrig, D.; Laquai, F.; Feng, X.; Müllen, K.; Butt, H.-J.; Floudas, G. *ACS Nano* **2012**, *6*, 9359–9365.

[60] Zhang, R.; Ungar, G.; Zeng, X.; Shen, Z. *Soft Matter* **2017**, *13*, 4122–4131.

[61] Pisula, W.; Tomović, Ž.; Simpson, C.; Kastler, M.; Pakula, T.; Müllen, K. *Chem. Mater.* **2005**, *17*, 4296–4303.

[62] Watson, M. D.; Fechtenkötter, A.; Müllen, K. *Chem. Rev.* **2001**, *101*, 1267–1300.

[63] Tomović, Ž.; Watson, M. D.; Müllen, K. *Angew. Chem. Int. Ed.* **2004**, *43*, 755–758.

[64] Samorí, P.; Severin, N.; Simpson, C. D.; Müllen, K.; Rabe, J. P. *J. Am. Chem. Soc.* **2002**, *124*, 9454–9457.

[65] Friedlein, R.; Crispin, X.; Simpson, C. D.; Watson, M. D.; Jäckel, F.; Osikowicz, W.; Marciniak, S.; de Jong, M. P.; Samorí, P.; Jönsson, S. K. M.; Fahlman, M.; Müllen, K.; Rabe, J. P.; Salaneck, W. R. *Phys. Rev. B* **2003**, *68*, 195414.

[66] Palermo, V.; Morelli, S.; Simpson, C.; Müllen, K.; Samorí, P. *J. Mater. Chem.* **2006**, *16*, 266–271.

[67] Feng, X.; Marcon, V.; Pisula, W.; Hansen, M. R.; Kirkpatrick, J.; Grozema, F.; Andrienko, D.; Kremer, K.; Müllen, K. *Nat. Mater.* **2009**, *8*, 421–426.

[68] Grimsdale, A. C.; Wu, J.; Müllen, K. *Chem. Commun.* **2005**, 2197–2204.

[69] Yan, X.; Cui, X.; Li, L. *J. Am. Chem. Soc.* **2010**, *132*, 5944–5945.

[70] Zhu, S.; Wang, L.; Li, B.; Song, Y.; Zhao, X.; Zhang, G.; Zhang, S.; Lu, S.; Zhang, J.; Wang, H.; Sun, H.; Yang, B. *Carbon* **2014**, *77*, 462–472.

[71] Yuan, B.; Sun, X.; Yan, J.; Xie, Z.; Chen, P.; Zhou, S. *Phys. Chem. Chem. Phys.* **2016**, *18*, 25002–25009.

[72] Zhu, S.; Song, Y.; Wang, J.; Wan, H.; Zhang, Y.; Ning, Y.; Yang, B. *Nano Today* **2017**, *13*, 10–14.

[73] Wang, J.; Xin, X.; Lin, Z. *Nanoscale* **2011**, *3*, 3040.

[74] Wöhrle, T.; Wurzbach, I.; Kirres, J.; Kostidou, A.; Kapernaum, N.; Litterscheidt, J.; Haenle, J. C.; Staffeld, P.; Baro, A.; Giesselmann, F.; Laschat, S. *Chem. Rev.* **2016**, *116*, 1139–1241.

[75] Boden, N.; Bushby, R. J.; Cammidge, A. N.; El-Mansoury, A.; Martin, P. S.; Lu, Z. *J. Mater. Chem.* **1999**, *9*, 1391–1402.

[76] Ito, S.; Herwig, P. T.; Böhme, T.; Rabe, J. P.; Rettig, W.; Müllen, K. *J. Am. Chem. Soc.* **2000**, *122*, 7698–7706.

[77] Grimsdale, A. C.; Müllen, K. *Angew. Chem. Int. Ed.* **2005**, *44*, 5592–5629.

[78] Nakano, T.; Morisaki, Y.; Chujo, Y. *Tetrahedron Lett.* **2015**, *56*, 2086–2090.

[79] Watson, M. D.; Jäckel, F.; Severin, N.; Rabe, J. P.; Müllen, K. *J. Am. Chem. Soc.* **2004**, *126*, 1402–1407.

[80] Wang, M.; Wudl, F. *J. Mater. Chem.* **2012**, *22*, 24297.

[81] Jäckel, F.; Watson, M. D.; Müllen, K.; Rabe, J. P. *Phys. Rev. Lett.* **2004**, *92*, 188303.

[82] Müllen, K.; Rabe, J. P. *Acc. Chem. Res.* **2008**, *41*, 511–520.

[83] Wu, J.; Watson, M. D.; Tchebotareva, N.; Wang, Z.; Müllen, K. *J. Org. Chem.* **2004**, *69*, 8194–8204.

[84] Wöhrle, T.; Beardsworth, S. J.; Schilling, C.; Baro, A.; Giesselmann, F.; Laschat, S. *Soft Matter* **2016**, *12*, 3730–3736.

[85] Bao, C.; Jin, M.; Lu, R.; Song, Z.; Yang, X.; Song, D.; Xu, T.; Liu, G.; Zhao, Y. *Tetrahedron* **2007**, *63*, 7443–7448.

[86] Kotha, S.; Kashinath, D.; Kumar, S. *Tetrahedron Lett.* **2008**, *49*, 5419–5423.

[87] Kukhta, N. A.; Volyniuk, D.; Peciulyte, L.; Ostrauskaite, J.; Juska, G.; Grazulevicius, J. V. *Dyes Pigm.* **2015**, *117*, 122–132.

[88] Bai, Y.-F.; Chen, L.-Q.; Hu, P.; Luo, K.-J.; Yu, W.-H.; Ni, H.-L.; Zhao, K.-Q.; Wang, B.-Q. *Liq. Cryst.* **2015**, *42*, 1591–1600.

[89] Aytun, T.; Santos, P. J.; Bruns, C. J.; Huang, D.; Koltonow, A. R.; de la Cruz, M. O.; Stupp, S. I. *J. Phys. Chem. C* **2016**, *120*, 3602–3611.

[90] Cremer, J.; Bäuerle, P. *J. Mater. Chem.* **2006**, *16*, 874–884.

[91] Dong, H.; Zhu, H.; Meng, Q.; Gong, X.; Hu, W. *Chem. Soc. Rev.* **2012**, *41*, 1754–1808.

[92] Kao, Y.-W.; Lee, W.-H.; Jeng, R.-J.; Huang, C.-F.; Wu, J. Y.; Lee, R.-H. *Mater. Chem. Phys.* **2015**, *163*, 138–151.

[93] Kushida, T.; Shuto, A.; Yoshio, M.; Kato, T.; Yamaguchi, S. *Angew. Chem. Int. Ed.* **2015**, *54*, 6922–6925.

[94] Ji, L.; Griesbeck, S.; Marder, T. B. *Chem. Sci.* **2017**, *8*, 846–863.

[95] Li, X.-C.; Wang, C.-Y.; Lai, W.-Y.; Huang, W. *J. Mater. Chem. C* **2016**, *4*, 10574–10587.

[96] Zhang, Y.; Hanifi, D. A.; Fernández-Liencres, M. P.; Klivansky, L. M.; Ma, B.; Navarro, A.; Liu, Y. *ACS Appl. Mater. Interfaces* **2017**, *9*, 20010–20019.

[97] Narita, A.; Wang, X.-Y.; Feng, X.; Müllen, K. *Chem. Soc. Rev.* **2015**, *44*, 6616–6643.

[98] Türp, D.; Nguyen, T.-T.-T.; Baumgarten, M.; Müllen, K. *New J. Chem.* **2012**, *36*, 282–298.

[99] Yen, H.-J.; et al. *Adv. Mater.* **2016**, *28*, 10250–10256.

[100] van Nostrum, C. F.; Picken, S. J.; Schouten, A.-J.; Nolte, R. J. M. *J. Am. Chem. Soc.* **1995**, *117*, 9957–9965.

[101] van Nostrum, C. F.; Nolte, R. J. M. *Chem. Commun.* **1996**, 2385–2392.

[102] Simpson, C. D.; Mattersteig, G.; Martin, K.; Gherghel, L.; Bauer, R. E.; Räder, H. J.; Müllen, K. *J. Am. Chem. Soc.* **2004**, *126*, 3139–3147.

[103] Metropolis, N.; Worlton, J. *IEEE Ann. Hist. Comput.* **1980**, *2*, 49–59.

[104] Rojas, R.; Hashagen, U. *The First Computers*; MIT Press, 2002.

[105] Hord, R. M. *The Illiac IV*; Springer-Verlag, 1982.

[106] Vetter, J. S. *Contemporary High Performance Computing*; CRC Press, 2013.

[107] Nickolls, J.; Dally, W. J. *IEEE Micro* **2010**, *30*, 56–69.

[108] Sodani, A.; Gramunt, R.; Corbal, J.; Kim, H.-S.; Vinod, K.; Chinthamani, S.; Hutsell, S.; Agarwal, R.; Liu, Y.-C. *IEEE Micro* **2016**, *36*, 34–46.

[109] Graham, S. L.; Snir, M.; Patterson, C. A. *Getting Up to Speed: The Future of Supercomputing*; National Academies Press, 2005.

[110] LeSar, R. *Introduction to Computational Materials Science*; Cambridge University Press, 2013.

[111] Deymier, P. A.; Runge, K.; Muralidharan, K. *Multiscale Paradigms in Integrated Computational Materials Science and Engineering*; Springer, 2016.

[112] Hartree, D. R. *Rep. Prog. Phys.* **1947**, *11*, 113–143.

[113] Raabe, D. *Computational Materials Science*; Wiley-VCH, 1998.

[114] Piela, L. *Ideas of Quantum Chemistry*; Elsevier, 2013.

[115] Magnasco, V. *Methods of Molecular Quantum Mechanics: An Introduction to Electronic Molecular Structure*; Wiley, 2009.

[116] Kaxiras, E. *Atomic and Electronic Structure of Solids*; Cambridge University Press, 2003.

[117] Martin, R. M. *Electronic Structure*; Cambridge University Press, 2004.

[118] Hinchliffe, A. *Molecular Modelling for Beginners*; Wiley, 2008.

[119] Ohno, K.; Esfarjani, K.; Kawazoe, Y. *Computational Materials Science*; Springer-Verlag, 1999.

[120] Jensen, F. *Introduction to Computational Chemistry*; Wiley, 2017.

[121] Heinecke, A.; Eckhardt, W.; Horsch, M.; Bungartz, H.-J. *Supercomputing for Molecular Dynamics Simulations*; Springer, 2015.

[122] van Duin, A. C. T.; Dasgupta, S.; Lorant, F.; Goddard, W. A. *J. Phys. Chem. A* **2001**, *105*, 9396–9409.

[123] Frenkel, D.; Smit, B. *Understanding Molecular Simulation*; Academic Press, 2002.

[124] Kotelyanskii, M.; Theodorou, D. N. *Simulation Methods for Polymers*; Marcel Dekker, 2004.

[125] Voth, G. A. *Coarse-Graining of Condensed Phase and Biomolecular Systems*; CRC Press, 2009.

[126] Torres, A. E.; Guadarrama, P.; Fomine, S. *J. Mol. Model.* **2014**, *20*, 2208.

[127] Rivero, P.; Jiménez-Hoyos, C. A.; Scuseria, G. E. *J. Phys. Chem. B* **2013**, *117*, 12750–12758.

[128] Nagai, H.; Nakano, M.; Yoneda, K.; Fukui, H.; Minami, T.; Bonness, S.; Kishi, R.; Takahashi, H.; Kubo, T.; Kamada, K.; Ohta, K.; Champagne, B.; Botek, E. *Chem. Phys. Lett.* **2009**, *477*, 355–359.

[129] Havenith, R. W. A.; Meijer, A. J. H. M.; Irving, B. J.; Fowler, P. W. *Mol. Phys.* **2009**, *107*, 2591–2600.

[130] Schröder, D.; Loos, J.; Schwarz, H.; Thissen, R.; Preda, D. V.; Scott, L. T.; Caraiman, D.; Frach, M. V.; Böhme, D. K. *Helv. Chim. Acta* **2001**, *84*, 1625–1634.

[131] Naghavi, S. S.; Gruhn, T.; Alijani, V.; Fecher, G. H.; Felser, C.; Medjanik, K.; Kutnyakhov, D.; Nepijko, S. A.; Schönhense, G.; Rieger, R.; Baumgarten, M.; Müllen, K. *J. Mol. Spectrosc.* **2011**, *265*, 95–101.

[132] Holm, A. I. S.; Johansson, H. A. B.; Cederquist, H.; Zettergren, H. *J. Chem. Phys.* **2011**, *134*, 044301.

[133] García-Cruz, I.; Martínez-Magadán, J.-M. *Pet. Sci. Technol.* **2007**, *25*, 67–80.

[134] Kruglova, O.; Mulder, F. M.; Kotlewski, A.; Picken, S. J.; Parker, S.; Johnson, M. R.; Kearley, G. J. *Chem. Phys.* **2006**, *330*, 360–364.

[135] Etchegoin, P. *Phys. Rev. E* **1997**, *56*, 538–548.

[136] Belviso, S.; Amati, M.; Rossano, R.; Crispini, A.; Lelj, F. *Dalton Trans.* **2015**, *44*, 2191–2207.

[137] Gallant, A. J.; Hui, J. K.-H.; Zahariev, F. E.; Wang, Y. A.; MacLachlan, M. J. *J. Org. Chem.* **2005**, *70*, 7936–7946.

[138] Maghsoumi, A.; Narita, A.; Dong, R.; Feng, X.; Castiglioni, C.; Müllen, K.; Tommasini, M. *Phys. Chem. Chem. Phys.* **2016**, *18*, 11869–11878.

[139] Fan, X.-L.; Wang, X.-Q.; Wang, J.-T.; Li, H.-D. *Phys. Lett. A* **2014**, *378*, 1379–1382.

[140] Hu, W.; Lin, L.; Yang, C.; Yang, J. *J. Chem. Phys.* **2014**, *141*, 214704.

[141] Karadakov, P. B. *Chem. Phys. Lett.* **2016**, *646*, 190–196.

[142] Bégué, D.; Guille, E.; Metz, S.; Arnaud, M. A.; Silva, H. S.; Seck, M.; Fayon, P.; Dagron-Lartigau, C.; Iratcabal, P.; Hiorns, R. C. *RSC Adv.* **2016**, *6*, 13653–13656.

[143] Monari, A.; Evangelisti, S.; Leininger, T. *J. Chem. Phys.* **2010**, *133*, 124301.

[144] Yurtsever, E. *Theor. Chem. Acc.* **2010**, *127*, 133–139.

[145] Rapacioli, M.; Spiegelman, F.; Talbi, D.; Mineva, T.; Goursot, A.; Heine, T.; Seifert, G. *J. Chem. Phys.* **2009**, *130*, 244304.

[146] Podeszwa, R. *J. Chem. Phys.* **2010**, *132*, 044704.

[147] Li, J.; Liu, Y.; Qian, Y.; Li, L.; Xie, L.; Shang, J.; Yu, T.; Yi, M.; Huang, W. *Phys. Chem. Chem. Phys.* **2013**, *15*, 12694.

[148] Gonthier, J. F.; Steinmann, S. N.; Roch, L.; Ruggi, A.; Luisier, N.; Severin, K.; Corminboeuf, C. *Chem. Commun.* **2012**, *48*, 9239–9241.

[149] Obolensky, O. I.; Semenikhina, V. V.; Solov'yov, A. V.; Greiner, W. *Int. J. Quantum Chem.* **2007**, *107*, 1335–1343.

[150] Zhao, Y.; Truhlar, D. G. *J. Phys. Chem. C* **2008**, *112*, 4061–4067.

[151] Mackie, I. D.; DiLabio, G. A. *J. Phys. Chem. A* **2008**, *112*, 10968–10976.

[152] Antony, J.; Alameddine, B.; Jenny, T. A.; Grimme, S. *J. Phys. Chem. A* **2013**, *117*, 616–625.

[153] Guan, Y.; Jones, M. L.; Miller, A. E.; Wheeler, S. E. *Phys. Chem. Chem. Phys.* **2017**, *19*, 18186–18193.

[154] Paraschiv, I.; Giesbers, M.; van Lagen, B.; Grozema, F. C.; Abellon, R. D.; Siebbeles, L. D. A.; Marcelis, A. T. M.; Zuilhof, H.; Sudhölter, E. J. R. *Chem. Mater.* **2006**, *18*, 968–974.

[155] Rapacioli, M.; Calvo, F.; Spiegelman, F.; Joblin, C.; Wales, D. J. *J. Phys. Chem. A* **2005**, *109*, 2487–2497.

[156] Cinacchi, G.; Prampolini, G. *J. Phys. Chem. C* **2008**, *112*, 9501–9509.

[157] Ding, L.-P.; Kuang, X.-Y.; Shao, P.; Zhong, M.-M. *Dalton Trans.* **2013**, *42*, 8644.

[158] Lao, K.-U.; Tsou, P.-K.; Lankau, T.; Yu, C.-H. *Phys. Chem. Chem. Phys.* **2012**, *14*, 138–147.

[159] Cornil, J.; Lemaur, V.; Calbert, J.-P.; Brédas, J.-L. *Adv. Mater.* **2002**, *14*, 726.

[160] Köse, M. E.; Long, H.; Kim, K.; Graf, P.; Ginley, D. *J. Phys. Chem. A* **2010**, *114*, 4388–4393.

[161] Cardia, R.; Malloci, G.; Bosin, A.; Serra, G.; Cappellini, G. *Chem. Phys.* **2016**, *478*, 8–13.

[162] Senthilkumar, K.; Grozema, F. C.; Bickelhaupt, F. M.; Siebbeles, L. D. A. *J. Chem. Phys.* **2003**, *119*, 9809–9817.

[163] Mikołajczyk, M. M.; Toman, P.; Bartkowiak, W. *Chem. Phys. Lett.* **2010**, *485*, 253–257.

[164] Sanyal, S.; Manna, A. K.; Pati, S. K. *ChemPhysChem* **2014**, *15*, 885–893.

[165] Chen, X.; Bai, F.-Q.; Tang, Y.; Zhang, H.-X. *J. Comput. Chem.* **2016**, *37*, 813–824.

[166] Yang, X.; Li, Q.; Shuai, Z. *Nanotechnology* **2007**, *18*, 424029.

[167] Zarate, X.; Schott, E. *RSC Adv.* **2014**, *4*, 15642.

[168] Navamani, K.; Senthilkumar, K. *RSC Adv.* **2015**, *5*, 38722–38732.

[169] Navamani, K.; Senthilkumar, K. *Phys. Chem. Chem. Phys.* **2015**, *17*, 17729–17738.

[170] Bhattacharyya, K.; Mukhopadhyay, T. K.; Datta, A. *Phys. Chem. Chem. Phys.* **2016**, *18*, 14886–14893.

[171] Deng, W.-Q.; Goddard, W. A. *J. Phys. Chem. B* **2004**, *108*, 8614–8621.

[172] Watanabe, S.; Shimodo, Y.; Morihashi, K. *Theor. Chem. Acc.* **2011**, *130*, 807–813.

[173] Yoshida, Y.; Isomura, K.; Kumagai, Y.; Maesato, M.; Kishida, H.; Mizuno, M.; Saito, G. *J. Phys.: Condens. Matter* **2016**, *28*, 304001.

[174] Sanyal, S.; Manna, A. K.; Pati, S. K. *J. Phys. Chem. C* **2013**, *117*, 825–836.

[175] Sancho-García, J. C.; Pérez-Jiménez, A. J. *J. Chem. Phys.* **2014**, *141*, 134708.

[176] Lee, C.; Sohlberg, K. *Chem. Phys.* **2010**, *367*, 7–19.

[177] Kosugi, T.; Miyake, T.; Ishibashi, S.; Arita, R.; Aoki, H. *Phys. Rev. B* **2011**, *84*, 020507(R).

[178] Sanyal, S.; Manna, A. K.; Pati, S. K. *J. Mater. Chem. C* **2014**, *2*, 2918–2928.

[179] Delgado, M. C. R.; Kim, E.-G.; da Silva Filho, D. A.; Brédas, J.-L. *J. Am. Chem. Soc.* **2010**, *132*, 3375–3387.

[180] Geng, Y.; Wang, J.; Wu, S.; Li, H.; Yu, F.; Yang, G.; Gao, H.; Su, Z. *J. Mater. Chem.* **2011**, *21*, 134–143.

[181] Chen, X.-K.; Zou, L.-Y.; Guo, J.-F.; Ren, A.-M. *J. Mater. Chem.* **2012**, *22*, 6471.

[182] Norton, J. E.; Brédas, J.-L. *J. Chem. Phys.* **2008**, *128*, 034701.

[183] Tsetseris, L. *Phys. Chem. Chem. Phys.* **2014**, *16*, 3317–3322.

[184] Cinacchi, G.; Colle, R.; Parruccini, P.; Tani, A. *J. Chem. Phys.* **2008**, *129*, 174708.

[185] Tsetseris, L. *J. Phys. Chem. C* **2014**, *118*, 1347–1352.

[186] Maliniak, A. *J. Chem. Phys.* **1992**, *96*, 2306–2317.

[187] Bast, T.; Hentschke, R. *J. Phys. Chem.* **1996**, *100*, 12162–12171.

[188] Kearley, G. J.; Mulder, F. M.; Picken, S. J.; Kouwer, P. H. J.; Stride, J. *Chem. Phys.* **2003**, *292*, 185–190.

[189] Cinacchi, G.; Colle, R.; Tani, A. *J. Phys. Chem. B* **2004**, *108*, 7969–7977.

[190] Cinacchi, G. *J. Phys. Chem. B* **2005**, *109*, 8125–8131.

[191] Merekalova, N. D.; Merekalov, A. S.; Otmakhova, O. A.; Talroze, R. V. *Polym. Sci. Ser. A Polym. Phys.* **2008**, *50*, 84–90.

[192] Kruglova, O.; Mulder, F. M.; Kearley, G. J.; Picken, S. J.; Stride, J. A.; Paraschiv, I.; Zuilhof, H. *Phys. Rev. E* **2010**, *82*, 051703.

[193] Muccioli, L.; Berardi, R.; Orlandi, S.; Ricci, M.; Zannoni, C. *Theor. Chem. Acc.* **2007**, *117*, 1085–1092.

[194] Andrienko, D.; Marcon, V.; Kremer, K. *J. Chem. Phys.* **2006**, *125*, 124902.

[195] Marcon, V.; Vehoff, T.; Kirkpatrick, J.; Jeong, C.; Yoon, D. Y.; Kremer, K.; Andrienko, D. *J. Chem. Phys.* **2008**, *129*, 094505.

[196] Cristinziano, P. L.; Lelj, F. *J. Chem. Phys.* **2007**, *127*, 134506.

[197] Yoneya, M.; Makabe, T.; Miyamoto, A.; Shimizu, Y.; Miyake, Y.; Yoshida, H.; Fujii, A.; Ozaki, M. *Phys, Rev. E* **2014**, *89*, 062505.

[198] Costa, J. L. L. F. S.; Simionesie, D.; Zhang, Z. J.; Mulheran, P. A. *J. Phys.: Condens. Matter* **2016**, *28*, 394002.

[199] Khanna, R.; Sahajwalla, V.; Hurt, R. *Carbon* **2005**, *43*, 67–77.

[200] Herdman, J. D.; Miller, J. H. *J. Phys. Chem. A* **2008**, *112*, 6249–6256.

[201] Totton, T. S.; Misquitta, A. J.; Kraft, M. *J. Chem. Theory Comput.* **2010**, *6*, 683–695.

[202] Khanna, R.; Waters, A. M.; Sahajwalla, V. *Comput. Mater. Sci.* **2010**, *49*, S108–S113.

[203] Totton, T. S.; Misquitta, A. J.; Kraft, M. *Phys. Chem. Chem. Phys.* **2012**, *14*, 4081–4094.

[204] Guan, Y.; Wheeler, S. E. *J. Phys. Chem. C* **2017**, *121*, 8541–8547.

[205] Wilson, M. R.; Duncan, P. D.; Dennison, M.; Masters, A. J. *Soft Matter* **2012**, *8*, 3348.

[206] Chen, D.; Totton, T. S.; Akroyd, J. W. J.; Mosbach, S.; Kraft, M. *Carbon* **2014**, *67*, 79–91.

[207] Chen, D.; Akroyd, J.; Mosbach, S.; Opalka, D.; Kraft, M. *Combust. Flame* **2015**, *162*, 486–495.

[208] Mao, Q.; van Duin, A. C. T.; Luo, K. H. *Carbon* **2017**, *121*, 380–388.

[209] Markovitsi, D.; Germain, A.; Millié, P.; Lécuyer, P.; Gallos, L.; Argyrakis, P.; Bengs, H.; Ringsdorf, H. *J. Phys. Chem.* **1995**, *99*, 1005–1017.

[210] Lemaur, V.; da Silva Filho, D. A.; Coropceanu, V.; Lehmann, M.; Geerts, Y.; Piris, J.; Debije, M. G.; van de Craats, A. M.; Senthilkumar, K.; Siebbeles, L. D. A.; Warman, J. M.; Brédas, J.-L.; Cornil, J. *J. Am. Chem. Soc.* **2004**, *126*, 3271–3279.

[211] Kruglova, O.; Mulder, F. M.; Siebbeles, L. D. A.; Kearley, G. J. *Chem. Phys.* **2006**, *330*, 333–337.

[212] Haverkate, L. A.; Zbiri, M.; Johnson, M. R.; Deme, B.; Mulder, F. M.; Kearley, G. J. *J. Phys. Chem. B* **2011**, *115*, 13809–13816.

[213] Kirkpatrick, J.; Marcon, V.; Nelson, J.; Kremer, K.; Andrienko, D. *Phys. Rev. Lett.* **2007**, *98*, 227402.

[214] Kirkpatrick, J.; Marcon, V.; Kremer, K.; Nelson, J.; Andrienko, D. *Phys. Status Solidi B* **2008**, *245*, 835–838.

[215] Kirkpatrick, J.; Marcon, V.; Kremer, K.; Nelson, J.; Andrienko, D. *J. Chem. Phys.* **2008**, *129*, 094506.

[216] Andrienko, D.; Kirkpatrick, J.; Marcon, V.; Nelson, J.; Kremer, K. *Phys. Status Solidi B* **2008**, *245*, 830–834.

[217] Troisi, A.; Cheung, D. L.; Andrienko, D. *Phys. Rev. Lett.* **2009**, *102*, 116602.

[218] Bag, S.; Maingi, V.; Maiti, P. K.; Yelk, J.; Glaser, M. A.; Walba, D. M.; Clark, N. A. *J. Chem. Phys.* **2015**, *143*, 144505.

[219] Bashir, A.; Heck, A.; Narita, A.; Feng, X.; Nefedov, A.; Rohwerder, M.; Müllen, K.; Elstner, M.; Wöll, C. *Phys. Chem. Chem. Phys.* **2015**, *17*, 21988–21996.

[220] Olivier, Y.; Muccioli, L.; Lemaur, V.; Geerts, Y. H.; Zannoni, C.; Cornil, J. *J. Phys. Chem. B* **2009**, *113*, 14102–14111.

[221] Marcon, V.; Kirkpatrick, J.; Pisula, W.; Andrienko, D. *Phys. Status Solidi B* **2008**, *245*, 820–824.

[222] Marcon, V.; Breiby, D. W.; Pisula, W.; Dahl, J.; Kirkpatrick, J.; Patwardhan, S.; Grozema, F.; Andrienko, D. *J. Am. Chem. Soc.* **2009**, *131*, 11426–11432.

[223] May, F.; Marcon, V.; Hansen, M. R.; Grozema, F.; Andrienko, D. *J. Mater. Chem.* **2011**, *21*, 9538.

[224] Saranya, G.; Santhanamoorthi, N.; Kolandaivel, P.; Senthilkumar, K. *Int. J. Quantum Chem.* **2012**, *112*, 713–723.

[225] Vehoff, T.; Baumeier, B.; Andrienko, D. *J. Chem. Phys.* **2010**, *133*, 134901.

[226] Vehoff, T.; Baumeier, B.; Troisi, A.; Andrienko, D. *J. Am. Chem. Soc.* **2010**, *132*, 11702–11708.

[227] Navamani, K.; Senthilkumar, K. *J. Phys. Chem. C* **2014**, *118*, 27754–27762.

[228] Idé, J.; Méreau, R.; Ducasse, L.; Castet, F.; Bock, H.; Olivier, Y.; Cornil, J.; Beljonne, D.; D'Avino, G.; Roscioni, O. M.; Muccioli, L.; Zannoni, C. *J. Am. Chem. Soc.* **2014**, *136*, 2911–2920.

[229] Navarro, A.; Fernández-Liencres, M. P.; García, G.; Granadino-Roldán, J. M.; Fernández-Gómez, M. *Phys. Chem. Chem. Phys.* **2015**, *17*, 605–618.

[230] Zhang, Z.; Horsch, M. A.; Lamm, M. H.; Glotzer, S. C. *Nano Letters* **2003**, *3*, 1341–1346.

[231] Kim, Y.; Alexander-Katz, A. *J. Chem. Phys.* **2010**, *132*, 174901.

[232] Kim, Y.; Ha, E.; Alexander-Katz, A. *Macromolecules* **2011**, *44*, 7016–7025.

[233] Avendaño, C.; Müller, E. A. *Soft Matter* **2011**, *7*, 1694–1701.

[234] Gong, M.; Yu, Q.; Ma, S.; Luo, F.; Wang, R.; Chen, D. *Macromolecules* **2017**, *50*, 5556–5564.

[235] von Lilienfeld, O. A.; Andrienko, D. *J. Chem. Phys.* **2006**, *124*, 054307.

[236] Veerman, J. A. C.; Frenkel, D. *Phys. Rev. A* **1992**, *45*, 5632–5648.

[237] Patti, A.; Belli, S.; van Roij, R.; Dijkstra, M. *Soft Matter* **2011**, *7*, 3533.

[238] Odriozola, G.; de J. Guevara-Rodríguez, F. *J. Chem. Phys.* **2011**, *134*, 201103.

[239] Morales-Anda, L.; Wensink, H. H.; Galindo, A.; Gil-Villegas, A. *J. Chem. Phys.* **2012**, *136*, 034901.

[240] Li, Z.-W.; Chen, L.-J.; Zhao, Y.; Lu, Z.-Y. *J. Phys. Chem. B* **2008**, *112*, 13842–13848.

[241] Li, Z.-W.; Sun, Z.-Y.; Lu, Z.-Y. *J. Phys. Chem. B* **2010**, *114*, 2353–2358.

[242] Purton, J. A.; Smith, W. *Mol. Simul.* **2010**, *36*, 796–800.

[243] Emerson, A. P. J.; Luckhurst, G. R.; Whatling, S. G. *Mol. Phys.* **1994**, *82*, 113–124.

[244] Bates, M. A.; Luckhurst, G. R. *J. Chem. Phys.* **1996**, *104*, 6696–6709.

[245] Caprion, D.; Bellier-Castella, L.; Ryckaert, J.-P. *Phys. Rev. E* **2003**, *67*, 041703.

[246] Chakrabarti, D.; Wales, D. J. *Phys. Rev. E* **2008**, *77*, 051709.

[247] Cienega-Cacerez, O.; Moreno-Razo, J. A.; Díaz-Herrera, E.; Sambriski, E. J. *Soft Matter* **2014**, *10*, 3171.

[248] Heinemann, T.; Palczynski, K.; Dzubiella, J.; Klapp, S. H. L. *J. Chem. Phys.* **2014**, *141*, 214110.

[249] Berardi, R.; Zannoni, C. *Mol. Cryst. Liq. Cryst.* **2003**, *396*, 177–186.

[250] Chakrabarti, D.; Wales, D. J. *Phys. Rev. Lett.* **2008**, *100*, 127801.

[251] Cienega-Cacerez, O.; García-Alcántara, C.; Moreno-Razo, J. A.; Díaz-Herrera, E.; Sambriski, E. J. *Soft Matter* **2016**, *12*, 1295–1312.

[252] Busselez, R.; Cerclier, C. V.; Ndao, M.; Ghoufi, A.; Lefort, R.; Morineau, D. *J. Chem. Phys.* **2014**, *141*, 134902.

[253] Rull, L. F.; Romero-Enrique, J. M. *Langmuir* **2017**, *33*, 11779–11787.

[254] Goto, M.; Takezoe, H.; Ishikawa, K. *J. Chem. Phys.* **2010**, *132*, 054506.

[255] Lamarra, M.; Muccioli, L.; Orlandi, S.; Zannoni, C. *Phys. Chem. Chem. Phys.* **2012**, *14*, 5368.

[256] de Luca, M. D.; Griffiths, M. K.; Care, C. M.; Neal, M. P. *Int. J. Electron.* **1994**, *77*, 907–917.

[257] Neal, M. P.; de Luca, M. D.; Care, C. M. *Mol. Simul.* **1995**, *14*, 245–258.

[258] Zewdie, H. *Phys, Rev. E* **1998**, *57*, 1793–1805.

[259] Cinacchi, G.; Tani, A. *J. Chem. Phys.* **2002**, *117*, 11388–11395.

[260] Heinemann, T.; Palczynski, K.; Dzubiella, J.; Klapp, S. H. L. *J. Chem. Phys.* **2015**, *143*, 174110.

[261] Martínez-Haya, B.; Cuetos, A. *Phys. Rev. E* **2010**, *81*, 020701(R).

[262] Hernández-Rojas, J.; Calvo, F.; Niblett, S.; Wales, D. J. *Phys. Chem. Chem. Phys.* **2017**, *19*, 1884–1895.

[263] Grecov, D.; Rey, A. D. *Mol. Cryst. Liq. Cryst.* **2003**, *391*, 57–94.

[264] Grecov, D.; Rey, A. D. *Rheol. Acta* **2003**, *42*, 590–604.

[265] Grecov, D.; Rey, A. D. *Carbon* **2004**, *42*, 1257–1261.

[266] de Andrade Lima, L. R. P.; Rey, A. D. *Chem. Eng. Sci.* **2004**, *59*, 3891–3905.

[267] de Andrade Lima, L. R. P.; Rey, A. D. *Chem. Eng. Commun.* **2006**, *193*, 1090–1109.

[268] Hong, S.; Chan, P. K. *Liq. Cryst.* **2006**, *33*, 295–306.

[269] Noroozi, N.; Grecov, D. *J. Non-Newtonian Fluid Mech.* **2014**, *208-209*, 1–17.

[270] Giustino, F. *Materials modelling using density functional theory*; Oxford University Press, 2014.

[271] Kohn, W. *Rev. Mod. Phys.* **1999**, *71*, 1253–1266.

[272] Hohenberg, P.; Kohn, W. *Phys. Rev.* **1964**, *136*, B864–B871.

[273] Kohn, W.; Sham, L. J. *Phys. Rev.* **1965**, *140*, A1133–A1138.

[274] Cohen, A. J.; Mori-Sánchez, P.; Yang, W. *Chemical Reviews* **2012**, *112*, 289–320.

[275] Tsuneda, T. *Density functional theory in quantum chemistry*; Springer, 2014.

[276] Dirac, P. A. M. *Math. Proc. Cambridge Philos. Soc.* **1930**, *26*, 376–385.

[277] Ceperley, D. M.; Alder, B. J. *Phys. Rev. Lett.* **1980**, *45*, 566–569.

[278] Vosko, S. H.; Wilk, L.; Nusair, M. *Can. J. Phys.* **1980**, *58*, 1200–1211.

[279] Perdew, J. P.; Wang, Y. *Phys. Rev. B* **1992**, *45*, 13244–13249.

[280] Becke, A. D. *Phys. Rev. A* **1988**, *38*, 3098–3100.

[281] Perdew, J. P.; Burke, K.; Ernzerhof, M. *Phys. Rev. Lett.* **1996**, *77*, 3865–3868.

[282] Zhang, Y.; Yang, W. *Phys. Rev. Lett.* **1998**, *80*, 890–890.

[283] Colle, R.; Salvetti, O. *Theor. Chim. Acta* **1975**, *37*, 329–334.

[284] Lee, C.; Yang, W.; Parr, R. G. *Phys. Rev. B* **1988**, *37*, 785–789.

[285] Becke, A. D. *J. Chem. Phys.* **1993**, *98*, 5648–5652.

[286] Adamo, C.; Barone, V. *J. Chem. Phys.* **1999**, *110*, 6158–6170.

[287] Israelachvili, J. N. *Intermolecular and Surface Forces*; Academic Press, 2011.

[288] Antony, J.; Grimme, S. *Phys. Chem. Chem. Phys.* **2006**, *8*, 5287.

[289] Grimme, S.; Antony, J.; Ehrlich, S.; Krieg, H. *J. Chem. Phys.* **2010**, *132*, 154104.

[290] Perdew, J. P.; Ruzsinszky, A.; Tao, J.; Staroverov, V. N.; Scuseria, G. E.; Csonka, G. I. *J. Chem. Phys.* **2005**, *123*, 062201.

[291] Mardirossian, N.; Head-Gordon, M. *Mol. Phys.* **2017**, *115*, 2315–2372.

[292] Ashcroft, N. W.; Mermin, N. D. *Solid State Physics*; Harcourt College Publishers, 1976.

[293] Thijssen, J. M. *Computational Physics*; Cambridge University Press, 2007.

[294] Schuchardt, K. L.; Didier, B. T.; Elsethagen, T.; Sun, L.; Gurumoorthi, V.; Chase, J.; Li, J.; Windus, T. L. *J. Chem. Inf. Model.* **2007**, *47*, 1045–1052.

[295] Pope, M.; Swenberg, C. E. *Electronic Processes in Organic Crystals and Polymers*; Oxford University Press, 1999.

[296] Valeev, E. F.; Coropceanu, V.; da Silva Filho, D. A.; Salman, S.; Brédas, J.-L. *J. Am. Chem. Soc.* **2006**, *128*, 9882–9886.

[297] Brédas, J.-L.; Beljonne, D.; Coropceanu, V.; Cornil, J. *Chem. Rev.* **2004**, *104*, 4971–5003.

[298] Hutchison, G. R.; Ratner, M. A.; Marks, T. J. *J. Am. Chem. Soc.* **2005**, *127*, 2339–2350.

[299] Senthilkumar, K.; Grozema, F. C.; Guerra, C. F.; Bickelhaupt, F. M.; Lewis, F. D.; Berlin, Y. A.; Ratner, M. A.; Siebbeles, L. D. A. *J. Am. Chem. Soc.* **2005**, *127*, 14894–14903.

[300] Löwdin, P.-O. *J. Chem. Phys.* **1950**, *18*, 365–375.

[301] Hansen, J.-P.; McDonald, I. R. *Theory of Simple Liquids*; Academic Press, 2006.

[302] Schlick, T. *Molecular Modeling and Simulation: An Interdisciplinary Guide*; Springer, 2010.

[303] Allen, M. P.; Tildesley, D. J. *Computer Simulation of Liquids (Oxford Science Publications)*; Clarendon Press, 1989.

[304] González, M. *École thématique de la Société Française de la Neutronique* **2011**, *12*, 169–200.

[305] Deserno, M.; Holm, C. *J. Chem. Phys.* **1998**, *109*, 7678–7693.

[306] Hockney, R.; Eastwood, J. *Computer Simulation Using Particles*; Taylor & Francis, 1988.

[307] Darden, T.; York, D.; Pedersen, L. *J. Chem. Phys.* **1993**, *98*, 10089–10092.

[308] Essmann, U.; Perera, L.; Berkowitz, M. L.; Darden, T.; Lee, H.; Pedersen, L. G. *J. Chem. Phys.* **1995**, *103*, 8577–8593.

[309] Andersen, H. C. *J. Chem. Phys.* **1980**, *72*, 2384–2393.

[310] Berendsen, H. J. C.; Postma, J. P. M.; van Gunsteren, W. F.; DiNola, A.; Haak, J. R. *J. Chem. Phys.* **1984**, *81*, 3684–3690.

[311] Nosé, S. *J. Chem. Phys.* **1984**, *81*, 511–519.

[312] Hoover, W. G. *Phys. Rev. A* **1985**, *31*, 1695–1697.

[313] Tuckerman, M. *Statistical Mechanics: Theory and Molecular Simulation*; Oxford University Press, 2010.

[314] Martyna, G. J.; Klein, M. L.; Tuckerman, M. *J. Chem. Phys.* **1992**, *97*, 2635–2643.

[315] Parrinello, M.; Rahman, A. *Phys. Rev. Lett.* **1980**, *45*, 1196–1199.

[316] Parrinello, M.; Rahman, A. *J. Appl. Phys.* **1981**, *52*, 7182–7190.

[317] Martyna, G. J.; Tobias, D. J.; Klein, M. L. *J. Chem. Phys.* **1994**, *101*, 4177–4189.

[318] Plimpton, S. *J. Comput. Phys.* **1995**, *117*, 1–19.

[319] Phillips, J. C.; Braun, R.; Wang, W.; Gumbart, J.; Tajkhorshid, E.; Villa, E.; Chipot, C.; Skeel, R. D.; Kalé, L.; Schulten, K. *J. Comput. Chem.* **2005**, *26*, 1781–1802.

[320] van der Spoel, D.; Lindahl, E.; Hess, B.; Groenhof, G.; Mark, A. E.; Berendsen, H. J. C. *J. Comput. Chem.* **2005**, *26*, 1701–1718.

[321] Fujimaki, Y.; Takekawa, M.; Fujisawa, S.; Ohshima, S.; Sakamoto, Y. *Polycyclic Aromat. Compd.* **2004**, *24*, 107–122.

[322] Luo, J.; Xu, X.; Mao, R.; Miao, Q. *J. Am. Chem. Soc.* **2012**, *134*, 13796–13803.

[323] Valiev, M.; Bylaska, E.; Govind, N.; Kowalski, K.; Straatsma, T.; Dam, H. V.; Wang, D.; Nieplocha, J.; Apra, E.; Windus, T.; de Jong, W. *Comput. Phys. Commun.* **2010**, *181*, 1477–1489.

[324] Yang, B.; et al. *ChemPhysChem* **2008**, *9*, 2601–2609.

[325] Laane, J. *Frontiers and Advances in Molecular Spectroscopy*; Elsevier Science, 2017.

[326] Isele-Holder, R. E.; Mitchell, W.; Ismail, A. E. *J. Chem. Phys.* **2012**, *137*, 174107.

[327] Wang, J.; Wolf, R. M.; Caldwell, J. W.; Kollman, P. A.; Case, D. A. *J. Comput. Chem.* **2004**, *25*, 1157–1174.

[328] Jorgensen, W. L.; Madura, J. D.; Swenson, C. J. *J. Am. Chem. Soc.* **1984**, *106*, 6638–6646.

[329] Jorgensen, W. L.; Severance, D. L. *J. Am. Chem. Soc.* **1990**, *112*, 4768–4774.

[330] Stewart, J. J. *J. Mol. Model.* **2013**, *19*, 1–32.

[331] Chantler, C. T. *J. Phys. Chem. Ref. Data* **2000**, *29*, 597–1056.

[332] Waasmaier, D.; Kirfel, A. *Acta Crystallogr.* **1995**, *A51*, 416–431.

[333] Parrinello, M.; Rahman, A. *J. Chem. Phys.* **1982**, *76*, 2662–2666.

[334] Ray, J. R. *Comput. Phys. Rep.* **1988**, *8*, 109–151.

[335] Nye, J. F. *Physical Properties of Crystals: Their Representation by Tensors and Matrices*; Oxford University Press, 1985.

[336] Hill, R. *Proc. Phys. Soc. London, Sect. A* **1952**, *65*, 349–354.

[337] Vanommeslaeghe, K.; Hatcher, E.; Acharya, C.; Kundu, S.; Zhong, S.; Shim, J.; Darian, E.; Guvench, O.; Lopes, P.; Vorobyov, I.; Mackerell, A. D. *J. Comput. Chem.* **2010**, *31*, 671–690.

[338] Yu, W.; He, X.; Vanommeslaeghe, K.; MacKerell, A. D. *Journal of Computational Chemistry* **2012**, *33*, 2451–2468.

[339] Vanommeslaeghe, K.; MacKerell, A. D. *J. Chem. Inf. Model.* **2012**, *52*, 3144–3154.

[340] Vanommeslaeghe, K.; Raman, E. P.; MacKerell, A. D. *J. Chem. Inf. Model.* **2012**, *52*, 3155–3168.

[341] Chen, L.; Mali, K. S.; Puniredd, S. R.; Baumgarten, M.; Parvez, K.; Pisula, W.; Feyter, S. D.; Müllen, K. *J. Am. Chem. Soc.* **2013**, *135*, 13531–13537.

[342] Oostenbrink, C.; Villa, A.; Mark, A. E.; Gunsteren, W. F. V. *J. Comput. Chem.* **2004**, *25*, 1656–1676.

[343] Theodorou, D. N.; Suter, U. W. *Macromolecules* **1985**, *18*, 1467–1478.

[344] Thomas, L. L.; Christakis, T. J.; Jorgensen, W. L. *J. Phys. Chem. B* **2006**, *110*, 21198–21204.

[345] Lee, J.-K.; Kim, J.-G.; Hembram, K. P. S. S.; Kim, Y.-I.; Min, B.-K.; Park, Y.; Lee, J.-K.; Moon, D. J.; Lee, W.; Lee, S.-G.; John, P. *Sci. Rep.* **2016**, *6*, 39624.

[346] Ziogos, O. G.; Theodorou, D. N. *Mol. Phys.* **2015**, *113*, 2776–2790.

[347] Beguin, F.; Frackowiak, E. *Carbons for Electrochemical Energy Storage and Conversion Systems*; CRC Press, 2009.

Index

X